CRANFIELD UNIVERSITY

ALEXANDER JAMES EDWARDS-SMITH

SUBSURFACE RADAR IMAGING FROM SPACE

CENTRE FOR ELECTRONIC WARFARE

PhD
Academic Year: 2014–2018

Supervisors: Dr. D. Andre, Prof. K. Morrison
May 2018

CRANFIELD UNIVERSITY

CENTRE FOR ELECTRONIC WARFARE

PhD

Academic Year: 2014–2018

ALEXANDER JAMES EDWARDS-SMITH

Subsurface Radar Imaging From Space

Supervisors: Dr. D. Andre, Prof. K. Morrison
May 2018

This thesis is submitted in partial fulfilment of the requirements for the degree of PhD.

Abstract

Ground Penetrating Radar (GPR) and Synthetic Aperture Radar (SAR) are two widely used techniques for acquiring radar images. GPR, as its name suggests, produces radar images of the below ground environment. SAR is a remote sensing technique which allows moving radar systems to produce radar images with dramatically improved resolutions over conventional radar systems.

Despite their benefits, both GPR and SAR suffer from certain limitations. In the case of GPR, the radar system has to be in close proximity with the subsurface volume being surveyed, which limits the process to relatively small areas that are easily accessible. SAR allows large areas to be surveyed rapidly from large distances, but cannot distinguish buried objects from surface objects.

This thesis focuses on a radar technique that offers the opportunity to overcome these limitations and allow subsurface radar imaging of large areas using radar data gathered by remote sensing systems. This novel technique is known as Virtual Bandwidth SAR (VB-SAR). VB-SAR utilises changes in soil moisture over a series of SAR images to differentiate buried objects from objects on the surface. In addition to this differentiation, VB-SAR also allows extremely high (centimetre scale) subsurface range resolutions to be obtained from SAR images with range resolutions measured in metres.

This research has experimentally demonstrated the basic feasibility of performing remote subsurface radar imaging with the VB-SAR scheme. Within the laboratory environment a buried target has been successfully imaged using VB-SAR and the fundamentals of VB-SAR have been verified. Dramatic increases in subsurface range resolutions have been demonstrated, as has the ability of the VB-SAR scheme to work correctly over a range of radar frequencies, observation angles and polarisations.

This laboratory work has been enabled by use of the Tomographic Profiling (TP) imaging scheme. TP is a synthetic aperture based imaging algorithm, but unlike conventional SAR TP produces images with a constant look angle over the entire imaging scene. This enabled the performance of the VB-SAR imaging scheme to be easily evaluated over a range of look angles using a single radar dataset and simplified the experimental setup.

In addition to the experimental work, simulation exercises have been conducted and image processors have been implemented. Simulation, using a simulator created as part of this work, has allowed testing of the VB-SAR scheme in a range of scenarios (side-looking SAR, different soils, multiple buried targets). The image processor work has implemented a high performance TP processor and a practical VB-SAR imager.

Acknowledgements

Firstly, I thank my Mother. Without her love, patience and encouragement over the last 29 years I would not be where I am now and none of this work would have been possible. Thank you, Mum, for all that you do for me.

The support and love of my wife, Nasyitah, is a daily joy. Thank you for always having faith in me and backing me in all that I do. I hope we have many years of joy and happiness together ahead of us.

Thank you to my supervisors, Prof. Keith Morrison and Dr. Daniel Andre. You have both been incredibly supportive and understanding throughout my time as a PhD student and I deeply appreciate your sharing of your experience, knowledge and ideas with me. In addition, thank you Dr. Ivor Morrow for chairing my review meetings and reviewing my thesis.

I would also like to thank my fellow students, friends, colleagues and family for their support, discussions and banter over the course of my studies. Thank you all for all the good times, and thank you for being there during the hard times. You have all contributed more to this research than you know.

Finally, I would like to thank Cranfield University for funding this PhD studentship and Martin-Baker Aircraft Co. Ltd. for allowing me time to complete my thesis.

Contents

List of Figures

List of Tables

List of Abbreviations

AIRSAR	Airborne Synthetic Aperture Radar
APS	Atmospheric Phase Screen
ATI	Along Track Interferometry
DEM	Digital Elevation Model
DInSAR	Differential Interferometric Synthetic Aperture Radar
DLR	German Aerospace Center [Deutsches Zentrum fr Luft- und Raumfahrt]
DORIS	Doppler Orbitography and Radiopositioning Integrated by Satellite
DSM	Digital Surface Model
DTM	Digital Terrain Model
FFT	Fast Fourier Transform
FM	Frequency Modulation
GB-SAR	Ground Based Synthetic Aperture Radar
GIS	Geographic Information System
GNSS	Global Navigation Satellite System
GPR	Ground Penetrating Radar
GPU	Graphics Processing Unit
GUI	Graphical User Interface
HF	High Frequency
IEEE	Institute of Electrical and Electronics Engineers

IFFT	Inverse Fast Fourier Transform
ISAR	Inverse Synthetic Aperture Radar
InSAR	Interferometric Synthetic Aperture Radar
IWS	Interferometric Wide Swath
JAXA	Japan Aerospace Exploration Agency
JPL	Jet Propulsion Laboratory
LEO	Low Earth Orbit
MATLAB	Matrix Laboratory
MIRAS	Microwave Imaging Radiometer with Aperture Synthesis
PSInSAR	Permenant Scatterer Interferometric Synthetic Aperture Radar
NASA	National Aeronautics and Space Administration
NDVI	Normalized Difference Vegetation Index
NESZ	Noise Equivalent Sigma Zero
RCS	Radar Cross Section
RF	Radio Frequency
RFI	Radio Frequency Interference
RMS	Root Mean Square
SAR	Synthetic Aperture Radar
SCR	Signal to Clutter Ratio
SIR	Shuttle Imaging Radar
SMAP	Soil Moisture Active Passive
SMC	Soil Moisture Content
SMOS	Soil Moisture and Ocean Salinity
SNR	Signal to Noise Ratio
SPDT	Single Pole Double Throw
SRTM	Shuttle Radar Topography Mission

SubSAR	Subsurface Synthetic Aperture Radar
TEC	Total Electron Count
TP	Tomographic Profiling
UHF	Ultra High Frequency
USDA	United States Department of Agriculture
UXO	Unexploded Ordinance
VB	Virtual Bandwidth
VB-SAR	Virtual Bandwidth Synthetic Aperture Radar
VHF	Very High Frequency
VNA	Vector Network Analyser
VWC	Vegetation Water Content

Chapter 1

Introduction

This thesis presents research performed at Cranfield University's Shrivenham Campus between February 2014 and February 2017. This work concentrated on demonstrating and validating the Virtual Bandwidth Synthetic Aperture Radar (VB-SAR) technique proposed by [1]. This work was funded by a bursary provided by Cranfield University.

This first chapter starts with a background and rationale review, detailing the motivations for studying the VB-SAR technique. It then describes the aim, research questions and methodology pursued by this work. Next, lists of original contributions made and published works is presented. Finally, an overview of the layout of this thesis is presented.

1.1 Background and Rationale

Radio Detection And Ranging, or Radar as it is universally known today, stems from James Clerk Maxwell's theory of electromagnetism and the experimental verification of that theory performed by Heinrich Hertz [2]. Since those earliest days, radar has been under continuous development for a wide variety of applications, from detecting aircraft

to imaging astronomical bodies. In all cases, the fundamental principle of transmitting an electromagnetic signal and receiving reflections of that signal from targets is the same. By applying different processing techniques to those echoes it is possible to implement a wide variety of techniques

One technique that has attracted a large amount of attention in recent years is Synthetic Aperture Radar (SAR). This technique allows a very large virtual antenna to be synthesised by applying sophisticated processing techniques to radar data collected using a small physical antenna which is moving during the data collection process. By using this technique a very high resolution image can be obtained despite using a small antenna (which would usually yield a very poor resolution). The era of space flight has driven the interest in this technique; it is extremely difficult to mount a large antenna on a satellite but the constant motion of an orbiting satellite generates an ideal platform for SAR imaging. A satellite in Low Earth Orbit (LEO) typically makes a complete orbit every 90 minutes which allows rapid acquisition of wide area imagery with a rapid revisit rate [3].

Another technique that has been extensively studied is Ground Penetrating Radar (GPR). In contrast to the space based SAR case this involves the radar system being in close proximity to the ground and moved slowly across the area being surveyed to provide an image of the below ground environment. The proximity is necessary to ensure separation of the strong ground return and any buried objects which are present. This approach works well for small area surveying in locations that are hazard free and freely accessible, such as archaeological surveys and locating voids in concrete structures but is poorly suited to large area surveying and examining hazardous or poorly accessible areas.

The ability to utilise the large scale coverage of SAR to provide below ground imagery as per GPR would represent a significant breakthrough for many applications and users. Detection and location of unexploded ordinance is one obvious area that would benefit from remote sensing techniques.

The VB-SAR technique, first proposed by [1] represents a method to achieve this significant breakthrough. By leveraging a change in soil moisture content (SMC) that occurs during a series of SAR image acquisitions a subsurface image can be constructed. By using the effect of the change in SMC to create the subsurface image a very high depth resolution is obtainable; this resolution is independent of the resolution of the radar system.

The VB-SAR process works using differential phase measurements acquired using a well established process, Differential Interferometic SAR (DInSAR). The use of DInSAR data means that there are no new data acquisition problems associated with the VB-SAR scheme. In an ideal case, soil moisture content (SMC) measurements are also available and are used to organise the DInSAR data and allow the application of an accurate depth scale to the subsurface images. Without accurate SMC measurements the VB-SAR process can still indicate the presence of buried targets.

This work aims to demonstrate the feasibility of the VB-SAR method and move it from theory to reality. In order to do this it is necessary to answer the fundamental question of "Does the VB-SAR process work in reality and what are the limitations of the process?". This thesis aims to answer this question using two tactics: simulation and experimentation.

1.2 Aim, Research Questions and Methodology

1.2.1 Research Aim

The aim of the work presented in this thesis is to investigate and validate the VB-SAR subsurface imaging technique. The key aim is to provide an experimental demonstration of the technique that unambiguously shows the technique working. Furthermore, this

work aims to give confidence that the VB-SAR process will work in the real world by exploring the range of conditions under which the technique is usable.

The VB-SAR method is a relatively undeveloped concept. Initial laboratory based experimentation [4] and software based simulation have both provided promising early results. There are several unanswered questions related to the general applicability of the scheme that remain, however.

The aim of this work is to develop the VB-SAR technique into a robust subsurface imaging system that can be applied to a variety of soils viewed from a spaceborne radar system. The steps proposed in order to achieve this are;

1. Demonstrate and characterise the behaviour of the VB-SAR imaging scheme in the laboratory.

2. Use the experimental work to validate, develop, and drive a radar simulator that can be used to rigorously test the VB-SAR scheme across a wider range of scenarios than is possible with the laboratory experimentation.

3. With knowledge gained from 1) and 2), investigate the ability of current airborne and spaceborne radar systems to detect subsurface targets.

1.2.2 Research Questions

1. Is the VB-SAR imaging scheme feasible in a laboratory environment?

2. Are there likely issues with operating a VB-SAR scheme in a non-laboratory environment?

3. What limitations does the VB-SAR scheme suffer from?

4. Given the current state of spaceborne SAR systems, is it possible to demonstrate the VB-SAR scheme with them?

1.2.3 Methdology

The methodology used in this research is a mixture of experimentation and simulation. The two methods compliment each other, the experimentation acting as a rigorous demonstration of the VB-SAR process across a relatively limited range of parameters and providing a means to check the accuracy of the simulation, whilst the simulation allows wide ranging exploration of the VB-SAR scheme beyond what is feasible in the laboratory.

1.3 Original and Novel Contributions

The major novel contributions of this work can be summarised as follows:

- The world's first experimental demonstration of the VB-SAR subsurface imaging technique as a method to acquire subsurface radar images from stand off distances. The basic single polarisation, single incidence angle and single real frequency band demonstration has been published at both conference [5] and journal level [6].

- Extended simulation and experimental demonstration of the VB-SAR imaging process over a range of incidence angles, polarisations and real frequencies, including split bandwidth/delta-k VB-SAR imaging.

- Development of a subsurface SAR simulator, capable of simulating the behaviour of buried targets over a range of soil types, moisture levels, radar frequencies and imaging geometries.

- Implementation of a Tomographic Profiling (TP) image processor in MATLAB, giving dramatically increased performance and utility over the existing processor written in Fortran.

- Creation of a practical VB-SAR imaging script in MATLAB, capable of using both real and simulated datasets

- Demonstration via simulation that VB-SAR using side-looking SAR systems is feasible.

1.4 Published Works

As part of this work, the following papers have been published;

1. A. Edwards-Smith, K. Morrison, S. Zwieback and I. Hajnsek, **"Verification of the Virtual Bandwidth SAR Scheme for Centimetric Resolution Subsurface Imaging From Space,"** in IEEE Transactions on Geoscience and Remote Sensing, vol. 56, no. 1, pp. 25-34, Jan. 2018. `https://doi.org/10.1109/TGRS.2017.2717340`

2. A. Edwards-Smith and K. Morrison, **"VB-SAR For Remote Stand-off Subsurface Imaging: First Demonstration,"** Proceedings of EUSAR 2016: 11th European Conference on Synthetic Aperture Radar, Hamburg, Germany, 2016, pp. 1-4. `https://ieeexplore.ieee.org/document/7559491/`
   (Placed second in "Best Student Paper" competition at EUSAR 2016)

3. K. Morrison, A. Edwards-Smith, S. Zwieback and I. Hajnsek, **"Virtual bandwith SAR (VB-SAR) for centimeter-scale vertical profiling through a soil at C-band**

from space," 2016 IEEE International Geoscience and Remote Sensing Symposium (IGARSS), Beijing, 2016, pp. 7419-7422. https://doi.org/10.1109/IGARSS.2016.7730935

4. S. Zwieback, I. Hajnsek, A. Edwards-Smith and K. Morrison, **"Depth-Resolved Backscatter and Differential Interferometric Radar Imaging of Soil Moisture Profiles: Observations and Models of Subsurface Volume Scattering,"** in IEEE Journal of Selected Topics in Applied Earth Observations and Remote Sensing, vol. 10, no. 7, pp. 3281-3296, July 2017. https://doi.org/10.1109/JSTARS.2017.2671025

5. S. Zwieback, I. Hajnsek, A. Edwards-Smith and K. Morrison, **"Imaging subsurface soil moisture dynamics using tomographic profiling: Observations and modelling,"** 2016 IEEE International Geoscience and Remote Sensing Symposium (IGARSS), Beijing, 2016, pp. 5256-5259. https://doi.org/10.1109/IGARSS.2016.7730369

6. R.K. Ningthoujam, H. Balzter, K. Tansey et al., **"Airborne S-band SAR for forest biophysical retrieval in temperate mixed forests of the UK"** in MDPI Remote Sensing, vol. 8, no. 7, pp. 609, 2016. https://dx.doi.org/10.3390/rs8070609

In addition to these published papers, posters have been presented at two student conferences; Wavelength 2016 (RSPSoc's student conference held at MSSL, Surrey) and the Defence and Security Doctoral Symposium 2015 (hosted by Cranfield University at the Defence Academy of the United Kingdom, Oxfordshire).

Papers 1. and 2., along with the two posters are contained within Appendix A of this thesis.

1.5 Thesis Outline

Chapter 1, *Introduction*, gives a brief overview of the research undertaken. It outlines the motivations for the research, discusses the aims of the project, highlights original contributions made by the project, lists peer reviewed work published during the course of this project and closes with an overview of the structure of this thesis.

Chapter 2, *Review of Radar Principles*, provides the reader with an introduction to the background principles of the VB-SAR process. The topics covered include a review of basic radar principles, the electrical behaviour and modelling of soils, and the techniques used to remotely measure soil moisture content.

Chapter 3, *Review of Radar Processing Techniques*, describes radar processing techniques of relevance to this work. The Synthetic Aperture Radar process is discussed, including its limitations and current spaceborne missions used for SAR. Methods for measuring phase using SAR (InSAR and DInSAR) are also detailed. Following this, the two techniques used extensively in this work (TP and VB-SAR) are introduced, explored and explained. In addition, a brief description of the MATLAB implementation of the TP and VB-SAR schemes produced during this work is provided.

After these three introductory chapters the following chapters are concerned with the work done and results obtained by this project.

Chapter 4, *Subsurface and VB-SAR Simulation*, details the simulation work performed during this project. Basic soil modelling is presented along with the use of the VB-SAR simulator to demonstrate the VB-SAR process. In addition to a basic initial demonstration, the impact of different observation angles, bandwidths and frequencies is explored. Finally, the ability of the VB-SAR scheme to differentiate targets buried at different depths directly above and below each other is demonstrated.

Chapter 5, *VB-SAR Demonstration*, contains the VB-SAR results obtained from the

experimental work. In this chapter the first experimental demonstration of the VB-SAR technique is presented, along with extended results (multiple incidence angles, polarisations, and varying real frequencies and bandwidths) which support the general applicability of the VB-SAR process.

Chapter 6, *Realworld Considerations*, discusses various additional considerations and limitations that will need to be considered for "real world" utilisation of the VB-SAR scheme. This includes operating VB-SAR in a "detection mode" when accurate SMC information is not available, the effect of a different soil texture and the operation of VB-SAR with side-looking SAR data. Finally, this chapter considers the ability of various existing airborne and spaceborne radar systems to detect buried targets.

Chapter 7, *Conclusions*, acts a closing chapter to this thesis. Within this chapter a summary of key results is presented, along with a list of original contributions made and a series of suggestions for future research efforts.

Appendix A, *Published Work*, contains both published first author papers, along with the two posters presented as part of this project.

Chapter 2

Review of Radar Principles

2.1 Introduction

This chapter presents fundamental overviews of several basic concepts that are used and referred to later in this thesis. This is intended to introduce the reader to specific concepts that they may not be familiar with.

The chapter starts with a review of some of the fundamental principles of radar. Topics such as the equations governing the basic detection range of a given radar system, the factors controlling the resolution of a particular radar and the basic principles of polarimetry are addressed.

Following this is a brief discussion of soils, and the theoretical modelling of them. The effects of soil on a propagating radar wave are also explored.

Finally, a review of techniques for remotely sensing SMC is presented. This review covers both passive (receive only) and active (transmit and receive) methods for sensing SMC.

2.2 Basic Concepts

2.2.1 Fundamental Principle of Radar

At a fundamental level, radar involves illuminating a target scene with electromagnetic waves and monitoring the reflected waves. By careful processing of the returned signals it is possible to detect and locate objects within the scene, building up a complete picture of the scene.

These electromagnetic waves are made up of propagating synchronised oscillating electrical and magnetic fields. These fields are perpendicular to each other and the direction of propagation. The frequency of these oscillations defines the position of the wave on the electromagnetic spectrum. This spectrum is categorised by the ITU from 3Hz (Extremely Low Frequency radio waves) to 300EHz (Gamma rays).

Within the overall spectrum is a section from 3MHz to 300GHz containing frequencies often used for radar purposes. This section is categorised into various frequency bands by IEEE Std 521-2002, as shown in Table 2.1. These IEEE frequency band designations are used throughout this thesis.

2.2.2 The Radar Equation

The power received by a monostatic radar system (a system which uses the same antenna for both transmitting and receiving signals) when observing a point target can be estimated using the following equation [7].

$$P_r = P_t \frac{G^2 \lambda^2 \sigma}{(4\pi)^3 R^4 l} \tag{2.1}$$

Where P_r is the power received by the radar system (measured at the receiver input), P_t is the power transmitted (measured at the receiver output), G is the gain of the antenna,

Designation	Frequency Span
HF	0.003 to 0.03 GHz
VHF	0.03 to 0.3 GHz
UHF	0.3 to 1 GHz
L	1 to 2 GHz
S	2 to 4 GHz
C	4 to 8 GHz
X	8 to 12 GHz
Ku	12 to 18 GHz
K	18 to 27 GHz
Ka	27 to 40 GHz
V	40 to 75 GHz
W	75 to 110 GHz
mm or G	110 to 300 GHz

Table 2.1: IEEE Std 521-2002 frequency bands

λ is the wavelength in use, σ is the radar cross section of the target, R is the range to the target and l is a term to account for losses in the radar system itself.

The same equation can be slightly modified and used for a bistatic radar system (a system which uses different antennas for transmitting and receiving- these antennas may or may not be co-located) as follows.

$$P_r = P_t \frac{G_t G_r \lambda^2 \sigma}{(4\pi)^3 R_t^2 R_r^2 l} \tag{2.2}$$

Where G_t is the gain of the transmit antenna, G_r is the gain of the receive antenna, σ is the radar cross section of the target, R_t is the range from the transmit antenna to the target and R_r is the range from the receive antenna to the target.

2.2.3 The Radar Range Equation

The maximum range, R, that a target can be detected at can be estimated according to the following equation, which is a modification and rearrangement of the basic monostatic

radar equation previously given in Equation 2.1 [7].

$$R = \left[\frac{P_m T_c G^2 \lambda^2 \sigma}{(4\pi)^3 (S/N)_0 k T_0 F l} \right]^{1/4} \tag{2.3}$$

When P_m is the mean transmitted power, T_c is the coherent processing duration, $(S/N)_0$ is the signal to noise ratio the system requires to detect a target, k is Boltzmann's constant, T_0 is the operating temperature and F is the receiver noise figure.

This equation shows that there are several ways to improve the maxiumum detection range of a given radar system for a particular target. Increasing the transmitted power and/or the processing duration increases the detection range. Equivalently, decreasing the required signal to noise ratio, operating temperature or system losses will have the same effect.

2.2.4 Radar Resolution

The resolution of a radar system is the minimum separation distance at which two targets can be distinguished from one another. For an imaging radar system there are two resolutions; range resolution, which is the resolution along the radar beam, and cross range resolution, which is the resolution perpendicular to the radar beam.

The range resolution is related to the bandwidth of the radar signal via the following equation

$$Res_R = \frac{c}{2B} \tag{2.4}$$

Where c is the speed of light in the medium of propagation and B is the bandwidth of the transmitted chirp. This shows that a higher bandwidth will give a higher resolution, however the bandwidth in use is invariably limited by statutory spectrum restrictions and the radar system's hardware.

The cross range resolution of the system is related to the width of the radar beam. This in turn is governed by the physical dimensions of the radar antenna in the case of a conventional radar system (certain techniques can be used to synthesise a larger antenna, as detailed in Chapter 3). The beamwidth from a particular antenna is given by:

$$\beta = \frac{\lambda}{D_{real}} \tag{2.5}$$

Where λ is the wavelength being transmitted and D_{real} is the physical dimension of the antenna aperture in the cross range dimension.

As the beamwidth spreads over the distance to a target, this results in a cross range resolution Res_{CR} of a real aperture radar system being given by:

$$Res_{CR} = \frac{\lambda R}{D_{real}} \tag{2.6}$$

This equation shows that, unlike range resolution, cross range resolution degrades with increasing range to the target. Again, synthetic aperture techniques can overcome this limitation, as discussed in Chapter 3.

2.2.5 Radar Cross Section

The Radar Cross Section (RCS) of an object is a measure of the amount of energy reflected back to the radar by an object versus the amount of energy incident on that object due to the radar. The RCS is usually used as a parameter to describe distinct man-made features (aircraft, vehicles etc.) whereas for natural distributed targets (grasslands, oceans etc.) the RCS per unit area (typically known as sigma-nought) is used.

The unit of RCS is m^2 and the value of RCS for a particular target is simply the physical size of a smooth sphere that would give the same return as the target of interest.

Hence, by definition, the RCS (σ) of a smooth sphere is given by;

$$\sigma = \pi r^2 \tag{2.7}$$

As long as

$$\lambda \ll r \tag{2.8}$$

and

$$\lambda \ll R \tag{2.9}$$

Where r is the radius of the sphere, λ represents the wavelength of the incident radiation and R is the range to the sphere.

Note that as the sphere is spatially uniform there is no dependency on orientation relative to the antenna and no dependency on frequency whilst the two conditions are satisfied. This makes a sphere an often used target for calibrating a radar system.

The RCS of other simple objects often include a dependency on frequency, for example the RCS of a flat plate is given by;

$$\sigma_{max} = \frac{4\pi w^2 h^2}{\lambda^2} \tag{2.10}$$

Where w and h are the width and height of the plate respectively, and assuming that λ is much smaller than w and h.

Note that in this case the return to the radar varies depending on the orientation (slope) of the plate, from a maximum when the plate directly faces the antenna (boresight) to a minimum (zero for an ideally thin plate) when the plate is orientated at 90 to the antenna (end-fire).

For more complex targets (such as vehicles or aircraft) there are many reflecting surfaces and shapes present. In these cases the RCS can vary wildly with the orientation of the target relative to the radar system [8], [9].

2.2.6 Sigma-Nought

Sigma-Nought (also known as Sigma-Zero or σ^0 or σ_0, the radar back scattering coefficient or the normalised radar cross section) describes the amount of backscatter the radar sees per unit area (typically pixel area) in the ground range when observing a particular type of ground;

$$\sigma^0 = 10log_{10}(\frac{RCS}{A}) \tag{2.11}$$

Where A is the ground area (or area of the pixel of interest). σ^0 is in dB. σ^0 is used for extended natural targets such as sea, bare soil, forests etc.; typical values are between +5dB and -40dB. Whilst σ^0 represents the RCS in ground range, the RCS per unit area of the incident wavefront (γ^0) can also be considered, by;

$$\gamma^0 = \frac{\sigma^0}{cos\theta_i} \tag{2.12}$$

Where θ_i is the angle of incidence. [10] show that σ^0 of a given soil is strongly dependent on the incidence angle, surface roughness and SMC.

2.2.7 Noise Equivalent Sigma Zero

NESZ is a measure of the level of noise in the system which in turn governs the smallest target return a particular radar system can theoretically discern. This is a measure of the sensitivity of the system and is expressed in dB; smaller values are better.

Typical values of NESZ specified for spaceborne SAR systems are between -18 and

-25dB; this varies for a particular system depending on which mode it is operating in [11], [12]. Airborne SAR systems typically have substantially lower NESZ values, as low as -50dB, representing dramatically improved sensitivity over spaceborne systems [13], [14]. For subsurface imaging, a low value of NESZ is critical as buried targets are usually severely attenuated by the soil and vegetation above them.

2.2.8 Polarimetry

The polarisation of an electromagnetic wave describes the shape drawn by the tip of the electric field vector over time when viewed in the direction of propagation. The general case is elliptical polarisation, where the tip of the electric field describes an ellipse over time. Specific cases are circular polarisation, where the electric field describes a circle, and linear polarisation where the electric field oscillates in one direction only.

For linear polarisation, the electric field oscillates in a single plane along the direction of propagation. This plane can be orientated at any angle, but two cases of particular interest to radar are the vertical and horizontal cases. As the names suggest, a vertically polarised wave has its electric field oscillating in the vertical direction, whereas a horizontally polarised wave has its electric field oscillating in the horizontal direction.

By illuminating a target in both horizontal and vertical polarisations, and observing the response of the target in both horizontal and vertical polarisations a complete set of backscattering coefficients can be collected. This are typically denoted as σ_{hh}, σ_{vv}, σ_{hv} and σ_{vh}, where the first subscript character denotes the polarisation of the transmitted wave and the second character denotes the polarisation of the reflected wave. A radar system is said to be fully polarimetric if it is capable of observing all four of these coefficients, and partially polarimetric if it can observe more than one of them. A fully polarimetric radar system can use the four measurements to synthesise the response of the target to any

combination of transmitted and reflected polarisations in a process known as polarisation synthesis. The scattering coefficients are split into two cases; copolarisation (often shortened to copol) when the transmitted and received waves are of the same polarisation, and crosspolarisation (or crosspol) when they are of different polarisations. For a given target, the backscattering coefficients can vary significantly with frequency, incidence angle and target rotation.

Within a typical scene different targets present different responses across the different polarisations. By comparing images acquired in different polarisations it is possible to identify particular features within the radar scene.

2.3 Soil Modelling

2.3.1 Introduction to Soils

When working with subsurface imaging radars the type(s) of soil encountered by the radar system can have significant effects on system performance, especially attenuation. For this reason it is important to consider what soil is, the classification methods used for soil and the interactions between soil and electromagnetic signals.

Soil is the top layer of the ground (excluding areas where bedrock is exposed) that provides a medium for plants to grow in. It is generally a complex mixture of weathered bedrock, decaying biological matter and water with different types of soil present in layers. At both a macro and microscopic level it is an inhomogeneous medium, which makes obtaining meaningful subsurface images challenging as radar backscattering occurs when radar waves are incident on a dielectric inhomogeneity. Conventional spaceborne radar processing techniques do not provide the necessary range resolution to resolve buried targets from such clutter or the soil surface itself; the range resolution of such systems

is much poorer than the penetration depth of the radar wave which can be as low as a wavelength [15].

Of particular significance to radar studies is the fact that the electrical properties of a soil at a given frequency varies with both the make up of the soil (which generally does not change within a given area) and the moisture content of the soil (which can rapidly change). This can make subsurface radar imaging a challenging affair (due to high levels of attenuation) but also gives the chance to exploit the changes in SMC that often occur to gain additional information about the subsurface scene.

2.3.2 Soil Texture

The main factor affecting the physical properties of soils is the relative amounts of sand, silt and clay within the soil, referred to as the "texture" of a soil. Sand, silt and clay Soils are typically classified into different types depending on this ratio of components. Unfortunately there is no international standard for soil types and no single international standard for defining what sand, silt and clay are.

One standard often used is the United States Department of Agriculture (USDA) soil triangle, shown in Figure 2.1 (illustration taken from [16]). The USDA defines clay particles as having diameters of less than 0.002mm, silt particles as having diameters between 0.002mm and 0.05mm and sand particles as having diameters between 0.05mm and 2mm.

Differing soil textures can have dramatic effects on how radar signals interact with the soil. However, the soil texture is a constant over the typical time periods of interest for radar imaging, leaving variation in SMC as the dominant influence on the soil's response to radar waves.

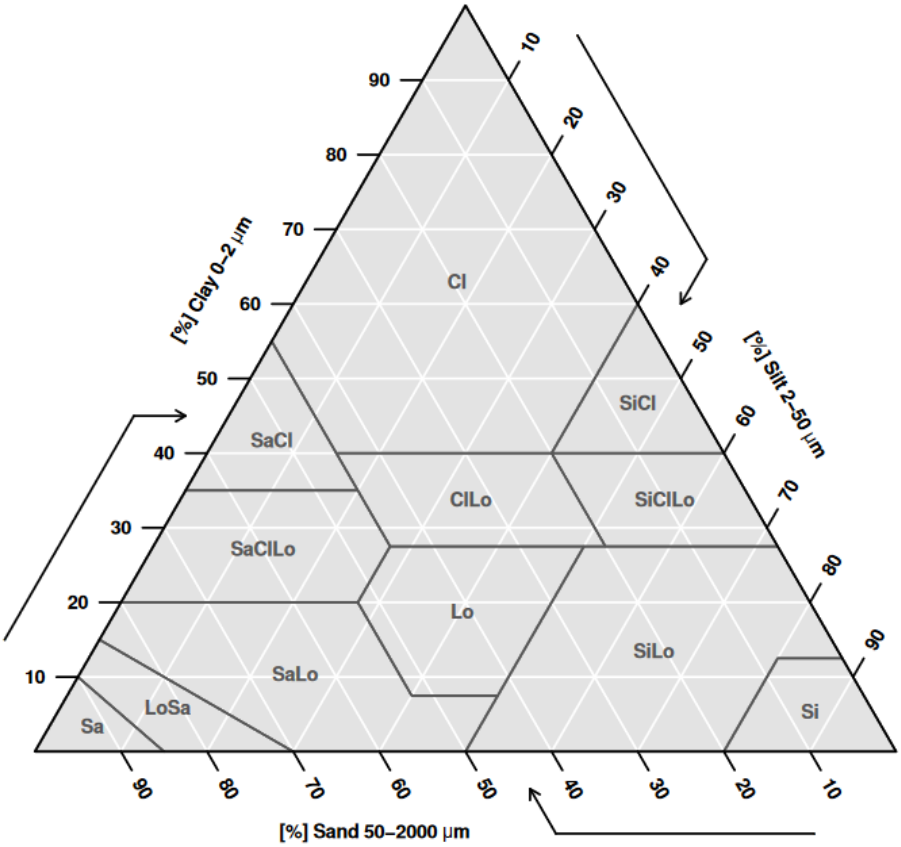

	abbr	name
1	Cl	clay
2	SiCl	silty clay
3	SaCl	sandy clay
4	ClLo	clay loam
5	SiClLo	silty clay loam
6	SaClLo	sandy clay loam
7	Lo	loam
8	SiLo	silty loam
9	SaLo	sandy loam
10	Si	silt
11	LoSa	loamy sand
12	Sa	sand

Figure 2.1: USDA soil triangle (Image and table taken from [16])

2.3.3 Electrical Modelling of Soil

As previously metioned, the electrical properties of a particular soil are heavily influenced by the water content of the soil. This is because dry soil has a relatively low dielectric constant ($\approx$ 2 - 4, dependant on the make up of the soil) and water has a relatively high dielectric constant (approximately 80).

The moisture content of soil is measured by the volumetric water content, given by

$$M_v = \frac{Vol_W}{Vol_T} \tag{2.13}$$

Where M_v is the volumetric water content, Vol_W is the volume of water present and Vol_T is the total volume (of both soil and water) present. The moisture content of soil often varies rapidly over time- for example, rainfall can rapidly increase the water content of upper soil layers.

In order to simulate radar interactions with a soil volume mathematical models attempt to relate a soil's physical properties (typically texture and moisture content) to its electrical properties at certain frequencies. There are multiple mathematical models published (e.g. [17, 18, 19, 20]) in the existing literature. A more detailed description and implementation of some of these models is presented in Chapter 4.

2.3.4 Electromagnetic Propagation Through Soil

The non-homogeneous nature of soil complicates subsurface imaging. Rather than the signal propagating through a medium with one dielectric constant and few anomalies the soil medium can heavily attenuate the radar signal and introduce clutter into radar images. Losses due to attenuation are typically very high compared to radars operating in air which means penetration depths are usually relatively shallow. However, by assuming that the

soil is homogeneous with respect to SMC and texture it is possible to predict how a radar signal may interact with the soil [4] .

The attenuation constant, α describes the attenuation experienced by a wave of a given wavelength, λ, travelling through a medium and is given by:

$$\alpha = k\sqrt{\varepsilon_r}[1+\tan^2\delta]^{1/4}\sin(\frac{\delta}{2}) \tag{2.14}$$

Where k is the wavenumber, given by $\frac{2\pi}{\lambda}$, ε_r is the real part of the relative permittivity of the medium ([17] shows that the real part of the relative permittivity of a soil dominates over the imaginary part) and δ is the loss tangent, given by:

$$\delta = \tan^{-1}(\frac{\varepsilon_i}{\varepsilon_r}) \tag{2.15}$$

Where ε_r is the real part of the relative permittivity of the medium and ε_i is the imaginary part of the relative permittivity of the medium

The attenuation coefficient can be used to calculate the losses experienced by a wave travelling through a known thickness of medium by:

$$A_x = A_0 e^{-\alpha x} \tag{2.16}$$

Where A_0 is the amplitude of the wave at the source, A_x is the amplitude of the wave at distance x, the distance the wave has propagated through the medium with the attenuation constant, α.

In addition to the naturally high attenuation experienced in moist soils the multiple layers present can cause additional losses in the path to a buried target by introducing reflections. The magnitude of this effect can be predicted by using the Fresnel Equations

at each boundary;

$$Reflec_s = |\frac{n_1 \cos\theta_i - n_2 \cos\theta_t}{n_1 \cos\theta_i + n_2 \cos\theta_t}|^2 \tag{2.17}$$

$$Reflec_p = |\frac{n_1 \cos\theta_t - n_2 \cos\theta_i}{n_1 \cos\theta_t + n_2 \cos\theta_i}|^2 \tag{2.18}$$

Where $Reflec$ is the reflection coeffecient (subscript s or p denoting s-polarisation or p-polarisation respectively) that gives the fraction of incident power that is reflected by the boundary, θ_i is the angle of incidence with the interface between the two layers, θ_t is the angle of transmission and n_1 and n_2 are the dielectric constants of the two layers.

The related transmission coeffecients (T_s and T_p) that give the fraction of incident power that is transmitted through the boundary are given by:

$$T_s = 1 - Reflec_s \tag{2.19}$$

and

$$T_p = 1 - Reflec_p \tag{2.20}$$

The net effect of this (heavy attenuation and scattering losses) is that subsurface targets will present very weak returns to a space-based system; this necessitates selecting satellites with as low an NESZ as possible, and as a high transmission power and range resolution as possible, in order to have the best chance of resolving subsurface targets.

Similar to the attenuation coefficient, there is a phase term, β, given by

$$\beta = k\sqrt{|\varepsilon|}\cos(\frac{\delta}{2}) \tag{2.21}$$

[17] show that the complex dielectric constant of a soil is dominated by its real part,

so δ is always small and $\cos(\frac{\delta}{2}) \approx 1$ at all moisture contents. Therefore the previous equation simplifies to:

$$\beta = k\sqrt{|\varepsilon|} \tag{2.22}$$

This shows that a radar wave of a given frequency travelling through a soil will experience a phase shift compared to the same wave travelling through freespace. This also implies that a change in soil dielectric (due to a change in SMC) will change the phase shift experienced by a given radar wave.

2.4 Derivation of Soil Moisture

The soil models mentioned previously use known SMC and soil texture to estimate the dielectric properties of a given soil. In this sense, they are being used in the "forward" direction. They can also be used in the "backward" direction, calculating SMC using the sensed dielectric properties and known soil texture.

In the real world, precise SMC information may not be available. For certain locations (easily accessible or reference sites in settled climates) in-situ SMC measurements may be available. However, it is highly likely that in-situ measurements will not be practical in all areas, and in any case collecting in-situ measurements are labour intensive for wide area surveying.

What is preferable at a global scale is to have some way of inferring SMC from remote sensing measurements. The are two possible methods to achieve this; active sensing (using radar systems which transmit and receive radar waves) and passive sensing (using microwave radiometers which only receive microwaves).

SMC sensing over large area is of significant interest to many different fields such

as weather prediction, climate modelling and drought monitoring [21]; to this end, two space based missions are currently dedicated to observing SMC; ESA's Soil Moisture and Ocean Salinity (SMOS) mission (using a single L-band (1.4GHz) radiometer which implements aperture synthesis for improved resolution [22]) and NASA's Soil Moisture Active Passive (SMAP) mission [21]. As its name suggests, SMAP was intended to use both active and passive techniques to derive SMC, however the active radar failed soon after launch so it is currently only using an L-band radiometer with a 6m aperture antenna.

2.4.1 Active Sensing of Soil Moisture

Active sensing of SMC is attractive for subsurface radar imaging as the moisture content of the upper soil layers may vary relatively quickly (due to rainfall etc.). This could mean that an in-situ SMC measurement would be valid for a few hours only, whereas an SMC measurement extracted from the same radar images used for subsurface imaging purposes would be inherently up-to-date and relevant.

[10] demonstrated that the surface backscatter measured by a radar system is dependent on incidence angle, surface roughness, and the dielectric properties of the soil surface (which, as previously noted, depend strongly on SMC and soil texture).

Within the laboratory environment, the incidence angle and surface roughness can be held constant and as such relative moisture content could be derived from σ_0 measurements using this method. In contrast, a typical radar scene imaged by a spaceborne SAR both of these properties will vary spatially over a scene (although the incidence angle at each pixel can be estimated from fundamental imaging geometry) and surface roughness is likely to vary temporally (due, for instance, to human activities such as ploughing).

As such, a model that relates both surface roughness and SMC to the measured backscatter is strongly desired. Soil texture is considered to be less critical; although

it is difficult to measure remotely over large areas and [23] indicates that soil texture retrieval using radar is currently under explored. The one relevant paper referenced, [24], shows limited success with soil texture retrieval. Fortunately, soil texture is expected to change slowly, if at all, and published maps of soil texture are available at reasonable resolutions, e.g. 1km [25].

2.4.1.1 Active Soil Moisture Sensing Algorithms

Given a known soil texture and a partially (HH, VV and HV) polarimetric radar system, [10] present a technique that allows surface roughness and SMC to be generated from a single frequency radar system. In this technique measurements of σ^0_{vv} , σ^0_{hh} and σ^0_{hv} are required. The copolarised and crosspolarised ratios (p and q respectively) are calculated by

$$p = \frac{\sigma^0_{hh}}{\sigma^0_{vv}} \tag{2.23}$$

$$q = \frac{\sigma^0_{hv}}{\sigma^0_{vv}} \tag{2.24}$$

Having calculated these ratios from the measured values, Equation 2.25 is iteratively solved for Γ_o, the Fresnel reflectivity at nadir

$$(\frac{2\theta}{\pi})^{1/3\Gamma_o}[1 - \frac{q}{0.23\sqrt{\Gamma_o}}] + \sqrt{p} - 1 = 0 \tag{2.25}$$

Once a value for Γ_o has been calculated it is possible to calculate the real part of the dielectric content of the soil in question by recalling that $\varepsilon \approx \varepsilon_r$ is valid for soil materials (in this case, at nadir at an air-soil interface, $n_1 \approx 1$, $\cos\theta_i = \cos\theta_t = 1$). Hence, using

Fresnel at nadir, ε_r is calculated from Γ_o via

$$\Gamma_o = |\frac{1-\sqrt{\varepsilon_r}}{1+\sqrt{\varepsilon_r}}|^2 \tag{2.26}$$

Now ε_r is known, and given the soil texture from another source, the method given by [17] may be used to calculate the SMC in the backwards direction. Finally, the RMS soil height, s, (a measure of surface roughness) can be calculated by solving

$$\sqrt{p} = 1 - (\frac{2\theta}{\pi})^{[1/3\Gamma_o]} exp(-ks) \tag{2.27}$$

where k is the wavenumber, given by $\frac{2\pi}{\lambda}$.

[26] present an alternative model that allows SMC extraction given only copolarised SAR data and knowledge of the soil texture. In this model, the backscatter coefficients, σ^0_{hh} and σ^0_{vv} are related to the incidence angle (θ_i), the real part of the dielectric constant (ε), the RMS height of the surface (h), the wave number k and the wavelength in cm, λ by the two equations shown below.

$$\sigma^0_{hh} = 10^{-2.75} \frac{\cos^{1.5}\theta}{\sin\theta^5} 10^{0.028\varepsilon\tan\theta} (kh\sin^{1.4}\theta)\lambda^{0.7} \tag{2.28}$$

$$\sigma^0_{hh} = 10^{-2.35} \frac{\cos^{3}\theta}{\sin\theta} 10^{0.046\varepsilon\tan\theta} (kh\sin^{3}\theta)^{1.1}\lambda^{0.7} \tag{2.29}$$

The limits of validity specified for this model are frequencies between 1.5 and 11GHz, surface roughness in the range of 0.3-3cm RMS height and the incidence angle being between 30 and 65°. Using these two equations together it is possible to calculate ε and h. Once ε is known and given knowledge of the soil texture it is possible to use the model presented by [17] to derive the SMC of the soil. [26] state that normalised difference

vegetation indexes (NDVI, a measure of the amount of vegetation present) up to 0.4 allow acceptable SMC retrieval.

Note that it is likely that the SMC will not be constant over a SAR scene ([27]) so this calculation may need to be repeated for each pixel, or perhaps groups of pixels if individual pixel computation is overly computationally demanding.

2.4.1.2 The SMAP Active Algorithm

SMAP's active portion uses an L-band radar operating in VV, HH and HV polarisations along with an unfocused SAR technique to give a 1km resolution SMC image after averaging. Measurements from the HV polarisation are intended to be used for correcting for the effects of vegetation. [28] details the theoretical basis of the algorithm. Firstly, it identifies the need to use a time series of observations in both co polar channels in order to solve an ambiguity between the dielectric constant of the soil and the roughness of the surface. By using a time series it is possible to assume that the surface roughness is constant over the series of observations which resolves the ambiguity.

The basic approach of the algorithm is to use a retrieval algorithm which searches for a value of SMC which provides the closest match between the observed backscatter and that predicted by a forward model. The algorithm estimates the surface roughness (assumed to be constant over the series of observations) in the scene and then uses that value to retrieve an estimate of the dielectric constant. In addition, an extra parameter, the numerical density of vegetation scatterers is calculated to handle biases between the forward model's simulations and the actual properties of the vegetation.

The original intention of the SMAP mission was to use the purely active radar measurements as both a research dataset and as a data source for the combined active/passive SMC product. The active part of the mission has been ended by a terminal failure of the

radar transmitter which means that only passive SMC products are available, the production of these is detailed in the next section.

2.4.2 Passive Sensing of Soil Moisture

As an alternative to actively sensed data, passively sensed data can also be used to estimate SMC. A key advantage of passive sensing over active sensing is that for passive sensing over bare/minimum vegetation cover SMC is the dominant influence on the received signal. The soil brightness temperature change influenced by realistic SMC variations is well within the sensitivities of microwave radiometers [29] and well within the sensitivity of practical spaceborne radiometers [30]. Both SMAP and SMOS use passive sensing techniques.

At lower frequencies, i.e. $\lambda \geq 10cm \therefore f \leq 3GHz$ the vegetation and surface roughness influences on passive measurements are much reduced and "moderate" vegetation coverage is acceptable [29].

[22] identify that L-band radiometry is optimum for surface SMC detection when compared to higher frequency radiometry, active radar, and optical sensing methods. However, passive methods are sensitive to RFI from a multitude of sources that may interfere with radiometer measurements. Despite the fact that SMOS operates in the protected part of L-band [31] significant RFI was initially experienced and resolving these issues required significant work with the operators of individual RFI emitters [32].

The key issue with passive SMC sensing for subsurface radar imaging is the very low spatial resolution obtained by both current missions; SMAP operates at a resolution of about 40km and SMOS produces products with a resolution of about 43km. Whilst this is sufficient for showing regional or global trends it would be insufficient for practical subsurface radar imaging, given that spaceborne radar produce images with resolutions in

the order of a few metres.

This resolution limitation for radiometers arises inherently from using a passive measurement; there is no possibility of synthesising a very large aperture using the movement of a small real aperture as can be done with active radar systems. Similarly, other radiometers that produce data suitable for SMC analysis (such as AMSR-2 aboard GCOM-W) suffer from a lack of resolution.

2.4.2.1 The SMOS Passive Algorithm

SMOS is a spacecraft with one instrument, the Microwave Imaging Radiometer with Aperture Synthesis (MIRAS), which operates at L-band to deduce soil moisture and ocean salinity (hence, SMOS). The aperture synthesis referred to in the name "MIRAS" is performed using multiple small radiometers mounted on three rigid booms extending from the main spacecraft body to give a significant boost to the ground resolution of the system (although the resolution is still very coarse compared to SAR systems). L-band is used because it is the lowest frequency band which is internationally protected from RFI emissions [33].

SMOS's SMC retrieval algorithm is rather complex and is described in detail by [34]. A very brief and grossly simplified summary is presented here.

The input data from SMOS to the retrieval algorithm is Level 1C radiometer data. This is multi-incidence angle brightness temperatures, which have been calibrated, formed into images, geolocated and segregated into sea and land datasets. Additional auxiliary data from other sources (soil texture, land use, meteorological data and other factors) are also input to the retrieval algorithm.

The core idea of the algorithm is to use an iterative approach to minimise the difference between the observed brightness temperatures and the brightness temperatures

predicted by a forward model which uses the auxiliary data and values for SMC. The reported SMC value is the one which minimises the difference between the output of the model and the observed data. This apparent simplicity is severely complicated by the need to take into account the beam pattern of the radiometer and the fact that a single SMOS pixel will inevitably (due to its 43km size) contain multiple different types of ground which needs to be taken into account when using the forward model [35].

2.4.2.2 The SMAP Passive Algorithm

SMAP's basic SMC retrieval algorithm (extensively detailed in [36]) uses single polarisation observations of the microwave brightness temperature of the surface. These are obtained from the SMAP Level-1 brightness temperature product which contain time-ordered, geolocated and calibrated brightness temperature measurements that have been resampled to SMAP's fixed 36km imaging grid. In addition, the SMC retrieval algorithm requires numerous other datasets;

- Surface temperature
- Vegetation Water Content (VWC) and vegetation opacity coefficient
- Vegetation single scattering albedo
- Surface roughness
- Land cover type
- Soil texture
- Data flags (land/water, RFI, urban area, ice/snow etc.)

The first step in the moisture retrieval is to correct the observed brightness temperature to take into account the presence of open water on the surface. This correction is simply applied by taking the proportion of the observed scene which is water, as shown below

$$T_B^{FOV} = \alpha T_B^{water} + (1-\alpha) T_B^{land} \tag{2.30}$$

Where T_B^{water} is the brightness temperature of water, obtained from a theoretical model which takes into account the physical surface temperature (obtained from a predictive model), T_B^{FOV} is the brightness temperature observed by the system, α is the proportion of the scene that is surface water and T_B^{land} is the brightness temperature of the land.

As SMAP operates at L-band, the brightness temperature of the surface observed by SMAP is proportional to its emissivity (e) multiplied by its physical temperature (T);

$$e = \frac{T_B^{land}}{T} \tag{2.31}$$

The emissivity of a given soil surface, e^{surf}, is related to its SMC. However, the emissivity observed by SMAP, e, is modified by various parameters as given by [37];

$$e = [1-\omega][1-\gamma][1+(1-e^{surf}\gamma] + e^{surf}\gamma \tag{2.32}$$

where ω is the single scattering albedo (which tends to be very small and is sometimes assumed to be zero at L-band, but the SMAP algorithm does not assume this) and γ is the one way transmissitivity of the vegetation, given by

$$\gamma = exp[-\tau \sec \theta_i] \tag{2.33}$$

where τ is the vegetation optical depth (which is related to the vegetation water content by a proportionality value, b, which varies depending on the frequency of observation,

polarisation and the type of vegetation).

Substituting Equation 2.33 into 2.32 and rearranging gives

$$e^{surf} = \frac{e - 1 + \gamma^2 + \omega - \omega\gamma^2}{\gamma^2 + \omega\gamma - \omega\gamma^2} \tag{2.34}$$

This equation allows correction of the observed emissivity for the effects of vegetation. In the SMAP processing chain, values of b and ω will be obtained from a look up table for each type of land cover and the VWC is derived from the NDVI obtained from other earth observation satellites. After correction for vegetation effects, the surface roughness must be corrected for to obtain the smooth surface soil emissivity (e^{soil}). SMAP uses the method given by [38] to find e^{soil};

$$e^{soil} = 1 - [1 - e^{surf}]exp[h\cos^2\theta] \tag{2.35}$$

where h is a parameter related to the frequency, polarisation, surface height standard deviation and geometric properties of the soil surface; the SMAP algorithm will obtain this value from a lookup table, dependent on the type of land cover. θ is the incidence angle. It is possible that the $cos^2\theta$ term may be reduced to a $\cos\theta$ term or dropped entirely to avoid over correction for roughness.

Finally, having obtained e^{soil} it is possible to obtain the dielectric constant of the surface via the Fresnel equations in both H and V polarisations;

$$e^{soilH} = 1 - |\frac{\cos\theta - \sqrt{\varepsilon_r - \sin^2\theta}}{\cos\theta + \sqrt{\varepsilon_r - \sin^2\theta}}|^2 \tag{2.36}$$

$$e^{soilV} = 1 - |\frac{\varepsilon_r\cos\theta - \sqrt{\varepsilon_r - \sin^2\theta}}{\varepsilon_r\cos\theta + \sqrt{\varepsilon_r - \sin^2\theta}}|^2 \tag{2.37}$$

Having obtained ε_r (the complex dielectric constant) from the appropriate Fresnel

equation the SMC can then be retrieved via a soil model; SMAP uses the model given by [20] as the default model. The SMAP mission requirement for SMC retrieval accuracy is +/-0.04cm^3/cm^3 volumetric accuracy in the top 5cm of the soil for VWC $\leq 5kg/m^2$. Supporting this, the instrument functional requirements for the radiometer specify a resolution of 40km and a total radiometric uncertainty of 1.3K.

2.4.3 SMC Sensing for Subsurface Radar Imaging

The choice of SMC data from active or passive sensors is not immediately clear. Actively sensed SMC benefits from potentially a much higher resolution (as it relies on σ^0 measurements which SAR techniques can provide at very high resolutions), however it requires polarisation diversity and can be severely influenced by other factors (such as the presence of vegetation).

In contrast, passively sensed SMC presents much lower resolution data but it is less susceptible to some kinds of interference (although RFI emitters can severely disrupt operations in particular areas). In addition, this SMC is a published product (rather than being generated independently), with quantified accuracies, and extensively researched and tested algorithms. Passive soil data is also globally available at reasonable update rates.

For subsurface radar imaging it is vital to have contemporary SMC measurements alongside subsurface radar data acquisitions. Rapid variations in SMC may occur due to rainfall events between a passive SMC acquisition and a radar acquisition. It is therefore preferable to use simultaneously acquired data for both subsurface radar imaging and SMC extraction; currently such a requirement is only satisfied by extracting SMC information from radar images using active SMC sensing techniques.

2.5 Summary

This chapter has given a brief introduction to certain basic principles that are used in the rest of this thesis. The basic principles of radar have been reviewed, alongside the fundamentals of soil modelling and the remote sensing of SMC. The next chapter builds on these principles and introduces specific radar processing and imaging techniques.

Chapter 3

Review of Radar Processing Techniques

3.1 Introduction

This chapter presents a review of several radar processing techniques that are of interest and relevance to this work.

Firstly, the basic principle of SAR is explored. The basic process is explained first, followed by a brief discussion of the limitations of the process. After this, the fundamentals of the SAR image processing algorithm used during this work to process acquired radar data into radar images is presented. Closing off the discussion of SAR is a review of current and historic spaceborne SAR systems.

Next, techniques for extracting phase information from a SAR data collection are discussed. This extraction of phase information is of critical importance for a real world implementation of the VB-SAR technique, as it is a phase-based technique.

Following this, the TP imaging process is described. This is an along-track radar imaging scheme introduced by [39], utilising synthetic aperture beamforming to produce a radar image with a constant reconstruction angle across a scene (unlike SAR). This scheme is of particular interest to this work as it enabled a relatively simple experimental

scheme utilising existing laboratory facilities. The imaging algorithm itself is described and the MATLAB implementation of the algorithm produced as part of this work is also presented.

The final radar technique discussed is the VB-SAR technique, which is the focus of this work. This technique, first described by [15], gives the potential to acquire subsurface radar images from airborne or spaceborne radar systems, in contrast to current techniques that require the radar system and target soil volume to be in relatively close proximity. Both the general principles of the scheme and the MATLAB VB-SAR processor implemented as part of this work are described.

Finally, the chapter is closed by a concluding review which summarises the contents of the chapter.

3.2 Synthetic Aperture Radar

The fundamental principle of radar is to detect distant objects by reflecting radio waves off of them. Within this fundamental concept there are a multitude of different techniques that process the radar data in different ways in order to optimise the resulting image for particular purposes.

One of these processing techniques is the SAR technique and its derivatives. This technique is of particular interest to this work as it allows very high resolution radar images to be collected over a wide area. SAR allows a very large radar antenna aperture to be synthesised from a relative small physical antenna mounted on a radar platform which is moving relative to a target scene. This aperture synthesis allows very high cross range resolutions to be obtained using a small antenna, overcoming the inverse tradeoff between antenna size and cross range resolution that blights real aperture systems. This means that SAR is extremely attractive to space based radar systems, where it is not feasible to use a

large physical antenna. The continuous motion of the radar system also allows very large areas to be rapidly imaged.

3.2.1 Fundamentals of SAR

SAR was originally developed in the early 1950s (it appears that Carl Wiley at the Goodyear Aircraft Corporation showed theoretically the principle of SAR in 1951 [40, 41] whilst independently Kovaly et. al at the University of Illinois reported their progress in operating a very early SAR system in 1952 [41] as a side development from missile guidance systems.

SAR is of particular interest for airborne or spaceborne radar systems which typically operate at large distances from their target scenes. Over such distance a real antennas beam would spread considerably, necessitating an implausibly long antenna to counter this spreading. Platform limitations prevent the realistic use of very large antennas; in the case of aircraft mass and aerodynamic limitations prescribe that a radar subsystem must be as lightweight and compact as possible, in the case of a spaceborne platform launch vehicle constraints (size, shape, lifting capacity and vibration environment) limit the size and weight of the radar subsystem.

SAR removes the need for a large physical antenna by using aperture synthesis to emulate a very large physical antenna. Not only that, but it also generates a cross range resolution that is independent of range, which is a substantial advantage for radar systems which operate at long distances from their targets. As an added bonus, the defined movement of aircraft and spacecraft relative to ground based targets is ideal for SAR and their rapid movement over the ground also allows rapid surveying of large areas.

3.2.2 SAR Parameters

3.2.2.1 Cross Range Resolution

As previously discussed in Chapter 2, the cross range resolution of a real antenna radar system is governed by the physical size of the antenna in the cross range direction and the distance to the target under observation, as per the following equation:

$$Res_{CR} = \frac{\lambda R}{D_{real}} \tag{3.1}$$

Where Res_{CR} is the peak to null cross range resolution and R is the range to the target.

This equation clearly shows that the larger an antenna is the better the cross range resolution it will give at a given distance. Unfortunately, as the range to the target increases the antenna size required to maintain a given resolution also increases.

Similarly, the cross range resolution degrades (becomes larger) as the radar wavelength increases. This means that as the frequency decreases, the cross range resolution will degrade. For subsurface radar imaging, this is a particular concern as lower frequencies offer better penetration into soil and are therefore preferred.

As an example, working Equation 3.1 for a spaceborne radar system operating in C-band (with a wavelength of 6cm) at an orbital height of 693km (a typical low earth orbit for a remote sensing spacecraft) with a radar inclination angle of 45°, a cross range resolution requirement of 25m gives a required antenna size of 2.35km.

Clearly it is totally unfeasible to mount such an antenna on a spacecraft and an alternative technique must be used to obtain radar images of reasonable resolution from a spacecraft.

The SAR technique takes advantage of the movement of a radar platform to synthesise a much larger antenna aperture than that given by the physical antenna. As the platform

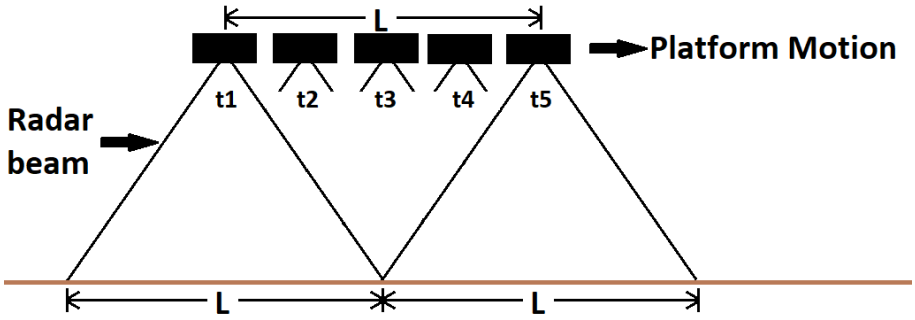

Figure 3.1: Fundamental SAR principle. Single radar sensor on a moving platform illuminates a target scene. Over time t1 to t5 a virtual antenna array is synthesised. Absolute maximum array length, L, limited by beamwidth on ground. Redrawn version of sketch in [42]

moves a given scatterer in the target scene is illuminated by the real antenna's main beam for a period of time, during which the scatterer is hit by a number of pulses which each produce an echo, which are recorded by the radar system in complex form (amplitude and phase). By processing the recorded echoes according to their phase shift it is possible to synthesise an antenna which is as long as the distance which the platform moves whilst the scatterer is still in the main beam of the real antenna.

As shown in Figure 3.1, the movement and operation of the radar platform can be thought of as a series of individual elements. For the simplest mode of SAR operation (unfocused), summing the returns from each of the individual antenna elements (in reality each transmitted pulse from the one antenna on the SAR platform) generates the synthetic aperture. This is directly equivalent to the summing performed by the electrical interconnections in a physical array antenna. This unfocused operation does not take into account the phase differences present in the returns from a single target over multiple elements.

In the SAR case, the cross range resolution is given by

$$X_{res} = \frac{\lambda R}{2L_{Eff}} \tag{3.2}$$

where L_{Eff} is the effective aperture of the SAR. Note that the factor of 2 in the denominator represents a factor of 2 improvement in resolution over that given by a real aperture radar system. This arises due to both the transmit and receive phase shifts giving the beam pattern in the SAR case, whereas in the real aperture case only the receive phase shift forms the antenna pattern [43].

From this, it may seem that the cross range resolution can be infinitely improved by increasing L_{Eff}. However, ignoring focusing issues and assuming a non-steerable antenna the factor that limits L_{Eff} (and hence the maximum cross range resolution) is the beamwidth of the SAR systems real antenna. This limitation arises due to the need to keep a given target in the view of all elements of the synthetic array. This limitation can be expressed as

$$L_{Max} = \frac{\lambda R}{D_{real}} \tag{3.3}$$

Where L_{Max} is the maximum possible length of the synthetic aperture. Note that this is simply the beamwidth of the antenna multiplied by the range, i.e. the width of the beam at range R.

From these last two equations we can examine the maximum obtainable resolution (by setting $L_{Eff} = L_{Max}$ and ignoring focusing issues),

$$X_{ResMax} = \frac{\lambda R}{2L_{Max}} = \frac{\lambda R D_{real}}{2\lambda R} = \frac{D_{real}}{2} \tag{3.4}$$

This derivation shows that the cross range resolution of a SAR system is directly proportional to the length of the real antenna on the platform (a smaller real antenna giving a better SAR resolution) and, crucially, is independent of both range and frequency. This range independence arises because targets at longer ranges are illuminated with a larger

synthetic aperture because the wider beam at further range allows those more distant targets to stay in the SAR's field of view for a longer period of time. However, the improvement in theoretical resolution an increasingly small real antenna would give must be considered against the lower SNR obtained with a smaller antenna (given the same transmit power); it is this tradeoff that drives the minimum size of the real antenna.

As per the Nyquist sampling theorem, the distance between adjacent samples in the synthetic aperture must not be greater than $\frac{\lambda}{2}$, otherwise severe ambiguities will be present in the produced SAR images.

3.2.2.2 Range Resolution

The range resolution (resolution in the same direction as the radar beam) of a SAR system is not improved by the movement of the platform and follows the standard pulsed radar relation to pulse width.

As such, the peak to null range resolution of a radar along the look (or slant) direction, Res_R is given by;

$$Res_R = \frac{c}{2B_r} \tag{3.5}$$

Where c is the speed of light in the medium of propagation and B_r is the real bandwidth of the transmitted chirp.

The radar waves from a non-nadir looking SAR are incident with the target scene at an angle termed the incidence angle (θ_i), which is the angle between the incident wave and the perpendicular to the surface. Hence the ground range resolution becomes dependent on this angle, via;

$$Res_R = \frac{c}{2B_r \sin\theta_i} \tag{3.6}$$

Note that this dependence on θ_i implies that the ground range resolution of a SAR system will vary over a single SAR image.

3.2.2.3 Unambiguous Range

There are two factors that limit the unambiguous range of a given radar system.

Firstly, the time gap between individual transmitted pulses limits the unambiguous range. A simple radar which repeatedly transmits pulses with an pulse repetition interval (PRI) of τ will have an unambiguous range given by:

$$R_{unambig} = \frac{c\tau}{2} \tag{3.7}$$

This limit arises because this is the maximum range a pulse can travel to and back to the radar system before the next pulse is transmitted. An object at a larger range than this may still present a detectable return to the radar system, but the reflection from this object will arrive back at the radar after the next pulse has been transmitted. This means that the radar will be unable to determine whether the reflection is from a distant objected illuminated by the first pulse or from a nearby object illuminated by the second pulse.

Secondly, in order to form a bandwidth to give range resolution, the output of the radar is stepped across a series of discrete frequencies. In a linear chirp, these frequencies are seperated by a fixed frequency, f_{step}.

These frequency steps lead to an unambiguous range for the system (assuming operation in free space) given by

$$R_{unambig} = \frac{c}{2f_{step}} \tag{3.8}$$

Where $R_{unambig}$ is the unambiguous range, c is the speed of light in a vacuum and f_{step} is the frequency step between adjacent frequencies in the transmitted chirp. This limit comes from the phase difference in the echoes caused by adjacent frequencies in the frequency sweep.

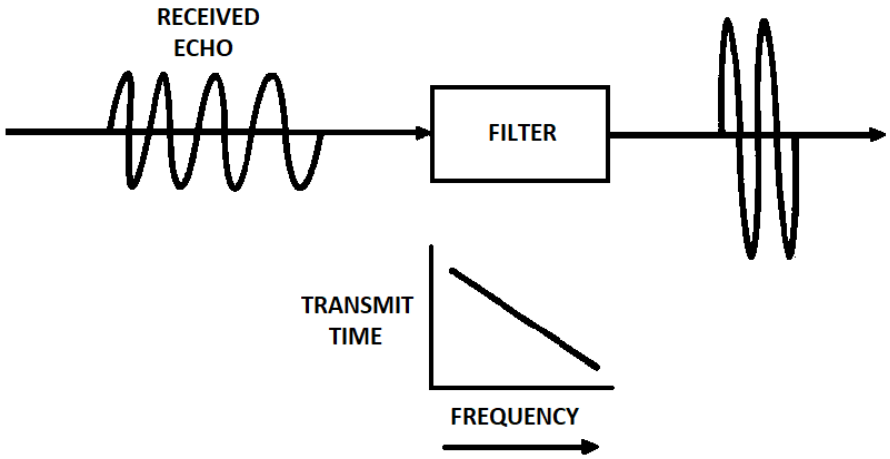

Figure 3.2: Pulse compression concept. An echo from a target illuminated by a frequency chirp is passed through a filter that has a time delay inversely proportional to frequency. This compresses the pulse in time (Taken from page 164 of [44])

3.2.2.4 Pulse Compression

From Equation 3.5 it is immediately apparent that an improvement in resolution can be obtained by utilising very short pulses (which increase the bandwidth of the signal). However, problems can start to be encountered with very short pulses as it becomes increasingly difficult (due to hardware limitations) to transmit ever shorter pulses with very high peak powers (high average power is necessary for good signal to noise ratio (SNR) which means that the shorter the pulse is in terms of time the higher the peak power must be).

Pulse compression can help bypass this problem of very high peak powers in short bursts. Pulse compression works by transmitting long duration modulated pulses and during the receiving process the pulses are compressed in time by decoding the previously applied modulation.

The simplest form of compression is the application of linear FM, as shown in Figure 3.2. The receive chain includes a filter that introduces a time delay that is inversely proportional to the frequency of the signal. This causes the received signal to bunch up, resulting in increased pulse amplitude and, crucially, decreased pulse width.

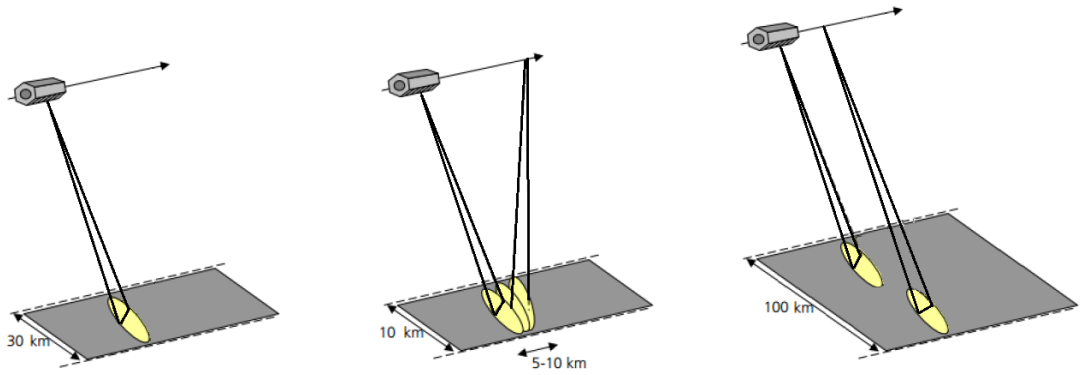

Figure 3.3: Principles of TerraSAR-X operating modes. From left to right, strip map, spotlight and scanSAR (Adapted from [45])

3.2.2.5 SAR Imaging Modes

Modern SAR systems (such as TerraSAR-X [45] and Sentinel-1 [46]) are capable of operating in multiple modes that allow different compromises between image coverage and resolution to be made. These modes and their names differ between different satellites, so as an example those modes implemented by TerraSAR-X are shown in Figure 3.3 and discussed below.

In the simplest mode, strip map (shown on the left of Figure 3.3), the real antenna beam from the SAR platform is at a fixed side-looking angle, sweeping along the target scene as the platform moves across. This produces a continuous image strip and balances good coverage with reasonable resolution.

As TerraSAR-X has the ability to electronically steer its antenna beam two additional imaging mode types are possible; spotlight and scanSAR.

In spotlight mode a single target scene of interest is held in the beam for longer by electronically steering the beam in the azimuth direction, as shown in the middle scenario in Figure 3.3. This provides multiple benefits to image quality; a longer synthetic array can be used compared to a non-steered antenna, as the beamwidth of the real antenna

is no longer the factor that determines when the target is in view of the radar and it is also possible use a narrower beamwidth whilst maintaining the original non-steered array length (or trade the narrower beamwidth and longer array possibilities to a happy mid-point). This will improve the signal to noise ratio of the system by increasing the antenna gain in the main lobe.

In contrast, in scanSAR mode resolution is traded for increased coverage. The elevation angle is varied via electronic beam steering (as demonstrated on the right of Figure 3.3) to sweep the beam repeatedly across the swath in the down range direction. As the beam is swept the swath width is dramatically increased but because the platform is moving at a constant speed the receive time is limited for each beam footprint, therefore resolution is degraded. However, for some applications this reduced resolution is an acceptable price to pay for improved coverage.

3.2.3 SAR Limitations

As previously discussed, SAR processing does not offer any range resolution improvement over using a real aperture radar system. In addition, there are several other limitations and issues that must be considered and possibly compensated for when using SAR imagery.

3.2.3.1 Speckle

Speckle is a type of noise inherent to SAR images. It is noise that results from the coherent summation of returns from different scatterers within a single resolution cell and is random in nature. An image displaying noticeable speckle is shown in the top half of Figure 3.4.

On homogeneous areas (such as grass land) where the individual scatterers are smaller

Figure 3.4: Above: SAR image displaying large amounts of speckle, Below: Same scene processed using the spatial multi-look technique to reduce speckle (From [47])

than a single pixel in the radar image the return from each scatterer within a single pixel will be coherently summed by the system into a single value for the entire pixel. As coherent summation involves phase statistically some pixels will experience more constructive combination of returns (and so appear brighter) and some will experience less constructive combination (and hence appear darker). It is this variation that causes speckle.

Speckle is a problem in SAR images as it can be mistaken for texture during further image analysis. It is therefore of great importance that speckle is removed or minimised. This is done in two main ways; correction during acquisition or removal during processing.

The first method of speckle removal, correction during acquisition, involves a technique called multi-look processing. This process is performed either in the frequency or spatial domain [48].

In the frequency domain the full bandwidth of the radar is divided into multiple bands. Each band produces an image of the same scene with reduced range resolution due to the lower bandwidth used. The resulting images are then incoherently summed together pixel by pixel which results in a lower speckle at the cost of lower spatial resolution. In the spatial domain a similar principle is employed, but the target is observed from multiple angles and the images produced are then incoherently added, as per the frequency domain method.

In both cases, the amount of speckle present decreases by a factor, approximately $\sqrt{n_{look}}$, where n_{look} is the number of looks or bands. To keep image resolution reasonably high, whilst obtaining an efficient reduction in speckle, an n_{look} of 3 or 4 is usually used. The effect of applying this to an image is shown in the lower half of Figure 3.4.

The second method of speckle removal, removal during processing involves applying filters to the raw images produced by the system that contain speckle. These filters vary in complexity but are usually adaptive filters which take local image statistics into account

when applying filtering. This means that areas with high speckle will be heavily filtered whereas those areas with less speckle will undergo less filtering [49].

3.2.3.2 SAR Image Distortions

Due to the geometry of SAR (the direct radar path to the target is in slant range, not ground range) several distortions are frequently seen; foreshortening, layover and shadowing. Foreshortening and layover effects are produced by the same issue (topographical features being mapped onto a flat horizontal 2-D image plane via the slant range), the features being observed and the imaging geometry influencing which one is experienced.

Foreshortening is illustrated in Figure 3.5. As shown, due to the observing geometry the peak of the hill is at the same slant range from the antenna as a point on the ground closer in ground range. Because the imaging plane is typically set to ground level the peak appears closer in ground range than it really is, distorting the hill's shape. The extreme case of this, where the peak maps to a point closer than the bottom of the hill is called layover and this is shown in Figure 3.6.

Coupled to foreshortening and layover is shadowing, which is demonstrated in Figure 3.7. In this case, the slope B-C and a distance down range of the hill is not visible in the radar image because the hill's topography blocks radar waves from illuminating those areas. Depending on geometry, shadowing can be combined with foreshortening and/or layover. These distortions mean that interpretation of SAR images in undulating terrain can be difficult and may require comparison with other sources of information, such as photographs or in-situ measurements of the topography.

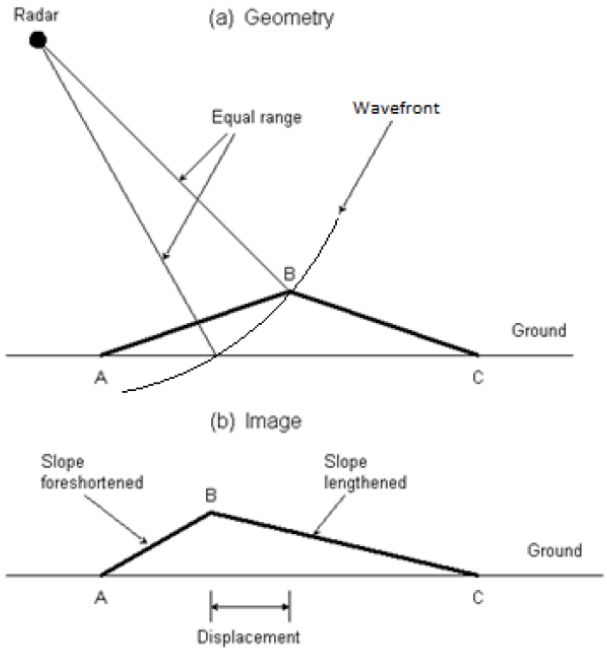

Figure 3.5: Foreshortening. Due to the equal slant range between the peak and a point on the ground the peak is displaced in the image (Modified from [47])

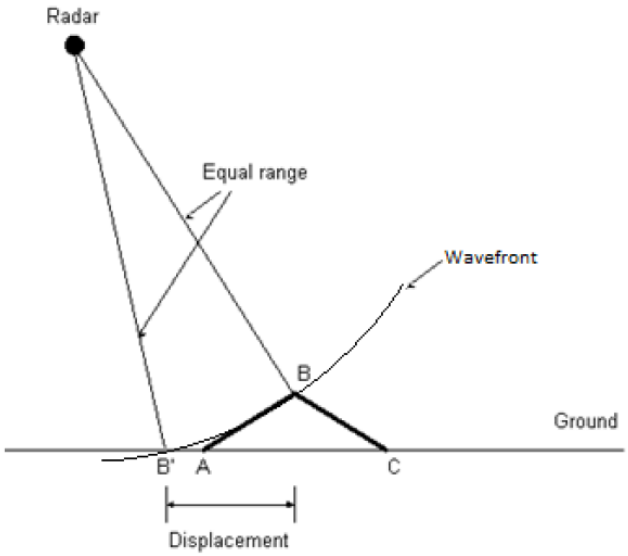

Figure 3.6: Layover. As per Figure 3.5 there are two equal slant ranges; one on the ground and the peak of the terrain feature. However, in this case the point on the ground is in front of the terrain feature; this leads to an extreme case of foreshortening known as layover (Modified from [47])

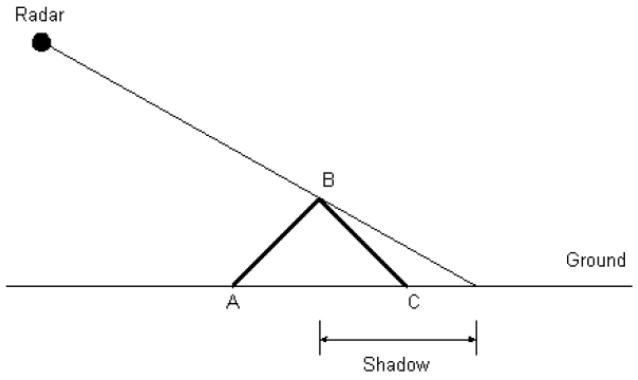

Figure 3.7: Shadowing. The geometry of the scene results in some areas not being illuminated by the radar (From [47])

3.2.3.3 SAR Ambiguities

Other artefacts can appear in SAR images; ambiguities (giving ghost repeats of targets as shown in Figure 3.8) can occur when returns from previous pulses overlap into the receive gate of the next pulse and can also be caused by strong targets sitting in the antenna side lobes.

3.2.4 The Backprojection SAR Processing Algorithm

The backprojection algorithm, described by [51] and presented in a MATLAB image formation toolbox by [52], is one of a multitude of algorithms that can be used to form SAR images. Given a SAR dataset consisting of a phase history in the frequency domain from each sample point across the synthetic aperture the following steps are necessary.

Firstly, a pixel grid is defined in space for the output image. The spacing of the grid is determined by the desired pixel size in the final image and the overall dimensions of the grid are controlled by the desired imaging area.

Considering each pixel in turn, the range from the antenna to each pixel relative to the range to the centre of the imaging scene from the antenna for this particular sample point,

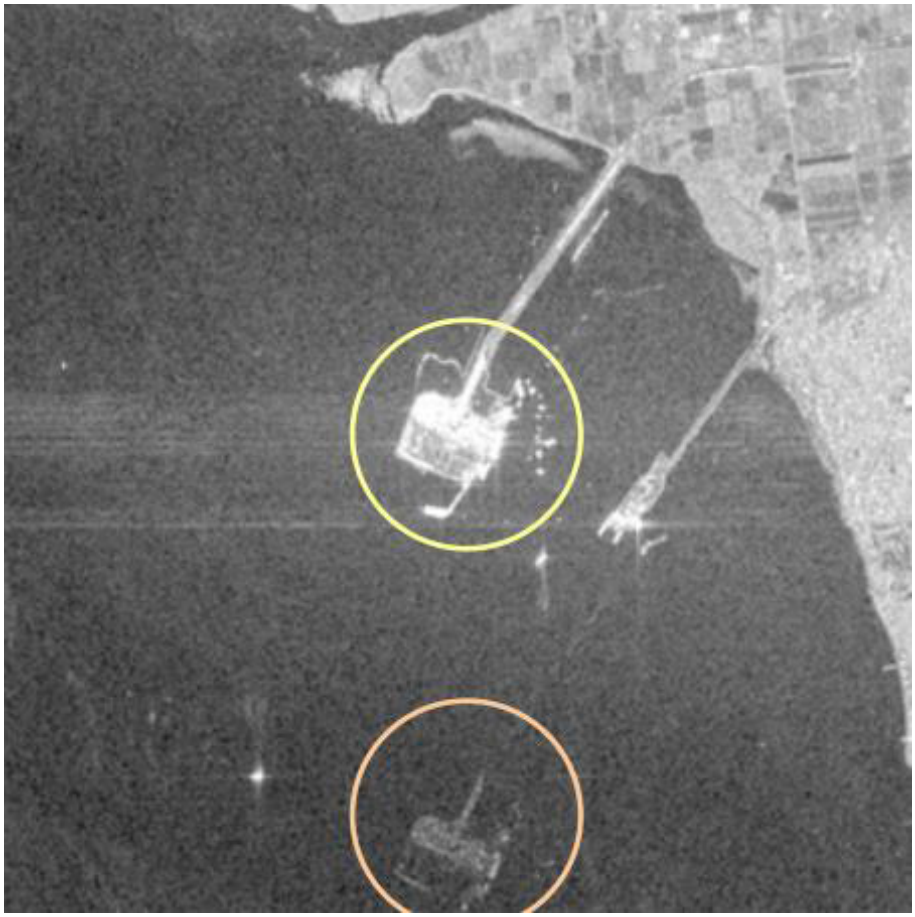

Figure 3.8: Radarsat-2 view of a coastline. ”Ghost” image in orange circle is a duplicate of the real feature in the yellow circle [50]

R_{diff}, is calculated using the following equation:

$$R_{diff} = \sqrt{(Ant_x - Pix_x)^2 + (Ant_y - Pix_y)^2 + (Ant_z - Pix_z)^2} - R_0 \tag{3.9}$$

Where Ant_x, Ant_y and Ant_z are the 3-D coordinates of the antenna position during this particular pulse, Pix_x, Pix_y and Pix_z are the 3-D coordinates of each pixel, R_0 is the distance to the centre of the pixel grid.

By applying an IFFT (zero padded as necessary, [52] recommend an IFFT length ten times that of the number of frequencies in each phase history) to the phase history from a single sample point in the synthetic aperture, the range profile for this single radar pulse is calculated.

At this point, the range between adjacent samples in the IFFT output, R_{FFTbin}, is simply

$$R_{FFTbin} = \frac{R_{unambig}}{n_{FFT}} \tag{3.10}$$

Where n_{FFT} is the number of points in the IFFT and $R_{unambig}$ is the unambiguous range of the system, calculated using Equation 3.8.

It is unlikely that this range step is the same as the range step between each of the pixel ranges previously calculated. In order to rectify this, an interpolation in range must be performed to calculate the signal at each pixel point across the imaging grid from the single pulse under consideration.

Finally, a phase correction must be calculated and applied to the resampled IFFT output to remove the phase gradient that appears across the image due to geometry, this phase correction is given by

$$\phi_{correc} = \exp(\frac{4i\pi f_1}{cR_{diff}}) \tag{3.11}$$

Where f_1 is the first frequency in the pulse and R_{diff} is the differential range to each pixel, given by Equation 3.9

The resampled and corrected IFFT output is then placed on the 2-D imaging grid using the range to each pixel to determine which IFFT output sample is placed on which pixel.

This process (range calculation, IFFT to form a range profile, interpolation to correct range sampling, phase correction and sample placement) must be performed for each pulse; the complete image is formed by summing the result from each pulse together.

The simplicity of this algorithm comes at the cost of high computational cost; the basic backprojection algorithm is not well optimised although it does lend itself to parallel processing and hence exploitation by GPU-based processors [52]. For this work, performed with relatively small numbers of small SAR datasets (each data file having 151 sample points with 1601 frequency points per sample) and images (200x200 pixels) the backprojection algorithm takes around 2.5s to form an image when implemented in MATLAB and run on a typical personal computer.

3.2.5 Existing Spaceborne SAR Systems

There are many SAR systems currently in orbit; Table 3.1 summarises those systems for which data is commercially available (there are other SAR systems, such as Germany's SAR-Lupe satellites, where data does not appear to be available for civilian use). For the systems listed data access terms vary in both price and availability; some (such as Sentinel 1) have an open access policy for data acquired during routine imaging and others (such as TerraSAR-X) require more detailed usage proposals to be submitted before data access is granted for non-commercial usage. Due to orbital dynamics the revisit times specified are only approximate; near the poles the revisit time will be much shorter than that near the equator (assuming the spacecraft is in a polar orbit). Radar systems that are only part

Name	Frequency	Maximum Resolution [m]	NESZ [dB]	Incidence Angle [°]	Revisit Time
TerraSAR-X/ TanDEM-X [53, 54, 55]	X-band	1.5	-19 to -23	20 to 55	11 days
Radarsat-2 [56, 57]	C-band	3	-23 to -31	10 to 60	3 to 5 days
Cosmo-SkyMed [58, 59, 60]	X-band	1	-22	25 to 50	4-16 days†
PALSAR-2 (ALOS-2) [12]	L-band	3	-24 to -28	8 to 70	14 days
Sentinel-1A/1B [61, 62, 63]	C-band	5	-22	18.3 to 46.8	6/12 days‡
Paz/SeoSAR [64]	X-band	1	$<$-21	15 to 60	11 days
RISAT-1 [65]	C-band	1	-20	12 to 55	25 days
RISAT-2	Classified				

Table 3.1: SAR system parameters for systems that are currently operating in orbit.
† 4 days with a constellation of 4 satellites, 16 days with one satellite.
‡ 6 days with a constellation of 2 satellites, 12 days with one satellite

of a satellites instrumentation are referred to by instrument name (satellite name).

In addition, there are multiple systems that have previously flown in space that are no longer producing data, their specifications are summarised in Table 3.2. These systems are still potential sources of useful data from their archives (although some systems, most notably SeaSat and SIR-A collected rather limited amounts of data); however as Table 3.1 shows more modern systems will usually comprehensively outperform these older systems. Information on some legacy systems is limited.

Of significant interest to subsurface imaging are the L-band systems, due to the lower frequency offering better penetration of soil. Further analysis of the applicability of certain SAR systems to subsurface radar imaging is presented in Chapter 6.

Name	Frequency Band	Maximum Resolution [m]	NESZ [dB]	Incidence Angle [°]	Revisit Time
ASAR (Envisat) [66]	C	30	-19 to -22	15 to 45.2	∼5 days
AMI (ERS-1) [67]	C	30	-20 to -24	16 to 50	8 days
PALSAR (ALOS) [68]	L	10	-23 to -32	7.9 to 60	46 days
Radarsat1 [69]	C	8	-22	10 to 59	∼6 days
SAR (JERS-1) [70]	L	18	-18	32 to 38	44 days
SAR1 (SeaSat) [71]	L	25	-21 +/- 5	17.4 to 23.6	
SIR-A (STS-2) [72]	L	40		47	
SIR-B (STS-41G) [73]	L	20		15 to 60	1 day
SIR-C (STS-59 and -68) [74]	L, C,X	13(L,C) 10(X)	-40(L), -35(C), -22(X)	20 to 55	
SRTM (STS-99) [75]	C, X	30		52	

Table 3.2: SAR system parameters for legacy systems

3.3 Extraction of Phase From SAR Data

3.3.1 Principles of Interferometric SAR

In a single SAR image the phase information is generally meaningless as across the image it contains both deterministic and random information. A single scatterer will present a deterministic phase response but in a typical imaging scenario there will be multiple scatters within a single pixel which leads to each pixel having a random overall phase response. In addition, the atmosphere will introduce a second random phase shift. In a single image it is impossible to filter out the random parts and be left with the useful deterministic part. However, by taking two SAR images from slightly different points at similar times it is possible to remove the random contributions (as, assuming limited time and imaging point separation between the two images, the same random components due to both multiple scatterers and the atmosphere should be present in both but the deterministic component should have slightly changed due to the different imaging geometry) and produce meaningful images.

Interferometric SAR (InSAR) extracts the phase from two slightly offset SAR images in this manner in order to obtain height information. InSAR takes two SAR images and subtracts the phase data of one from the phase data of the other and so only deterministic phase information remains. The derivations presented here for both InSAR and Differential InSAR (DInSAR) are based on that presented by [76] with additional background from [77] and [78].

Figure 3.9 shows the basic geometry of a general InSAR scheme. $A1$ and $A2$ are the two radar platforms with a baseline, B, of known distance between them. ρ is the path length from the first antenna to the target point, and $\rho + \delta\rho$ is the path length from the second antenna to that same target. Z is the altitude of the sensing platform. From this,

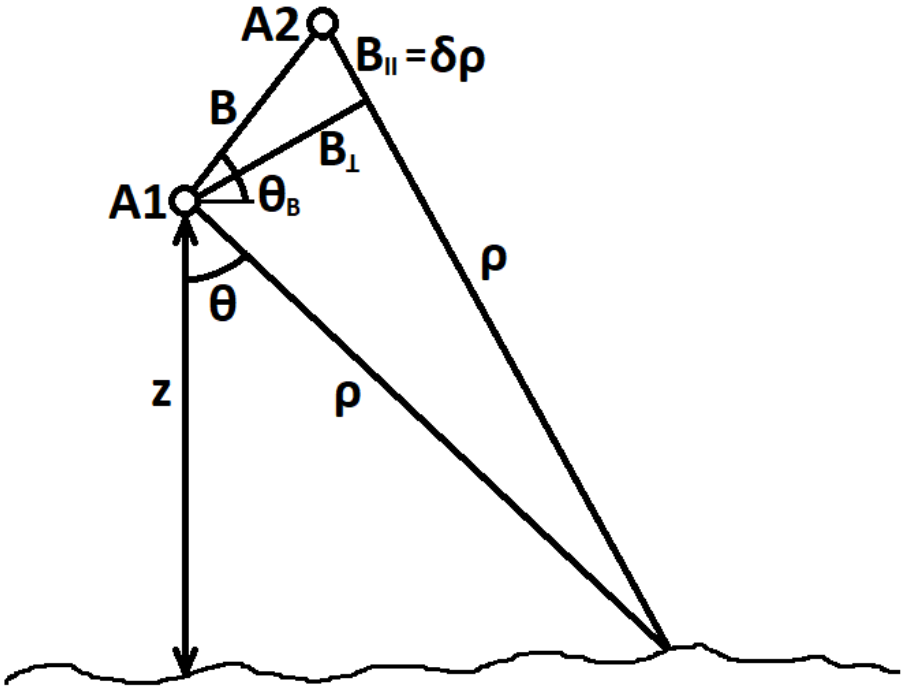

Figure 3.9: Basic InSAR Geometry (Redrawn version of sketch shown in [76])

the phase difference (φ) measured is;

$$\varphi = \frac{2a\pi\delta\rho}{\lambda} \tag{3.12}$$

Where λ is the wavelength and a is 2 for multiple pass interferometry (where A1 and A2 are acquired by the same radar at different times) and 1 for single pass interfereometry (where A1 and A2 are acquired at the same time, using a radar with a transmit and receive antenna at A1, and an extra receive antenna at A2). This arises because in the case of multiple pass interferometry pulses are both transmitted and received at A2, meaning the round trip is $\delta\rho + \rho + \rho + \delta\rho$. However, in the single pass case A2 only receives that are transmitted at A1, therefore the round trip is $\rho + \rho + \delta\rho$.

By trigonometry (law of cosines) it can be seen that

$$\delta\rho \approx B\sin(\theta - \theta_B) \tag{3.13}$$

Or equivalently

$$\delta\rho \approx B_{||} \tag{3.14}$$

Where $B_{||}$ is the component of the baseline that is parallel to the look direction. Equations 3.12 and 3.13 can be combined to form

$$\varphi = \frac{2a\pi B\sin(\theta - \theta_B)}{\lambda} \tag{3.15}$$

As the height of the target point changes (relative to Z, which is either constant or corrected for from platform orbit data), $(\theta - \theta_B)$ will vary and hence φ will similarly vary. In addition, note that there is also a dependence on B, the baseline distance, which implies that B must be accurately known in order to accurately retrieve the target point height change.

The variation of φ, when mapped over a complete image, produces an interferogram, an example of which is shown in Figure 3.10. Note that a raw interferogram can only display phase within the band $\pm\pi$. Real terrain variations will inevitably be larger than this and will create 2π jumps in the displayed phase. Therefore, further processing, including phase unwrapping (which seeks to correct these 2π phase jumps) , is necessary before terrain elevation information can be extracted from this interferogram. This process is described in Section 3.3.2.5.

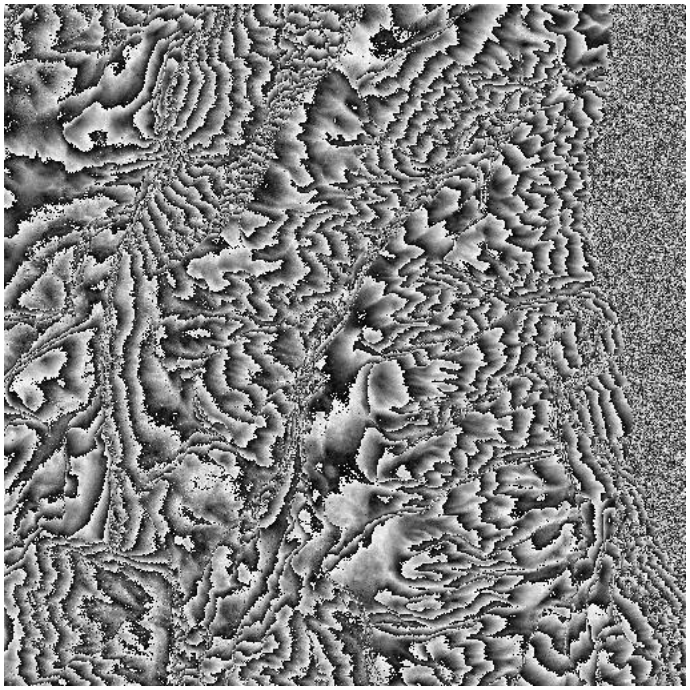

Figure 3.10: Raw phase interferogram [79]

3.3.2 InSAR Work Flow

3.3.2.1 Baseline Creation

The critical basis for InSAR is to have two SAR images of the same scene taken from slightly different positions at similar times.

One method of obtaining the two images needed for InSAR processing is to collect the two images at the same time using two radar systems; either two separate radar systems or a transmit/receive pair coupled with another receive only system. These can either be on the same platform (as per the SRTM, see upper part of Figure 3.11) or two platforms flying in formation (as per the TanDEM-X constellation, shown in the lower part of Figure 3.11). In the case of the SRTM, the fixed baseline of 60m was chosen in order to give an acceptable measured height noise whilst being practical to stow inside the Space Shuttle's payload bay [80].

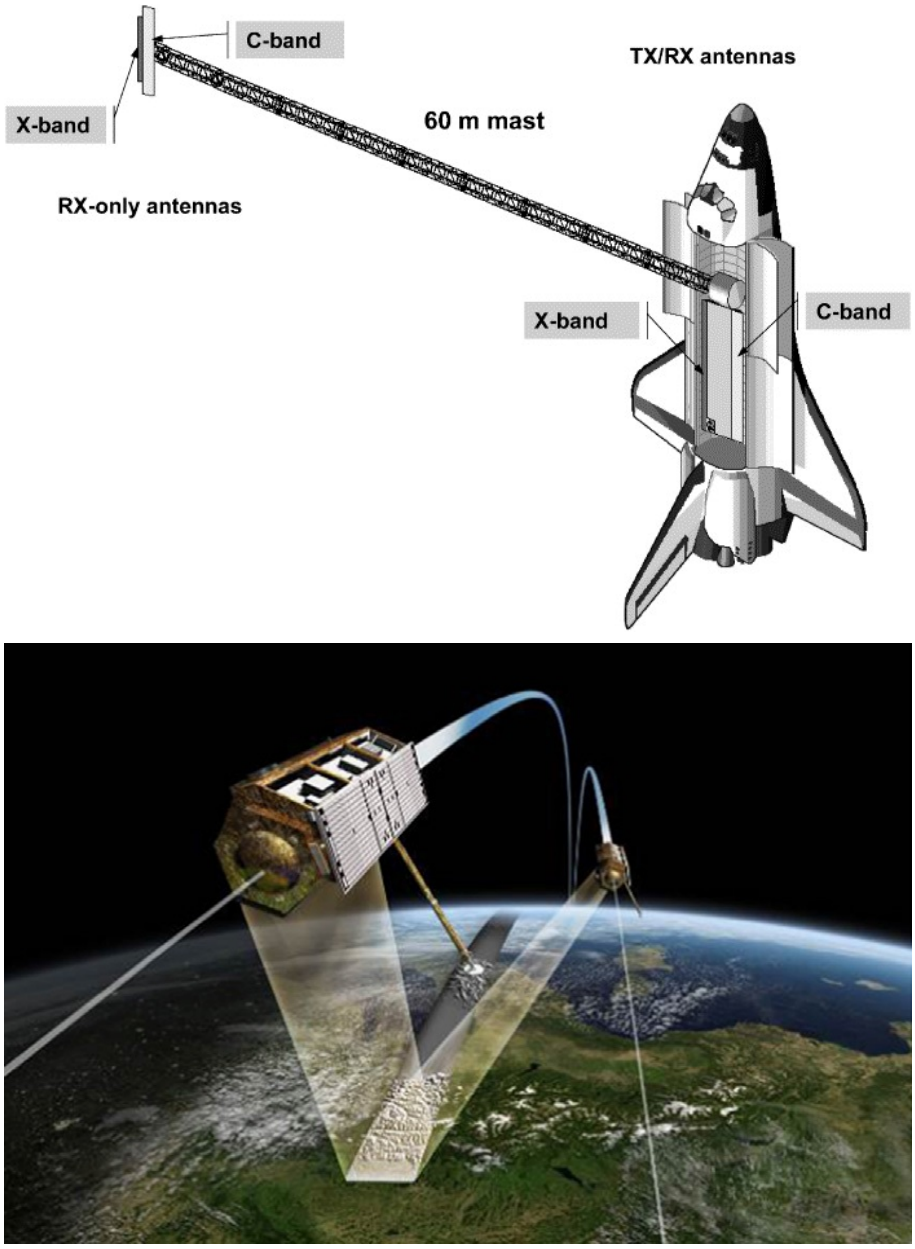

Figure 3.11: Single pass InSAR acquisitions.
Top: Sketch of SRTM deployed on the STS [81]. Note single transmitter (TX), dual receiver (RX) architecture for each band which implements the two pass geometry shown in Figure 3.9.
Bottom: TanDEM-X constellation performing interferometry (from [82]).

In Section 3.3.1 the following equation for phase difference was presented;

$$\varphi = \frac{2a\pi B \sin(\theta - \theta_B)}{\lambda} \tag{3.16}$$

Note the dependency on B (baseline distance). This implies that the baseline distance must be precisely known in order to relate the measured phase difference to a change in target height; on a single platform system this is a relatively easy task (although the challenges of designing and implementing a rigid, lightweight support structure that fits inside a typical launch vehicle must not be underestimated), with a constellation this can be achieved by means of precise orbit data, usually either GPS location information or by using a system such as DORIS [83].

Single pass InSAR avoids temporal changes that may affect multiple pass InSAR, particularly atmospheric effects and terrain deformation. Note, however, that terrain deformation is information that is of great interest, particularly in areas with geological activity or potential subsidence problems.

Multiple pass InSAR is distinct from single pass InSAR in that one radar system images the target scene on separate occasions (in the case of a spaceborne system, usually the next orbit that revisits the scene), in order to obtain temporal diversity. Decorrelation effects due to scene changes mean that the revisit period must be relatively short.

3.3.2.2 Along-Track Interferometry

All the scenarios considered so far have had the antenna separation baseline orientated across the direction of platform movement to some degree. However, it is possible to have the baseline orientated along the movement direction ([84]). Such an arrangement is known as Along-Track Interferometry (ATI) and is used for discerning the movement of scatterers in a scene (non-moving scatterers presenting an interferometric phase of zero).

Typical uses include ocean current and traffic flow monitoring. The interferometric phase for a moving scatterer in this situation is given by

$$\varphi_{ATI} = \frac{4\pi}{\lambda}\frac{B_{ATI}V_R}{2V} \tag{3.17}$$

Where φ_{ATI} is the ATI phase, λ is the wavelength of the radar, B_{ATI} is the along track baseline length, V_R is the line of sight component of the scatterer's velocity (which is the variable of interest) and V is the along track velocity of the platform.

3.3.2.3 Image Registration

Before an interferogram can be produced the two SAR images must be precisely aligned. Registration is the process of aligning the two images and compensating for any relative distortions in the images due to the slightly different viewpoints [85].

The first part of this process is to select one image as a master and one as a slave. The slave image is mapped onto the master image; the master is unchanged whilst the slave is altered to precisely align with it so that each pixel in one image represents exactly the same ground area as the same pixel in the other image.

There are many different methods of registration. There are two main classifications of registration methods; intensity based and feature based. As their names suggest, intensity based methods use correlation metrics to compare and match intensity patterns whereas feature based methods use reference points (typically strong, constant scatterers) common to both images to align the pair. At this point, the interferogram can be created by calculating the phase difference between the two precisely aligned images.

3.3.2.4 Flat Earth Removal

The interferogram produced by two aligned SAR images contains phase variances caused by two factors (assuming single pass InSAR so negligible atmospheric/temporal decorrelation); terrain elevation (which is the factor of interest) and a cyclic variation that would be present on a flat scene that arises from the InSAR geometry. This second contribution/variation is relatively easy to calculate and remove in a process known as Flat Earth Removal [86].

3.3.2.5 Phase Unwrapping

The multiple edges in a raw interferogram come about because phase can only be measured between $\pm\pi$; however, as the elevation differences in the view of the SAR are likely to be greater than the wavelength in use the reported phase difference (φ) will be;

$$\varphi = \varphi^{|} + 2\pi n \tag{3.18}$$

Where n is an integer value and $\varphi^{|}$ is the 0 to 2π phase difference displayed in the interferogram.

The process of extracting φ is called phase unwrapping and is a non-trivial task in a real radar image that is two dimensional, contains noise and contains a variety of different terrain types [87].

3.3.3 Differential Interferometric SAR

Differential Interferometric SAR (DInSAR) is similar to multiple pass InSAR in that temporally diverse SAR images are used to generate interferograms. Where DInSAR differs is that instead of producing one interferogram and extracting terrain or displacement in-

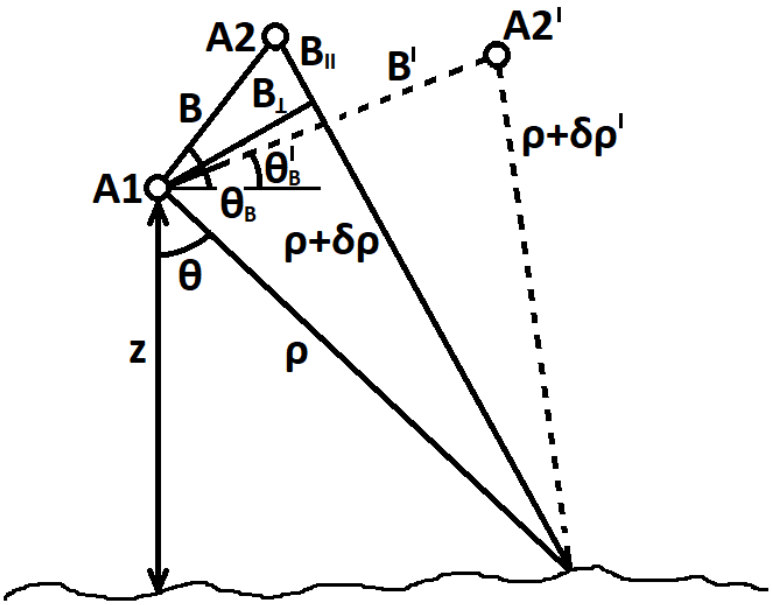

Figure 3.12: DInSAR imaging arrangement. Note one orbit path (A1) is common to both interferograms. (Redrawn version of sketch shown in [76])

formation from it, two or more temporally separated interferograms are produced which allows changes in elevation down to millimetre-scale to be detected and precisely monitored [88]. If used with multiple pass InSAR the DInSAR process uses the geometry shown in Figure 3.12.

$A1$ is a common orbit path (used twice; once in each interferometric pair), $A2$ is the second orbit for the first interferometric pair and $A2'$ is the second orbit for the second interferometric pair. Note that 3 passes are made; $A2$ and $A2'$ are separate images but $A1$ is one image used in the formation of both interferometric images in the DinSAR pair.

If there is no temporal or spatial decorrelation (ρ and θ are unchanged between interferometric pairs) then, from previous discussions

$$\varphi = \frac{4\pi\delta\rho}{\lambda} \tag{3.19}$$

and

$$\delta\rho = B_{||} \tag{3.20}$$

Hence, for the first interferogram

$$\varphi = \frac{4\pi B_{||}}{\lambda} \tag{3.21}$$

and the second interferogram

$$\varphi' = \frac{4\pi B'_{||}}{\lambda} \tag{3.22}$$

where φ' is the phase difference in the second interferogram and $B'_{||}$ is the component of the second interferogram's baseline parallel to the look direction. If there is terrain movement (from an earthquake, for example) between the two interferograms the phase difference in the second interferogram will be given by

$$\varphi' = \frac{4\pi(B'_{||} + \Delta\rho)}{\lambda} \tag{3.23}$$

where $\Delta\rho$ is the path length change due to the terrain movement. Noting that from the terms for the phases in the first and second interferograms

$$\frac{\varphi}{\varphi'} = \frac{B_{||}}{B'_{||}} \tag{3.24}$$

It is possible to write

$$\varphi' - \frac{B'_{||}\varphi}{B_{||}} = \frac{4\pi\Delta\rho}{\lambda} \tag{3.25}$$

From this equation it is possible to calculate $\Delta\rho$ (and hence elevation changes) for each point in the scene, as λ is a known value for the radar system, $B'_{||}$ and $B_{||}$ are known from orbital information and φ and φ' are the results of producing each interferogram in the DInSAR pair.

Three pass DInSAR is seldom used due to atmospheric delay errors affecting the

reference (first) interferogram. It is possible to reduce the number of passes to two by comparing a single interferogram (formed from two passes) to a reference interferogram generated using a DEM and orbital models rather than building two separate interferograms from three platform passes. This process removes the problems with atmospheric errors affecting the reference interferogram but is susceptible to errors or artefacts within the DEM.

The high resolution of DInSAR elevation monitoring comes about because it is a phase-based technique. The VB-SAR technique that will be demonstrated by this work also uses phase changes over a series of radar images to produce subsurface depth profiles at very high resolutions. Due to this, a real world implementation of the VB-SAR scheme would use DInSAR image stacks.

3.3.4 Acquisition Requirements for InSAR and DInSAR

3.3.4.1 Critical Baseline

As the baseline of the InSAR system increases, the baseline correlation coefficient decreases due to the increasing difference between the two views of the same scene. Eventually this coefficient reaches zero and the images are decorrelated. The length of the baseline when this decorrelation occurs is called the Critical Baseline (B_c) and is calculated by

$$B_c = \frac{\lambda R B \tan\theta}{c} \tag{3.26}$$

Where λ is the frequency in use, R is the range to the target scene, B is the bandwidth in use, θ is the incidence angle and c is the speed of light [89].

3.3.4.2 Permanent Scatterer InSAR

PSInSAR is a relatively new scheme (first developed by [90]) that examines the phase history of permanent scatterers in the scene to improve accuracy over standard InSAR. A permanent scatterer is an object within a SAR scene that is not affected by temporal or geometrical decorrelation (gives the same response at all times and all look angles). The permanent scatterers must also give locally strong returns to ensure a good SNR. Permanent scatterers are smaller than the image resolution and are usually man-made objects. Once identified and monitored the permanent scatters can be used to estimate and remove atmospheric phase effects (caused by the time difference between the two SAR acquisitions used for InSAR). In order for this technique to be effective there must be at least 5 permanent scatterers per km^2 [91].

3.3.4.3 Coherence

Coherence is a statistical measure of likeness. In the case of an InSAR interferogram made up of two SAR images it is the measure of how alike the two images are. The coherence of the signals ($S1$ and $S2$) received by the two antenna apertures is given by;

$$\gamma = \frac{|\langle S_1 S_2^* \rangle}{\sqrt{\langle S_1 S_1^* \rangle \langle S_2 S_2^* \rangle}} \tag{3.27}$$

Decorrelation between the two images can be due to a number of factors;

$$\gamma_{SP} = \gamma_{SNR} \gamma_B \gamma_V \tag{3.28}$$

Where γ_{SP} is the coherence coefficient for single pass InSAR, γ_{SNR} is the noise coherence coefficient, γ_B is the baseline coherence coefficient and γ_V is the volumetric coherence coefficient. Volumetric decorrelation is caused by the fact that SAR pixels can contain

scatterers that are distributed both in the ground plane and height (for example, a tree).

The multiple pass InSAR scheme has two other potential sources of decorrelation; temporal (γ_t) and rotational, γ_φ, (caused by the field of view rotation due to observing the same scene from slightly different perspectives,). As with the γ_{SP} expression, these two terms are multiplicative so the multiple pass InSAR coherence coefficient (γ_{MP}) is given by;

$$\gamma_{MP} = \gamma_{SNR}\gamma_B\gamma_V\gamma_t\gamma_\varphi \tag{3.29}$$

Note that the coherence coefficients are multiplied together to give the final correlation factor; this means that relatively small levels of decorrelation due to each effect can have large effects on the quality of the final image or, equally, one poor (low) coherence term can have a large effect [77].

3.4 Tomographic Profiling

3.4.1 Review of the Tomographic Profiling Process

The SAR processes previously described produce images in which the imaging plane is horizontal, which for typical surface surveying/mapping applications is ideal. However, this geometry means that one pixel on the ground is formed from a combination of the surface return and any subsurface returns that may be present. For the initial experimentation with subsurface imaging the ability to separate the subsurface target return from the surface return is valuable. This can be achieved using the backprojection algorithm by rotating the imaging plane 90° so it is vertical. In this plane, vertical resolution is given by the radar's bandwidth and the synthetic aperture is used to form horizontal resolution.

A disadvantage of operating conventional SAR in this fashion is that there is no control over the incidence angle with respect to the ground surface. For this project the ability

to vary the incidence angle with the ground at process time, rather than collection time, would be a substantial advantage.

[39] describes the TP process and its application to obtain the vertical backscattering profile through volumes. TP involves constructing a synthetic beam from a sub-set of the full synthetic aperture, setting the angle of this beam via a phase ramp across the sub-aperture, computing a range profile for that single beam and then repeating this process along the synthetic aperture to build a complete image of the scene. An overview of this technique is shown in the upper part of Figure 3.13. Significantly, this approach allows the incidence angle in the produced image be varied at process time by varying the phase ramp across the sub-aperture. The only limitation on incidence angle is that the incidence angle the processing is performed at must be within the beam of the real antenna, otherwise severe distortions will be present in the final image.

In addition to being able to vary the incidence angle at process time, the TP process has the substantial advantage over SAR imaging of having a fixed incidence angle across the produced image. This is very useful for exploring the effect of different incidence angles on the produced images and any technique that makes use of those images.

Considering the lower part of Figure 3.13, a scan with length L is constructed using individual measurement points spaced by dx. A sub-aperture, of width $D = n(dx)$, is made up of n points of the full scan. r_1 to r_n, are the ranges from each antenna position within the sub-aperture to a point, P, at a vertical distance from the platform of Z with an incidence angle of i, which is constant across the image.

Range resolution along the synthetic beam is generated in the standard fashion for a stepped frequency radar using a linear chirp, so range resolution is governed by the equation

$$Res_R = \frac{c}{2B_r} \tag{3.30}$$

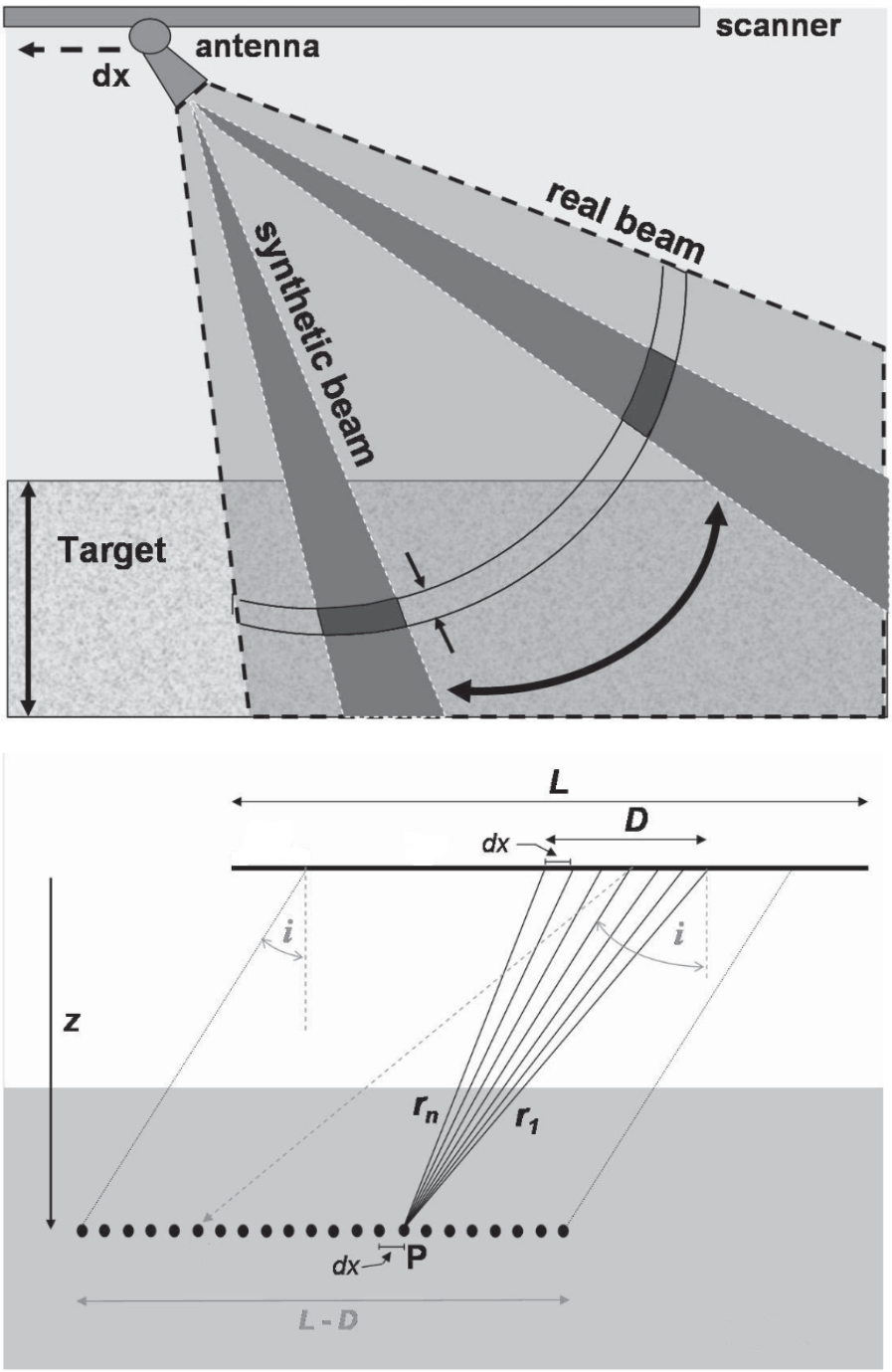

Figure 3.13: General overview of the TP process. Adapted from [39]
Upper: Conceptual sketch showing how the TP process produces a narrow synthetic beam from data gathered by a wide real beam and allows the synthetic beam's incidence angle to be varied.
Lower: Detailed schematic of TP image formation process.

Where Res_R is the range resolution, c is the speed of light in free space and B_r is the bandwidth of the radar pulse.

Cross range resolution across the image is governed by the width of the sub-aperture, which controls the beamwidth of the synthetic beam via

$$Res_{CR} = \frac{\lambda R}{2D\cos i} \tag{3.31}$$

Where Res_{CR} is the cross range resolution, λ is the wavelength in use, R is the range, D is the width of the sub-aperture and i is the beam angle.

As per the SAR case, the Nyquist sampling theorem states that in order to avoid aliasing the following inequality must be satisfied.

$$dx \leq \frac{\lambda}{2} \tag{3.32}$$

Cross track resolution (the resolution perpendicular to the direction of antenna motion) is not enhanced by the TP technique and so is governed by the beamwidth in the cross track direction of the physical antennas used. In practical terms, all returns in the cross track direction are summed by the antenna's transmit and receive functions so a narrow real beam in this direction is highly preferable in order to prevent spurious returns appearing in the final image.

In contrast to the cross track case, it is preferable to have a very wide real beam in the cross range direction. A wider beam enables a wider range of synthetic beam angles to be used whilst keeping the synthetic beam entirely within the real antenna beam. However, the tendency of objects outside the imaging volume of interest to appear in the TP image via sidelobes must be considered and the beamwidth/imaging area carefully controlled in order to avoid this issue.

Whilst the range and cross range resolutions are useful for characterising the performance of a TP reconstruction, for practical imaging it is likely that the horizontal and vertical resolutions are of more interest. These are both given by the projections of the range and cross range resolutions onto the vertical and horizontal along track planes. Specifically;

$$Res_V = Res_R \cos(i) + Res_{CR} \sin(i) \tag{3.33}$$

Where Res_V is the vertical resolution and i is the reconstruction angle.

and

$$Res_H = Res_R \sin(i) + Res_{CR} \cos(i) \tag{3.34}$$

Where Res_H is the horizontal resolution.

Significantly, compared to side-looking SAR systems, these resolutions do not vary across the imaged scene which allows for precise analysis of the produced images.

Note that Equation 3.31 would seem to suggest that a very large sub-aperture is preferable in order to obtain the best Res_{CR} and hence the best vertical and horizontal resolutions. However, recall that in order to image the complete row, the sub-aperture is slid along the full aperture. This gives a pixel spacing across the image of dx, and an image width of

$$W_{image} = (L - D)dx \tag{3.35}$$

where W_{image} is the width of the output image, L is the length of the entire scan, D is the sub-aperture length and dx is the sample point spacing. Considering Equations 3.31 and 3.35 together clearly shows that improved Res_{CR}, given by an increase in D, comes at

the expense of a narrower image.

In order to produce a complete image, the radar system must measure the scene over a bandwidth, B_r consisting of m frequencies at all sample points. In order to produce a final TP image pixel, I, at a defined point, p, the distances, r, from the all the sample points in the sub-aperture that illuminates the pixel in question are calculated using

$$r_n = \sqrt{Z^2 + (dx(n - n_{mid}) - Z\tan i)} \tag{3.36}$$

Where r_n is the beam range from sub-aperture point n to the reconstruction point, Z is the vertical distance from the platform to the reconstruction point, dx is the spacing between samples fed to the TP processor, n is the position of the current sample point within the sub-aperture, n_{mid} is the position of the middle sample point within the sub-aperture and i is the desired synthetic beam angle.

The following equation is used to give the final pixel value:

$$I_p = \sum_{m=1}^{M} \sum_{n=1}^{N} G_{nm} W(m) W(n) exp[\frac{j4\pi f_m r_n}{c}] \tag{3.37}$$

Where I_p is the final value of pixel p, m is the number of the frequency under consideration, n is the sample point under consideration, f_m is the actual frequency under consideration, r_n is the range to the pixel from the sample point under consideration, and W(m) and W(n) are the Hamming weights in the frequency and spatial domains respectively (if Hamming weighting is being used). M is the total number of frequencies in the complete radar pulse and N is the number of sample points in the sub-aperture.

The TP algorithm allows pixel spacing to be controlled independently of resolution. Pixel spacing is controlled in the horizontal direction by selecting how many (if any) scan points to exclude from the reconstruction. For instance, given a scan point spacing (dx) of 2cm, using every sample point to reconstruct a TP image would give a horizontal pixel

spacing of 2cm but discarding every other sample would give $dx = 4cm$. Obviously this discarding will mean that for a constant desired cross range resolution across different pixel spacings the number of samples in each sub-aperture will need to vary so that the actual length, D, of the sub-aperture remains constant.

In the vertical direction, pixel spacing can be arbitrarily controlled; the only depth dependence in Equation 3.37 is within r_n. Considering Equation 3.36 which calculates r_n it is seen that Z can be independently set in order to control vertical pixel spacing.

An example image produced by the TP process is shown in Figure 3.14. This image was acquired during the experimental work performed for this study; the scene consists of a wooden trough directly below the radar platform filled with sand. Several targets were buried in the sand trough.

Within the image, the surface of the sand is clearly visible at around 180cm below the antennas and the bottom of the trough can be seen at around 325cm below the antennas. In addition, a strong response from a buried trihedral reflector can be seen in approximately the centre of the image, several weaker returns from other buried objects can be seen to the right of the trihedral and a volume containing a sand and gravel mixture can be seen above the buried trihedral. The refractive index of the sand has caused the returns from within the sand volume to appear further away from the antennas than they actually are. This is because the TP imaging algorithm considers that every point within the scene is in freespace, so those points within the sand volume are shifted in the produced image.

The strong horizontal bands within 100cm of the antenna result from antenna cross talk; they can be effectively removed using a DC subtraction process (subtracting the average value of each row in the final image from each pixel in that row).

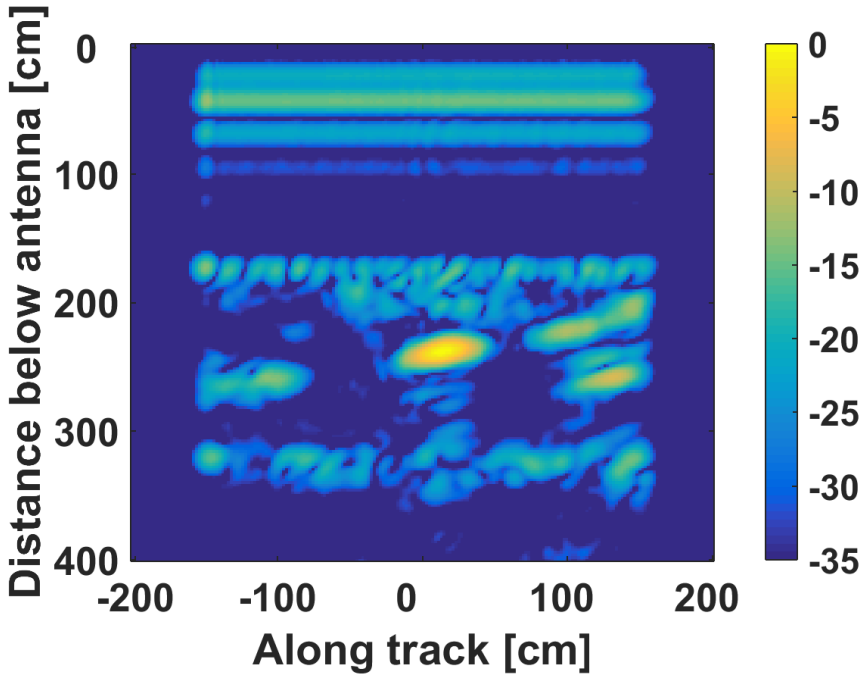

Figure 3.14: Example image produced by the TP process, showing antenna cross talk, sand surface and buried targets. Colour scale in dB.

3.4.2 Implementation of a TP Processor for VB-SAR

As previously noted, the TP process is an attractive method of forming radar images from radar data collected in the laboratory as it well suits the radar geometry in use and allows several parameters of interest to be varied at process time rather than collection time. For this work MATLAB was used to implement a practical TP processor. This processor handled the entire TP imaging cycle, automating the opening of the data files from the laboratory radar system, extracting the radar data from them, performing the TP process and creating output files which could subsequently be used by other software in addition to visual images.

Performance of the processor was a particular concern as the work performed for this study would involve producing thousands of TP images from hundreds of raw data files in order to study the behaviour of the VB-SAR scheme across incidence angles, image

resolution, real frequency etc. Considerable improvements in process speed were obtained compared to the existing TP processor which was implemented in FORTRAN by the Authors of [39]; using MATLAB also allowed considerably improved code readability. Additional pre- and post-processing operations were added to the code and the code is written in a modular fashion such that additional functionality can be easily added if desired.

The TP processing ”core” was written in a function; this allowed an external control script to set various parameters to control the processor and then call it. In addition, it meant that applying the TP processor to a stack of radar data files could be easily performed by having the control script automatically call the TP processor for each data file in turn. A list of the parameters, and a brief description of each, is given in Table 3.3. A flowchart overview of the TP processor is shown in Figure 3.15.

The TP processor firstly opens the raw data file produced by the radar system and extracts various parameters from the file header (start frequency, stop frequency, number of frequency points, number of scanner positions, distance between scanner positions, date and time of scan and polarisation). Some of these (the frequency and position parameters) are used within the TP processor, whereas the date and time is preserved and used to timestamp the produced TP images.

Next, the TP processor calculates the numerical indexes of the frequency points required to achieve the start and stop frequencies and the unambiguous range the calling script has specified. At this point there is also a ‘sanity check’ to ensure that the user has not tried to call the function with a greater range resolution requested than the start and stop frequencies specified can support. If they have, the function warns the user and displays the maximum range resolution it can achieve.

Having set the parameters to deal with the range resolution the TP processor then calculates the requirements for the cross slant range resolution, namely the size of the

Parameter	Description
depth_pixel_spacing	Pixel spacing in depth [m]
freq_start	Frequency to start processing at [Hz]
freq_stop	Frequency to start processing at [Hz]
depth_resolution	Depth resolution [m] used as a check to ensure the user is not looking for more resolution that freq_start and freq_stop allow [m]
CSRange_resolution	Cross slant range resolution required [m]
CSRange_pixel_spacing	Cross slant range pixel spacing [m]
FFT_length	Length of the FFT used within the TP process
depth	Extent of the imaging grid in the vertical dimension [m]
width	Extent of the imaging grid in the horizontal dimension [m]
gamma_degrees	Incidence angle [°]
unambig_range	Unambiguous range required [m]
zstart	Vertical distance below the antennas to start processing [m]
cll	Correction for cable length [m]
print_image	Save scaled image as .png [toggle]
save_data	Save raw data as CSV file [toggle]
dc_correc	Enable/Disable DC removal in the frequency domain of the raw data
do_calib	Enable/Disable application of calibration coefficients to raw data
apply_windows	Enable/Disable application of windowing in both frequency and position (within sub-aperture) dimensions
do_range_correction	Enable/Disable correction for R^x attenuation
range_correc_exponent	Set exponent for do_range_correction parameter
do_shearing	Enable/Disable shearing to correct for imaging geometry
db_diff	Dynamic range to present .png image over [dB]

Table 3.3: Control parameters implemented in the MATLAB TP processing function.

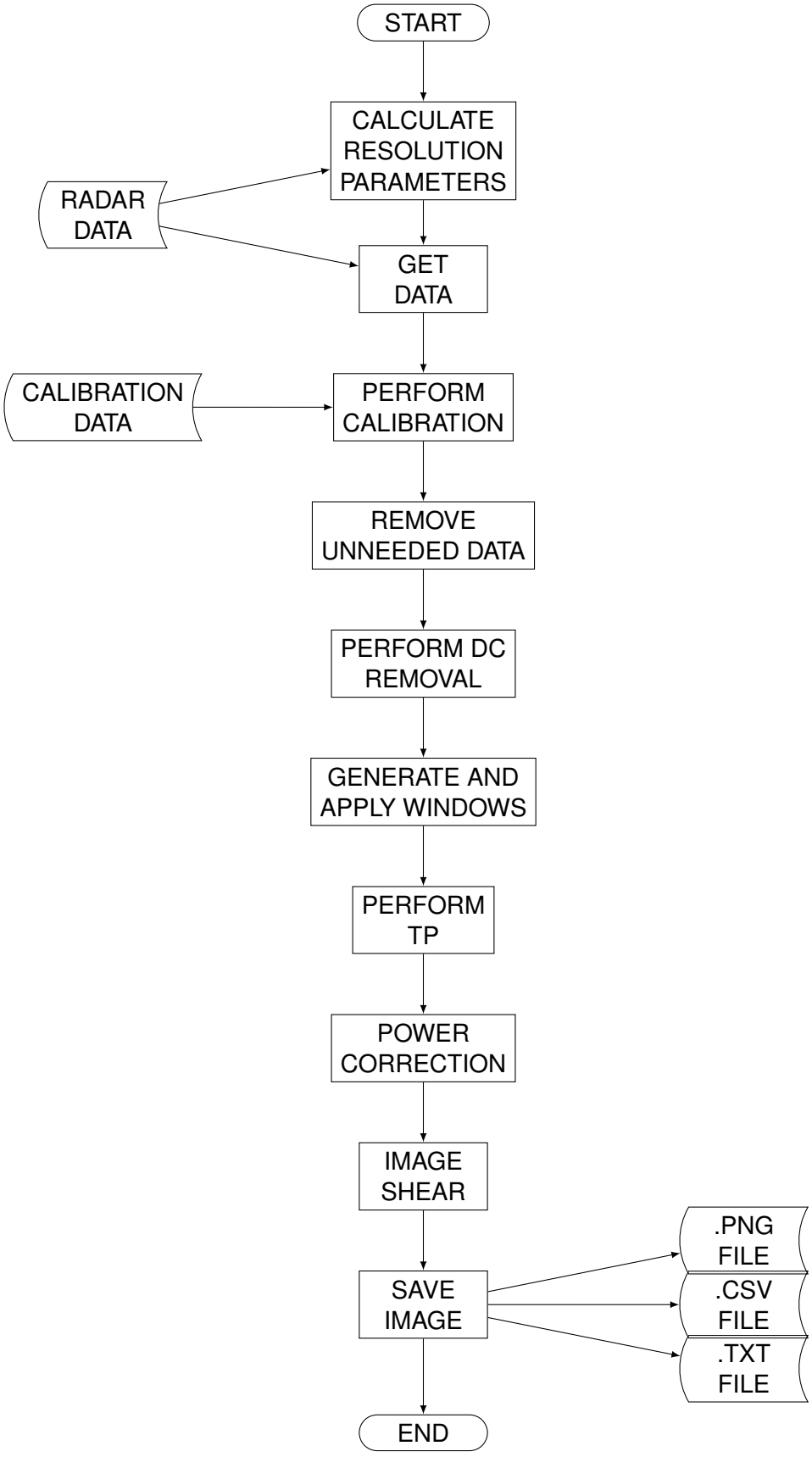

Figure 3.15: Flowchart of the TP processor.

synthetic sub-aperture used to synthesise the virtual beam. It is first calculated as a length, and then translated to a number of scanner positions by using the sample spacing value extracted from the header of the data file. Again, a 'sanity check' is performed to ensure that the cross slant range resolution is not higher than the data can support.

At this point the radar data file and calibration file (if specified) are loaded by the TP processor. Due to the data files consisting of both blocks of data (delimiter separated complex variables) and human readable text this required a custom file reading module. The radar and calibration data are consolidated into two complex matrices as the files are read.

If the user has opted to apply a calibration file and/or a (range) correction for electrical cable length these corrections are done on the raw data, immediately after file reading. For simplicity's sake the application of calibration coefficients and cable length correction factor was done prior to cutting the data down to only the frequencies required to achieve the imaging requirements, the computational penalty for this simplicity was not significant.

DC removal, window generation (in both frequency and sub-aperture domains) and windowing in the frequency domain are the next operations, immediately prior to the actual TP process. Again, as shown in Table 3.3 the application or not of these operations is controllable by the user.

At this point, using the frequency parameters calculated earlier, the processor cuts out the unneeded frequency points from the calibrated radata data.

The TP processing section implements the equation given in Equation 3.37. This part is heavily optimised, so much so that the processing time for the TP section is insignificant compared to the time taken for file reads from and writes to a mechanical hard disk. This part of the code implements Equation 3.37, frequency by frequency and row by row.

The first step in this process is to calculate a "focusing function" which is the electrical

path length between each point in the sub-aperture and the reconstruction point. As the processor works row by row and steps the virtual beam across the imaging scene the focusing function is the same for each reconstruction point in a given row. The focusing function is then convolved with the prepared raw radar data, and stored in a temporary matrix which is updated as each frequency is processed. Finally, the temporary matrix is Fourier transformed to produce the focused image.

After forming the TP image the post processing steps are applied, if requested. In order of application they consist of the range power correction (to correct for $Range^x$ losses, x being specified by the user to enable correction in high loss mediums), shearing (to correct for the incidence angle in use) and normalisation/conversion to dB for plotting in the output .png.

Processed images are saved in either or both .png and delimiter separated variable formats. The .png images are plotted in dB and have a dynamic range set by the user, whereas the delimiter separated variable files contain the raw complex data before normalisation. Typically the .png images are only produced for the first few images in a processing run and are used to check that the TP processor has been configured correctly. The date and time of each scan is saved in a .txt file which allows functions using the produced TP images to organise the series of images into the correct order.

3.5 Virtual Bandwidth-SAR

3.5.1 VB-SAR Introduction

Typical Ground Penetrating Radar (GPR) techniques involve having the radar system in very close proximity (typically, for commercial systems, GPR antennas are mounted on a wheeled platform which is traversed over the area of interest) to the soil surface. Whilst

GPR techniques produce useful subsurface images it is a labour intensive technique which makes surveying large areas difficult. In addition, the need to have the radar system close to the ground means that areas that are difficult to access (for reasons such as the presence of unexploded ordnance (UXO) or very remote areas) are impractical to image.

Considerable benefits could be obtained by using air or spaceborne SAR systems to identify and map subsurface features; such SAR systems routinely survey very large areas and the remote nature of the sensing means that most areas are easily accessed. The VB-SAR technique (developed by [1]) offers the possibility of using such SAR systems to detect and locate buried features and targets.

VB-SAR proposes a novel application of DInSAR that allows for discrimination of surface and subsurface features in SAR images. The scheme operates by examining sets of DInSAR images that span changes in M_v (volumetric soil moisture content). In this situation, subsurface features will show a change in phase response over the series of images (due to the changing electrical properties of the soil), but surface features will not. This difference allows subsurface scatterers to be separated from surface scatterers; the subsurface features appearing at their correct depths and the surface return appearing at zero depth. In addition, targets at different depths within the soil volume experiencing soil moisture changes will be correctly resolved at their different depths.

3.5.2 VB-SAR Theory

As shown in Section 3.2.2.2, the range resolution of a SAR system is linked to the bandwidth of the radar pulse. The VB-SAR technique, introduced in [1] demonstrates a method that utilises the variation in electrical properties of a given soil as its moisture content varies to synthesise a very large bandwidth, giving a very high subsurface range resolution. During initial development this technique was also known as “Zero Bandwidth

SAR" (ZB-SAR), but this name is no longer used.

For a wave propagating through a soil with a complex dielectric constant ($\varepsilon = \varepsilon_r + \varepsilon_i$) to a given depth, z, the following equation describes the wave ([92]).

$$S(z) = S_0 exp(-\alpha) exp(-j\beta z) \tag{3.38}$$

Where S_0 represents the wave at zero depth, α is the attenuation constant and β is the phase constant, which is given by:

$$\beta = k\sqrt{|\varepsilon|}cos(\frac{\delta}{2}) \tag{3.39}$$

Where k is the wavenumber ($= \frac{2\pi f}{c}$), $|\varepsilon| = \sqrt{\varepsilon_i^2 + \varepsilon_r^2}$ and $\delta = tan^{-1}\frac{\varepsilon_i}{\varepsilon_r}$.

Using the soil model provided by [17], it is possible to show that ε_i is very small for sandy soils, which in turn means that $cos(\frac{\delta}{2})$ will always be approximately 1 and $|\varepsilon|$ will be approximately ε_r. This in turn allows β to be simplified to:

$$\beta = \frac{2\pi}{c} f_R \sqrt{\varepsilon_r} \tag{3.40}$$

ε_r of a given soil is strongly dependent on the moisture content of the soil ([17], [20]). If the same scene was to be observed at two different times, it is highly likely that the soil moisture content (SMC), and hence ε_r, will have changed. In this case Equation 3.40 can be rewritten to;

$$\beta = \frac{2\pi}{c} f_R \Delta\sqrt{\varepsilon_r} \tag{3.41}$$

Where $\Delta\sqrt{\varepsilon_r}$ is the change in soil refractive index between the two observations. This shows that a change in soil dielectric is equivalent to a change in the real frequency (f_r of the radar system. This implies that by repeatedly imaging the same area whilst the soil

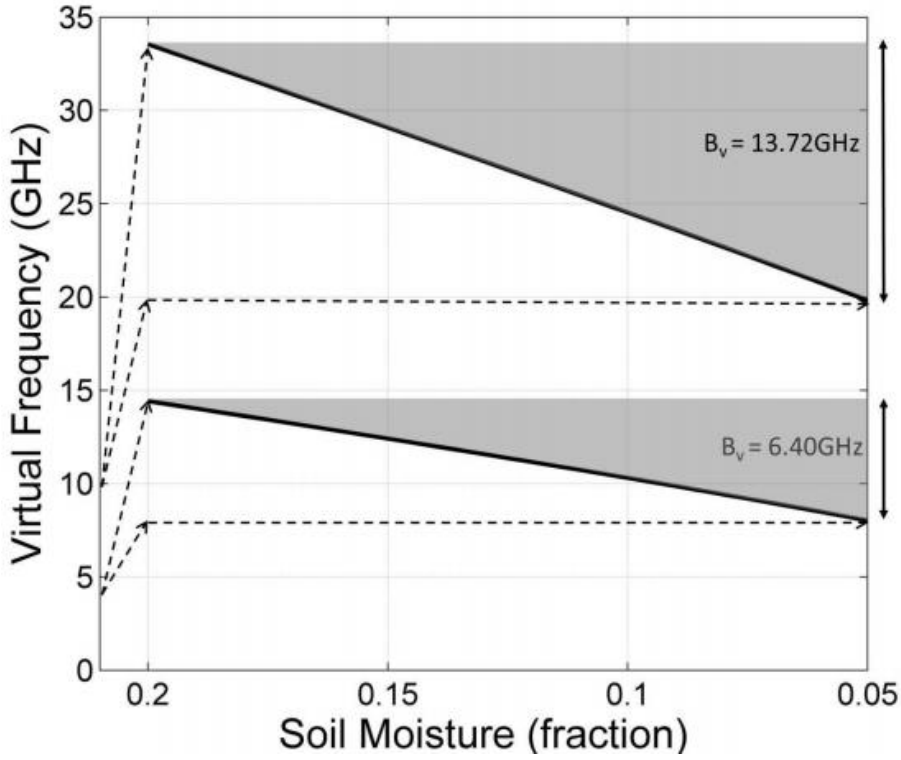

Figure 3.16: Simulation of real frequencies of 4GHz and 10GHz generating virtual bandwidths in a sandy soil during an SMC change (95% sand, 5% clay). ([1])

moisture is changing (drying out after rainfall, for instance) a virtual bandwidth, B_v can be created, given by;

$$B_v = f_R \Delta \sqrt{\varepsilon_r} \tag{3.42}$$

The fact that $\Delta\sqrt{\varepsilon_r}$ is a multiplicative term in Equation 3.42 and the fact that ε_r of a given soil is strongly dependant on soil moisture content means that relatively small changes in soil moisture can generate very large virtual bandwidths.

Figure 3.16 demonstrates how an SMC change from 20% to 5% causes a real frequency of 4GHz to have a virtual bandwidth of 6.40GHz over that soil moisture change and a real frequency of 10GHz to have a virtual bandwidth of 13.72GHz over the same moisture change.

These virtual bandwidths can be placed in a slightly modified version of Equation 3.5

to show that a virtual bandwidth can provide a subsurface resolution (Res_v) given by

$$Res_v = \frac{c}{2B_v} \tag{3.43}$$

In the two examples in Figure 30 this equation gives a resolution of 2.3cm and 1.1cm. This gives a vast improvement over typical spaceborne SAR range resolutions (which are typically on the metre scale) and allows sub-wavelength resolution for subsurface targets.

Returning to consider phase, and recalling from Equation 3.40 that β is given by:

$$\beta = k\sqrt{\varepsilon_r} \tag{3.44}$$

It can be seen that the phase change, $\delta\phi$, caused by the change in SMC is given by:

$$\delta\phi = 2kd(\sqrt{\varepsilon_{rm}} - \sqrt{\varepsilon_{rn}}) \tag{3.45}$$

Where $\sqrt{\varepsilon_{rm}}$ is the soil refractive index at time m, $\sqrt{\varepsilon_{rn}}$ is the soil refractive index at time n, d is the vertical thickness of the wet layer and the factor of 2 accounts for the two-way path through the soil volume.

[93] examine the effects of incidence angle on the phase change during changes in SMC. Firstly, they take into account the incidence angle, i, without considering refraction at the air/soil boundary. This gives the following equation:

$$\delta\phi = \frac{2kd}{\cos i}(\sqrt{\varepsilon_{rm}} - \sqrt{\varepsilon_{rn}}) \tag{3.46}$$

Considering refraction at the air/soil boundary, the following equation for phase change

is found:

$$\delta\phi = \frac{2kd}{\cos i}\left(\frac{\sqrt{\varepsilon_{rm}}}{\cos t_m} - \frac{\sqrt{\varepsilon_{rn}}}{\cos t_n}\right) \tag{3.47}$$

Where t_m and t_n are angles of transmission at times m and n, respectively, and are given via Snell's law:

$$t_x = \sin^{-1}\left[\frac{\sin_i}{\sqrt{\varepsilon_x}}\right] \tag{3.48}$$

[93] shows that when the effects of refraction are taken into account, the phase change seen over an SMC variation is almost independent of incidence angle (over the range 0° to 60°). A noticeable difference in phase changes is shown at low soil moisture levels between the 0° and 30° cases, but the magnitude of this difference is massively reduced compared to a simulation which ignores the effects of refraction.

In summary, VB-SAR theory states that by transmitting a real bandwidth into a soil that is experiencing a change in moisture content (and hence a change in dielectric constant) a range of virtual frequencies will be generated, forming a virtual bandwidth. Because the dielectric properties of a given soil are strongly dependent on the SMC very large virtual bandwidths can be created, giving very high subsurface resolutions.

3.5.3 VB-SAR Processing Flow

During the following discussions on VB-SAR processing, the following terms shall be used:

1) Phase history: In VB-SAR parlance, "phase history" refers to the phase trend of a given target or pixel over a change in SMC.

2) Amplitude history: Similarly, "amplitude history" refers to the amplitude trend of

a given target or pixel over a change in SMC.

3) Complex history: The combined amplitude and phase history of a given target or pixel.

As previously discussed in Section 3.5.2, the basic principle of VB-SAR is to use the complex phase and amplitude history of a pixel (which contains a buried object) generated by a change in SMC to produce a high resolution image of that buried target. In order to generate this image correctly, the complex history must be sampled over a linear SMC change in order to generate a linearly sampled virtual bandwidth. The use of SMC directly rather than soil refractive index is valid as the soil models show that the refractive index of a given soil is almost linear over reasonable soil moisture changes.

Unfortunately, the chances of the SMC change being linear over a series of InSAR acquisitions are minimal, therefore it is necessary to resample the complex history using interpolation between scans. This requires knowledge of the SMC in each InSAR image, which can either be obtained from in-situ measurements, estimated from the SAR images themselves using one of the methods in the published literature ([29], [94]) or obtained from other remote sensing sources [28] as discussed in more detail in Section 2.4.

After this resampling the complex history is passed through an FFT in order to form a depth profile of the subsurface below the selected ground pixel. This process of resampling and passing through an FFT can be repeated over the entire radar scene in order to produce a full 3-D view of the subsurface volume below the radar scene. Depending on the distribution of soil moisture within the SAR scene it may be possible to use the same SMC history for every pixel or more localised SMC histories may need to be measured. Using an inaccurate SMC history for a given pixel would distort the subsurface depth profile produced for that pixel.

The depth profiles produced in this manner lack any absolute depth information. In order to apply the correct depth scale to such a VB-SAR image the unambiguous range

generated by the virtual bandwidth must be considered.

In order to calculate this depth scale, recall that the unambiguous range of a linear FM radar operating in free space is given by

$$R_{unambig} = \frac{c}{2f_{step}} \tag{3.49}$$

Where $R_{unambig}$ is the unambiguous range, c is the speed of light in a vacuum and f_{step} is the frequency step between adjacent frequencies in the transmitted chirp.

In the VB-SAR process, as for conventional SAR, the output of the FFT represents the entire unambiguous range. From this it follows that the range represented by each FFT bin is

$$R_{FFTbin} = \frac{R_{unambig}}{n_{FFT}} \tag{3.50}$$

Where R_{FFTbin} is the range represented by each FFT Bin and n_{FFT} is the number of bins in the FFT.

$R_{unambig}$ must also be calculated, and for VB-SAR this is done in the following manner. Firstly, the total virtual bandwidth is calculated using Equation 3.42, the SMC in the first and last images and the soil model presented by [17]. Next, the virtual frequency step is calculated by dividing the virtual bandwidth by the number of images in the dataset passed to the VB-SAR routine. Finally, this virtual frequency step, f_{vstep} is used to calculate the unambiguous range via

$$R_{unambig} = \frac{c}{2f_{vstep}} \tag{3.51}$$

However, this equation for unambiguous range assumes propagation within free space. As VB-SAR operates within a soil having a refractive index $\neq 1$ this FFT bin equation

must be modified to:

$$R_{FFTbin} = \frac{R_{unambig} n_{av}}{n_{FFT}} \tag{3.52}$$

Where n_{av} is the average refractive index of the soil over the phase history and can be calculated using the soil model presented by [17].

Note that this value for R_{FFTbin} is only ever an approximation as the refractive index of the soil changes over the drying process. In addition, the real R_{FFTbin} will vary between columns unless the intial wetting and subsequent drying processes are perfectly uniform.

Once R_{FFTbin} has been calculated placing a depth scale on the depth profile produced by VB-SAR is a simple exercise.

It is possible to perform VB-SAR using only the phase history of pixels as well as the complex pixel history. However, in order to create an accurate image the amplitude histories must also be included so that the surface return and the returns from any buried features are scaled in amplitude appropriately.

3.5.4 Practical VB-SAR Processor Implementation

A VB-SAR processor has been implemented within a MATLAB function which performs VB-SAR on one pixel within the source image each time it is called. The overall processing flow of the VB-SAR function as implmented is shown in Figure 3.17. As with the TP processor implemented as part of this project, the VB-SAR processor was designed to be as flexible as possible and configurable by various parameters passed to it via the calling function. These parameters are listed in Table 3.4. The application of this VB-SAR processor to an actual dataset is described in Chapter 5.

The function uses four data sets to perform VB-SAR; the time each scan was taken, a reference phase trend from a buried trihedral (used to calculate SMC), the complex history for the TP pixel in question and the complex correction factor (the phase and amplitude

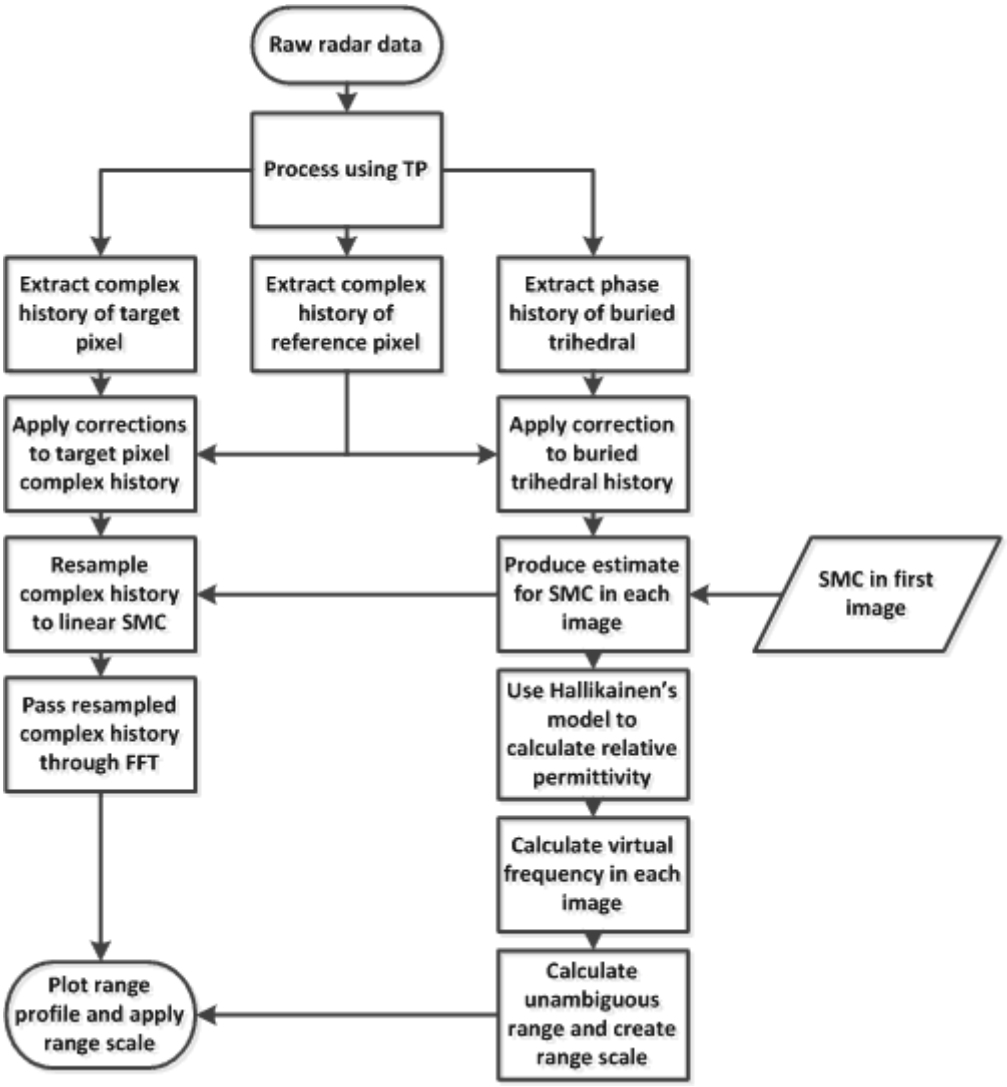

Figure 3.17: Flowchart of the implemented VB-SAR processing function

Parameter	Description
use_ampls	Toggle whether to feed both phases and amplitudes to FFT or just phase to the FFT
FFT_length	FFT length to use
do_hamming	Toggle application of hamming window to the data being fed to the FFT
added_water	Amount of water added to soil volume [ml]
depth_start	Depth to start output [cm in air]
depth_spacing	Distance between samples in output [cm in air]
depth_finish	Depth to finish output [cm in air]
start_scan	Number of scan in DInSAR stack to start VB-SAR processing at
stop_scan	Number of scan in DInSAR stack to stop VB-SAR processing at
do_dc_sub	Toggle whether DC removal
do_time_correc	Toggle whether extrapolation through periods of non-sampling
centre_freq	Centre real frequency of input pixel data, used to calculate refractive indices and virtual frequencies in use
phase_moisture_relationship	Relationship between phase response and water change, [°/ml]
soil_clay	Clay content of soil [%]
soil_sand	Sand content of soil [%]

Table 3.4: Control parameters implemented in the MATLAB VB-SAR processing function.

Parameter	Description
scan_timings	Vector of scan timings, in seconds with initial scan set to zero
reference_phase_trend	Corrected and unwrapped phase trend extracted from a buried reference trihedral; used to derive a moisture history for the data pixel
pixel_data	Complex value history for the pixel to be used as the data source for VB-SAR.
correction.phase	Phase history for a reference trihedral (or cross talk) pixel to be used to correct pixel_data
correction.ampl	Amplitude history for a reference trihedral (or cross talk) pixel to be used to correct pixel_data

Table 3.5: Data inputs to the VB-SAR processor.

Parameter	Description
fft_output	VB-SAR depth profile for the pixel of interest
fftbin_depth	Depth each output fft bin represents. Calculated to take into account the average refractive index of the soil [m]
unambig_range	Unambiguous range in free space resulting from the virtual bandwidth [m]
delta_f	Virtual frequency step size
VB_res	Resolution resulting from virtual bandwidth (does not take into account soil refractive index) [m]
VB	Virtual bandwith [Hz]
n_start	Refractive index of the soil at the start of the data set
n_stop	Refractive index of the soil at the end of the data set
n_av	Average refractive index of the soil over the data set
f_start	Start virtual frequency
f_stop	Stop virtual frequency

Table 3.6: Outputs produced by the VB-SAR processor.

history of either a surface reference trihedral or the antenna cross talk), as listed in Table 3.5.

The function is also fed a structure of parameters that control the operation of the processor, including the FFT length to use, whether to use the pixel amplitude history as well as the pixel phase history and whether to apply a hamming window to the pixel data. These parameters are listed in Table 3.6.

The first stage in the process is to correct the pixel history. This includes phase unwrapping (necessary as otherwise phase ambiguities may be erroneously resampled to very rapid phase changes during the resampling processes) and amplitude and phase corrections using the complex correction factor to remove variations induced by variations in the radar system over the course of the VB-SAR acquisition.

Once the pixel history has been corrected, the pixel history and reference phase history must be resampled to a linear time base. Ideally this is unnecessary as the critical resampling in VB-SAR processing is to obtain a linear soil moisture step.

However, periods of non-sampling or irregular sampling may create errors that need to be corrected. If during a period of non-sampling the phase has changed by less than 2π between adjacent samples then temporal resampling alone will approximately fix (via linear interpolation) the error.

If, on the other hand, the phase changes by more than 2π between samples then temporal resampling itself cannot correct the error (as there is an additional phase wrapping ambiguity introduced), and the first phase unwrapping may also fail to correct this ambiguity. In this case, it is necessary to correct the error using the phase trend (in °/unit time) adjacent to the error. The automation of this process (identification and correction of such errors) is simplified if the sampling is evenly spaced in time.

Next, the reference phase history extracted from the buried trihedral is used to create a moisture history. This involves applying the moisture/phase relationship derived during

the wetting period to the difference in phase at each scan relative to the phase in a reference scan where the water content was precisely known (in reality, either the reference dry soil scan taken before the start of water addition or a scan in the wetting period). If SMC information is available, this step can be bypassed.

Considering laboratory experimentation, using the wettest scan's phase as a reference may introduce uncertainty; it has to be assumed that the soil moisture content in that wettest scan was uniform and simply the total water added during the experiment divided by the volume of wet soil above the trihedral. This assumption is flawed, as some water will have inevitably escaped this defined volume.

The dry scan presents a much better reference as it is simply the difference in the reference phase between the dry scan and the scan under consideration that drives the moisture calculation. This process generates an estimate of the moisture content of the soil above the target at each scan which is later used to apply a depth scale to the VB-SAR output.

In order to linearise the moisture sampling, MATLAB's $interp()$ function is used to linearise the temporally resampled and corrected phase and amplitude histories of the pixel being processed using the linear moisture vector as the query points and the moisture content estimate as the sample points.

The (artificially generated) reference linear moisture history is then passed to a function that implements the dielectric model presented by [17] in order to calculate the soil refractive index which is needed to generate the depth scale as discussed in Section 3.5.3

Finally, the outputs (the pixel's phase and amplitude histories) of this resampling are placed back into complex form, hamming weighted if specified by the function call and fed into an FFT of the length specified in the function call.

The function will return the output of this FFT (which is the VB-SAR depth profile) and a list of VB-SAR parameters including virtual bandwidth, the theoretical VB-SAR

range resolution and the depth per FFT bin. From these parameters the calling script can easily apply a depth scale to the produced VB-SAR depth profile. Implementing the VB-SAR processor as a function ensures maximum flexibility; it is trivial to apply it to single pixels or entire images.

3.6 Summary

This chapter has presented a brief overview of several radar techniques and detailed the implementation of those chosen for use during this work.

This chapter started with a presentation of the SAR technique. The background theory of the process was discussed, along with some limitations of the method. Next, the mathematical basis of the processing algorithm used in this work was presented. Finally, key parameters of current and historic spaceborne SAR systems were presented.

Following this the extraction of meaningful phase information from SAR was considered. Both InSAR and DInSAR methods were discussed, along with the acquisition requirements of both methods.

Next, the TP technique was described. This is also a process that makes use of synthetic aperture techniques, but has the key benefit (for this work) over SAR of maintaining a constant incidence angle across a radar scene. In addition, that incidence angle can be varied at process time, rather than requiring multiple data collections. The TP algorithm itself was explained and the MATLAB implementation of the process produced during this work was also detailed.

Finally, the VB-SAR subsurface imaging technique which is the focus of this work was presented. This technique offers the ability to acquire high resolution subsurface radar images using remote sensing techniques, as opposed to the current subsurface radar systems that are required to be in close proximity to the area of interest. The theoretical

background of the method was first presented, and then the MATLAB implementation of a practical VB-SAR processor was described.

Chapter 4

Subsurface and VB-SAR Simulation

4.1 Introduction

This chapter presents the simulations carried out as part of this work. These simulations were designed to test several key assumptions and features of the VB-SAR imaging process before proceeding to the laboratory based experimentation.

Firstly, a brief review of the soil models used is presented. These models are used by all the subsurface simulations presented here to predict the electrical properties of a particular soil containing a certain amount of water.

Next, a simple ray tracing simulation scheme is shown. This simulation used Snell's law to calculate the electrical path length through the soil to a buried target. By altering the distribution of water in the soil above a buried target it is possible to show whether the distribution of soil moisture is likely to affect the VB-SAR process.

Following this, Fresnel's equations are applied to simulate the reflectively of moist soils. This enabled predictions to be made about which polarisation scheme is likely to give the best subsurface images.

After these relatively simplistic simulations a more representative subsurface radar

simulator is discussed and presented. This simulator extended an existing SAR simulator to be able to handle subsurface targets, again using the soil models previously presented. This simulator is capable of emulating both an along track radar system (as used for the TP scheme) and a side looking radar system (as would be used in a real-world application of VB-SAR).

The subsurface radar simulator is then demonstrated. An example scene is constructed containing both surface and subsurface targets and both the TP processor and an existing backprojection imager are used to verify that the simulator is working as expected.

Finally, the VB-SAR scheme is tested using the simulated radar data. Several key features of VB-SAR are tested, namely;

1. The ability of the VB-SAR imaging scheme to enhance the subsurface resolution above that given by the original radar images
2. The effect varying the incidence angle of the radar wave has on VB-SAR is explored
3. The real frequency independence of the VB-SAR process is explored
4. The ability of the VB-SAR scheme to resolve buried targets buried at different depths in the same subsurface column is demonstrated

4.2 Review of Soil Modelling Techniques

4.2.1 Modelling of Electrical Properties of Soil

As perviously discussed in Chapter 2, the electrical properties of soil are strongly related to the texture of the soil, the moisture content of the soil and the radar frequency in use. Within the published literature, there are many different models and formulae that attempt to represent these dependencies.

For this work, three different soil models were selected from the literature, implemented in MATLAB and compared. All three models aim to calculate the complex dielectric constant of moist soil, but the three models have different ranges of validity and inputs. The three models chosen were taken from [17], [19] and [20].

[17] presents an empirical model that uses the sand and clay content of the soil under consideration to characterise its texture. The equations presented use the two texture parameters, along with moisture content and coefficients calculated for set frequencies (1.4GHz and 2 to 18GHz in steps of 2GHz) to fit the equation to the measured data. This limits the application of the model to fixed frequencies, but the model itself is very easy to implement and is very flexible as it can be applied to any soil texture. In addition, interpolation can be used to apply the model to intermediate frequencies.

[19] takes a different approach to soil modelling. Rather than defining coefficients for a set range of frequencies, coefficients for different soil textures at particular frequencies are given and there is emphasis on modelling the Debye dielectric relaxation (the time required for dipolar molecules within a material to reorientate themselves after an alternating electric field is applied to the material) processes within the soil rather than measuring dielectric constants and fitting equations to those measurements. This model is somewhat limited in application as it is only directly applicable to certain soils at certain frequencies, though again it is possible to use interpolation to allow for other frequencies.

[20] expands the model of [19] by using the texture of the soil (characterised by clay content in this case) to calculate the coefficients the model uses to derive the dielectric properties of the soil. Whilst this is a limited representation of textures it does allow greater flexibility than the model presented by [19] which was strictly limited to the selected soils studied in that paper. As per the previous models, frequency choice is limited without interpolation.

Figure 4.1 shows the refractive index (which is the square root of the magnitude of the

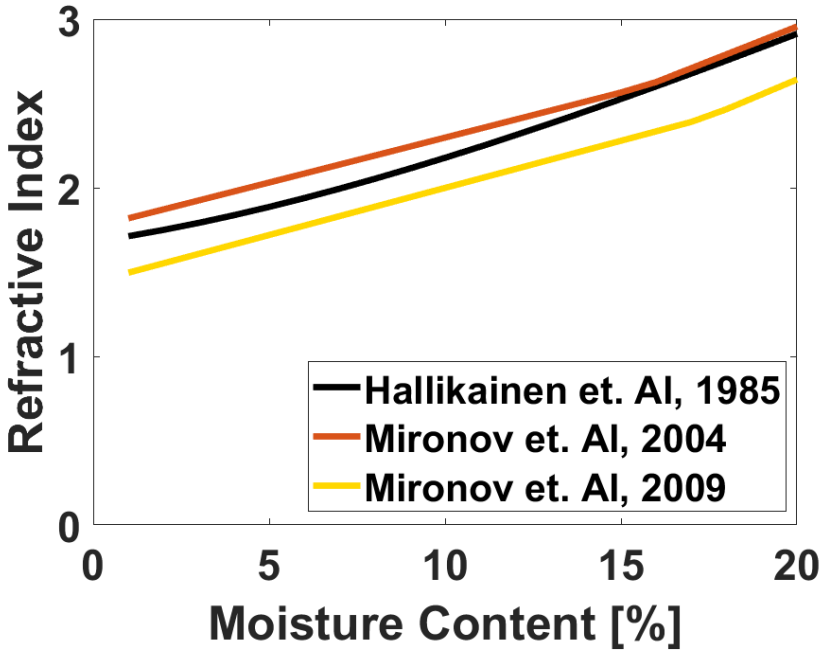

Figure 4.1: Comparison of the three different soil models at 4GHz in a soil of 5.02% sand, 47.38% clay (referred to as Field 5 soil in the papers). Plotted over 0-20% moisture.

complex dielectric constant at a given frequency) calculated by the three models at 4GHz in a standard soil. The results align well with each other as can be seen; although this is only a test of one soil type at one frequency the plotting code can be very easily modified to check the model's relative performance in other situations as necessary.

For the simulations presented here to explore the general behaviour of the VB-SAR imaging scheme the absolute accuracy of the soil models relative to real soil is not critical. However, during actual VB-SAR imaging an accurate soil model is important as accurate reconstruction of soil dielectric constant from SMC measurements is necessary to obtain an accurate sub surface depth scale. One possible method of overcoming this could be to seed the VB-SAR scene with buried targets at known depths, then apply a depth scale such that the known targets appear at the correct depth in the VB-SAR depth profiles. However, this may not be feasible for VB-SAR imaging of large or inaccessible areas and

it assumes that the SMC is uniform across the imaging scene.

For the simulations and VB-SAR processing performed as part of this work it was decided to use the Hallikainen model. This choice was made due to the flexibility of the model and the ease of implementation. The model proposed by Hallikainen is very simple to implement, consisting of a single polynomial of the following form:

$$\varepsilon_c = (a_0 + a_1 S + a_2 C) + (b_0 + b_1 S + b_2 C) m_v + (c_0 + c_1 S + c_2 C) m_v^2 \tag{4.1}$$

Where ε_c is either the real or imaginary part of the complex dielectric constant, S is the percentage of sand in the soil, C is the percentage of clay, m_v is the volumetric water content of the soil and a_0, a_1, a_2, b_0, b_1, b_2, c_0, c_1 and c_2 are coefficients which vary with frequency, soil texture and whether the real (ε_r) or imaginary (ε_i) part of the complex dielectric constant is under consideration.

Although only certain frequencies are listed in the table of coefficients it is possible to estimate the complex dielectric constant at other frequencies by calculating (ε_i) and (ε_r) at two frequencies either side of the frequency of interest and applying interpolation.

4.3 Application of Ray Tracing Models to TP

Using the model presented by [17], simple simulations were run. A soil volume consisting of multiple layers of soil with different SMCs or soil textures above a buried target was considered, and the path of a radar wave down to the depth of that target was modelled in the following manner.

For a radar wave interacting with the soil surface at a given angle of incidence the angle of refraction was calculated using the dielectric constant calculated by the soil model. This angle of refraction was used to calculate the physical path length of the wave through

the first layer of soil and the angle of refraction became the angle of incidence with the next soil layer; this process was repeated for each layer until the target was reached. The electrical path length to the target was calculated by summing the electrical path length in each layer together,

In each different scenario every possible layer ordering was simulated; this thoroughness was ensured by using MATLABs perms() function to generate the list of layer orderings to simulate.

Two key simplifications were made; a fixed point of entry with the soil was used (and hence variable platform and target points rather than the more realistic case of fixed platform and target points with a varying point of refraction as soil moisture varies), and the interface between the soil and air was modelled as being ideal (smooth) instead of considering the more realistic rough surface of soil. In reality, surface roughness modifies the amount of backscatter seen by a radar from a given soil surface. In the case of a monostatic radar system, rougher soil surfaces generally present stronger backscatter from a given soil (smooth surfaces giving a more specular reflection of radar energy away from the radar system). However, the difference between rough and smooth varies over incidence angle and frequency; near nadir the smooth surface can give stronger backscattering [10].

By stacking multiple layers above one another and calculating the electrical path length to a particular depth it was possible to explore the effects of different moisture and soil texture combinations on a buried target.

It was found that the distribution of water above a buried target will not significantly alter the phase response of the target as long as the total water content above the target is constant. The method used to explore this was to set up a vector containing the moisture content in each layer and use MATLABs perms() function to produce all possible orderings of the layers. A two permutation representation of this simulation is shown in the

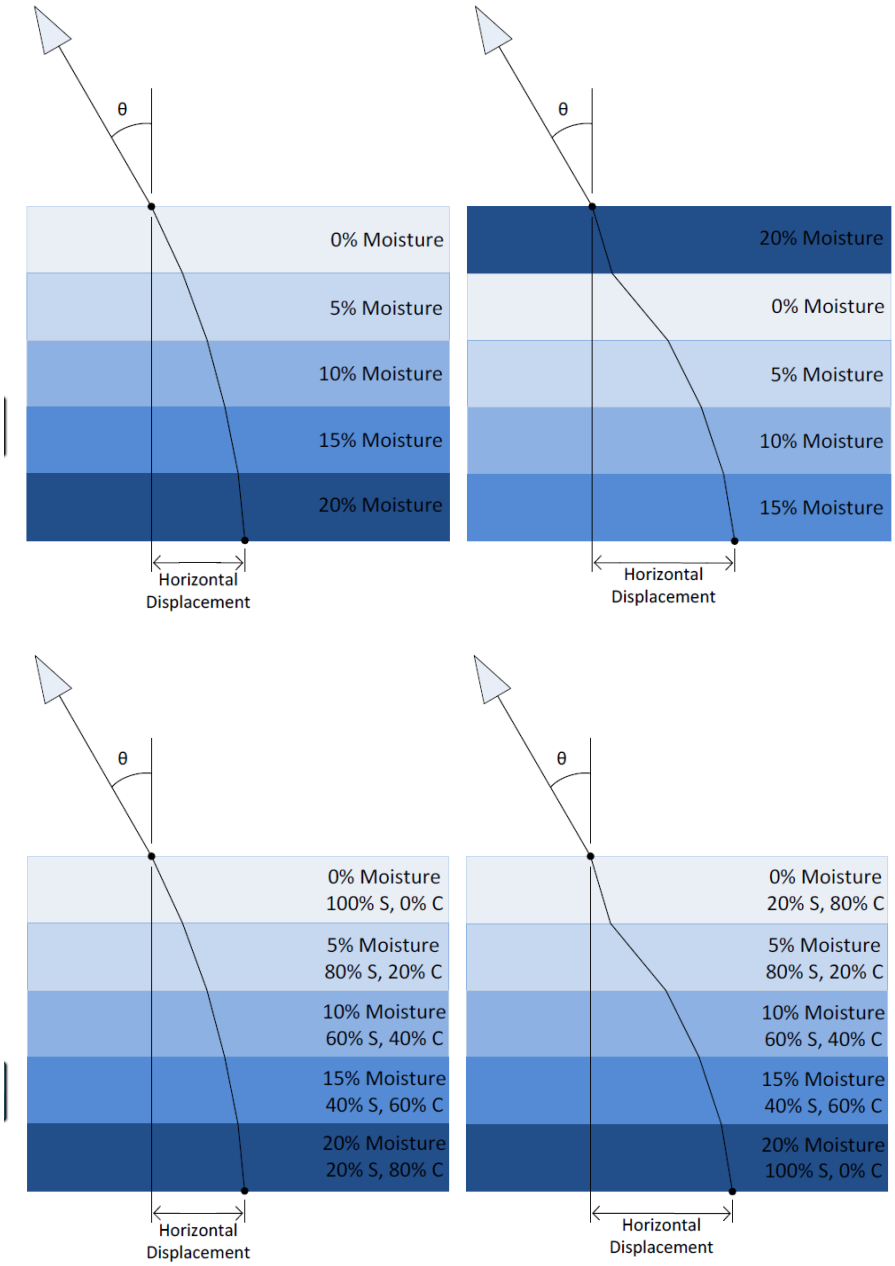

Figure 4.2: Conceptual sketches of the soil volume simulations performed. "S" in the sketches refers to sand, "C" refers to clay.
Top: Two permutations of the water distribution simulation. (angle of incidence) is held constant whilst the horizontal displacement and electrical path length through the soil are measured (variation in horizontal displacement and effect of refraction grossly exaggerated for clarity). In this simulation all layers were modelled as having 100% sand content.
Bottom: Two permutations of the soil texture arrangement simulation. (angle of incidence) is held constant whilst the horizontal displacement and electrical path length through the soil are measured (variation in horizontal displacement and effect of refraction grossly exaggerated for clarity)

upper part of Figure 4.2.

This simulation showed that the path length variation for different orderings was minimal. For example, given a target buried at 20cm, under 5 distinct layers of soil comprised of 100% sand with 0, 5, 10, 15 and 20% moisture illuminated at a 20° incidence angle the phase variation was 0.0°. This result agrees with the prediction made by [93] that the moisture distribution above the target is not significant for VB-SAR, it is only the total amount of moisture that is significant.

In addition, the effect of different soil texture arrangements above the target was explored. This script took in a sand content for each layer (the number of layers being 5), held the SMC within each layer at a fixed value (so that the soil textures moved but the moisture did not) and evaluated the phase response of the target under each arrangement of soil textures. A two permutation subset of this simulation is illustrated in the lower part of Figure 4.2.

Again, the phase variation was found to be minimal. For example, a target buried under 20cm of soil, with 5 layers of soil with sand contents of 0, 20, 40, 60 and 80% (with the balance being clay) experiences a maximum phase variation over all possible orderings of sand contents of 3.1° when illuminated by a radar beam with an incidence angle to the top soil surface of 20°.

4.4 Polarimetric Simulations

The VB-SAR process itself does not have any polarisation dependencies. Therefore, in theory the only difference in VB-SAR images acquired using different polarisations should be due to the polarisation dependent response of the buried target (for example, corner trihedrals have a strong co-polar response but a weak cross-polar response) and the different amounts of reflection experienced at medium boundaries (e.g. air/soil, dry

soil/wet soil).

The reflection losses and transmissivites at a plane boundary between two materials can be easily approximated using the Fresnel coefficients. These can be calculated using the refractive indices of the materials on each side of the boundary, as shown in Equations 4.2 and 4.3 (reflectivities), and Equations 4.4 and 4.5 [95]. These equations are the general case for media that may not be non-magnetic (such as certain soils containing iron-bearing compounds).

$$r_p = \frac{(\frac{n_1}{\mu_1})\cos\theta_t - (\frac{n_2}{\mu_2})\cos\theta_i}{(\frac{n_1}{\mu_1})\cos\theta_t + (\frac{n_2}{\mu_2})\cos\theta_i} \tag{4.2}$$

$$r_s = \frac{(\frac{n_1}{\mu_1})\cos\theta_i - (\frac{n_2}{\mu_2})\cos\theta_t}{(\frac{n_1}{\mu_1})\cos\theta_i + (\frac{n_2}{\mu_2})\cos\theta_t} \tag{4.3}$$

$$t_p = \frac{2(\frac{n_1}{\mu_1})\cos\theta_i}{(\frac{n_1}{\mu_1})\cos\theta_t + (\frac{n_2}{\mu_2})\cos\theta_i} \tag{4.4}$$

$$t_s = \frac{2(\frac{n_1}{\mu_1})\cos\theta_i}{(\frac{n_1}{\mu_1})\cos\theta_i + (\frac{n_2}{\mu_2})\cos\theta_t} \tag{4.5}$$

Where n_1 and n_2 are the refractive indices of the two materials, μ_1 and μ_2 are the permeabilities of the two materials, θ_i is the incidence angle and θ_t is the transmission angle. For the non-magnetic soils under consideration here μ_1 and μ_2 are set as the permeability of free space ($4\pi * 10^7$ H/m).

However, for radar purposes it is the intensity reflectivity (R_s and R_p) and transmissivities (T_s and T_p) that are of interest. These are given by;

$$R_p = |r_p|^2 \tag{4.6}$$

$$R_s = |r_s|^2 \tag{4.7}$$

$$T_p = 1 - R_p \tag{4.8}$$

$$T_s = 1 - R_s \tag{4.9}$$

It is clear that these parameters would depend on two things in a typical VB-SAR scenario; the refractive index of the soil and the incidence angle. The incidence angle is simply related to the imaging geometry of the radar system which varies across the imaging scene in the case of a side-looking SAR (or is set by the reconstruction angle chosen in the case of TP) and the refractive index of the soil is governed by the frequency in use (set by the radar system), the soil moisture and the soil texture. From this, it became clear that a simulation across a range of incidence angles, soil moistures and polarisations was warranted.

The results of running this simulation are shown in Figure 4.3. The incidence angles chosen correspond to the range over which Sentinel-1's Interferometric Wide-swath mode (IW) [3, 96] operates. IW mode is the normal observation mode for Sentinel-1. The upper part of Figure 4.3 shows the transmission intensity travelling into the soil from the air and the lower part of Figure 4.3 shows the transmission intensity for the return path from the soil through the air to the radar platform. As can be seen, the V polarisation sees better transmission through the boundary in both directions.

In addition, Figure 4.4 shows the combined transmission intensity for the round trip between the platforms transmit antenna and receive antenna. This appears to show that VV is the optimal polarisation combination to ensure maximum combined transmission

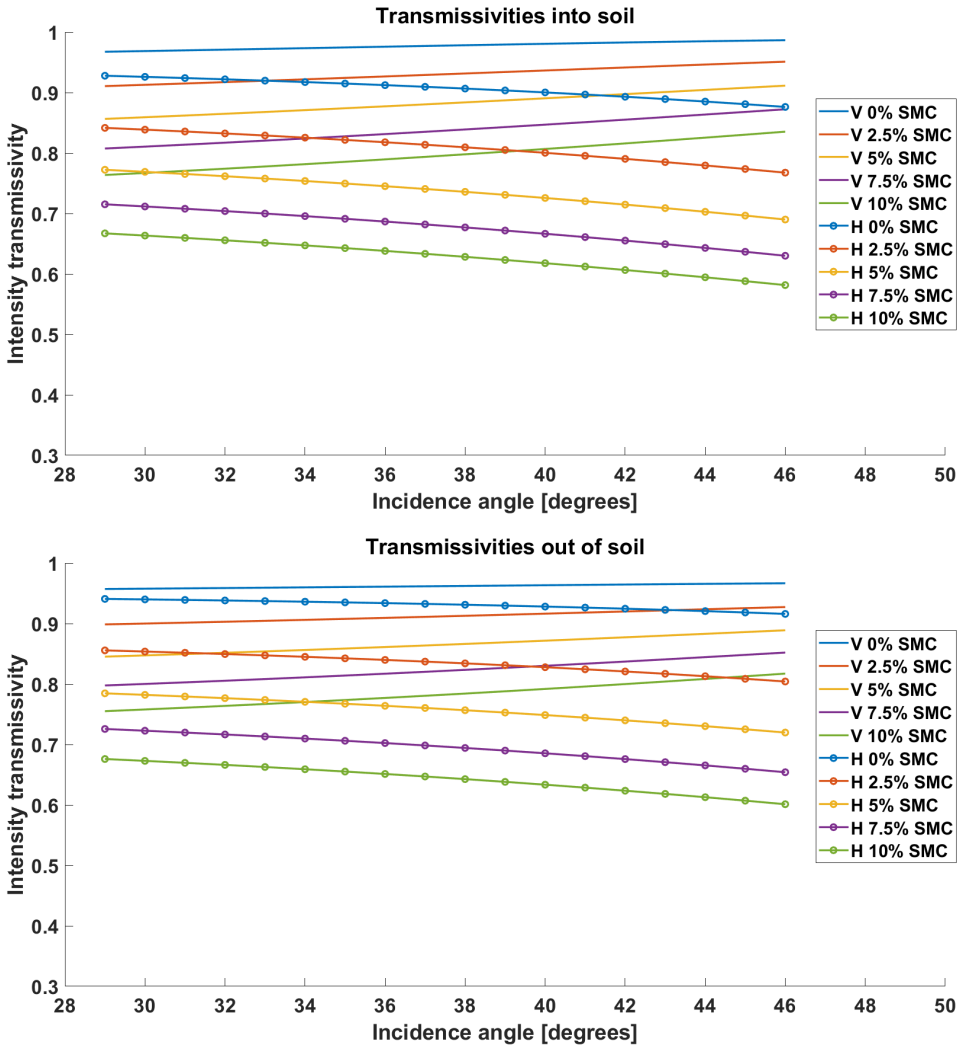

Figure 4.3: One way simulations of transmission intensities for 100% sand.
Top: Simulation of transmission intensity from air into soil in both V and H polarisations. Colours denote soil moisture consistently across polarisations.
Bottom: Simulation of transmission intensity from soil into air in both V and H polarisations. Colours denote soil moisture consistently across polarisations.

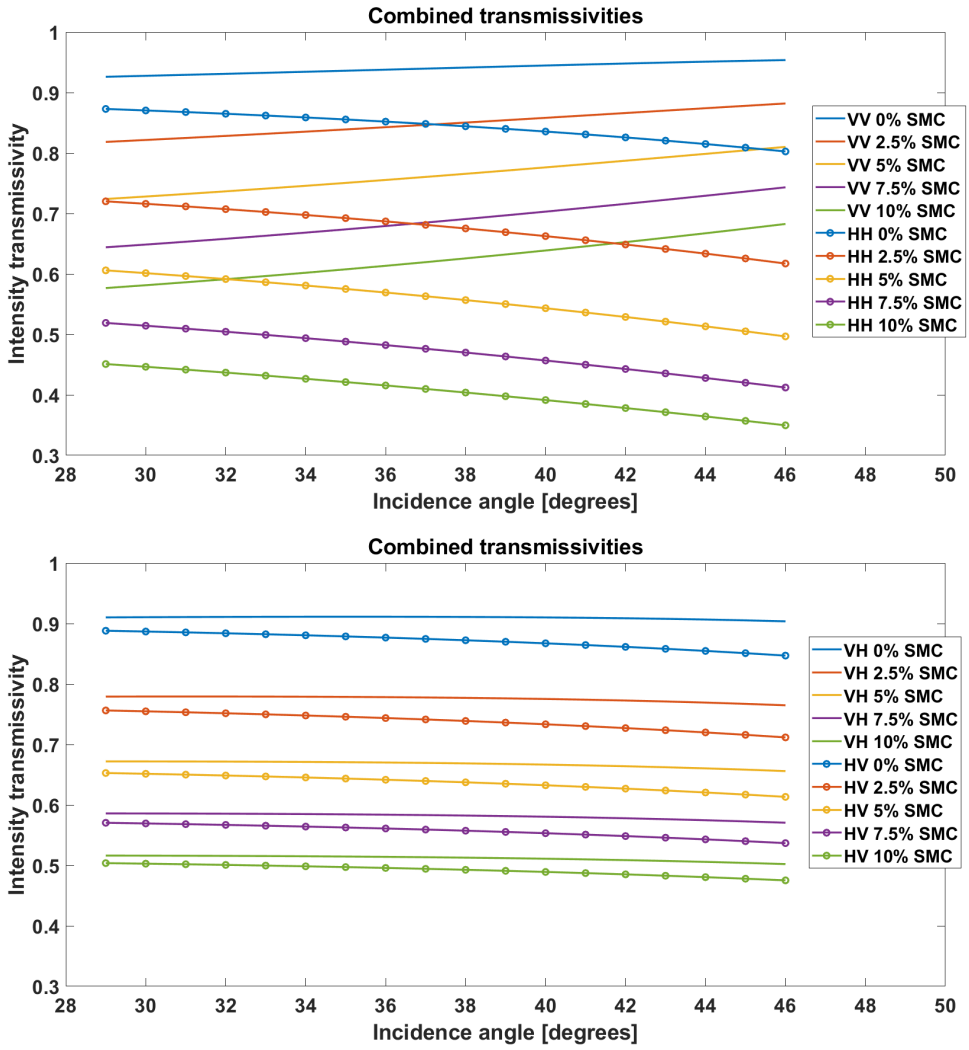

Figure 4.4: Two way simulations of transmission intensities for 100% sand.
Top: Simulation of 2 way transmission intensity in both VV and HH polarisations. Colours denote soil moisture consistently across polarisations.
Bottom:Simulation of 2 way transmission intensity in both VH and HV polarisations. Colours denote soil moisture consistently across polarisations.

across the air/soil boundary and that in the crosspolarisation case, the VH polarisation is superior to HV for a given SMC and incidence angle.

However, VH being superior to HV would violate polarimetric reciprocity, which holds that the observations in HV and VH should be equal [97]. [98] state that this is due to the Fresnel coefficients being defined for plane waves, which assumes an infinite surface, and the correct solution can be found using the Huygens-Fresnel principle. This would be beyond the scope of this work, and it is suggested that this could be investigated during future work, either during further simulation or experimentally.

4.5 SAR Simulation

Once the simple ray tracing models had drawn to a close, work started on a more realistic model, one that simulates a realistic imaging process using subsurface targets. [52] present a SAR simulator that is implemented in MATLAB.

The simulator presented by [52] is a relatively simple freespace simulator that calculates the pathlength to each target at each radar position. It then works out the phase that this corresponds to at each frequency within the transmitted pulse before passing the computed data to the backprojection algorithm also described by [52]. This simulator code formed the basis of the SAR simulator formulated as part of this project which was then heavily modified to be applicable to subsurface radar simulation.

4.5.1 The SAR Simulator

The original simulator presented by [52] used a circular flight path, with each antenna point being described by a 3-D position, (Ant_x, Ant_y, Ant_z). This makes it possible to describe any series of antenna positions during a radar data collection scan, for this work

the flight path was always linear.

The original simulator assumed monostatic operation, so the radar path length, R to a single target from a particular antenna position was calculated via:

$$R = 2 * \sqrt{(Ant_x - Targ_x)^2 + (Ant_y - Targ_y)^2 + (Ant_z - Targ_z)^2} \tag{4.10}$$

Where, similar to the antenna case, ($Targ_x$, $Targ_y$, $Targ_z$) describes the position of a single point target.

The phase history of that pulse at a single frequency point is then calculated via

$$Ae^{-2i\pi Rf} \tag{4.11}$$

Where A is the amplitude of the particular target and f is the frequency (in Hz) under consideration.

Should more than one point target be present in the scene the phase history at a single antenna position for a given frequency is calculated via

$$\sum_{R=R_1}^{R_n} Ae^{-2i\pi Rf} \tag{4.12}$$

Where $R_1, R_2, R_3, ...R_n$ are the ranges to each point target in the radar scene. This complex value is then stored as the first frequency response of the radar scene at that antenna position, the process being repeated for each frequency point in the radar pulse at that point. The simulator then moves onto the next values of [Ant_x, Ant_y, Ant_z] and repeats this process until the entire radar scan is complete.

The antenna separation of the radar system used for this study is just under a tenth of the distance from the antennas. In order to make the simulation more representative of the radar system used the simulator was modified to operate in bistatic mode, with the

transmit and receive antenna positions being separately defined by $[Tx_x, Tx_y, Tx_z]$ and $[Rx_x, Rx_y, Rx_z]$ respectively. The transmit and receive path lengths are than calculated separately before being summed and then used to calculate the total radar path length to and from each target as:

$$R_{Tx} = \sqrt{(Tx_x - Targ_x)^2 + (Tx_y - Targ_y)^2 + (Tx_z - Targ_z)^2} \tag{4.13}$$

$$R_{Rx} = \sqrt{(Rx_x - Targ_x)^2 + (Rx_y - Targ_y)^2 + (Rx_z - Targ_z)^2} \tag{4.14}$$

$$R = R_{Tx} + R_{Rx} \tag{4.15}$$

The phase histories were then calculated as before using Equation 4.12.

More significant were the modifications needed to allow simulation of subsurface targets. These involved splitting the path phase calculation into two parts; the above surface path (through air) and the sub surface path (through the soil) as illustrated in Figure 4.5.

In a simulated radar scene, the locations of the radar platform and the (buried) target(s) are known; the refraction point (where the radar wave enters the soil) on the soil surface is unknown and this must be calculated for the path lengths to be calculated correctly. The solution to this involves applying Snell's law, but not in its "classic" form shown in Equation 4.16, where the point of refraction is fixed.

$$\frac{\sin\theta_1}{\sin\theta_2} = \frac{n_2}{n_1} \tag{4.16}$$

In order to perform this simulation a method must be found to calculate the point of refraction, given knowledge of the antenna's position, the target's position and the dielectric properties of the two mediums (in the case of the subsurface simulator, the two

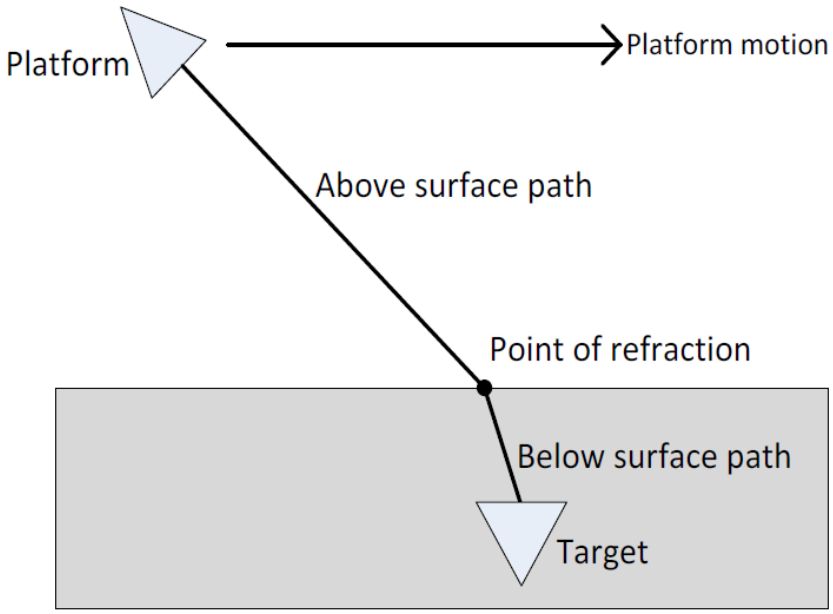

Figure 4.5: Simplified (monostatic 2-D) overview of the SAR simulator modified for subsurface radar simulation. The point of refraction on the surface is related to the properties of the soil, the radar frequency and the relative positions of the radar platform and target.

mediums are air and soil).

[99] present a method of solving for the refraction point which is attractive for implementation in MATLAB. By presenting the problem as a quartic polynomial it is possible to calculate solutions using MATLAB's roots() function, which is a rapid process. However, upon implementing this method an error in the paper was discovered; results obtained from this paper using both the quartic and Ferrari methods are consistent but both fail the consistency check of being substituted back into Snell's law in its classic form. The Authors were contacted regarding this discrepancy and an error in the paper was confirmed but a solution was not forthcoming.

[100] present an alternative method of solving for the point of refraction (the point on the ground at which the ray enters the ground on the way to the target, denoted as ($Refrac_x$,0)) in a 2-D scenario (x-y plane) at the surface of a single layer of soil when all other variables (position of target ($Targ_x$,$Targ_y$), position of platform (Ant_x,Ant_y), re-

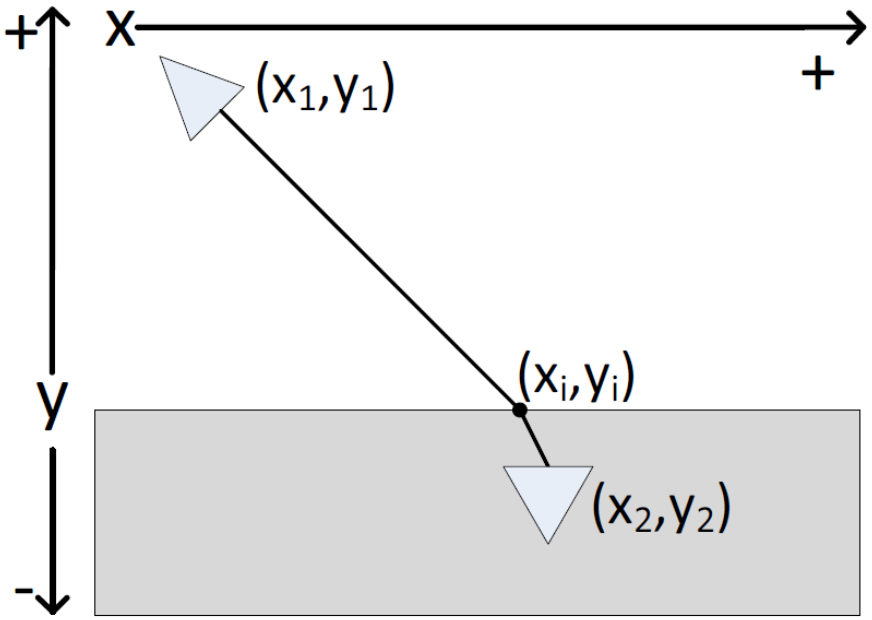

Figure 4.6: Single layer Snell's law situation solved by Dziewierz and Gachagan. By definition, $Refrac_y$ (depth of soil surface) is 0

fractive index of first layer (n_1) and refractive index of second layer(n_2)) are known. This situation is shown in Figure 4.6. Note that this is only a 2-D solver, not suitable for sidelooking radar simulation but adequate for along track (TP style) imaging.

The significant equation derived within the paper is

$$\frac{((Refrac_x - Ant_x)/\sqrt{(Refrac_x - Ant_x)^2 + Ant_y^2})}{((Targ_x - Refrac_x)/\sqrt{(Targ_x - Refrac_x)^2 + Targ_y^2})} = \frac{v_1}{v_2} \tag{4.17}$$

Where v_1 and v_2 are the speeds of light in the first and second layers. By noting that

$$n_1 = \frac{c}{v_1} \tag{4.18}$$

and

$$n_2 = \frac{c}{v_2} \tag{4.19}$$

it is possible to rearrange this equation to the following form, so it can be used with the output (refractive index) of a soil model and the refractive index of air.

$$\frac{((Refrac_x - Ant_x)/\sqrt{(Refrac_x - Ant_x)^2 + Ant_y^2})}{((Targ_x - Refrac_x)/\sqrt{(Targ_x - Refrac_x)^2 + Targ_y^2})} = \frac{n_2}{n_1} \tag{4.20}$$

The only issues with this model are that it does not work with more than one soil layer (though, as shown later, it can be modified to solve for two soil layers in some situations) and that it is a double-quadratic equation which is somewhat slow to solve directly within MATLAB. [100] do present optimised C-code to solve it more efficiently; within MATLAB the solve() function can handle it but this is very slow, particularly when it is considered that this must be solved at least once for each position of the radar (ideally it will be solved at each frequency too when using a frequency dependent soil model), and if a sequence of scenes containing varying SMC is to be simulated (as is needed to test VB-SAR) there will be a different set of solutions for each image. Therefore, implementing Equation 4.20 directly would result in an impractically slow simulation.

Solving this equation directly gives a range of possible values for $Refrac_x$, with only one being the correct solution. This correct solution can be selected by discarding the complex results and selecting the result that shows $Refrac_x$ lying between the platform (Ant_x) and target ($Targ_x$) positions. By noting that only one plausible (real and in a feasible position relative to the platform and target) solution exists and rearranging Equation 4.20 to

$$\frac{((Refrac_x - Ant_x)/\sqrt{(Refrac_x - Ant_x)^2 + Ant_y^2})}{((Targ_x - Refrac_x)/\sqrt{(Targ_x - Refrac_x)^2 + Targ_y^2})} - \frac{n_2}{n_1} = 0 \tag{4.21}$$

it is possible to solve for the point of refraction very quickly. To solve, a vector of possible values of $Refrac_x$ is assembled; these values are simply a range of real values

between Ant_x (the platform's x-position) and $Targ_x$ (the target's x-position) equally spaced by an arbitrarily set "precision" parameter (this can be set to on the order of 0.1mm and simulation speed remains reasonable). Equation 4.21 is then evaluated at all these positions using vectorised code (a very rapid operation in MATLAB) and the value of $Refrac_x$ that gives the closest to zero result is returned as the correct value of $Refrac_x$.

A flowchart showing the implementation of this algorithm (including the 3-D extension discussed in the following paragraphs) is shown in Figure 4.7. Note that if the radar platform is directly above the buried target (nadir case) or if the target is not below the surface no refraction occurs and so the ground coordinates of the target are returned directly, instead of calculating the ground coordinates of the point of refraction.

Whilst the trough scanner can be thought of as a two dimensional problem with the targets and antennas existing on the same two dimensional plane, sidelooking SAR is obviously a three dimensional problem. Fortunately, [100] present a 3-D variation of their equation. In this, a helper coordinate system is introduced that rotates and translates the platform, target and point of refraction locations so they lie on the same plane. The 2-D version was used for initial simulation of the trough scanner but the 3-D version was implemented for the sidelooking simulation presented in Chapter 6, validated against the 2-D version and then used for all simulations.

The helper coordinate system is translated by the vector (Ant_x,0,Ant_z) (i.e. the origin of the helper system is set to lie on the plane of refraction directly below the platform) and rotated by α so that the platform, point of refraction and buried target lie on the same 2-D plane. This allows representation of the radar platform's position in the helper coordinate system as

$$Ant_{xh} = 0, Ant_{yh} = Ant_y, Ant_{zh} = 0 \tag{4.22}$$

and representation of the buried target position in the helper coordinate system as

$$Targ_{xh} = \sqrt{(x_2 - x_1)^2 + (z_2 - z_1)^2}, Targ_{yh} = Targ_y, Targ_{zh} = 0 \tag{4.23}$$

By remembering that the point of refraction on the soil surface in the helper coordinate system has a height, $Refrac_{yh}$, which is by definition zero, and the z coordinate is 0 as the helper system is still a 2-D system, the refraction point is simply represented by

$$Refrac_{xh} = Refrac_{xh}, Refrac_{yh} = Refrac_{zh} = 0 \tag{4.24}$$

The solution for $Refrac_{xh}$ (the x-coordinate of the point of refraction in the helper coordinate system) is then found as before, but using the helper coordinates for the antenna and buried target, by

$$\frac{((Refrac_{xh} - Ant_{xh})/\sqrt{(Refrac_{xh} - Ant_{xh})^2 + Ant_{yh}^2})}{((Targ_{xh} - Refrac_{xh})/\sqrt{(Targ_{xh} - Refrac_{xh})^2 + Targ_{yh}^2})} - \frac{n_2}{n_1} = 0 \tag{4.25}$$

Finally, the helper coordinate system is transformed back to the original coordinate system, transforming the point of refraction in the helper coordinate system back to the point of refraction in the original coordinate system via the following 3 equations:

$$Refrac_x = Ant_x + Refrac_{xh} \cos\alpha \tag{4.26}$$

$$Refrac_y = 0 \tag{4.27}$$

$$Refrac_z = Ant_z + Refrac_{xh} \sin\alpha \tag{4.28}$$

The calculation for the point of refraction is repeated for the transmit and receive antenna positions, giving a transmit point of refraction $(Tx_{xi}, Tx_{yi}, Tx_{zi})$ and a receive point of refraction $(Rx_{xi}, Rx_{yi}, Rx_{zi})$. These two 3-D coordinates are then passed back to the SAR simulator which uses them to calculate the above and below ground path lengths for both the transmit and receive paths (R_{Txair}, R_{Rxair}, R_{Txsoil} and R_{Rxsoil}) which are used to calculate the phase data, via the following equations:

$$R_{Txair} = \sqrt{(Tx_x - Tx_{xi})^2 + (Tx_y - Tx_{yi})^2 + (Tx_z - Tx_{zi})^2} \tag{4.29}$$

$$R_{Rxair} = \sqrt{(Rx_x - Rx_{xi})^2 + (Rx_y - Rx_{yi})^2 + (Rx_z - Rx_{zi})^2} \tag{4.30}$$

$$R_{Txsoil} = \sqrt{(Tx_{xi} - Targ_x)^2 + (Tx_{yi} - Targ_y)^2 + (Tx_{zi} - Targ_z)^2} \tag{4.31}$$

$$R_{Rxsoil} = \sqrt{(Rx_{xi} - Targ_x)^2 + (Rx_{yi} - Targ_y)^2 + (Rx_{zi} - Targ_z)^2} \tag{4.32}$$

The two air and two soil path lengths are then summed to give R_{air} and R_{soil}, the total ranges in air and soil respectively.

From these two path lengths, the phase history of the scene for a given frequency is calculated using a modified version of Equation 4.12 as follows:

$$\sum_{R_{air}, R_{soil} = R_1}^{R_n} A e^{-i(R_{air} k_{air} + R_{soil} k_{soil})} \tag{4.33}$$

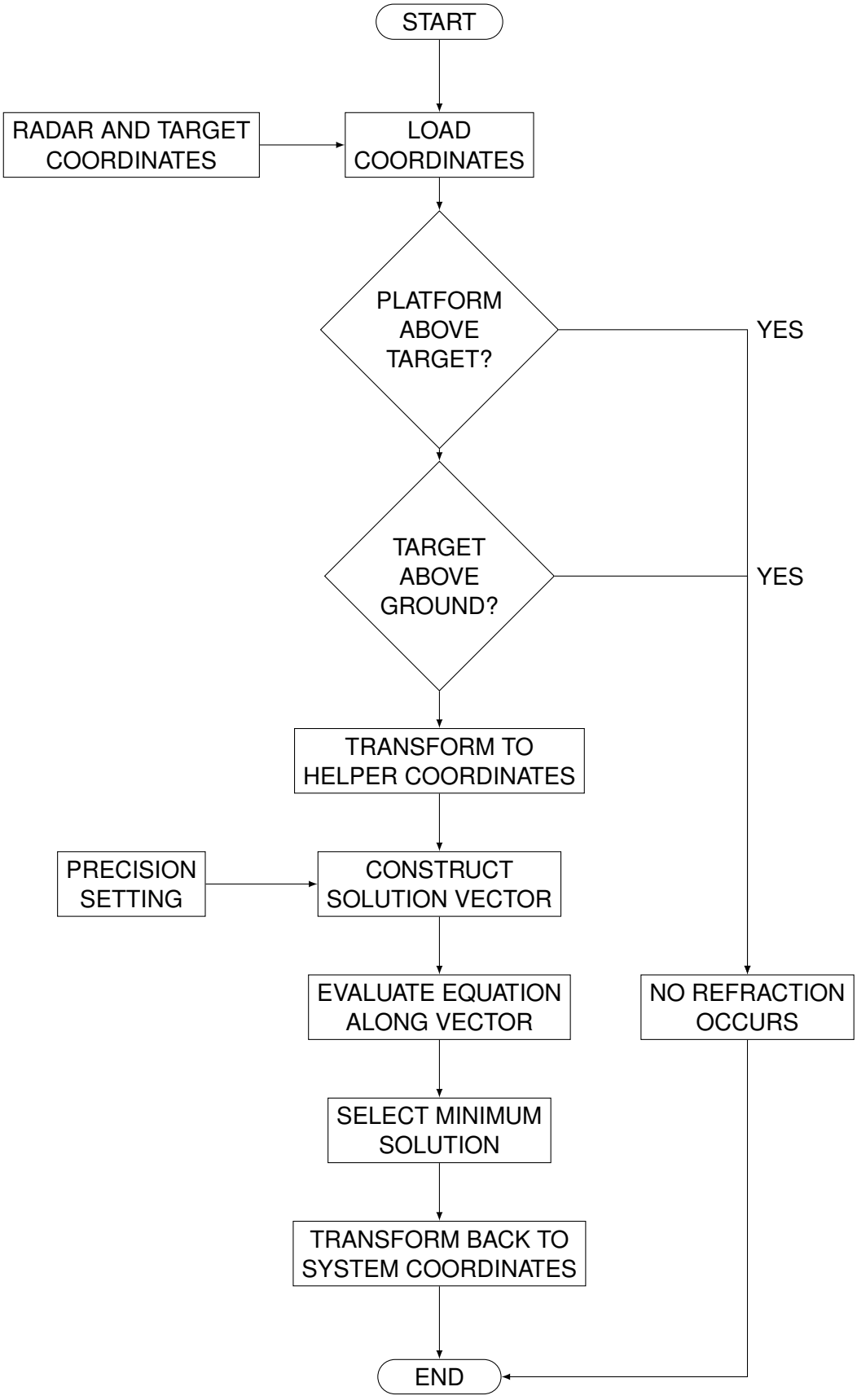

Figure 4.7: Flowchart of the implemented TP algorithm.

Where k_{air} and k_{soil} are the wavenumbers in air and soil, respectively, given by:

$$k_{soil} = \frac{2\pi f n_{soil}}{c} \tag{4.34}$$

$$k_{air} = \frac{2\pi f n_{air}}{c} \tag{4.35}$$

Due to the refractive index of the soil being frequency dependent, the calculation of soil refractive index, point of refraction, the air and soil ranges, and the phase history of the scene must be repeated at each frequency step in the radar pulse. The modified SAR simulator uses an interpolated Hallikainen soil model.

In addition to the modifications made to the simulation algorithm, the file output code was also modified. By including a file header and formatting the simulated radar data in the same manner as the GB-SAR system does for real data it was possible to pass the simulated data directly to the same image processing code that would be used for the real radar data collected as part of the experimental study. This reduced the possibility of errors, by removing the need to create and maintain two separate sets of image processors.

4.5.2 Two soil layer simulation

[4] identify that small amounts of moisture applied to the top of the soil surface can sit in a thin layer, rather than uniformly spreading down to the trihedral. This means a three layer simulation; air, wet layer of soil and dry layer of soil with two unknown points of refraction to solve for. This situation is illustrated in Figure 4.8.

By representing the problem as a set of two simultaneous equations, similar to the

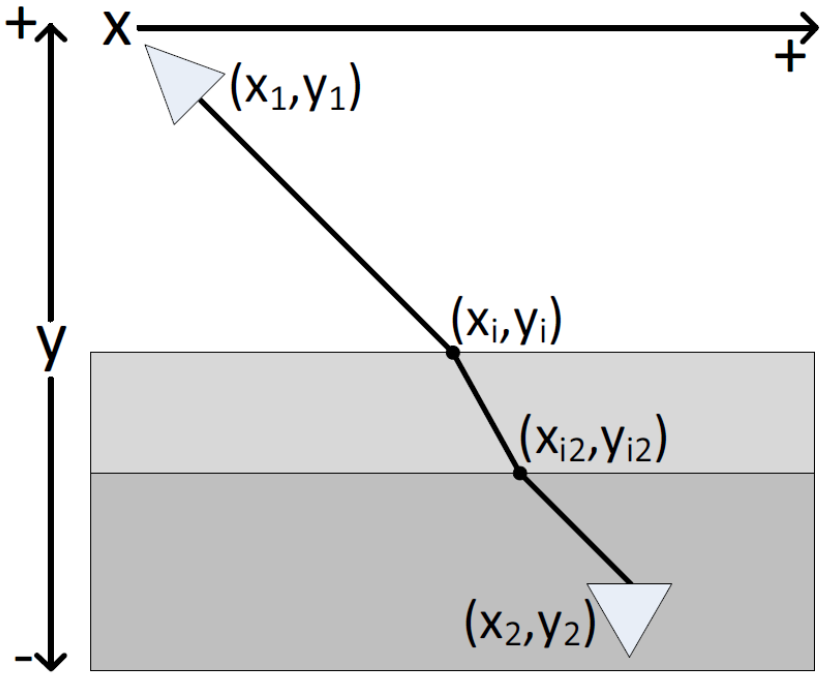

Figure 4.8: Twin layer expansion of Dziewerz and Gachagan's situation. Depth of top soil surface (y_i) is once again set to 0

single layer case:

$$\frac{((x_i - x_1)/\sqrt{(x_i - x_1)^2 + (y_i - y_1)^2})}{((x_{i2} - x_i)/\sqrt{(x_{i2} - x_i)^2 + (y_{i2} - y_i)^2})} = \frac{n_2}{n_1} \tag{4.36}$$

And

$$\frac{((x_{i2} - x_i)/\sqrt{(x_{i2} - x_i)^2 + (y_{i2} - y_i)^2})}{((x_2 - x_{i2})/\sqrt{(x_2 - x_{i2})^2 + (y_2 - y_{i2})^2})} = \frac{n_3}{n_2} \tag{4.37}$$

It is possible to solve for both points of refraction (x_i and x_{i2}), as long as the depth of the first layer is known or defined as part of the simulation setup.

In a similar fashion to the original (single layer) solver this two layer solver produces a range of solutions; the correct solution can be selected by discarding the complex results, ensuring that the solutions for the two points of refraction lie between the platform (x_1) and target (x_2) positions and making sure that the selected solution for x_{i2} lies between

x_i and x_2. This extension is solvable within MATLAB using the solve(), though at a considerable increase in computing expense over the single layer case.

This two layer extension was not used for the simulations presented in the next sections due to the previous ray tracing simulations showing that the total water content above the buried target that influences the VB-SAR process, rather than the distribution of the water. Using the single soil layer model allowed rapid simulations of individual radar scenes which in turn allowed complete VB-SAR sequences to be simulated in reasonable time.

4.6 VB-SAR Imaging Simulation

The aim of the simulator was to provide an environment in which various different scenarios could be tested, from the very simple initial test of the VB-SAR process involving high resolution images of a single buried target through to multiple buried targets being resolved from low resolution images.

The simulator was configured to emulate the setup of the GB-SAR system (see Chapter 5); the two antennas on the platform were set at the correct positions, the movement of the platform over the course of a scan was matched to the real data and the frequency pulse was matched to that used during the experimental work detailed in Chapter 5, as listed in Table 4.1.

4.6.1 Initial Testing

The initial testing of the simulator involved basic functionality tests, checking that the simulator outputs could be correctly processed by both the SAR and TP image processors into focused images and buried targets behave as expected. To test this, a simple scene was

Parameter	Value
Bandwidth	2GHz
Centre Frequency	5GHz
Height of antenna cluster	1.59m
Cross range position of antenna	0m
Antenna movement between pulses	0.02m
Number of frequencies per pulse	1601
Total number of pulses	151

Table 4.1: Basic simulator parameters

set up with a few surface targets and a single buried target at 30cm depth. The attenuation of the soil was ignored and each target was set to a relative amplitude of 1. The output from the simulator was then fed into the two processors, with each processor using the full 2GHz of simulated bandwidth, and the results examined.

The SAR and TP outputs are both shown in Figure 4.9. The outputs from both processors are as expected; the targets appear at the correct locations and the surface targets have focused well.

The TP image has a lower cross range resolution due to the smaller synthetic aperture used to produce each synthesised beam and the outermost surface targets have faded in the TP image due to the synthetic beamforming process causing the valid imaging region to be smaller than the total platform movement over the course of the acquisition. The movement of the point of refraction as the radar antennas moved over the scene has caused the buried target to noticeably defocus in the SAR processed image.

This scene was resimulated 100 times over a SMC change of 9.6% to 3.5%, each simulated scan was then also processed by the two imaging processors using all 2GHz of the simulated real bandwidth.

From these series of high resolution images the isolated phase history of the buried target could be extracted from both the SAR and TP images. This would be expected to

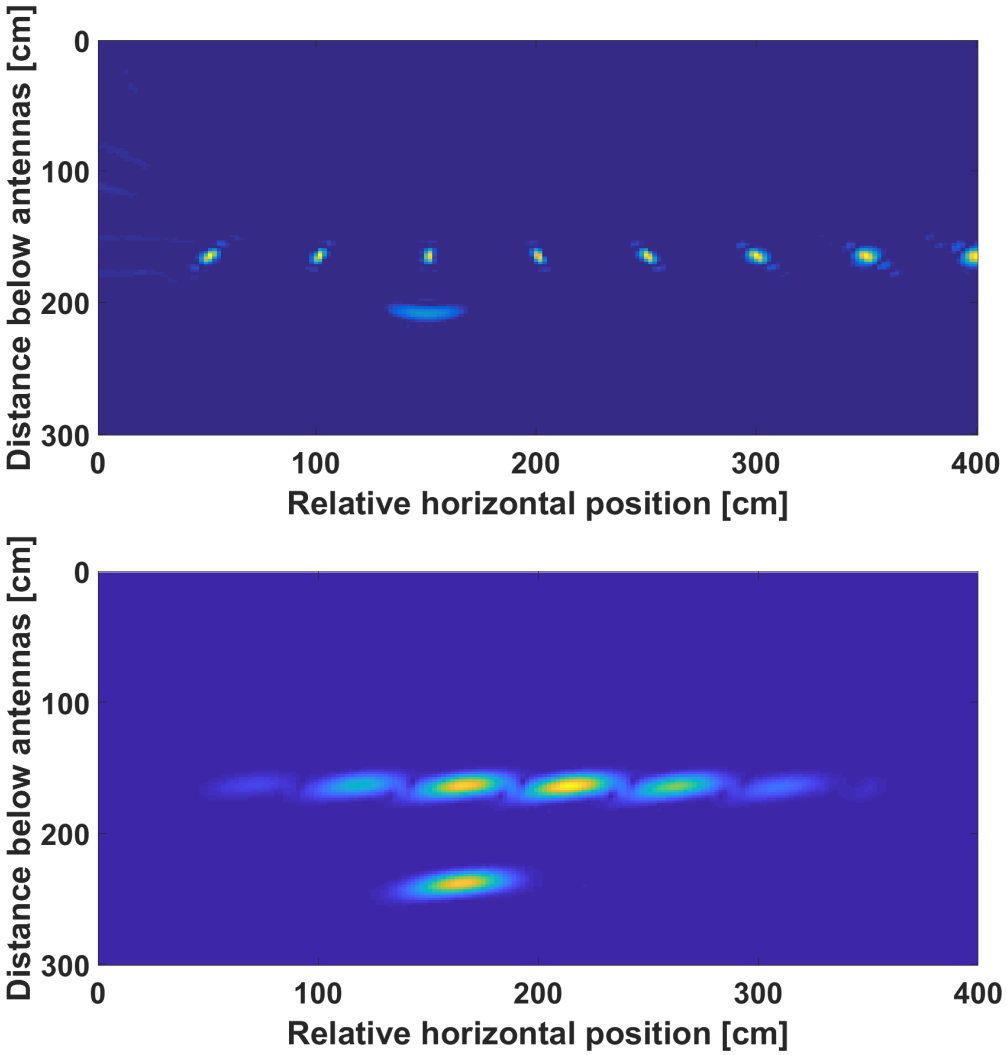

Figure 4.9: Simple simulated scene processed at high resolution using the SAR processor (top) and TP processor (bottom).

provide an extremely "clean" VB-SAR depth profile with the buried target's response being the sole peak as the buried target's return is completely isolated from other scatterers' returns in each source image. The two phase histories were then fed into the VB-SAR processor, in order to produce a VB-SAR depth profile of the buried trihedral. The depth profiles so produced are shown in Figure 4.10.

As can be seen, the TP derived depth profile looks as expected, a well defined peak at the correct depth. However, the SAR derived depth profile shows a very slightly deeper peak response with higher sidelobe levels. At the low SMC levels used during this simulation the phase shift of the buried target is predicted to be slightly dependent on the incidence angle of the radar wave with the soil surface [93]. The TP images were produced at an incidence angle of 0° whereas the SAR process effectively used an incidence angle which varied during the formation of each image, which caused a slight variation in the phase response of the buried target over the simulation. This led to the slightly deeper target response and the higher sidelobes. The effects of incidence angle variation are studied in more detail in Section 4.6.3.

In a realworld SAR deployment this effect is not predicted to cause significant problems, as it is only a very slight depth inaccuracy (2cm) and higher SMC levels would tend to reduce the influence of refraction [93].

4.6.2 VB-SAR Range Resolution Enhancement

The initial simulation of VB-SAR using high resolution source images demonstrated that the VB-SAR processor could produce depth profiles with the buried target placed at the correct depth. However, one of the promises of VB-SAR is that by acquiring a series of low range resolution images an improved resolution can be synthesised using the virtual bandwidth generated by the change in soil properties over the series of source images.

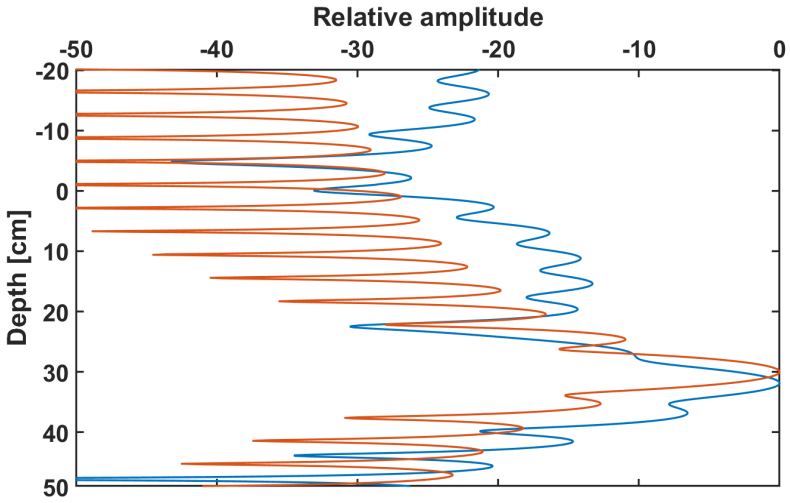

Figure 4.10: VB-SAR depth profile extracted from the simple simulated scene processed at high resolution using the SAR processor (blue trace) and TP processor set to an incidence angle of 0° (red trace).

To test this, the same simulated radar scans as used for the previous VB-SAR simulation were reprocessed using the TP processor at a range resolution of 1m (low enough to ensure that the returns from the buried targets and the surface target directly above it merged together) by only using the first 150MHz of the simulated file. The result of this limited bandwidth processing on the first simulated scene in the sequence is shown in Figure 4.11. This clearly shows that the surface and buried target's returns have merged together (shown by the stronger response in the area of the buried target) and resolving them is impossible at this low range resolution.

From these low resolution source images the complex history (both phase and amplitude, using the predicted attenuation of the soil) of the pixel containing the strongest return in the vertical column containing the buried target in the first image was extracted from each image, and passed to the VB-SAR processor. The depth profile displayed in Figure 4.12 was produced by the VB-SAR processor. As can be seen, the VB-SAR processor has correctly separated both the surface target and the buried target, placing them

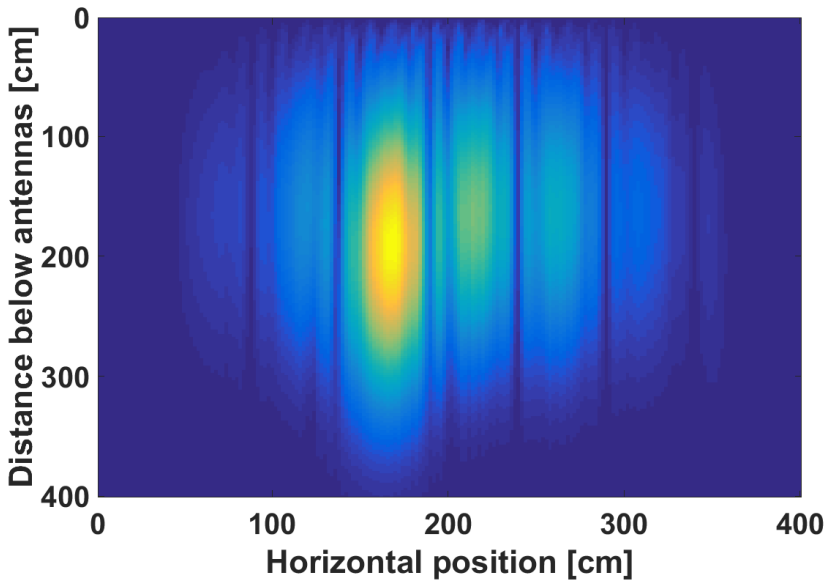

Figure 4.11: Simple simulated scene processed at low range resolution using the TP processor and the first 150MHz of the simulated bandwidth. TP reconstruction angle set to 0°.

both at their proper depths. The different amplitudes are explained by the soil attenuation reducing the strength of the buried target, relative to the surface target which experiences no attenuation.

4.6.3 Multiple incidence angle VB-SAR

One of the key issues with performing VB-SAR in the real world is the effects of incidence angle on the phase response of a given subsurface target. In a side-looking SAR scene the incidence angle of the radar beam varies across the image. Therefore, a significant dependency on incidence angle would case variations in the depth profiles produced by VB-SAR over such an imaging scene.

[93] shows that the effects of refraction substantially reduce the incidence angle dependency, especially at higher SMCs where the phase response is almost totally independent of incidence angle. The combination of the SAR simulator and the TP imager allows

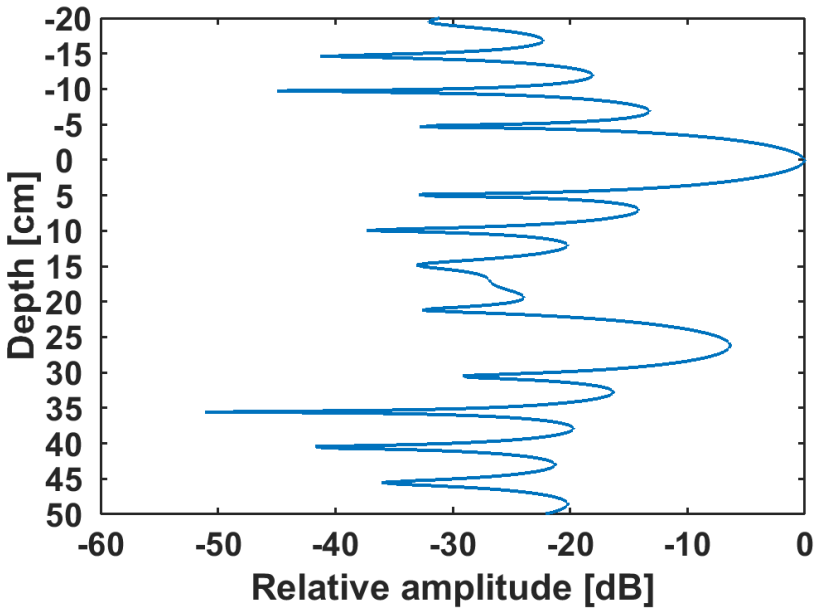

Figure 4.12: VB-SAR depth profile produced using low resolution TP images as the data source. Both surface and buried targets resolved and placed at the correct depths.

this effect to be accurately simulated and analysed.

For this simulation, the simulator was set to use a 100% sand soil and a target buried at 26.5cm below the soil surface. In order to test the relationship between incidence angle dependency and SMC values two sets of radar data were produced; one covering the SMC range 0 to 0.1 and the other covering an SMC range of 0.2 to 0.3. The TP processor was configured to use 500MHz of bandwidth during image processing, and produced images across the incidence angle range of 0°to 40°, in steps of 10°. The phase response of the buried target was then extracted from each image and this produced the two plots and inset shown in Figure 4.13.

As can be seen, the simulation has validated the calculations in [93]; the lower SMC data shows some incidence angle dependency (although much reduced compared to that which would be expected without the effects of refraction) and the higher SMC data shows a much reduced incidence angle dependency over that seen in the other plot. In addition,

the inset demonstrates that the variation seen at low SMC values is proportional to the incidence angle in use.

It is clear from this simulation that the variations in phase response induced by a change in incidence angle are insignificant and should not significantly affect the VB-SAR imaging process.

4.6.4 Multispectral VB-SAR

One significant aspect of the VB-SAR imaging scheme is that it should operate correctly, regardless of the centre frequency of the real bandwidth in use. This is significant, as confirming it would allow the VB-SAR scheme to be used with radar data from a variety of radar systems which use different frequencies.

Using the same simulated data as before, the total real bandwidth of 2GHz could be subdivided into multiple narrower frequency bands. A real bandwidth of 150MHz in each band as previously used to demonstrate range resolution improvement was chosen as a basis to demonstrate the frequency independence of the VB-SAR process. The 2GHz real bandwidth was divided into 13 sequential frequency bands spanning the range 4 to 5.95GHz

The phase history (without amplitude/soil attenuation data, in order to make the comparisons across different frequency bands more straightforward) was extracted from the pixel with the highest amplitude in the column containing the buried target during the first scan. The phase histories extracted from each band are shown in Figure 4.14, after unwrapping and aligning to 0° for the inital scan.

As expected from the different frequencies each band has a slightly different total phase shift over the same soil moisture change, due to the frequency dependence of the refractive index. This should not cause variations in the depth of the target in the different

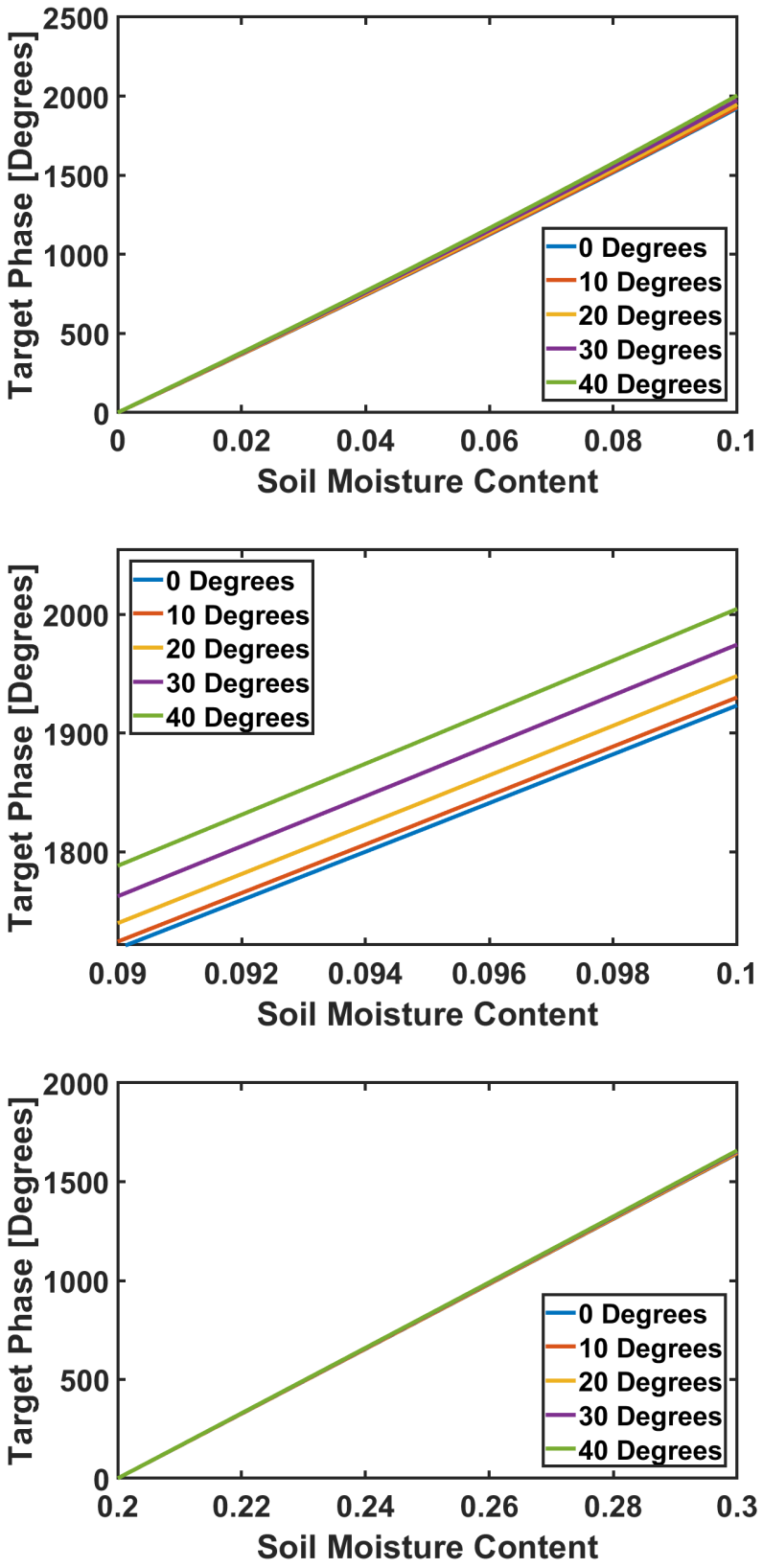

Figure 4.13: Top: Phase histories extracted from a buried target at varying TP incidence angles over an SMC range of 0 to 0.1. Phase unwrapping applied.
Middle: Inset of upper plot, highlighting variances due to incidence angle effects.
Bottom: Phase histories extracted from a buried target at varying TP incidence angles over an SMC range of 0.2 to 0.3. Phase unwrapping applied.

band VB-SAR depth profiles as, in theory, the VB-SAR processor should compensate by applying the calculated average refractive index to the depth profile when applying a depth scale; this would cause each depth profile to correctly line up across real frequency bands.

What is not expected are the deviations from the expected straight line phase history. The deviations may be due to the surface and buried trihedral returns interfering with each other and modulating each other's phase. A check for this was made by processing a scene with only a single buried target in it and no surface targets present. This was then TP processed using the same 150MHz wide real frequency bands as previously used. Again, the phase history of the strongest response in the column containing the buried target in each band was extracted and plotted in the low plot in Figure 4.14. As can be seen, there is no deviation from the expected straight line in this instance which provides strong evidence for the deviations being caused by interference between the buried target and the surface target(s). These deviations could explain the very slight distortions (uneven sidelobes of both the surface and buried target) seen in Figure 4.12.

The phase histories shown in the top part of Figure 4.14 can then be fed to the VB-SAR processor which will produce depth profiles as previously described. The result of this VB-SAR processing is shown in Figure 4.15. As shown by the plots, the merged surface and buried target returns have been resolved successfully in all bands and the two responses have been successfully lined up in every band, showing that the VB-SAR processor is indeed correctly adjusting itself to compensate for the differing phase shifts seen in each band. This provides strong evidence that the VB-SAR process is indeed independent of the real frequencies used to construct the original radar images. In addition, the deviations away from a straight line have not substantially distorted the depth profiles produced by the VB-SAR process.

As an additional check of the implemented VB-SAR processor, the 150MHz wide

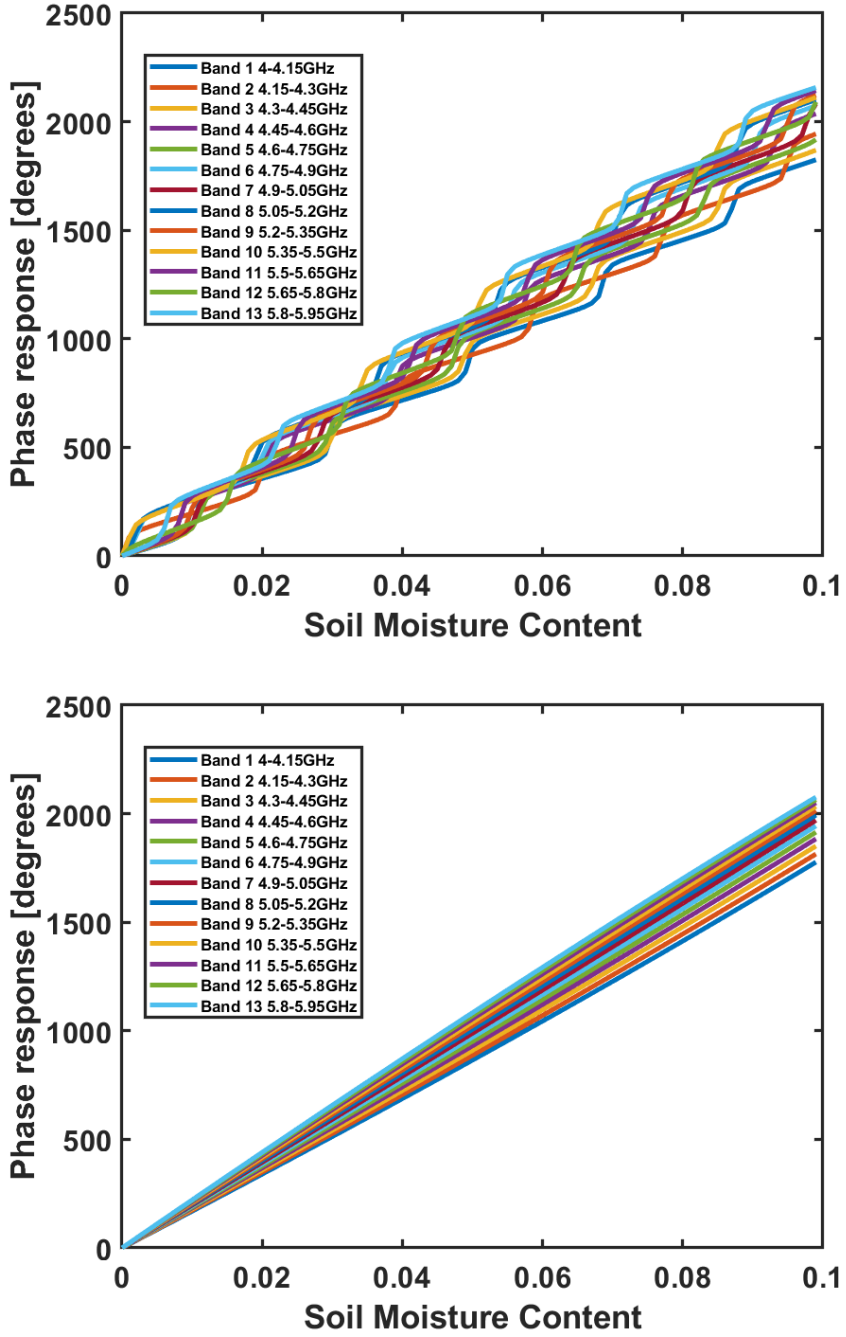

Figure 4.14: Top: Phase histories extracted from scenes containing one buried target below multiple surface targets processed using the TP processor with 150MHz wide frequency bands.
Bottom: Phase histories extracted from scenes containing only one buried target and no surface targets processed using the TP processor with 150MHz wide frequency bands.

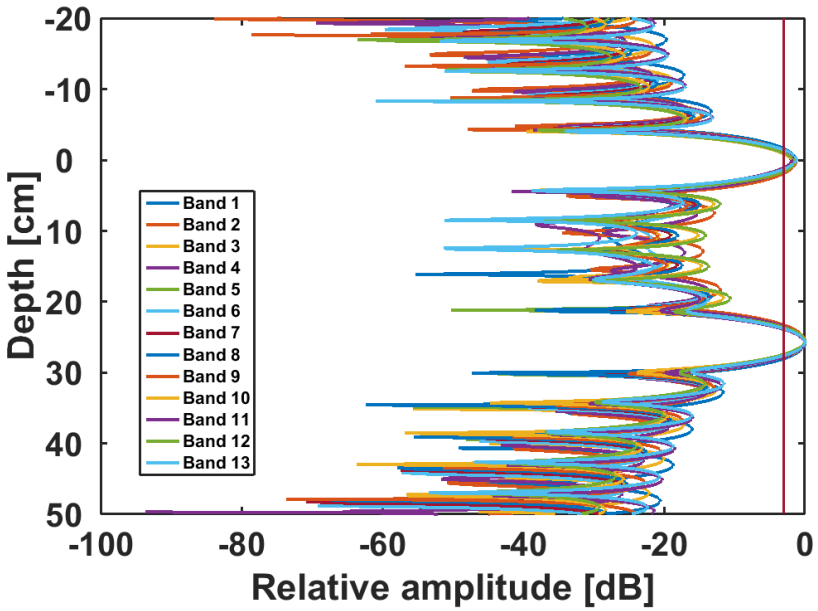

Figure 4.15: Results of the VB-SAR processor using the phase histories extracted from the simulated scene processed at low TP resolution. Horizontal line shows -3dB point.

real bandwidth phase histories were reprocessed with the DC subtraction functionality (intended to suppress potentially overwhelming surface returns in real radar data) of the VB-SAR processor enabled. This serves to check that the DC subtraction module is working correctly and not distorting the target peak or introducing spurious responses. The result of applying this is shown in Figure 4.16, which demonstrates that the DC subtraction is working as intended and removing only the surface's peak whilst leaving the buried target's response untouched.

The effectiveness of the DC subtraction scheme can also be evaluated by comparing the DC subtracted depth profiles shown in Figure 4.16 against depth profiles produced from simulated scene where there were no surface targets present. The two scenes and series of simulated radar scans were identical, aside from the lack of surface targets in the new series. The comparison of the two scenes is shown in Figure 4.17; as can be seen from the similarity of the two sets of plots the DC subtraction process is working well and

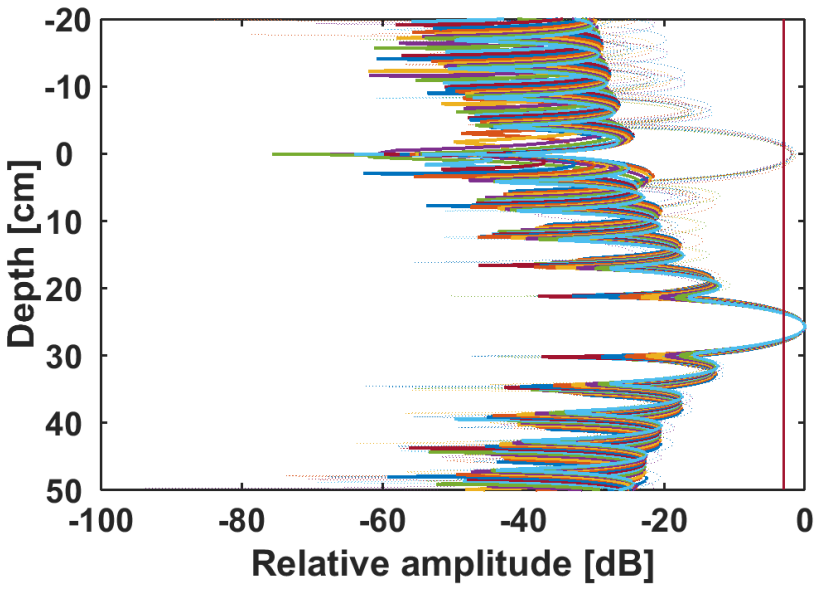

Figure 4.16: Results of the VB-SAR processor using the phase histories extracted from the simulated scene processed at low TP resolution. Thick solid lines indicate DC-subtracted results, thin dotted lines indicate results with no DC subtraction applied. Horizontal line shows -3dB point. Band colourings as per Figure 4.15.

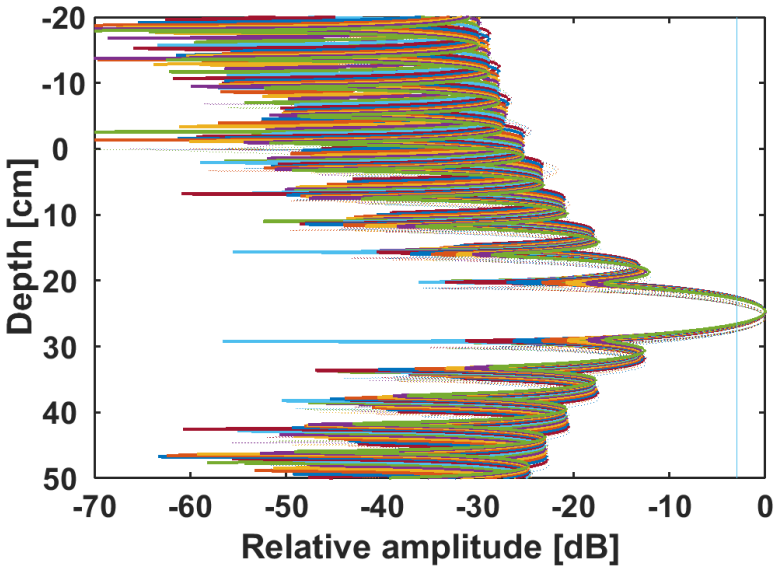

Figure 4.17: Comparison of VB-SAR depth profiles produced using 150MHz bandwidth TP images of a scene containing just a buried target (strong, solid lines) and a scene containing a buried target and a surface target processed with DC subtraction enabled in the VB-SAR processor (fainter, dotted lines).

not distorting the depth profiles.

4.6.5 Multitarget Multispectral VB-SAR

The simulations presented so far all involved a single buried target, with or without a surface target in the same vertical column as the buried target. Whilst the VB-SAR processor appeared to be correctly locating the depth of a single buried target, it was felt that demonstrating the correct placement of multiple buried targets in a single column would be a more rigorous demonstration.

In order to perform this demonstration, a radar scene consisting of three targets, buried directly above and below one another at depths of 25, 40 and 80cm below the soil surface was constructed and simulated over an SMC change of 9.6% to 3.5% as per the previous simulations. As with the previous multispectral simulation the simulated radar scans were

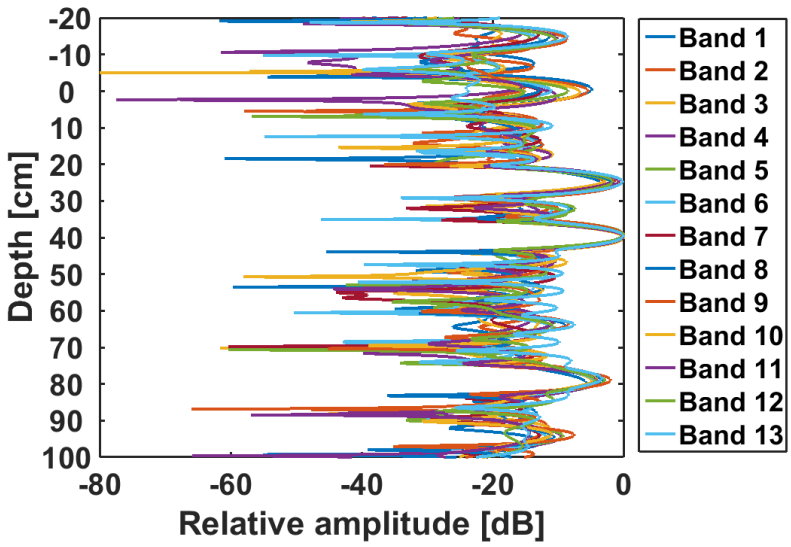

Figure 4.18: Results of the VB-SAR processor using the phase histories extracted from a scene with a vertical stack of three buried targets processed at low TP resolution. Buried targets placed at 25, 40 and 80cm below the soil surface.

processed into radar images using the TP processor. As before, 13 sequential sub bands each of 150MHz real bandwidth were used to produce a multispectral image set for VB-SAR processing.

The results of VB-SAR processing of each real frequency band is shown in Figure 4.18. As can be seen, the three buried targets have been correctly resolved at 25, 40 and 80cm depth in each band. The apparent appearance of surface and above surface responses appears to be due to sidelobes, only appearing in certain bands. In an actual VB-SAR implementation it would be reasonable to artificially suppress any above surface responses, however they are shown here for completeness.

The successful location of multiple buried targets in a single vertical column served to prove that the VB-SAR processor could correctly determine depth positions of targets buried at varying depths and that the correct determination of the single target's depth was not simply fortuitous. In addition, it demonstrated that the VB-SAR processor is not "spot on" at one particular depth with accuracy degrading at other depths.

4.7 Simulation summary

The aim of the simulations performed was to gain an understanding of the effects of different factors on the VB-SAR process.

The initial ray tracing simulation showed some interesting results for situations with many soil texture and/or moisture layers which would be difficult to simulate with the "full" SAR simulator. These indicated that the ordering of moisture layers above a target of interest does not affect the VB-SAR process but it is the total amount of moisture above the target that is significant. Similarly, it showed that the ordering of the soil texture above a target does not change the results of VB-SAR so long as the same layers are present.

However, the later work involving the SAR simulator and the VB-SAR processor is much more significant. This pairing allowed realistic simulation of the subsurface SAR imaging process and testing of the VB-SAR processor under strictly controlled conditions.

The first test was to check that the SAR simulator could produce valid images as expected. This was performed by using two image processors (a standard back projection SAR algorithm processor published in the existing literature and a relatively novel process dubbed TP which is detailed in Section 3.4) to process data produced by the simulator. This revealed that the simulator is working as expected and placing targets in the correct positions for both above and below ground cases.

Following this, the VB-SAR simulation commenced using data from the images produced using the simulated data. First, images were produced at high range resolutions (using all the simulated bandwidth to isolate all the targets from each other) using both the TP and SAR image processors, this allowed testing of the best case (input data only containing the buried trihedral's response over a precisely defined soil moisture change) scenario which should produce a clean target peak at the correct depth. In the TP image based VB-SAR the peak appeared at precisely the correct depth, whereas in the SAR im-

age based VB-SAR the peak appeared very slightly deeper, with higher sidelobe levels. This is believed to be a result of the effects of incidence angle variations at the low SMC levels used in the simulation. The depth error was less than 2cm (7%) and therefore not significant.

After this initial testing the range resolution of the TP images was lowered by taking the first 150MHz bandwidth from the output of the simulator. This lowered the range resolution to 1m which ensured that the return from the surface merged with the return from the subsurface target, giving the VB-SAR process the opportunity to separate the two returns in depth whilst improving the range resolution over that present in each input image. The VB-SAR processor successfully resolved both targets at their correct depths and demonstrated a substantial improvement in range resolution.

Within the 2GHz bandwidth produced by the SAR simulator it is possible to select many 150MHz wide sub bands and construct images using each band, then extract phase data from each band and process it separately using the VB-SAR process. Producing 13 such bands sequentially across the full bandwidth served to test the frequency independence of the VB-SAR process. This test was also successfully passed with both the surface and buried trihedral responses appearing at the correct depth in all bands. The functionality of the DC-subtraction scheme implemented within the VB-SAR processor was also tested; the DC-subtraction scheme reduced the surface response by over 40dB in all bands and did not distort the buried trihedral's response in any way.

The effects of multiple buried targets placed directly above and below each other was also tested across the 150MHz sub bands. This served to check that the VB-SAR process worked across a range of target depths and ensure that multiple buried targets in a single column did not cause problems. Both of these criteria were met; every target was resolved at its correct depth and no significant interaction between targets was noticed.

Chapter 5

VB-SAR Demonstration

5.1 Introduction

This chapter presents the experimental VB-SAR demonstration and analysis performed during this work.

Initially, a brief description of the laboratory facility used is presented.

Next, an overview of the experimental procedure is presented. Initial radar images collected are shown, and an analysis of the system's performance over the course of the experiment is presented. The response of the buried trihedral to the changing moisture content of the sand is shown and corrections for system variations are devised and applied. Commentary on how the different polarisations behave is provided, in order to set the scene for the polarimetry that is later presented.

The chapter then moves on to an initial demonstration of VB-SAR under ideal conditions at one incidence angle and one polarisation. This serves to build confidence that the VB-SAR processor implemented is working correctly. The ability of the VB-SAR process to enchance the subsurface range resolution above that given by the real bandwidth used is also demonstrated.

Following this VB-SAR at different incidence angles and using different polarisations is shown. These results are particularly significant as it paves the way for using VB-SAR with sidelooking airborne and spaceborne SAR systems, where the incidence angle will vary across the imaging scene. The ability of VB-SAR to operate in different polarisations also enchances the utility of the scheme as it allows polarimetric techniques to be used.

Finally, the VB-SAR scheme is tested across a range of real bandwidths and centre frequencies. This shows that the VB-SAR scheme is applicable across a range of frequencies, which is promising for real world applications as it gives the possibility of using lower frequencies than the C-band used for this work which would allow better soil penetration.

5.2 The Laboratory Environment

The trough scanner is part of the GB-SAR measurement facility at Cranfield University's Shrivenham campus. An overview image of the system making a measurement is shown in Figure 5.1.

The trough scanner itself consists of a linear scanner approximately 4m long mounted at a height of approximately 3m. On the moving platform a fully polarimetric cluster of four antennas is mounted along with RF amplifiers and a pair of RF switches which are used to select polarisations. The antenna mount allows positioning of the antennas at physical incidence angles in the range 0° to 40°.

The RF source and measurement instrument is a Vector Network Analyser (VNA). This allows operation in the frequency range of 1-13.5GHz with different antennas. The polarisation of the system is selected by software controlled RF switches which switch the appropriate antennas in and out of the transmit and receive paths.

A key feature of the scanner is that the movement and positioning of the moving

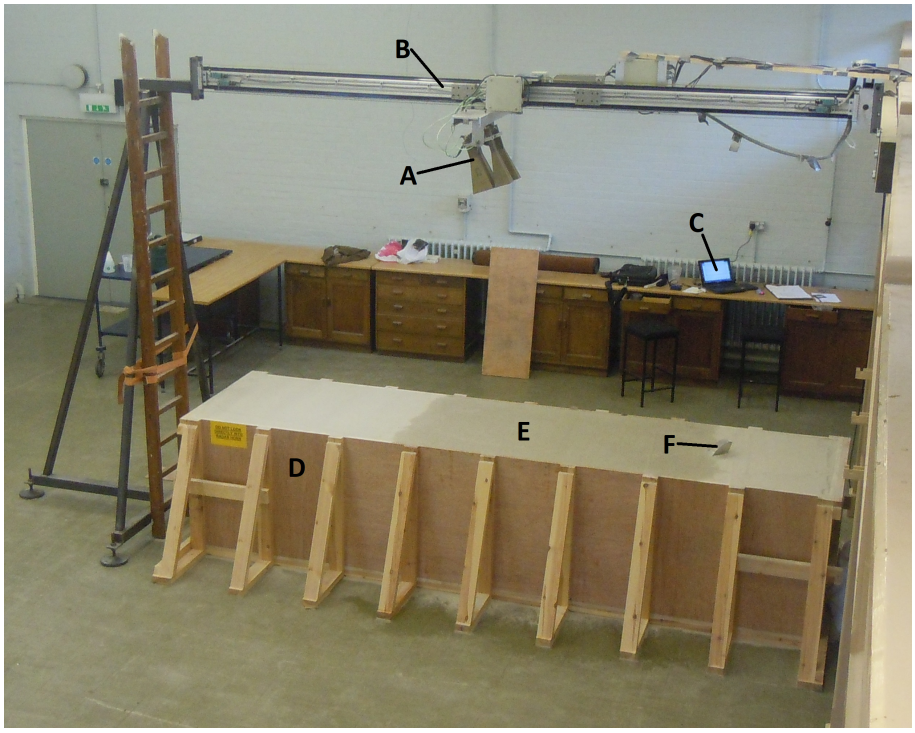

Figure 5.1: Overview of the trough scanner system. Antenna cluster (labelled 'A') runs along linear scan rail 'B' under control of laptop 'C'. Sand trough containing buried targets is labelled 'D'. 'E' is the wetted area above a buried target and 'F' is a reference trihedral placed on the sand surface.

platform is precisely controlled allowing the use of synthetic aperture techniques. The motion of the platform is controlled by an integrated software suite which automates the platform motion and the control of the VNA. This automation makes collecting data over long periods of time very easy; this functionality is of particular utility for this work as the drying processes observed take place over many weeks. Complex radar data recorded by the system are automatically formatted into delimited text files which allows easy analysis of the recorded data

The trough itself is sturdily constructed from plywood and is approximately 1m wide, 0.9m tall and 4m long. For this work the trough was primarily filled with fine kiln dried sand, aside from an area which was filled with a gravel/sand mixture for a related study. The presence of this gravel/sand mixture did not significantly affect the results of this work. Sand was used for this work as it is much easier to handle than a typical soil and is universally reliably and repeatably available.

5.3 Experimental Work

The experimentation performed for VB-SAR testing used the trough scanner and sand trough previously described. The experiment undertaken was similar to Experiment A in [4]. A trihedral was buried at a depth of 26.5cm under sand mixed with gravel. The mixture was 10% gravel, 90% kiln dried sand (by volume) mixed by hand. The gravel mixture was used to fill in a 1m by 1m wide area 25cm deep above the trihedral, as shown in Figures 5.2 and 5.3.

In addition to the buried trihedral, several trihedrals were placed on the surface of the sand trough as shown in Figure 5.4. Once these trihedrals had been placed they remained undisturbed throughout the experiment. These were intended to provide fixed reference targets (free from any refraction and sand induced effects) which would indicate any phase

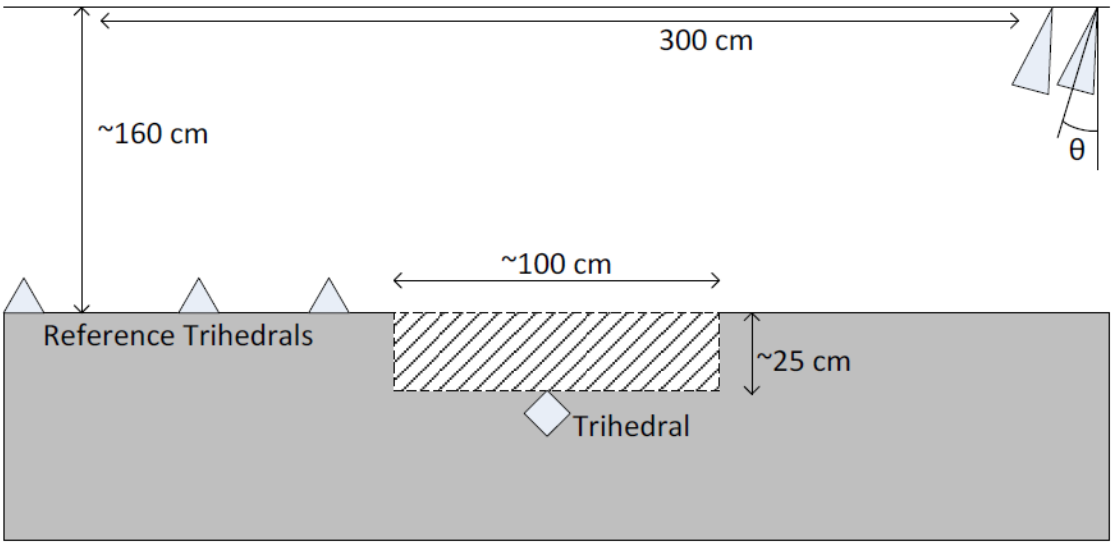

Figure 5.2: Sketch (not to scale) of the experimental setup. The hatched area indicates the area containing gravel/sand mixture. θ indicates the physical angle of antennas (20° in this experiment); note antenna mounting ensures all 4 antennas are at the same angle although only 2 antennas are seen from this perspective.

Figure 5.3: 1m x 1m area containing gravel mixture. Trihedral buried 26.5 cm below surface in roughly the centre of the gravel area

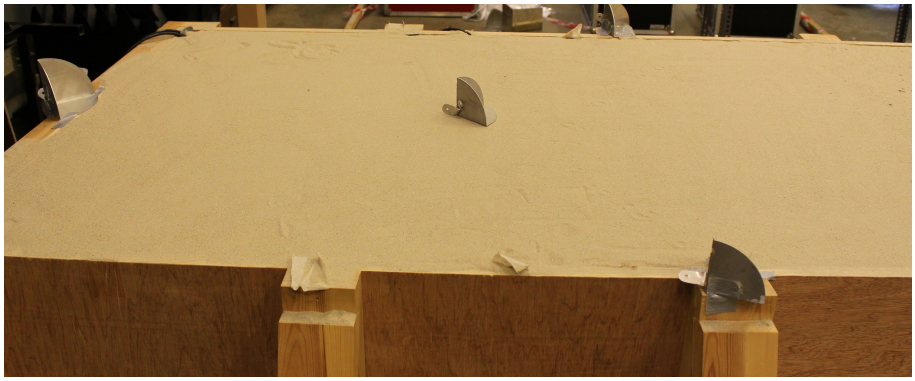

Figure 5.4: Arrangement of reference trihedrals

or amplitude variations in the radar system as the experiment progressed.

The surface of the entire trough was smoothed as much as possible (some issues were experienced with the gravel snagging under the beam used for smoothing and creating small trenches in the surface, these trenches were filled in with sand and smoothed by hand). After smoothing the sand and placing the reference trihedrals the scene was held constant during the experiment, aside from the addition of an extra reference trihedral during the early stages of the experiment and the controlled addition of water.

The radar system was configured to use a 2GHz bandwidth consisting of 1601 discrete frequencies at each sample point along the scan. The antenna platform moved 2cm between samples and each scan consisted of 151 samples, giving a total movement of 3m. Each complete scan was stored as a separate data file; each file contained a human-readable header which contained scan parameters and the complex radar data.

The experiment was split into two stages; firstly controlled amounts of water were added to the surface of the sand above the buried trihedral, then the sand was left to dry out naturally. The first stage allowed the phase response of the buried trihedral to the moisture content of the sand to be characterised, in terms of $^{\circ}/ml$. This relationship, and the phase response of the buried trihedral during the wettest scan, could subsequently be used to estimate the sand moisture in each scan during the drying period when direct

moisture measurements were not available.

In total, 610 HH, 611 VH and 618 VV data files were collected over the course of the experiment which ran for 36 days. The VH data is of limited utility because the buried target was a trihedral which shows a very weak crosspolar response and so is obscured by sand attenuation even at relatively low sand moisture levels. Accordingly, most of the analysis concentrated on the VV and HH polarisations. However, there is no apparent reason or evidence that the VB-SAR process would not work with crosspolar data if an appropriate buried target was available.

Each data file was processed using TP; an example image so produced is shown in Figure 5.5. As can be seen, the imaging process has resolved the buried target of interest (highlighted by Arrow 'A', with an indication of the gravel mixture visible immediately above it), two surface reference trihedrals placed on the side of the trough (being the same distance away from the antennas the two have merged into the response labelled 'B') and a single reference target placed on the sand surface (Arrow 'C'). The surface of the sand is visible at about 150cm below the antenna and the concrete floor of the sand trough is just visible at the very bottom of the image. The bright returns below 'B' and 'C', and to the left of the buried trihedral are objects (plastic sheet and moisture probes) left in the trough after previous experiments.

The use of the TP technique allowed the influence of incidence angle to be explored. Furthermore, the flexibility of the TP processor implemented as part of this work allowed the effect of different amounts of real bandwidth to be explored.

5.3.1 Wetting Period

As previously detailed, the first part of the experiment involved the controlled addition of water to the sand and gravel above the buried target. The sand used was kiln-dried, so it

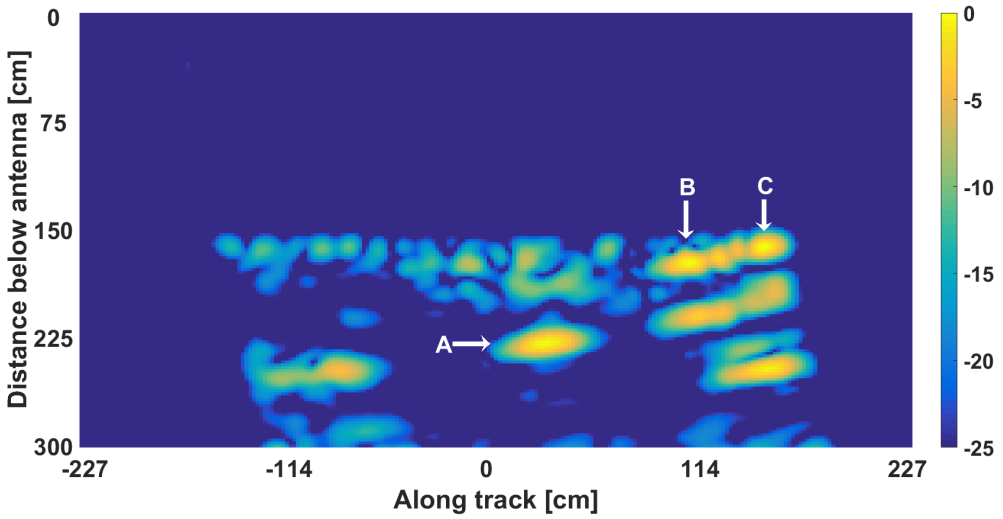

Figure 5.5: Example VV TP image from laboratory investigation. Produced using last scan taken during the experiment. Colour bar scale in normalised dB. Refer to text for details of features.

could be assumed that the SMC at the start of the wetting period was 0%.

The wetting period itself was split into two stages. During the first stage of the wetting period, water was added in 200ml steps with the scene being reimaged after each water addition, up to a total of 2000ml water added. Once the correct operation of the radar system and the TP processor had been verified the rate of moisture addition was increased to steps of 2000ml, up to a total addition of 26000ml. This two stage addition allowed the phase/SMC response of the buried target to be accurately characterised during the initial stage (whilst the buried target SCR was high) and also allowed a relatively large SMC change to be induced within two days. This large SMC change gave a large virtual bandwidth, allowing high resolution VB-SAR imaging to be conducted.

The phase and amplitude trends of the buried trihedral were extracted from each image by locating the local maximum magnitude in the area of the trihedral and then extracting the phase and amplitude of the complex value of that pixel. By repeating this process over the series of scans taken during water addition in each polarisation the trends were

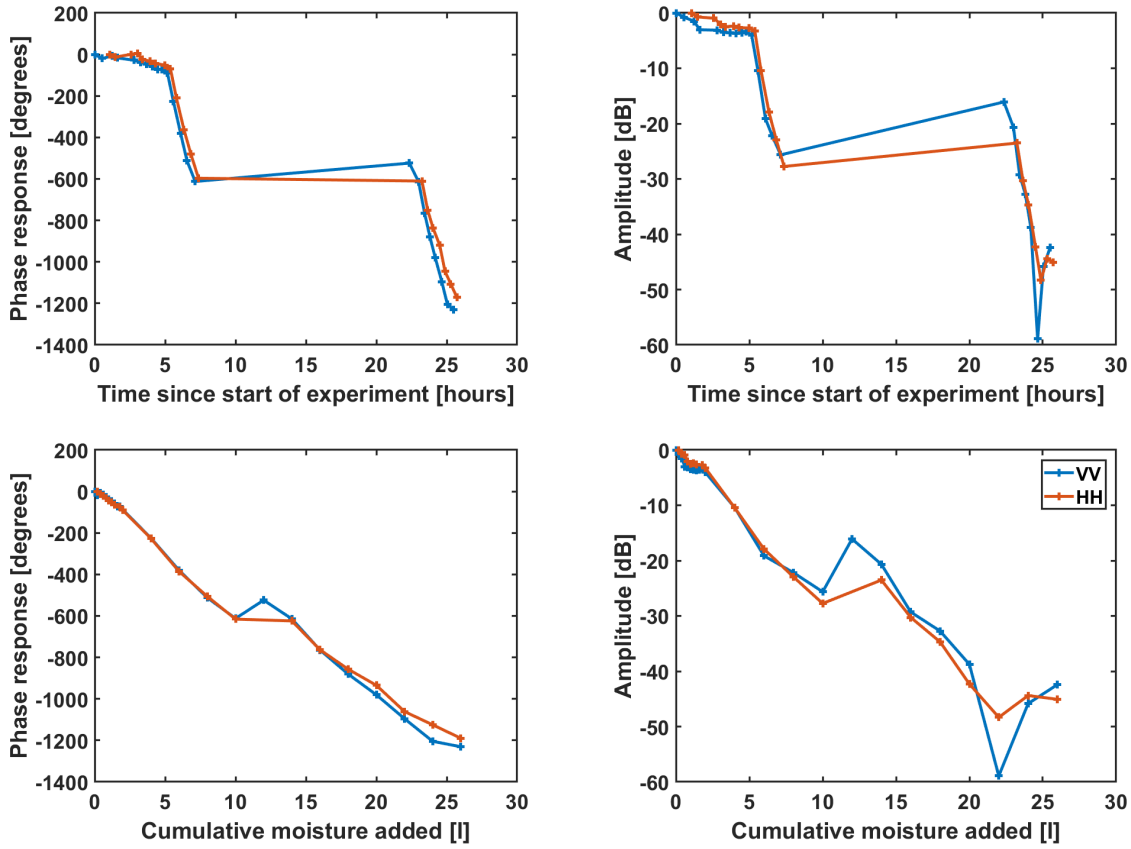

Figure 5.6: Plots of buried trihedral phase (left) and amplitude (right) responses extracted from TP images. Blue plots are VV polarisation, red are HH polarisation.
Top: Responses plotted against time since start of experiment.
Bottom: Responses plotted against total amount of water added.

extracted. Figure 5.6 shows the phase and amplitude responses of the buried trihedral during the wetting period.

The combination of plotting target response against both time and total moisture addition helps to understand anomalies in the responses. The response versus time plot is particularly useful as it highlights the fact that there was a period of approximately 15 hours (overnight) during which no water was added, which explains the apparent increase in phase in VV after 10000ml of water addition. Furthermore, it highlights that the flatness in HH at this point is caused by a missing scan.

The plots of amplitude and phase against moisture shown in Figure 5.6 are of more interest to this work as they will confirm or refute the premise that the phase response of the trihedral shows a linear response to the moisture content of the sand.

As expected, the general trend in amplitude shows attenuation increasing as water is added and the phase response is nearly linear. The minor unevenness in both plots at 800ml and 1800ml is due to a slight delay between water additions, during which time the sand dried out and/or water permeated away from the volume of sand above the trihedral. The pronounced inconsistency at 10000ml seen in both plots is due to no moisture being added during the night. It is not clear whether this was a result of drying or moisture travelling below the target (so the volume of water above the target decreases). The tail off of phase and amplitude changes above 20000ml of water is believed to be due to the trihedral return starting to be obscured by clutter as the attenuation of the wet sand above the buried target increased.

From these plots it was possible to establish the relationship between the quantity of water added and the amplitude/phase. By using the data from zero moisture up to and including 1400ml of water (this subset of data was chosen as it represented the best data; water addition was very linear with respect to time and the trihedral was still clearly visible and hence dominating its pixel) values of $-2.26x10^{-3}$ dB/ml and $-6.5x10^{-2}$ °/ml were obtained. This phase relationship will be subsequently used to estimate the SMC in each scan during the drying period.

These plots also support the prediction made by [4] that only the phase variation is linear with respect to SMC. As predicted, the phase/moisture plot is very linear (aside from the previously noted unevenness cause by delays in moisture addition) and the amplitude/moisture relationship is somewhat irregular, especially at higher SMC levels.

5.3.2 Drying Period

After the addition of water was complete, the scene was continuously imaged with approximately 80 minutes between each image. As time progressed the moisture content of the sand decreased; the experiment was left running until the phase change of the buried target became insignificant between scans.

During the drying process two electric fans were used to intermittently blow air across the wetted area of sand. These were positioned to be well outside of the scanners main lobe at all points within the scans and their air flow was carefully aligned to avoid blowing sand particles off the surface of the sand. This increased the rate of sand drying which shortened the experiment. However, the rate of drying was still slow enough that the moisture content change between images was small, which generally avoided phase ambiguities (other than during the initial drying which was very rapid due to evaporation from the upper sand). This also ensured that the virtual frequency steps were small which kept the unambiguous range in the VB-SAR images very high.

Some difficulties were experienced with the system control software during the first week of this drying phase; most significantly most of the first weekend's data was not acquired and sampling was somewhat intermittent for the rest of the first week. Once some minor changes had been made to the system software the system proved reliable and acquired images at a regular 80 minute spacing. The system returned the antennas to their home position (detected by fixed micro-switches) after each set of images was acquired to ensure there was minimal cumulative positioning error over the course of the experiment.

The phase and amplitude responses of the trihedral over the entire drying period are shown in Figure 5.7. These plots were generated with the TP pixel spacing in both the vertical and horizontal dimensions set to 4cm. This size of pixel spacing allowed a single

fixed pixel to be monitored over the entire series of images and a valid complex history to be produced despite the changing refractive index of the sand as it dried. If a smaller pixel spacing was used, this refractive index change could cause the peak response to move to a different pixel within the TP images. These plots have been plotted against elapsed time (rather than scan number) in hours to highlight periods of non sampling. The phase trend has been unwrapped to remove phase wraps by using MATLAB's unwrap() function under close supervision.

Pronounced irregularities are immediately noticeable in the plots. Firstly, in the early stages (before 200 hours elapsed time) the periods of non-sampling caused by system faults are visible. In the case of the amplitude response, these present themselves as generally benign patches which do not affect the rest of the trend (the very early distortions seen are believed to be due to the trihedral reponse being highly attenuated and the non-linearity of amplitude with SMC previously seen in Figure 5.6). However, in the case of the phase trend, it can be seen that two of these periods of non-sampling have introduced an error to the rest of the phase trend (the first is very obvious, the second less so). This error requires all the subsequent samples to have an offset added to them to correct them. This offset is calculated by applying the rate of phase change around the non sampling error to the period of non sampling.

This non-sampling correction has been applied to the phase history shown in 5.8. As can be seen, this has smoothed the early stages, and more importantly has corrected the rest of the phase history. However irregularities still remain especially after 200 hours elapsed time where marked increases and subsequent decreases in the phase response are seen which imply fluctuations in the sand's moisture content. As no additional water was added to the sand after the initial wetting period it is clear that these phase decreases are not due to an increase in the moisture content of the sand, and are in fact some artefact caused by either the environment in the laboratory or the radar system itself.

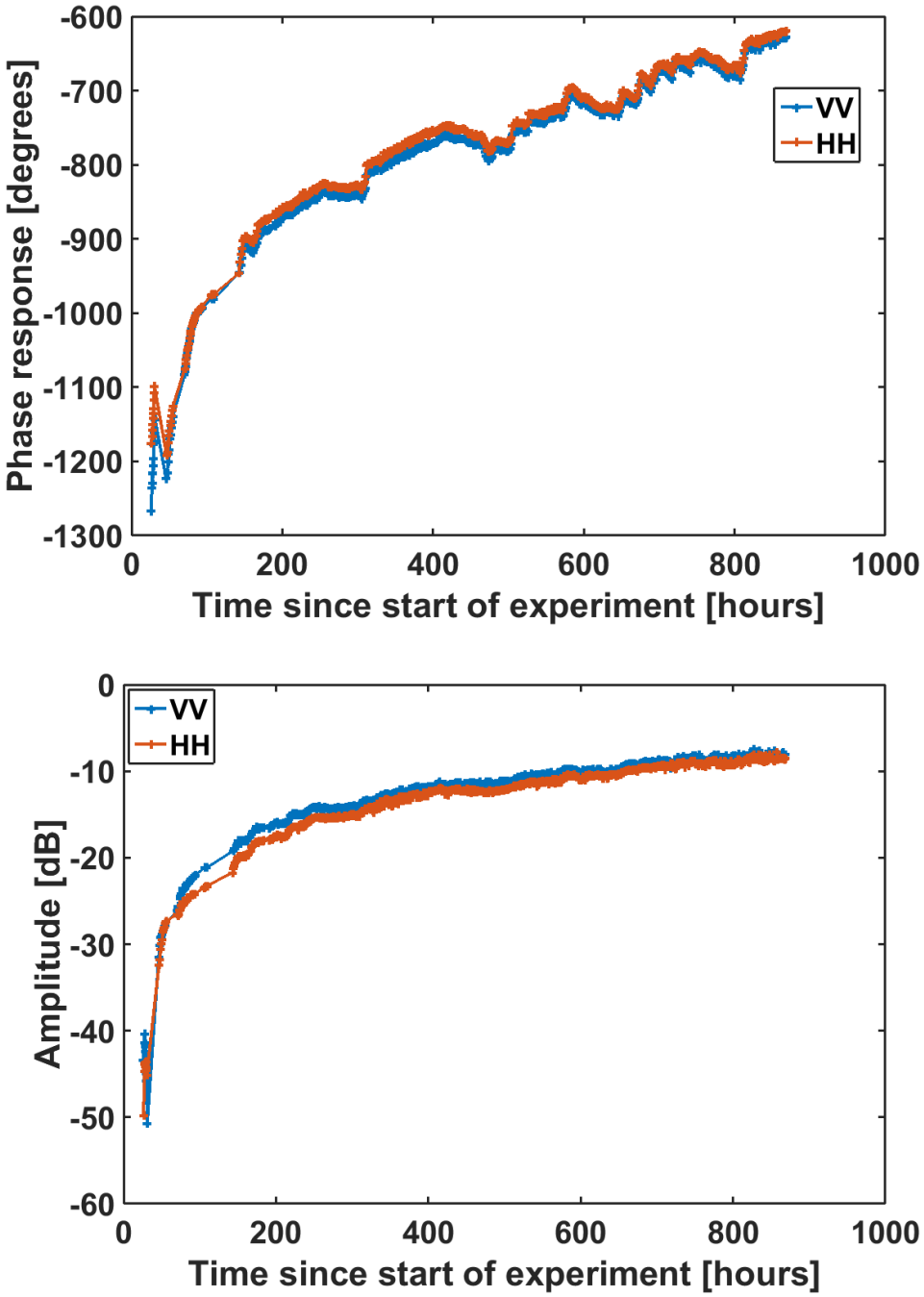

Figure 5.7: Top: Phase response of buried trihedral in VV and HH polarisations during drying period after unwrapping but before correction for periods of non-sampling and system variations. 0° refers to the phase response of the buried trihedral in the first scan of the experiment.
Bottom: Amplitude response of buried trihedral during drying process before correction for periods of non-sampling and system variations. 0dB refers to the amplitude response of the buried trihedral in the first scan of the experiment.

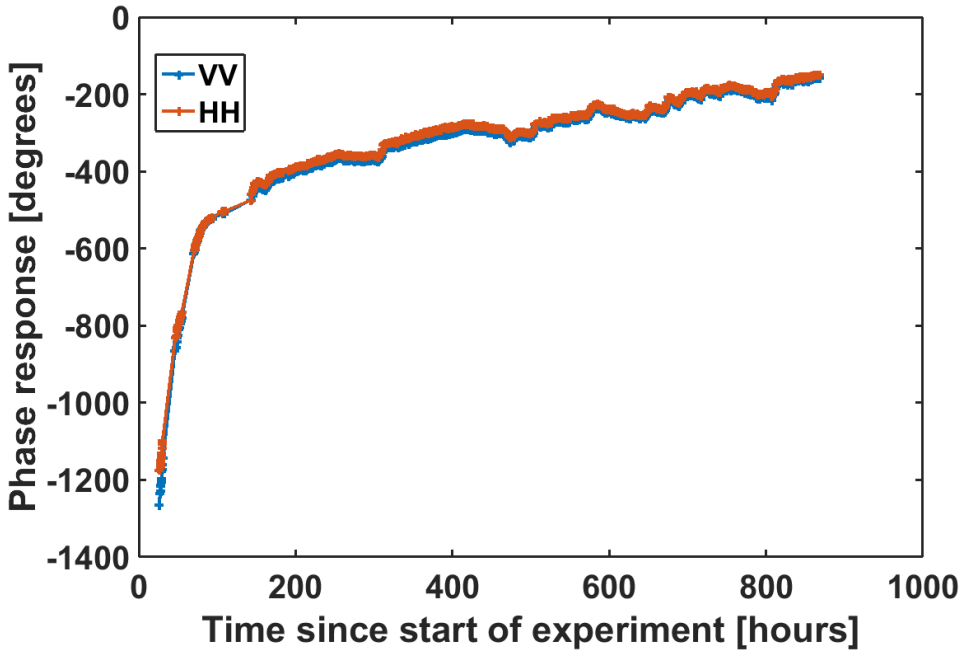

Figure 5.8: Phase response of buried trihedral during drying process corrected for periods of non-sampling.

The same effect is present in both the returns from a surface reference trihedral and the averaged phase from the strongest antenna cross talk line that appears near the top of each image, as shown on the left of Figure 5.9, and the average amplitude from the same cross talk line and the same reference trihedral as shown in Figure 5.9. In an ideal situation all of these graphs would show a constant phase and amplitude response over the course of the experiment [101]. The presence of these effects in both the reference trihedral and antenna cross talk phases and (albeit at a much lower level) amplitudes shows that this is due to variations within the radar system itself and not due to trihedral movement or antenna position variations; if they were due to either of those factors deviations between the reference trihedral and cross talk phases would be expected. In addition, the effects are clearly common across all 3 polarisations.

The phase variations are somewhat cyclical, appearing to be on an approximately 24

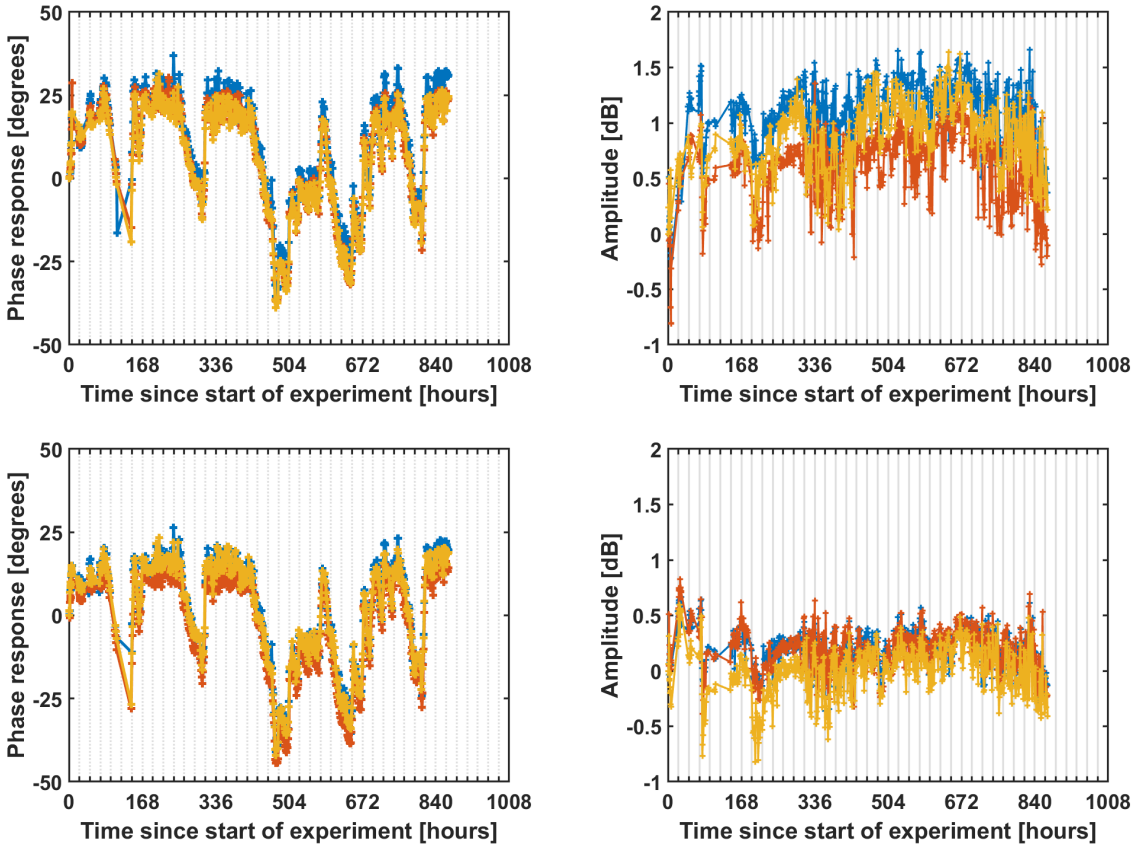

Figure 5.9: Blue traces are VV data, red are HH data and yellow are VH data Left: Phase response from surface reference trihedral (top) and antenna cross talk (bottom) over the course of the experiment. Note strong periodicity over both 24 and 168 hour periods and almost identical behaviour between polarisations. All trends normalised to 0° at first point.
Right: Amplitude response from surface reference trihedral (top) and antenna cross talk (bottom) over the course of the experiment. Note similar behaviour between polarisations but much weaker periodicity than seen in the reference phase histories. All trends normalised to 0dB at first point.

hour cycle which ceases every 120 hours (5 days) for 48 hours (2 days). The most obvious explanation for this is that the system is sensitive to ambient temperature variations and the building's heating system is causing these variations (the system warming up during the day and cooling overnight when the heating is off, and then cooling down even more when the heating is off over the weekend). Definitive proof of this relationship can only come from temperature logging, but for the purposes of this study the effect can be negated by using a reference trihedral's phase to correct the rest of the pixels within each TP image.

In contrast to the phase case, the amplitude variations appear to be much less periodic; little evidence of day/night and weekly cycles are present. This could be explained by the phase variation being caused by the physical expansion and contraction of the cabling within the system and the amplitude variation being caused by amplifier gain variations. It is likely that the amplifiers within the system are relatively stable over small temperature changes but due to the very short wavelengths in use and the long cable runs the system phase is highly sensitive to temperature.

The thermal coefficient of expansion for electrolytic tough pitch copper (the material typically used for electrical cable) is given as 16.8 ppm/°C by [102]. Assuming a 10°C temperature variation within the laboratory, and 15m total cable length, this would give a cable length variation of approximately 0.26mm due to temperature variations. At 5GHz, the wavelength in use is 6cm, therefore the thermal expansion represents 0.043 of a wavelength, which implies a phase variation of 15.4°. This is in the order of the amount of phase variation seen in 5.9; the differences being explainable by inaccuracies in the assumptions made and the possibility of phase variations also being induced by the VNA and amplifiers.

The idea of correcting the recorded histories by using the returns from the reference trihedral or antenna cross talk has been demonstrated by subtracting the phase response of

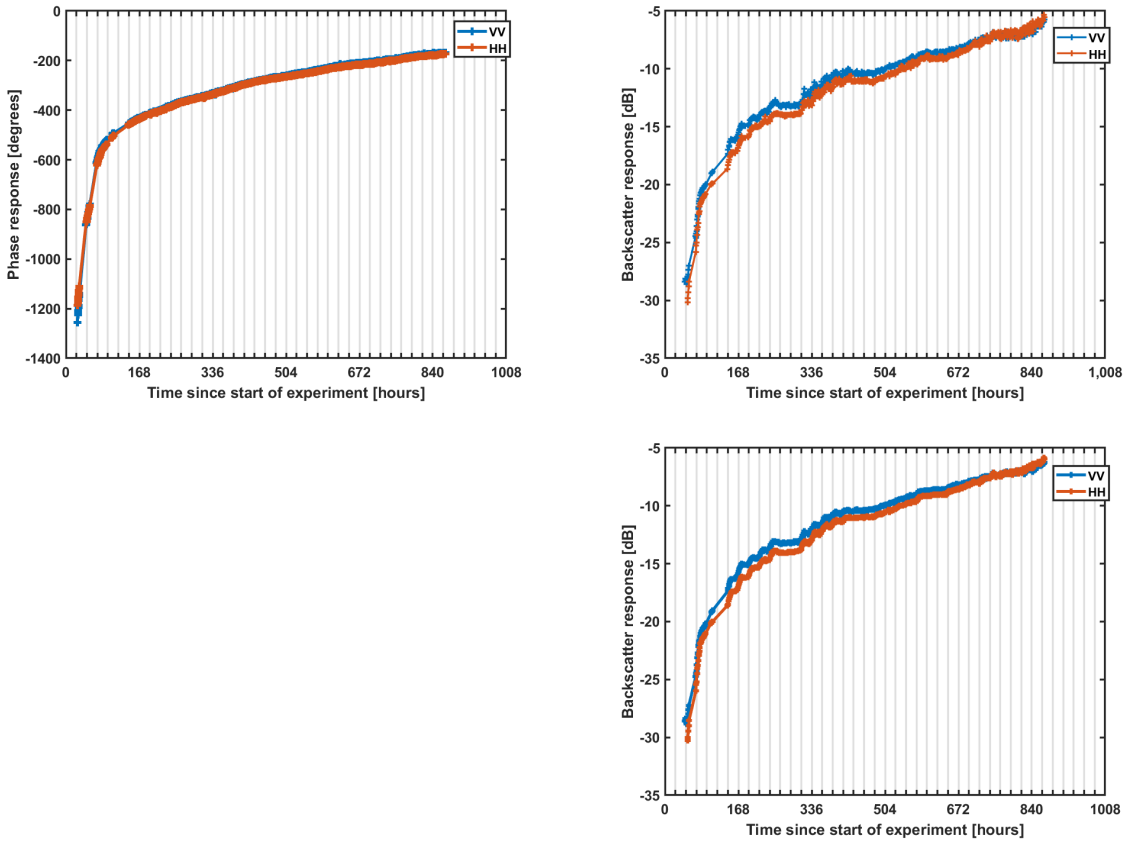

Figure 5.10: Left: Plot of phase response from buried trihedral, system variations removed using phase response of surface trihedral.
Right: Amplitude response from buried trihedral corrected using surface reference trihedral (top) and antenna cross talk (bottom) amplitude histories in both VV and HH polarisations.

the surface trihedral (plotted in Figure 5.9) from the phase response of the buried trihedral (previously plotted in Figure 5.8) The result of this process is shown on the left side of Figure 5.10. As can be seen, the cyclic phase variations previously seen have been removed from the data. This correction process has been applied to all future phase plots in this thesis and was applied to all phase data prior to VB-SAR processing. Despite the similar reference trihedral phase histories across polarisations each polarisation used its own phase correction data in order to ensure maximum accuracy.

In contrast to the phase case, the amplitude correction performed by subtracting the

reference trihedral's amplitude from the buried trihedral's amplitude (and, as an alternative, using the average cross talk amplitude as a source of correction data) has been less successful in removing the amplitude corrections, as shown on the right side of Figure 5.10. In fact, attempting to correct the amplitude appears to have exacerbated the fluctuations away from an ideal (smooth) curve. Due to this, no further corrections have been applied to amplitude histories used within this thesis. This can be explained by the low sensitivity of the amplitude to temperature variations.

From the plot of phase shown in Figure 5.10, by having prior knowledge of the water/phase relationship (derived from the data acquired during the addition of water to the scene) it is possible to calculate the moisture present in the sand above the trihedral over the set of images. This is important as direct measurements of the moisture content of the sand were not made (to avoid moisture sensing probes interfering with the radar image) and the VB-SAR process requires absolute moisture measurements in order to make depth measurements.

It is interesting to note that the initial rate of phase change (and hence sand drying) was rapid, and the rate of drying tailed off to a roughly linear trend. This could be explained by the sand near the surface drying relatively quickly through evaporation during the initial drying phase (the lower layers drying more slowly as the upper layers of sand block their evaporation) or by moisture sinking below the trihedral.

5.3.3 Polarimetric Considerations

In the trough scanner experiment virtually every scan collected was a triplet comprising a separate VV, HH and VH acquisition. In order to minimise wear on the scanner's RF switches polarisations were only switched at the end of each acquisition. This meant that between each polarisation in a particular scan there was an approximately 8 minute offset,

rather than acquiring all polarisations at each sample point in the scan before moving onto the next sample point. This time offset translates into an average sand moisture change of 2.6ml between each polarisation in a single triplet across the experiment; an inconsequential difference.

Subsequent VB-SAR demonstrations are shown across multiple polarisations. The VB-SAR process was consistently applied across all three polarisations.

The first stage in this polarimetric testing was to have the TP processor work through the HH and VH images in addition to the VV images already shown and discussed. Examples of TP images in the three polarisations are shown in Figure 5.11. From these example images it is clear that each polarisation sees different responses from the same scatters in the scene, as would be expected.

Comparing the two copolarisations (VV and HH) it appears that the VV polarisation receives stronger returns from subsurface objects than the HH polarisation. This is presumed to be due to the higher transmissivities through the air/sand and sand/air interfaces for VV polarisation as was predicted by the transmissivity calculations shown in Chapter 4.

In contrast, the crosspolarisation (VH) image shows very poor returns from the surface and subsurface. The significant return is from the two surface reference trihedrals that fall in the same range bin. This is believed to be due to the return from the edges of the trihedrals. As there are two trihedrals combined in a single range bin this return dominates the other (single) surface trihedral visible.

Although a full polarimetric calibration was not performed it was realised that it would be possible to check the VV and HH polarisations by comparing the amplitude of a surface reference trihedral across the two polarisations. Theory predicts that they should present the same amplitude response in both copolarisations (the VH channel could not be checked in this way as the trihedral would present a much weaker, and difficult to

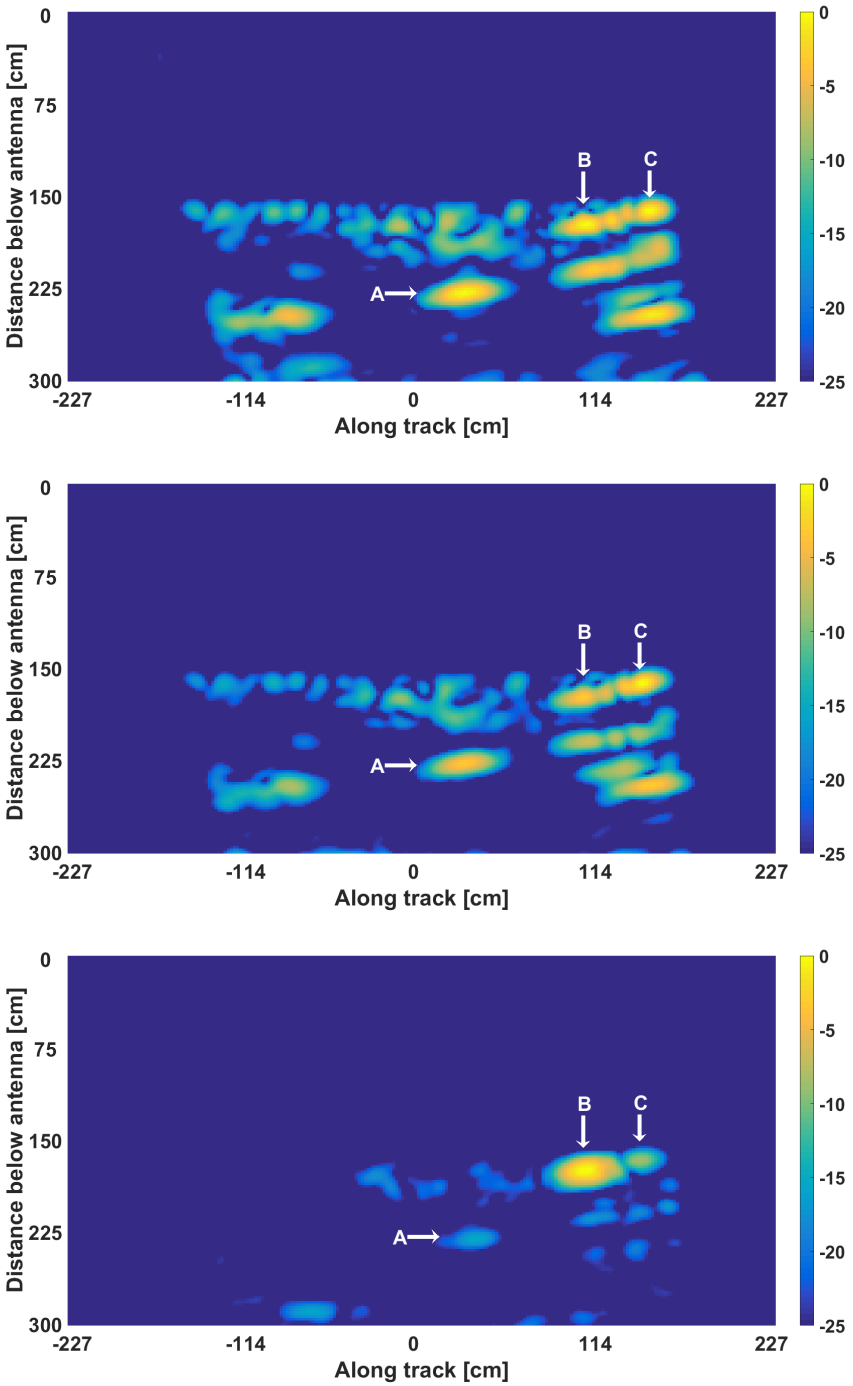

Figure 5.11: Example TP image from VV acquisition (top), HH acquisition (middle) and VH acquisition (bottom). Produced using last scan taken during the experiment. Colour bar scale in normalised dB. Arrow 'A' is the buried trihedral, Arrow 'B' is the response of two separate trihedrals that are the same distance away from the antennas (although placed on each side of the sand trough) and Arrow 'C' is the response of a single reference target.

predict, response); any difference could be used to scale the amplitude of the channels relative to each other. In contrast to the reference trihedral, the antenna cross talk ratio is not a good correction source as the antenna mounting arrangement and the shape of the horn antennas will influence that ratio. However, comparison of the cross talk and the reference trihedral ratios will show if any variation in the ratios over the course of the experiment are due to internal system variations affecting each channel independently (in which case the two ratios should move together) or external factors.

The ratios of the VV and HH responses are shown in Figure 5.12 for both the surface reference trihedral and the average antenna cross talk. As can be seen, the two polarisations are in reasonably close agreement so it was felt that initial polarimetric experimentation without full calibration (but scaling the VV image by a factor of 1.25- the inverse of the average HH/VV trihedral ratio) would be valid. The changes in the ratio over the course of the experiment are unexpected; the non-perfect agreement between the cross talk and reference trihedral suggests that these are not solely due to internal system variations. In addition, the lack of polarimetric calibration means that the absolute phases between polarisations are not directly comparable. However, because the VB-SAR process uses the differential phase across a change in moisture within a given polarisation this does not affect the demonstration of VB-SAR.

As the VV and HH phase histories have previously been shown to be similar, for the initial VB-SAR demonstration only VV polarisation was used. Polarimetric VB-SAR results are shown later within this chapter.

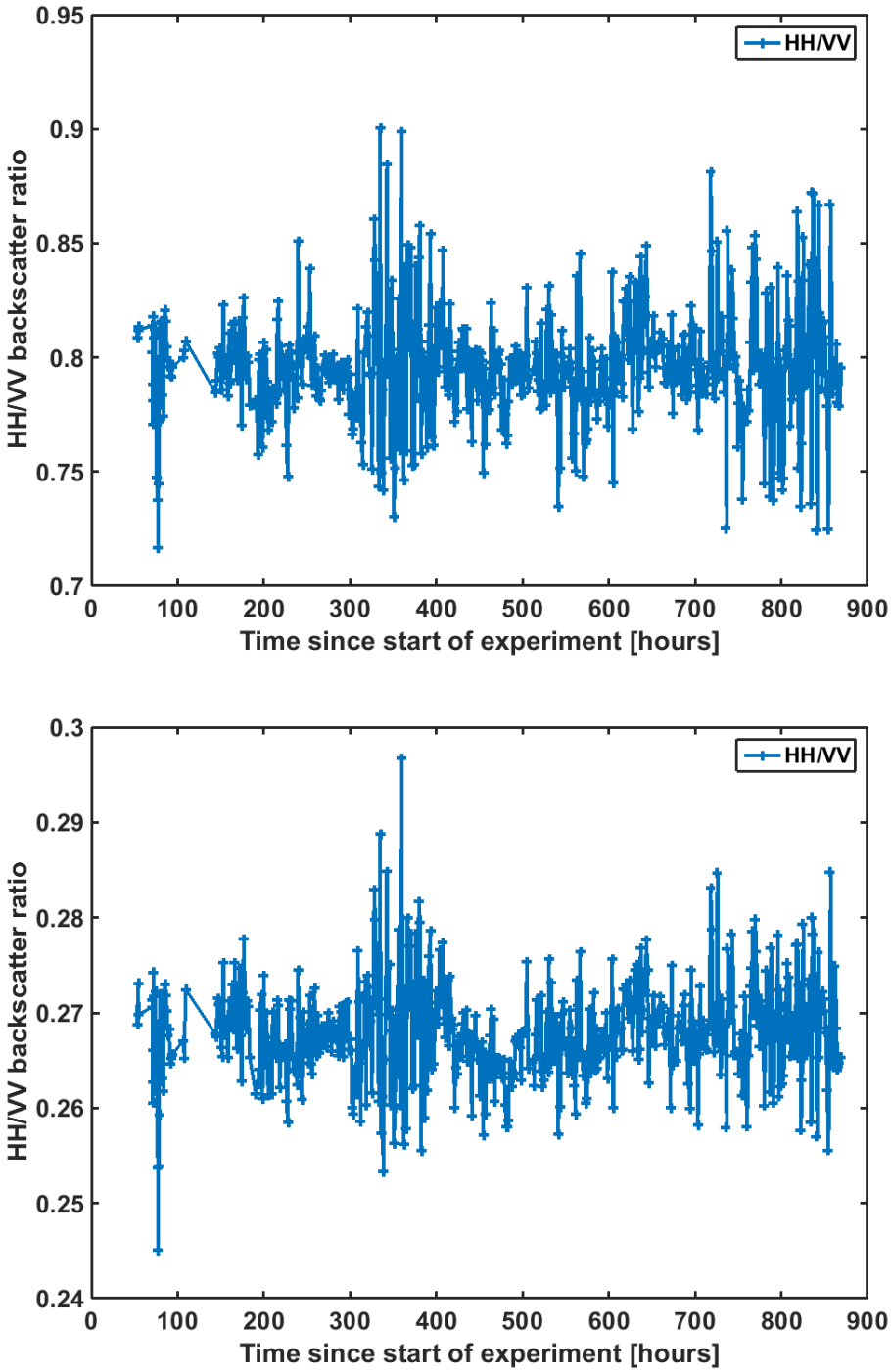

Figure 5.12: Comparison plot of surface trihedral (above) and average antenna cross talk (below) amplitudes in VV and HH. Early part of amplitude histories not plotted as reference trihedral not present. Large difference in ratios between plots due to antenna cross talk strength being different between polarisations.

5.4 VB-SAR Results

5.4.1 Initial VB-SAR Demonstration

Once the radar data collected from the trough scanner had been processed to form images, VB-SAR experimentation began. For the initial VB-SAR demonstration two VV polarisation image sets were formed using the TP process at a reconstruction angle of 20°. One set was high resolution, using the full 2GHz real bandwidth and the other was a lower resolution set which only used the first 150MHz of the real bandwidth. The full real bandwidth allowed an initial best case demonstration to be performed, when the return from the buried target was separated from the surface return. Conversely, the lowered real bandwidth set presented a more realistic demonstration of the VB-SAR scheme and allowed the VB-SAR process to resolve both the surface return and the buried target return from a combined return in the real bandwidth images.

5.4.1.1 High Resolution Derived VB-SAR

As discussed in Section 3.5.3, two methods of obtaining a linear phase change (and hence linear moisture steps) for VB-SAR processing are feasible. Firstly, there is simply using a pseudo-linear part of the phase history and passing that subsection through the VB-SAR processor directly. Secondly, it is possible to use the entire phase history by resampling the phase history to a linear soil moisture change and then passing the resampled phase history through the VB-SAR processor.

These two methods were compared in the first stage of VB-SAR performed, which used only the phase history of the single TP pixel corresponding to the maximum return of the buried trihedral. This phase history is shown in Figure 5.13 after corrections for system variations and periods of non sampling have been implemented. Note that due to

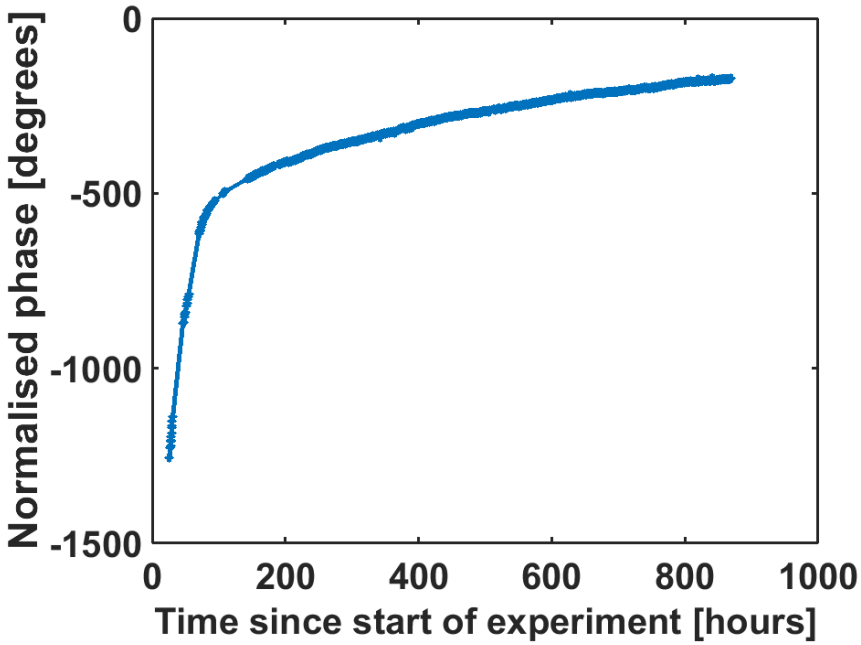

Figure 5.13: Phase history used for initial single pixel VB-SAR. Sample points highlighted

the use of the high resolution image data this pixel only contained the buried target, so no ground response is expected to be seen in any other the VB-SAR depth profiles produced.

The section chosen for the simple pseudo-linear phase history VB-SAR was from 250 hours after the start of the experiment to the end of the data set. As previously mentioned, this negates the need to perform a resampling to linear moisture change. As can be clearly seen, this subset excludes the majority of the phase change, hence the virtual bandwidth is severely limited and as a result the resolution obtained by the VB-SAR process will be poor.

The VB-SAR processor running a 10000 bin FFT calculated the parameters shown in Table 5.1 for this dataset. As expected, the resolution given by the VB-SAR process is low (significantly lower than the resolution given by the 2GHz of real bandwidth in use). Despite this, the maximum response depth of 28.6cm is in excellent agreement with the

Average refractive index of sand	1.907
Unambiguous range in sand	260.43m
Resolution	0.43m
Depth per FFT bin	0.026m
Maximum response depth	0.286m

Table 5.1: VB-SAR parameters for the pseudo linear phase history

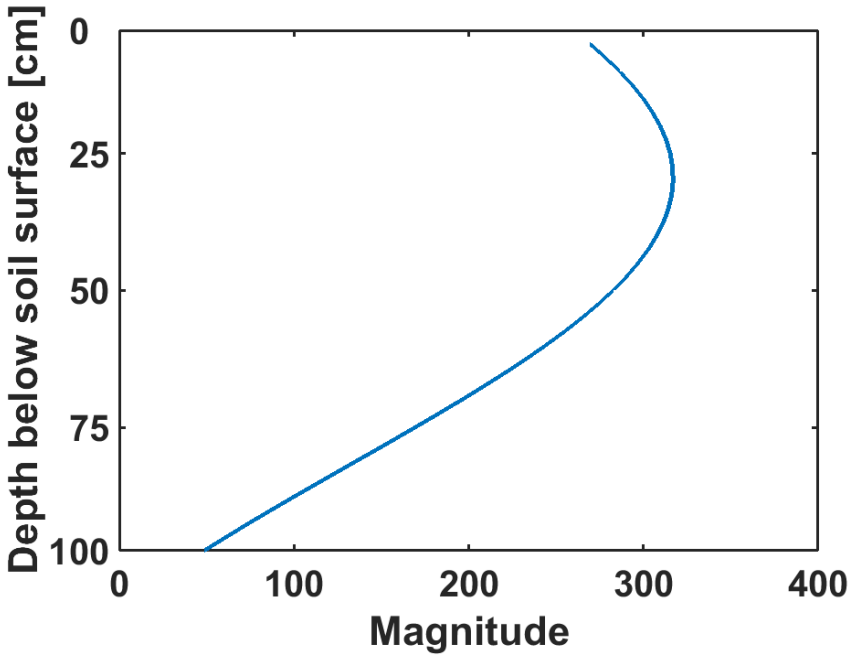

Figure 5.14: Initial VB-SAR depth profile formed using the pseudo linear part of the buried trihedral's phase history

actual depth of the buried trihedral which indicates the VB-SAR process is working as expected.

The depth profile produced by applying VB-SAR to this subset is shown in Figure 5.14. As expected, this subset provides very limited VB-SAR resolution but, crucially, the peak of the buried trihedral's response appears at the correct depth.

Using the full phase history shown in Figure 5.13 requires an extra resampling step in the processor to produce a constant sand moisture change between samples. As can be seen, using the entire phase history will give an large increase in phase change (and

Average refractive index of sand	2.215
Unambiguous range in sand	46.05m
Resolution	0.04m
FFT Bin Depth	0.010m
Maximum response depth	0.306m

Table 5.2: VB-SAR parameters for the full phase history

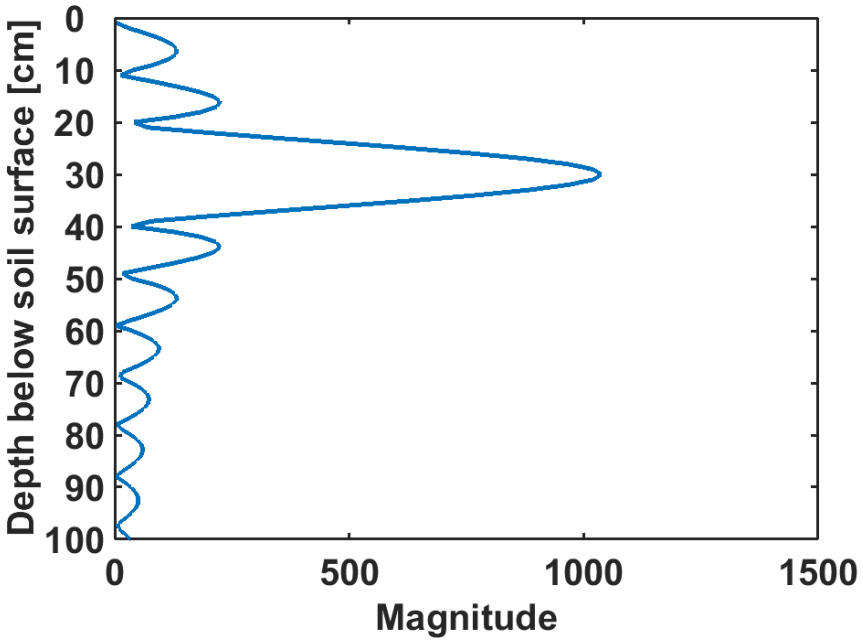

Figure 5.15: Initial VB-SAR depth profile formed using the entirety of the buried trihedral's phase history

hence moisture change) over the subset previously used, which will via Equation 3.42 give a large increase in the virtual bandwidth and hence significantly improve the obtained subsurface range resolution. The depth profile shown in Figure 5.15 and the parameters listed in Table 5.2 were obtained using this full phase history.

As can be seen from both the table and depth profile, using the full phase history has substantially improved the VB-SAR resolution. In addition, it has decreased the unambiguous range (due to the change in f_{step}), altered the average sand refractive index the VB-SAR processor reports (due to the average sand moisture across the phase history

having increased) and the depth of maximum response has increased slightly. Despite this, the unambiguous range (which is the unambiguous range in sand depth) is still more than sufficient for any likely realistic subsurface imaging scenario and the reported depth of the buried trihedral tallies well with the actual depth of the trihedral.

The loss of depth accuracy when using the full phase history is slightly troubling. To recap, the trihedral was buried at a depth of approximately 26.5cm below the sand surface, the reported depth for the pseudo linear phase history VB-SAR was 28.6cm and the reported depth using the full phase history was 30.6cm. This shows a depth variation of approximately 20%. One explanation for this issue is that the soil model in use is less accurate at higher SMC levels for the sand in use in the GB-SAR laboratory, as the use of the full phase history with linearisation would be expected to improve the accuracy of the VB-SAR depth profile. Errors in SMC estimation can be discounted as a possible cause, as due to the method used to estimate SMC it would be expected that the SMC estimates were more accurate at the start of the experiment.

In the full phase history case, a correction factor can be calculated, based on the reported depth and the actual depth of the buried trihedral. This is simply

$$\frac{30.6}{26.5} = 1.155 \tag{5.1}$$

Therefore, referring back to Equation 3.52, the correct average refractive index for the sand over the entire phase history would be

$$\frac{2.215}{1.155} = 1.92 \tag{5.2}$$

Using this lower value for the average refractive index would result in a lower range being represented by each FFT bin, which would in turn shift the entire depth profile slightly to the correct depth.

One possible explanation for the inaccuracy of the soil model (taken from [17]) is that the model is derived from 5 different soils, none of which is 100% sand. As mentioned in Section 4.2.1, there are numerous other soil models available in the published literature and one of these could be used in place of the model used here. Further study would be necessary to see if one of the alternative models provides a more accurate representation of the sand used. Alternatively, direct measurements of the refractive index of the sand used could be made across a range of soil moistures and frequencies, and the results used during VB-SAR processing.

The final step with this single TP pixel VB-SAR approach is to include the amplitude history as well as the phase history in the input to the FFT. This weights each phase point correctly, whereas previously each phase point had been implicitly assigned a weight of 1. The use of amplitude is necessary when utilising lower real bandwidths which cause returns from buried targets and/or the surface to merge. In that situation, one pixel's data contains information from multiple targets and the use of amplitude ensures that the various features present in a single VB-SAR produced depth profile are scaled correctly relative to each other.

The result of including the amplitude history in the VB-SAR process is shown in Figure 5.16. The reported depth of maximum response, average refractive index of the sand and other VB-SAR parameters have not been affected by the amplitude history, but the magnitude of the peak response and the shape of the peak have. The sidelobes have merged and increased due to the fact that the amplitude of the data varies over the complex history due to the variation in attenuation caused by the sand above the buried target. However, the fact that the buried target still appears at the correct depth provides reassurance that the VB-SAR processor is working as expected.

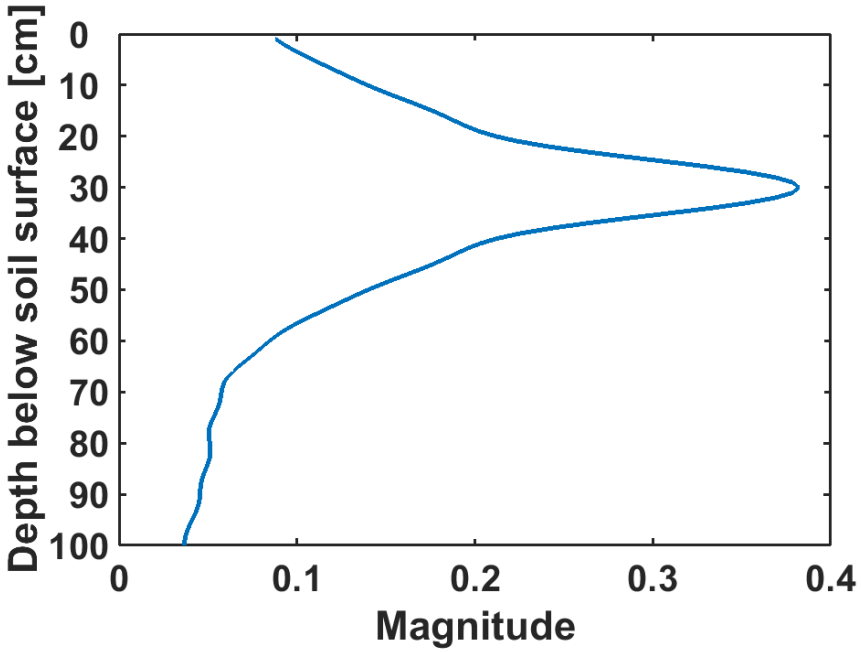

Figure 5.16: Initial VB-SAR depth profile formed using the entirety of the buried trihedral's phase and amplitude histories

5.4.1.2 Low Resolution Derived VB-SAR

Although the single pixel VB-SAR results are reassuring (in that the target peak appears at the expected depth) the usage of a single pixel from the 2GHz real bandwidth TP images is not representative of the data from a spaceborne or airborne sidelooking SAR system. In a sidelooking SAR system, a single pixel from such a SAR system represents all backscattering from an area of ground; above surface targets, the surface itself and buried targets.

This implies that in order to realistically test VB-SAR with TP images the VB-SAR processor must be operated in such a way that each VB-SAR depth profile produced contains responses from both the surface and the buried target. Three different ways of achieving this have been considered:

1. Sum each column of complex TP pixels, and feed the single result from each col-

umn into the VB-SAR processor

2. Pass single complex TP pixels to the VB-SAR processor and sum the outputs of the VB-SAR processor for each pixel together to form a complete depth profile.

3. Reprocess the raw scanner data with the TP processor operating at a much lower radiometric resolution (i.e. an artificially restricted bandwidth), and feed a single complex pixel from each column into the VB-SAR processor

Proposal 1 is not feasible with the TP processor in its current form. This is because the TP processor is not phase preserving in that the phase of a scatter is not directly related to the range to the scatter. This means that during a summation along a column the phase would not add in a meaningful manner.

Proposals 2 and 3 are both technically feasible, however proposal 3 represents a more realistic emulation of the real-world airborne/spaceborne SAR situation; such systems typically operate with a real bandwidth of much less than 2GHz and the target summation is effectively done within the real bandwidth domain, rather than the virtual bandwidth domain. In addition, the TP processor created easily allows TP images to be reconstructed using a subset of the real bandwidth.

By restricting the bandwidth to 150 MHz a slant range resolution of 1m in freespace was achieved. The cross slant range resolution in the along track dimension was kept at 35cm as per the initial VB-SAR testing. This does not affect the validity of the results shown as VB-SAR only provides a resolution improvement in the slant range dimension.

By using a slant range resolution of 1m the antenna cross talk returns were isolated from the sand volume returns. Within the sand volume, the slant range resolution was improved by the higher refractive index, i.e.

$$R_{SRS} = \frac{R_{SR}}{n} \tag{5.3}$$

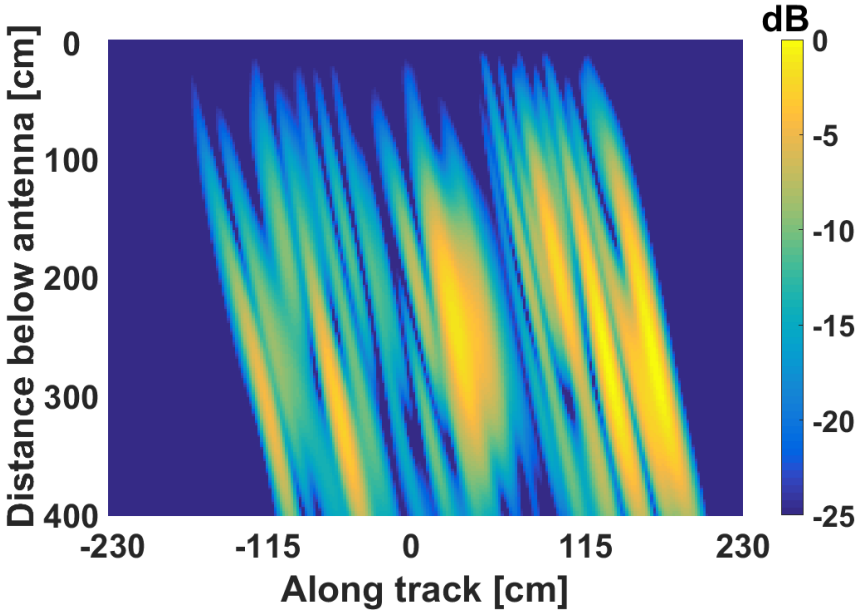

Figure 5.17: Low resolution TP image reconstructed using 150MHz bandwidth. Antenna cross talk removed for clarity.

Where R_{SRS} is the slant range resolution within the sand volume. In the case of the entire drying period, n was replaced with n_{av} to provide a general estimate of the slant range resolution within the sand in each scan. n_{av} was calculated to be 2.215 across the dataset, so R_{SRS} is approximately 45cm.

An example TP image processed at 1m slant range resolution is shown in Figure 5.17. The antenna cross talk has been removed for clarity. As can be seen when compared to Figure 5.5, the lowered resolution has made it impossible to visually distinguish between returns from the surface of the sand and returns from objects within the sand.

From this series of low resolution TP images, a single pixel (the highest amplitude pixel from the return overlying the buried trihedral) from each image was passed to the VB-SAR processor. This is an experimental implementation of the simulation shown in Section 4.6.4. In the simulated case, unexpected undulations were seen in the phase history of the buried trihedral when a surface target was also present. In this experimental

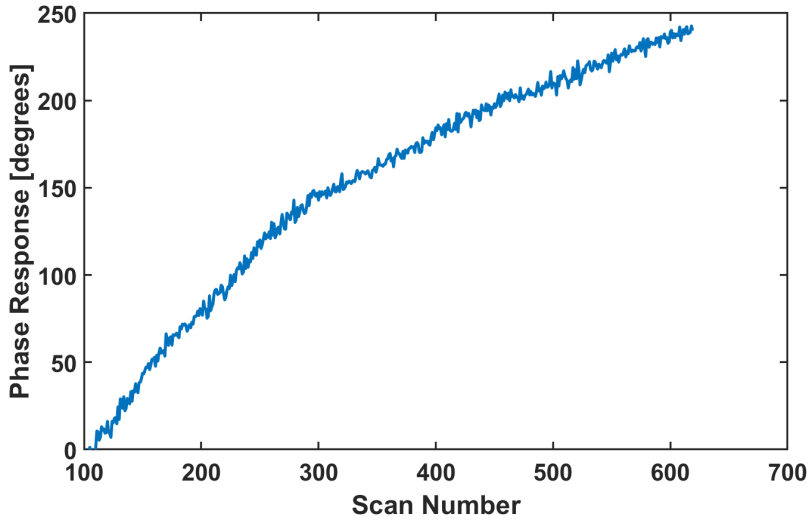

Figure 5.18: Phase history extracted from low resolution TP images reconstructed using 150MHz bandwidth.

data, the surface itself acts as the surface target.

Plotting the latter part of the experimental phase history, shown in Figure 5.18, does not show the same undulations. It is possible that the undulations are not visible because the surface response is much weaker than the buried trihedrdal's response in the experimental data, whereas in the simulation the two responses had the same amplitude. Note that the phase response in Figure 5.18 is less smooth than that in Figure 5.13 due to the lower range resolution decreasing the SCR.

The pixel passed to the VB-SAR processor will contain contributions from the surface return, the buried trihedral and the sand itself. As such, VB-SAR should be able to resolve these from each other. The depth profile extracted from the TP image is shown in Figure 5.19. As can be seen, the surface and buried target responses are completely combined and inseparable.

In contrast, the VB-SAR depth profile produced (using the pixel marked by "X" in Figure 5.19 from each low resolution TP image) is shown in Figure 5.20. This profile was

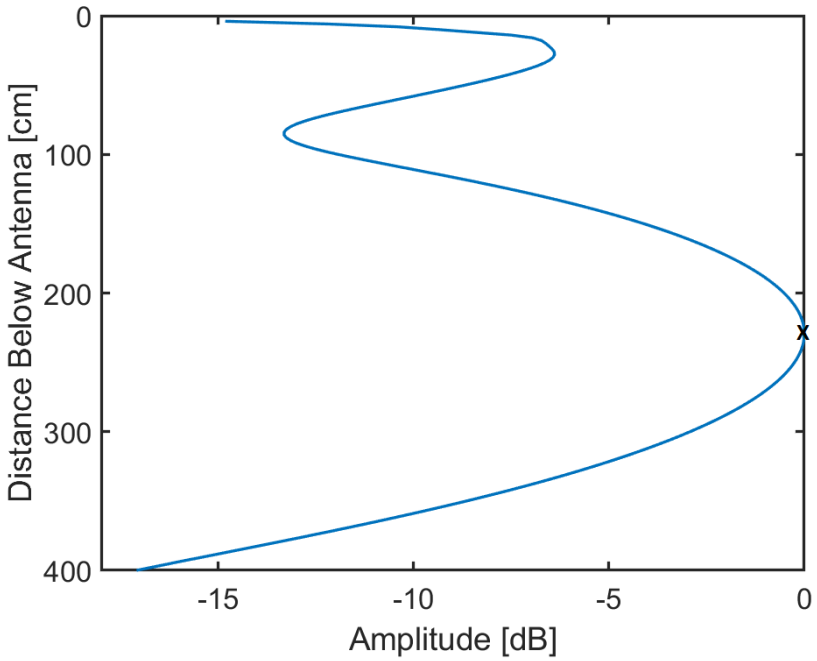

Figure 5.19: Depth profile on the column containing the buried target extracted from a low resolution TP image reconstructed using 150MHz bandwidth. Antenna cross talk shown, note that it is resolved from the response of interest.

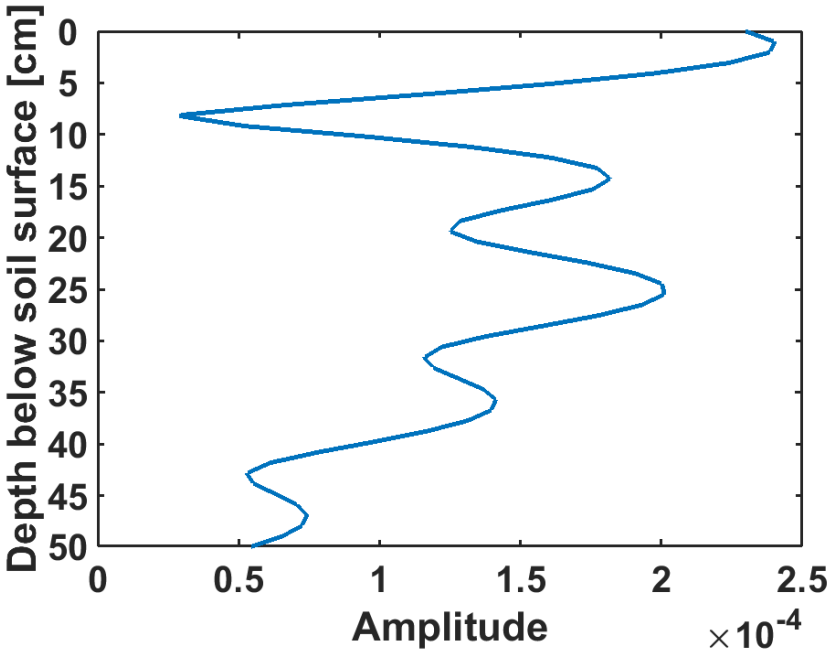

Figure 5.20: VB-SAR depth profile produced using data from low resolution TP images constructed using 150MHz bandwidth.

produced by using the complex history. As can be seen, the buried trihedral response is somewhat difficult to distinguish from the sidelobes of the surface return and interpretation of the subsurface scene is difficult.

By repeating the depth profile formation process across the sand volume it is possible to form a complete subsurface image. By referring to this image shown in Figure 5.21 several deductions can be made. Firstly, the uneven response across the sand surface shown in Figure 5.5 has been preserved across the image due to use of both parts of the complex phase history rather than only the phase history. Secondly, outside of the wetted area all of the subsurface returns have been resolved at the surface. This is because there is no subsurface phase change in those areas and explains why on the left of the image (where there are no surface trihedrals) the surface return is noticeably stronger than it is in the wetted area. Effectively all the returns caught within the slant range resolution cell

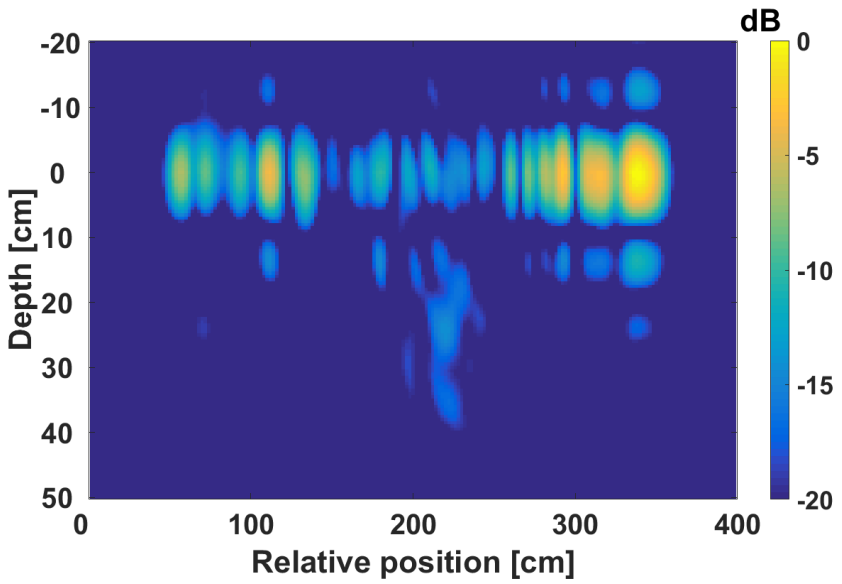

Figure 5.21: VB-SAR image constructed using complex history from low slant range resolution TP images.

have been summed together and appear as one return at the surface.

It was realised that as the sand surface return is above the sand moisture it should present a near zero phase shift across the series of TP images. This was confirmed by studying the phase response of the surface extracted from the high slant range resolution TP images, shown in Figure 5.22, which displayed a phase change that is much smaller than that shown by the buried trihedral. The early oscillations before the phase response had reached -20 degrees could be due to scanner homing issues. The sand swelling in response to the addition of moisture and then shrinking during drying could also help explain the overall shape of the phase history. However, a phase shift of 40 degrees at 4GHz corresponds to a physical movement of approximately 8mm. This implies an extremely large displacement compared to that previously reported [103] so swelling and shrinking of the sand can be discounted as possible causes. It is also interesting to note that unlike the buried trihedral phase history the surface phase history shows little long

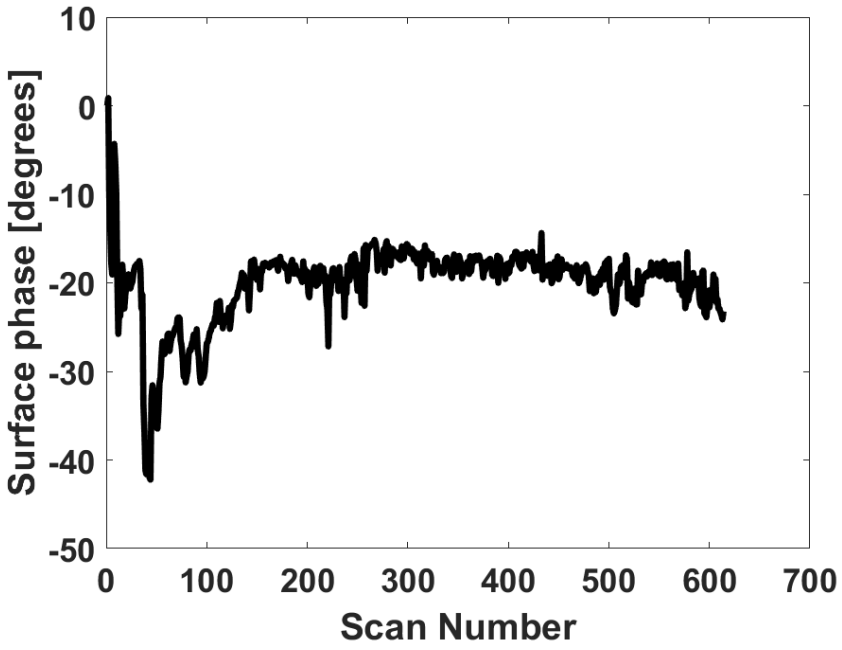

Figure 5.22: Phase history of the sand surface over the entire experiment, including both wetting and drying periods.

term trend after scan 200 but that the initial part of the surface phase history resembles the buried trihedral's phase history. This suggests that the phase change seen early on could be a response to sand moisture, but that the surface had dried by scan 200. The effect of this phase shift can be seen in Figure 5.20, where the surface response appears fractionally (˜1cm) below the actual surface position at zero depth.

Applying a DC removal (subtracting the mean value of the complex history from each point within that history) to the complex history before VB-SAR processing started gave the VB-SAR depth profile shown in Figure 5.23. As can be seen, the surface response and its sidelobes have been almost entirely removed from the depth profile, allowing the subsurface scene to be much more easily interpreted.

The complete image formed with DC removal enabled is shown in Figure 5.24, an image plotted in normalised dB with a shear applied to correct the imaging geometry.

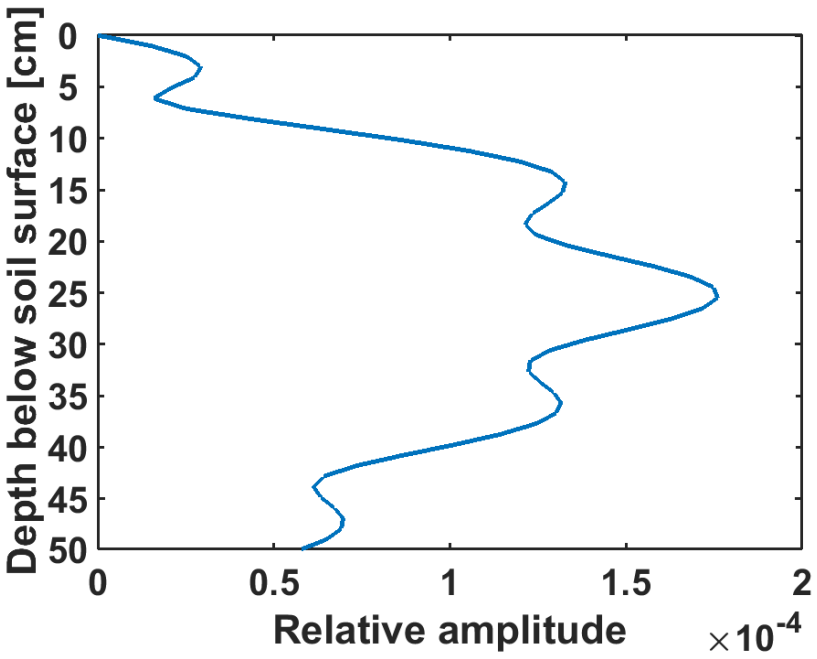

Figure 5.23: VB-SAR depth profile constructed using complex history from low slant range resolution TP images with DC subtraction applied.

Again, the DC removal has made the image easier to interpret and the removal of the strong surface returns has highlighted the sub surface responses. In this image the buried trihedral is clearly resolved and visible, with small sidelobes visible above and below it. The two distinct returns to the left of the upper trihedral sidelobe may be returns from the sand/gravel mixture present above the buried trihedral.

5.4.2 Incidence Angle and Polarisation Effects

The previous sections have presented VB-SAR results in VV polarisation only at a single incidence angle. However, one of the key assumptions made in the theoretical VB-SAR models and validated in Chapter 4 is that the phase shift from a buried target is independent of incidence angle. This is important as the incidence angle will vary across a scene observed by a side-looking SAR system; incidence angle independence would remove

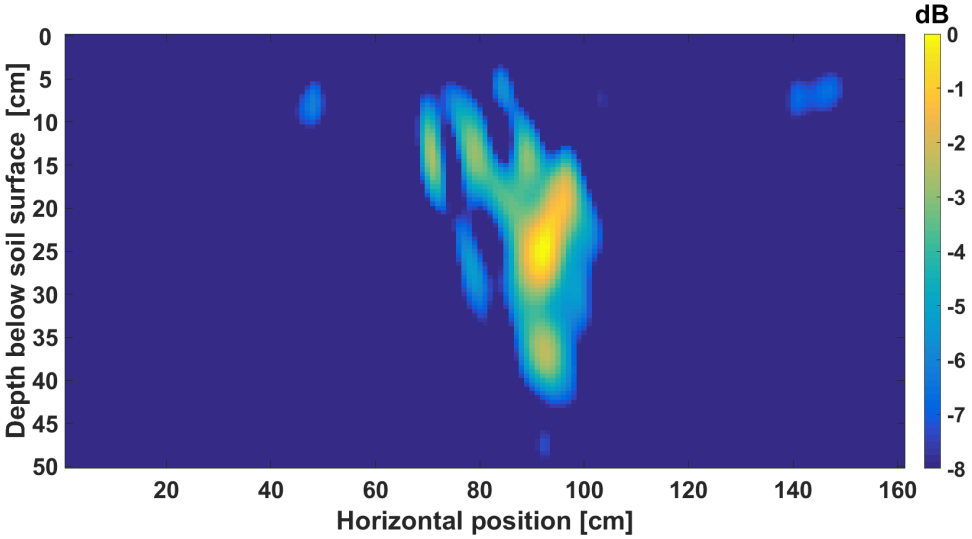

Figure 5.24: VB-SAR image constructed using complex history from low slant range resolution TP images with DC subtraction applied.

the need for an incidence angle compensation step in the VB-SAR processor. In addition, the ability of the VB-SAR process to work in different polarisations would significantly increase the utility of the VB-SAR scheme.

Unlike conventional SAR processors, the TP algorithm allows easy testing of the effects of incidence angle by allowing the incidence angle to be kept constant across the imaging scene and arbitrarily varied at process time (within the limits of the real antenna's beamwidth). The procedure used was to process part of the drying image stack across a range of TP incidence angles and extract the phase history of the buried trihedral as previously done. For this study, the incidence angle was varied from 0°to 40° in steps of 10°. All of the polarisations collected during the experiment (VV, HH and VH) were investigated, with the work limited to the scans in which the buried trihedral was visible in all polarisations. At 40° reconstruction the buried trihedral is not visible in the VH images (due to the weak response of the trihedral in cross polar data), so this angle is excluded from the plots presented.

Initially the full 2GHz of bandwidth collected was used by the TP processor, in order

to isolate the buried trihedral's return from the surface return which allows meaningful comparisons between the different phase histories to be made. The results of this data extraction are shown in Figure 5.25. As can be seen the VV and HH results generally show good agreement with each other over the reconstruction angle range. In comparison, the VH polarisation shows larger deviations at higher reconstruction angles. In the case of the VH anomalies this is probably due to the decreased Signal to Clutter Ratio (SCR), a finding supported by the fact that the phase histories that best match with the copolar histories are those at 10° and 20°, angles which would give the highest SCR due to the orientation of the trihedral.

Further investigation is needed for the VV and HH cases as the phase shift variation is approaching 20% over an angle range of 40° which is a reasonably representative angle range compared to spaceborne SAR systems (see Tables 3.1 and 3.2). Significantly, in the two copolar cases the phase shifts seen generally increase with increasing incidence angle, suggesting that there is some incidence angle dependence present.

This effect was predicted at SMC levels below 10% by [93] and demonstrated in the SAR simulator in Section 4.6.3. However, both of those evaluations predicted that the variation over incidence angle would be much smaller (as a percentage of the overall phase shift) than that seen here. It is possible that this excess incidence angle dependence is an artefact of using a single target at a fixed angle (so the apparent physical depth of the target is varying across incidence angles). Further investigation is warranted in order to be sure of the cause of this effect, perhaps using a target such as a sphere.

In addition, these plots show that between the VV and HH polarisations there is a small difference in the observed phase shifts at lower incidence angles, with the HH polarisation seeing a slightly smaller phase shift. However, this difference is much smaller than those between different incident angles within the same polarisation, so is not considered to be significant. The fact that the high incidence angles show excellent agreement between VV

and HH could signify that the VV-HH variation is caused by the effect which is causing the incidence angle variation affecting VV and HH differently. Again, further work using a target that presents a more consistent return over observation angle is needed to be sure.

These phase histories extracted from the high resolution TP images can be fed into the VB-SAR processor to produce depth profiles. The outputs from the VB-SAR processor using these phase histories are shown in Figure 5.26. These depth profiles have been produced using phase only VB-SAR in order to isolate and highlight any incidence angle/polarisation induced affects.

As can be seen the process has worked well with the VV and HH polarisations, however there is a small difference in the peak response depth between the two polarisations- the HH peaks appearing slightly shallower than the VV peaks. This is in line with the previous observation that the phase shifts seen in HH are slightly smaller than VV. In all cases aside from the 0° HH set the observed peak depth is within 20% of the actual target depth, and the variation in reported depth follows the trends seen in the phase history plots. In comparison to the well structured VV and HH results the VH results are significantly distorted. This comes about as a direct result of the distorted phase histories previously seen, which are in turn suspected to be due to the low SCR of the trihedral in this polarisation. This underlines the need for future work to use a variety of subsurface targets.

As previously demonstrated, it is also possible to perform VB-SAR processing across a stack of low range resolution TP images, in order to allow the VB-SAR processor to resolve both the surface and buried target returns. In order to show the utility of this over a range of incidence angles the TP processor was used to artificially lower the range resolution from the real bandwidth to 1m and produce lower resolution images at reconstruction angles of 0°, 10°, 20° and 30°. At this resolution examining the buried target's phase history directly is not valid as the buried target's response has merged with the surface

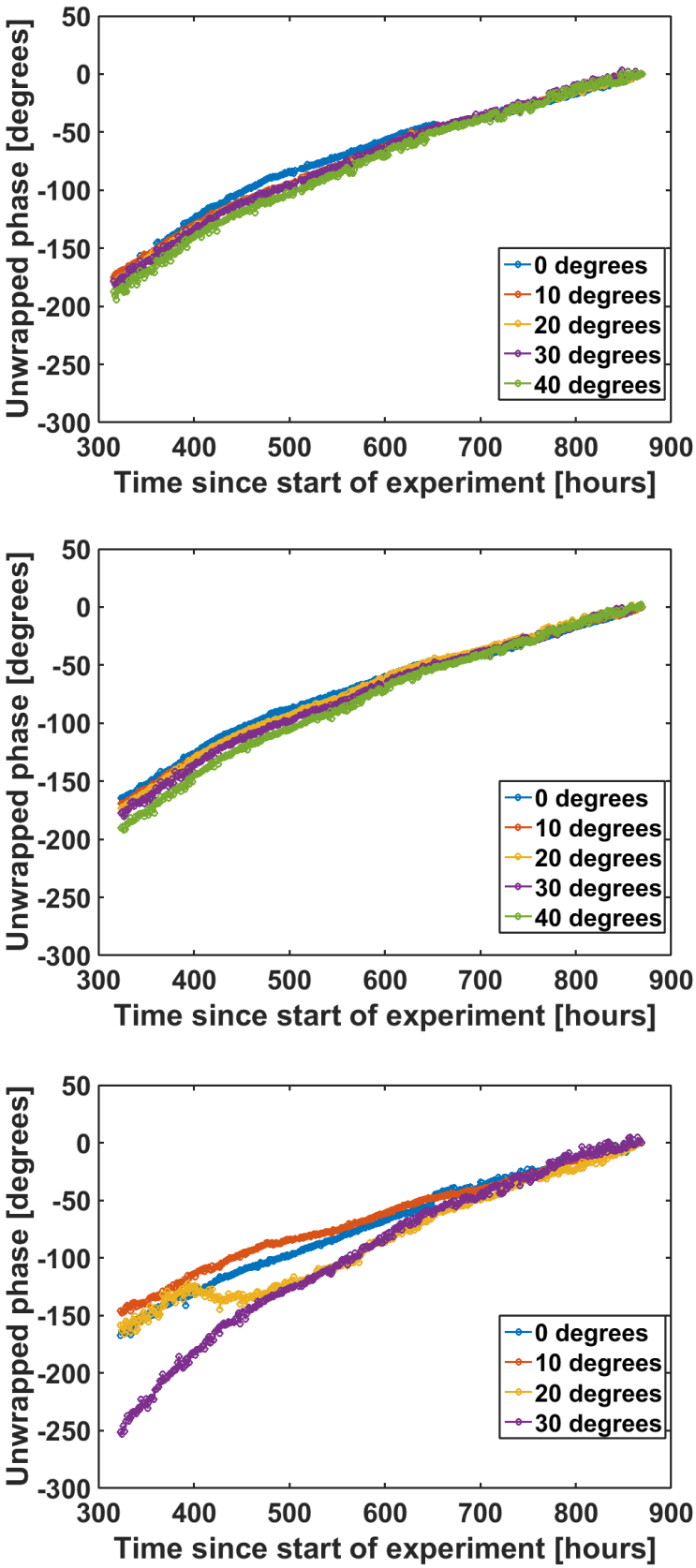

Figure 5.25: Plot of phase response from buried trihedral in VV (top), HH (middle) and VH (bottom) across incidence angles. System variations removed using phase response of surface trihedral

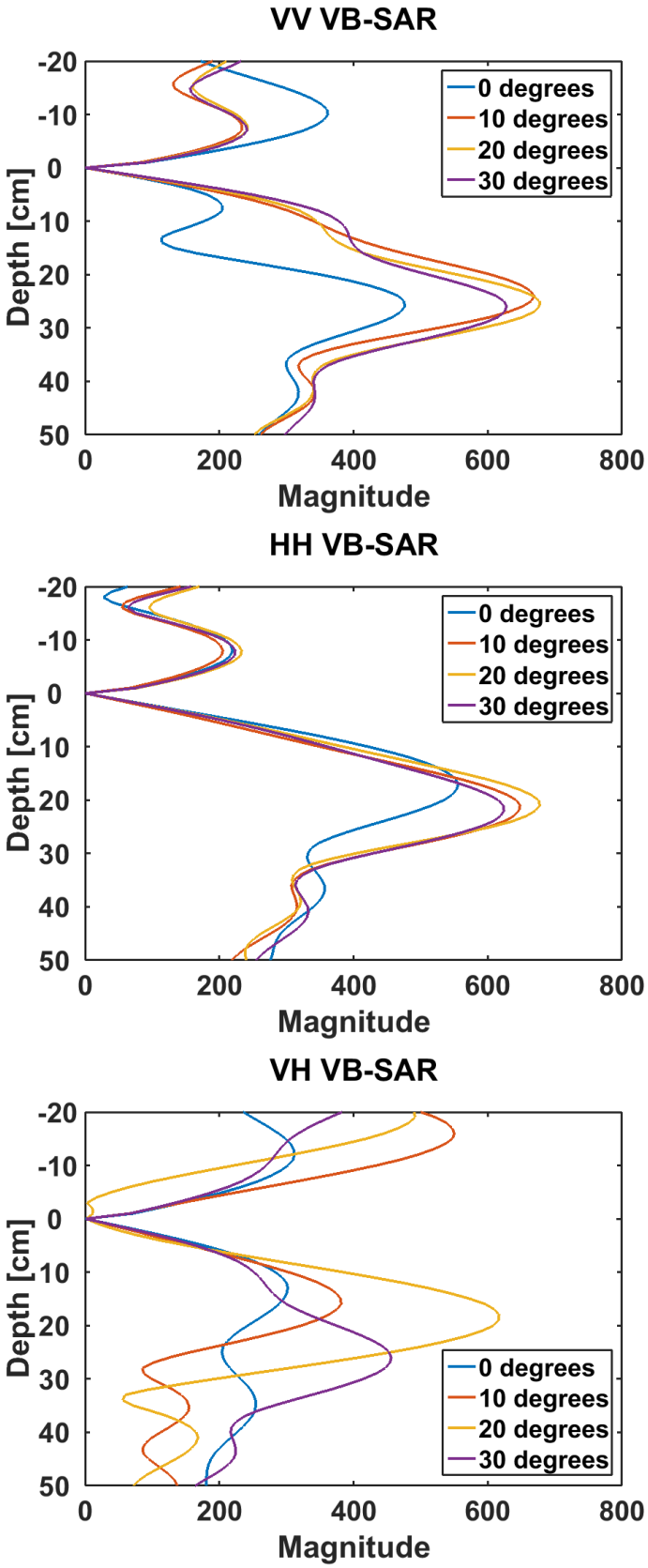

Figure 5.26: Phase-only VB-SAR in VV (top), HH (middle) and VH (bottom) across multiple incidence angles, produced using phase histories shown in Figure 5.25. These phase histories are formed using high-resolution TP images.

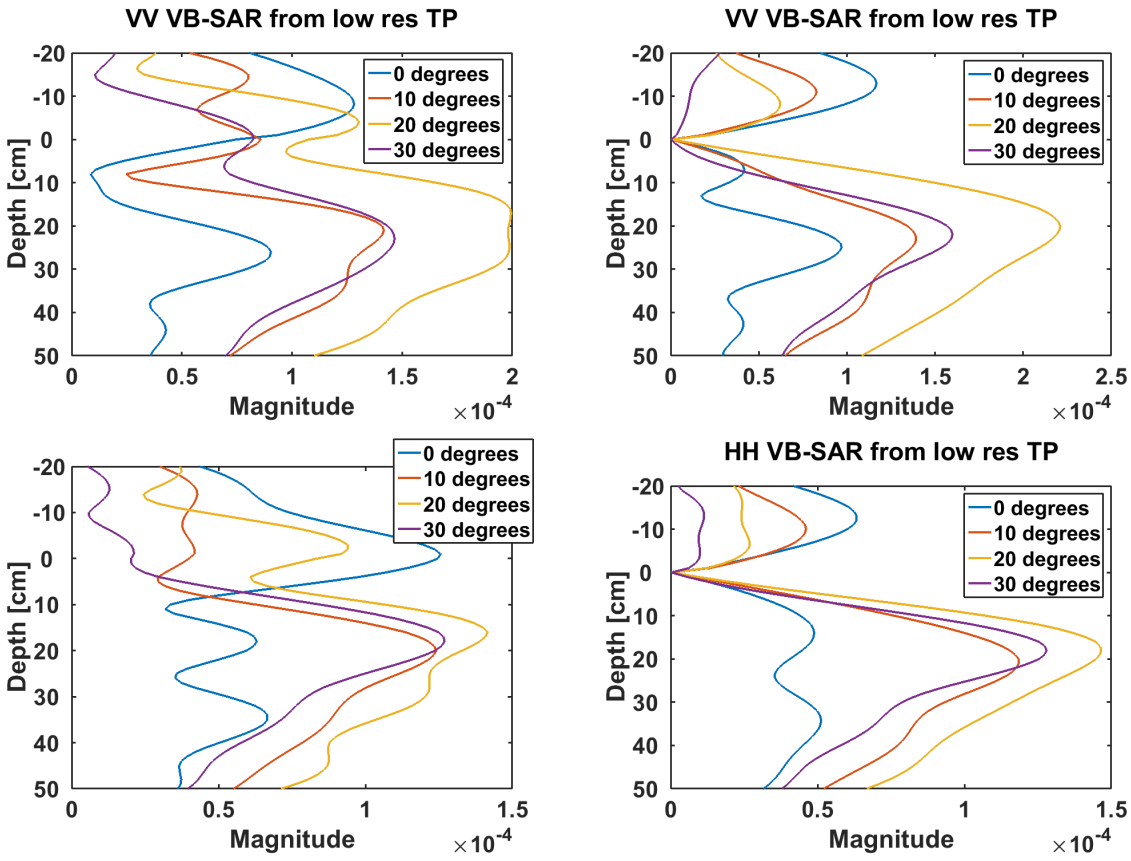

Figure 5.27: Left: Phase and amplitude VB-SAR in VV (top) and HH (bottom) across multiple incidence angles, produced using complex histories extracted from TP images with 1m range resolution
Right: Phase and amplitude VB-SAR in VV (top) and HH (bottom) across multiple incidence angles, produced using complex histories extracted from TP images with 1m range resolution. DC subtraction applied to suppress surface response.

and soil volume returns. Due to the poor response of the trihedral in VH polarisation the trihedral is not resolvable from the low resolution TP images, the small response of the trihedral being overwhelmed by the clutter (surface and sand volume returns).

The results of performing VB-SAR on these low resolution images in VV and HH polarisations are shown on the left of Figure 5.27. In these depth profiles the complex history has been used as opposed to the phase-only histories used for the high resolution TP VB-SAR. The use of the complex history allows the surface and buried target responses

to be correctly scaled relative to one another. As expected, given the orientation of the trihedral and the strong response of the surface at 0° the 0° case shows the lowest trihedral amplitude/surface amplitude ratio, the 20° case shows the highest ratio and the 10° and 30° cases are in the middle.

By applying a DC subtraction scheme during the VB-SAR process, the surface return was suppressed in the two depth profiles shown on the right of Figure 5.27 were produced. This has highlighted the trihedral's return in each depth profile. Again, the 0° case has the weakest return from the trihedral, the 20° case has the strongest return and the two other cases have trihedral return strengths in between the 0° and 20° cases.

In all cases the buried target appears within approximately 20% of its actual depth, showing that the VB-SAR process is working well across a range of incidence angles. However, some variation is visible, with the peak subsurface response appearing shallower than the buried trihedral. One possible explanation for this is that the response of the gravel/sand mixture above the target may be interfering with the target. Again, as mentioned in the analysis of the target phase histories, more work is required to understand the causes and possible consequences of this effect.

5.4.3 Multispectral VB-SAR

5.4.3.1 1GHz Sub Bands

In addition to varying the reconstruction angle the TP processor allows subsampling of the frequency data before it is passed through the TP process, as has previously been done in order to generate low real resolution TP images and demonstrate the resolution improvement offered by VB-SAR.

This bandwidth subsampling also gives the opportunity to investigate any real frequency dependent behaviour of VB-SAR. Demonstrating frequency independence would

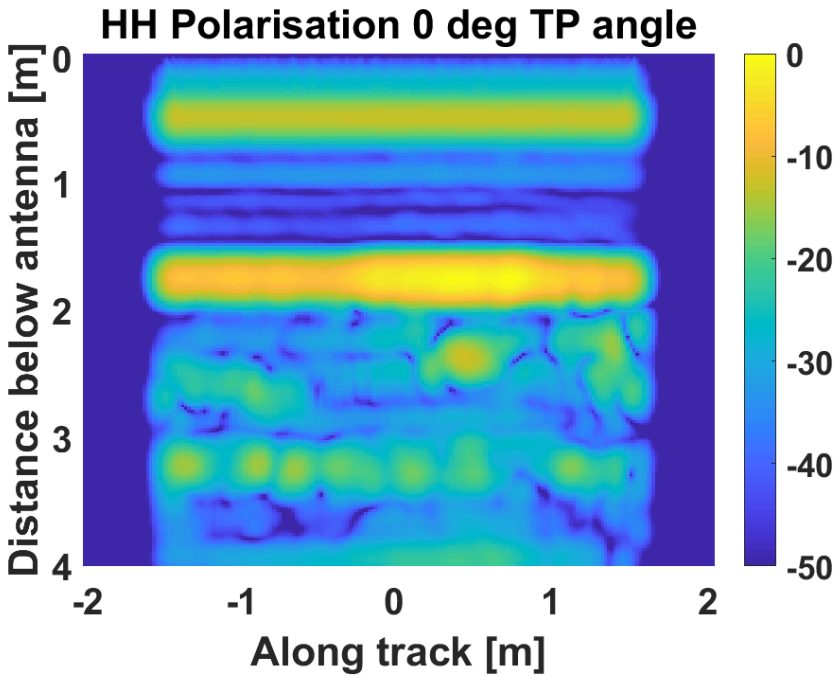

Figure 5.28: Example 4-5GHz TP image showing clear resolution of the surface return and the buried trihedral response. Colourbar scale is in dB.

massively increase the utility of the VB-SAR scheme, as it would allow lower frequency airborne and spaceborne radars to be used which would give much improved soil penetration than that seen at C-band.

2GHz of bandwidth was used during this experiment. By splitting this bandwidth into two sub bands of 1GHz bandwidth each (4-5GHz and 5-6GHz) a slant range resolution of 15cm in freespace was obtained, sufficient to separate the surface and buried trihedral returns as confirmed by Figure 5.28. This gave the widest possible frequency separation which ensured that any frequency dependent effects were maximised. This process was repeated over a range of reconstruction angles and polarisations.

For a buried target, different illumination frequencies should cause two effects. Firstly, the refractive index of a given soil varies with frequency, which will influence the phase history due to the change in refractive index. Secondly, the shift in wavelength will also

influence the phase history; shorter wavelengths would be expected to give larger phase shifts. As such, comparison of the phase response of the buried trihedral in the two sub bands could provide an indirect measurement of sand moisture.

After TP processing in both bands the phase histories of the buried trihedral were extracted, corrected and plotted across all three polarisations, giving the results shown in Figure 5.29. From these plots it is clear that across incidence angles in VV and HH polarisations the lower frequency sub band shows a consistently smaller phase shift than the higher frequency sub band as would be expected. The situation in VH is less clear with large distortions clearly visible in most bands. It is postulated that these distortions are caused by the poor SCR given by a trihedral in VH polarisation and that future work with a more appropriate buried target would remove them. Due to the large distortions and uncertainty about the consistency of the trihedral response in VH polarisation it was decided not to include the VH data in further analysis.

Plotting the difference between sub bands against the moisture content of the sand as shown in Figure 5.30 shows that there is a good correlation between the sand moisture content and the phase difference between the two bands in VV and HH polarisations. This suggests that dual band phase measurements of a buried target are an excellent metric for measuring soil moisture; it is likely that given a suitable buried target that this would extend to cross polarisations as well.

The phase and amplitude histories extracted from the two sub bands in each polarisation can then be fed through the VB-SAR processor. As the real bandwidth in use is 1GHz the range resolution in the TP image stacks will be 15cm in freespace. Given that the target trihedral is buried at 26cm below the sand surface this means that the buried target and sand surface cannot be resolved by the VB-SAR process when a single pixel is used as that single pixel cannot contain both surface and buried trihedral responses. The results of this are shown in Figure 5.31.

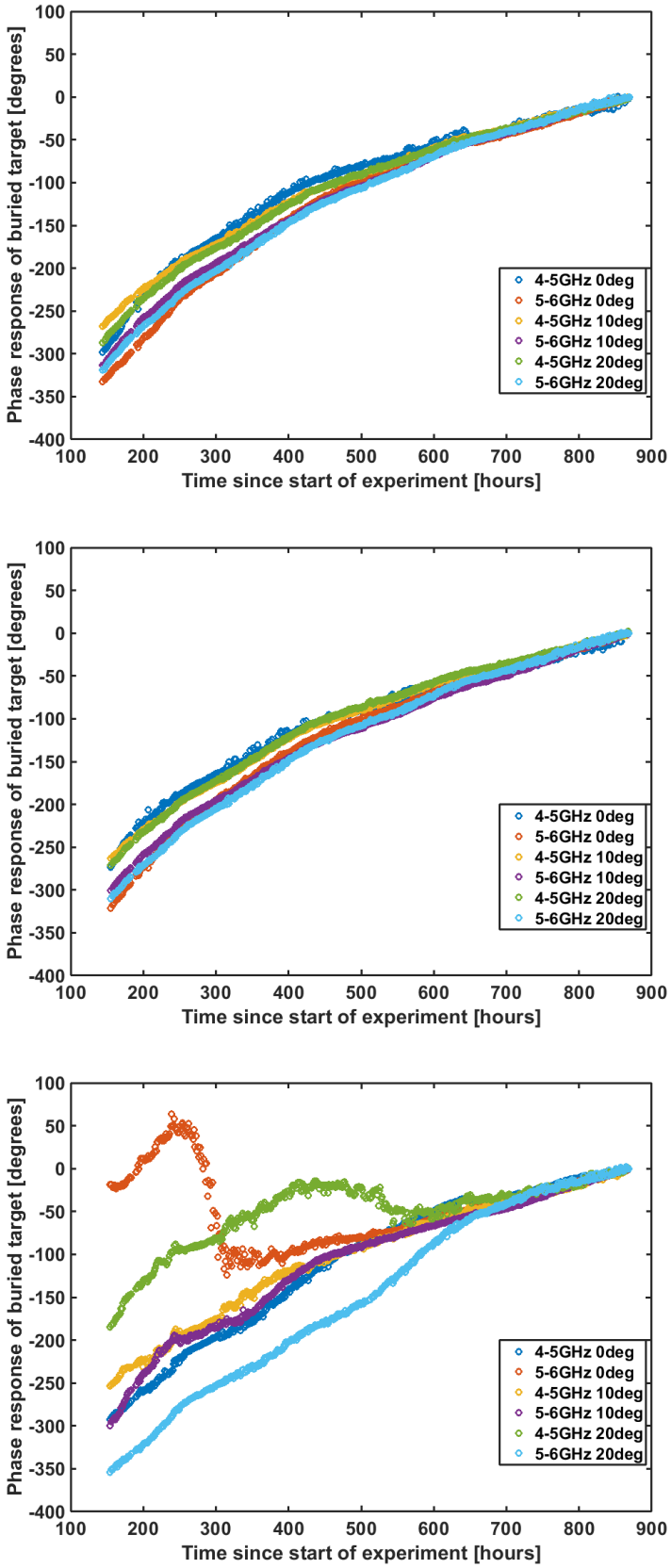

Figure 5.29: Plot of phase response from buried trihedral in VV (top), HH (middle) and VH (bottom) in the two sub bands at 0°, 10° and 20° reconstruction angles. System variations removed using phase response of surface trihedral

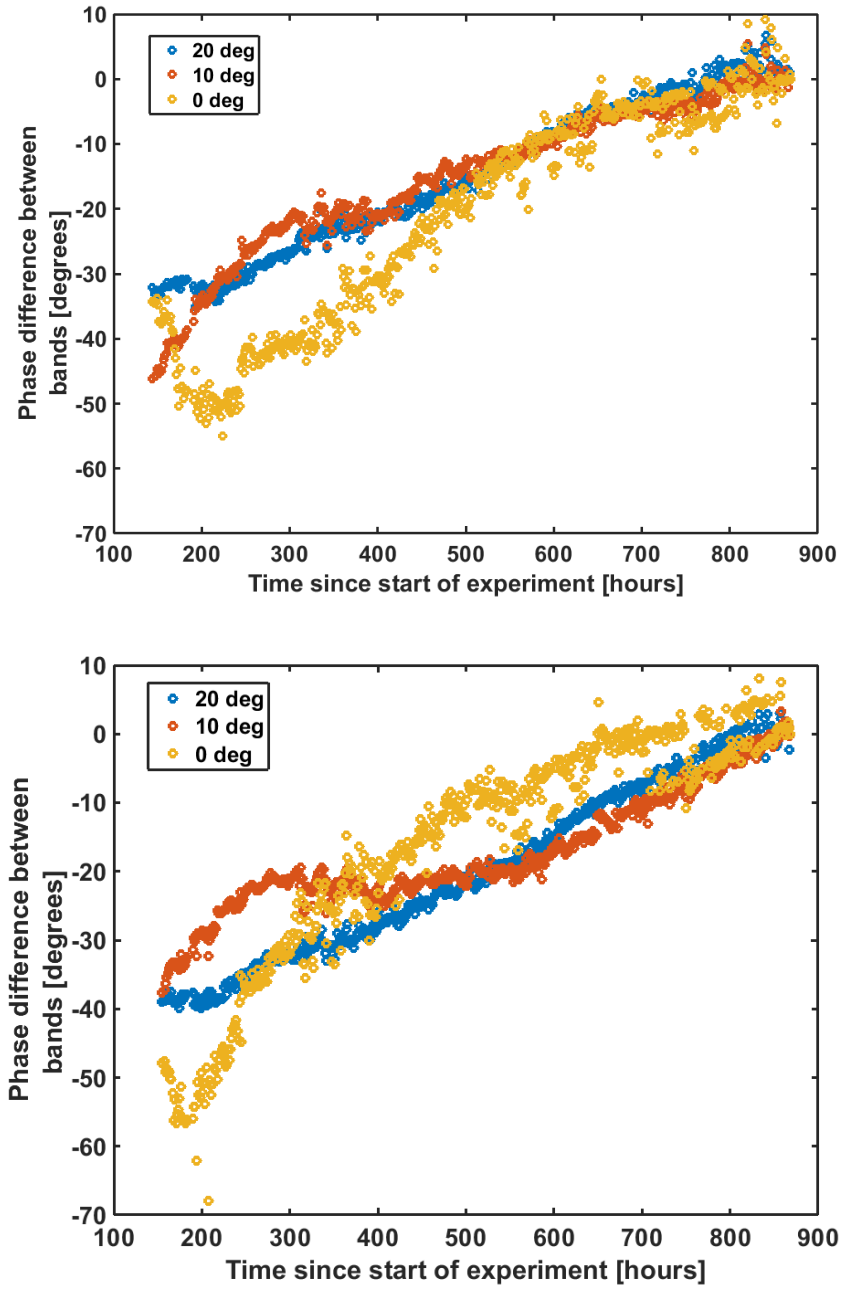

Figure 5.30: Comparison of the phase difference between the two 1GHz sub bands at a range of incidence angles in VV (top) and HH (bottom) polarisation.
In VV Pearson's correlation coefficient is 0.992 at 20° (blue markers), 0.965 at 10° (red markers) and 0.958 at 0° (yellow markers).
In HH Pearson's correlation coefficient is 0.994 at 20° (blue markers), 0.937 at 10° (red markers) and 0.925 at 0° (yellow markers).

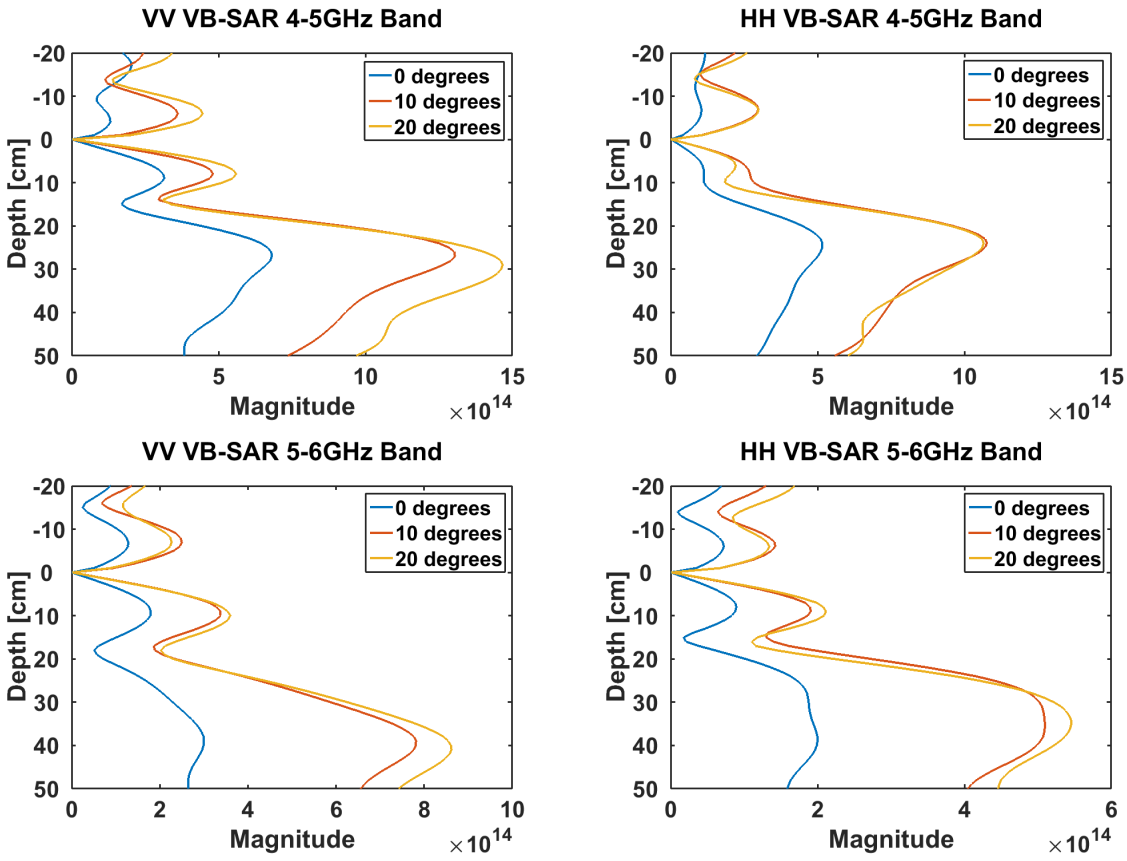

Figure 5.31: Left: VV VB-SAR results obtained by using complex histories and DC subtraction extracted from the 4-5GHz (top) and 5-6GHz (bottom) real frequency band TP stack
Right: HH VB-SAR results obtained by using complex histories and DC subtraction extracted from the 4-5GHz (top) and 5-6GHz (bottom) real frequency band TP stack

These figures show that the VB-SAR process is working correctly across both bands and both polarisations, with the apparent exception of the 5-6GHz band in VV, where the target peak is appearing substantially deeper than expected. Of particular interest is the change in the amplitude of the buried trihedral's response as the incidence angle changes, as could be anticipated the response gets weaker as the incidence angle moves away from 20°. Also significant is the decrease in the amplitude of the buried trihedral across all incidence angles in the upper band compared to the lower band. This effect was expected and is due to the increased sand attenuation at the higher frequency.

5.4.3.2 500Mhz Sub Bands

Using two 1GHz wide frequency bands for TP processing allowed investigation of the effects of sand moisture on the phase seen in the two bands and showed promising results. However, it did not allow thorough investigation of the link between the band in use and the phase response of the buried trihedral as the sand dried; using just two bands and trying to draw a conclusion would be akin to plotting two points and trying to deduce a relationship from them. By using four bands a more meaningful result can be obtained yet the bandwidth, and hence range resolution, is still high enough to resolve the buried trihedral and sand surface separately enabling easy analysis of the buried trihedral's phase history. As previously demonstrated, the trihedral return in VH is poor and so VH results are not shown here.

The extracted phase histories are shown (after correction and unwrapping) in Figure 5.32. As can be seen, the phase change over the sand moisture change generally increases as the centre frequency of the TP reconstruction increases, as would logically be expected due to the decreasing wavelength of the radar wave. Pleasingly, the change in overall phase shift is very similar between bands in VV which supports the wavelength dependency theory. However in HH the changes between bands are slightly less even, further investigation is needed to confirm why this occurs.

By plotting the difference between the phases in the different bands it is possible to derive the relationship between the phase difference and sand moisture. The plots are shown in Figure 5.33.

From a VB-SAR perspective, this change in phase response over a given change in soil moisture would tend to shift the output peak in depth. However, because the VB-SAR processor takes the real centre frequency into account when calculating the virtual frequencies in use and uses a frequency dependent soil model to calculate the soil refrac-

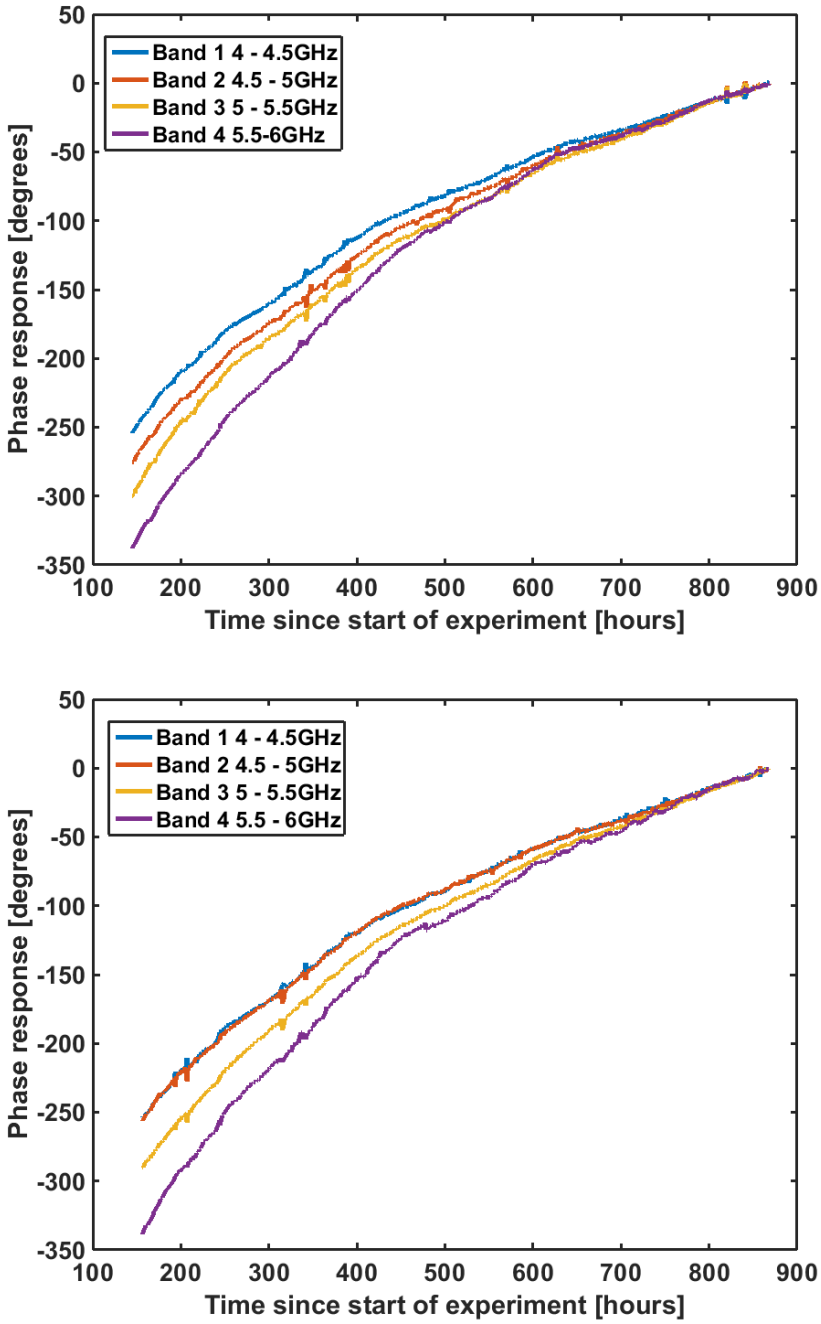

Figure 5.32: Phase history of buried trihedral across the four 500MHz wide bands in VV (top) and HH (bottom). TP reconstruction used 10° incidence angle.

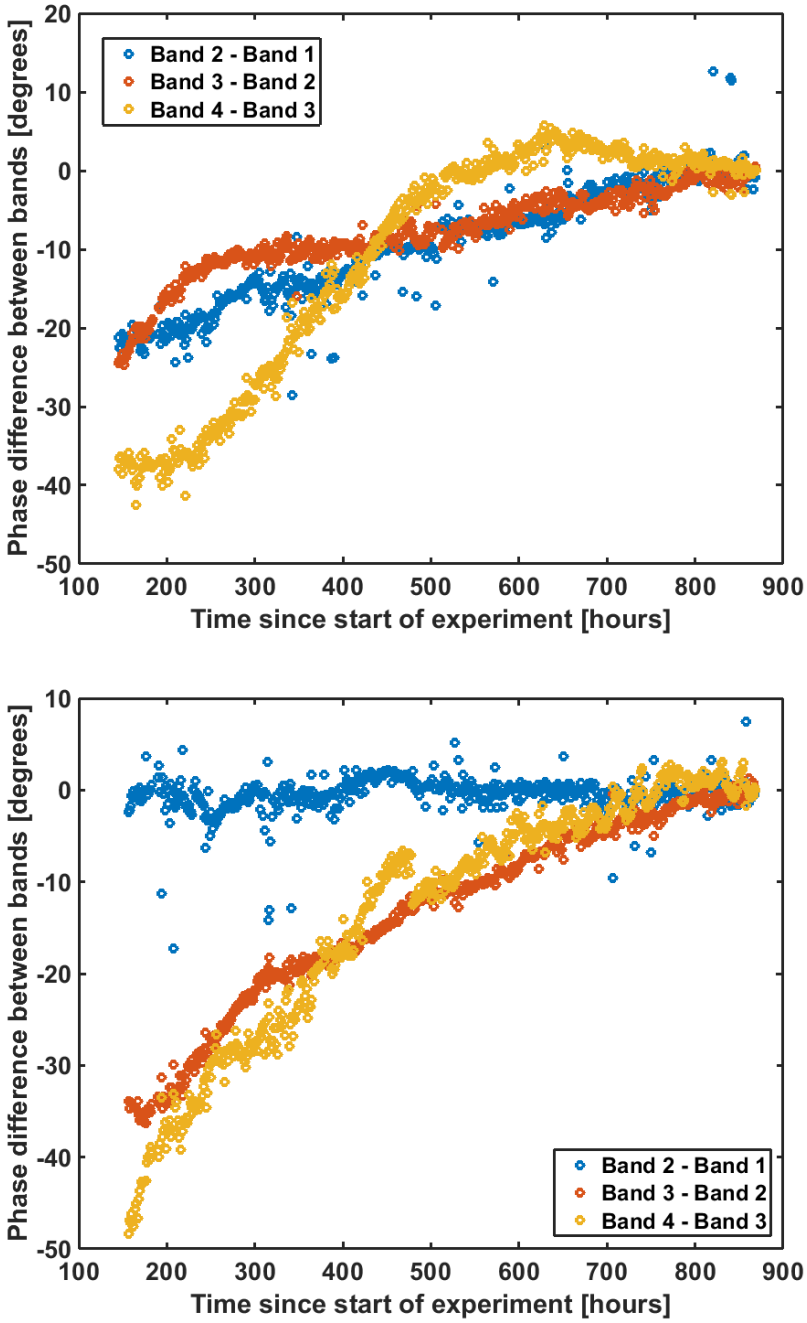

Figure 5.33: Comparison of the phase difference between the four 500MHz sub bands at a range of incidence angles in VV (top) and HH (bottom) polarisation. TP reconstruction used 10° incidence angle.
In VV Pearson's correlation coefficient is 0.963 for the first two bands, 0.935 for the second and third bands and for the third and fourth bands it is 0.904.
In HH Pearson's correlation coefficient is 0.157 for the first two bands, 0.975 for the second and third bands and for the third and fourth bands it is 0.948.

tive index the depth scale will be shifted for the different bands so the output peaks should line up with each other, as is shown in Figure 5.34 which shows the results of applying the VB-SAR process to the phase histories extracted from the 500MHz wide sub bands.

In these depth profiles the VB-SAR processor is working well and placing the buried target's peak response close to its actual depth, indicating that the VB-SAR process as implemented does not show a strong frequency dependency and can be reasonably expected to work across a range of frequency bands.

5.4.3.3 150MHz Sub Bands

After the two and four band VB-SAR demonstration it was realised that a more thorough demonstration of the VB-SAR technique could be performed using multiple, narrower, frequency bands across the real bandwidth. The TP processor created during this project enables easy usage of arbitrary frequency bands and hence is well suited to this investigation. Significantly, by using much narrower real bandwidths the centre frequency of the band used to form the TP images would move substantially between bands and it would give an opportunity to compare VB-SAR results obtained from none adjacent real frequency bands, which would tend to highlight any frequency dependencies of the VB-SAR process.

To this end, the real bandwidth was subdivided into 13 bands each 150MHz wide, continuously covering the range 4-5.95GHz. This produced a freespace range resolution of 1m in each band, which is sufficiently low to merge the surface and buried trihedral returns and allow the VB-SAR process to demonstrate the range resolution enhancement in each band. However, this merging does mean that the buried target's phase response is not directly examinable and so it is not presented here.

The 13 sub bands were processed in VV and HH polarisations at incidence angles of

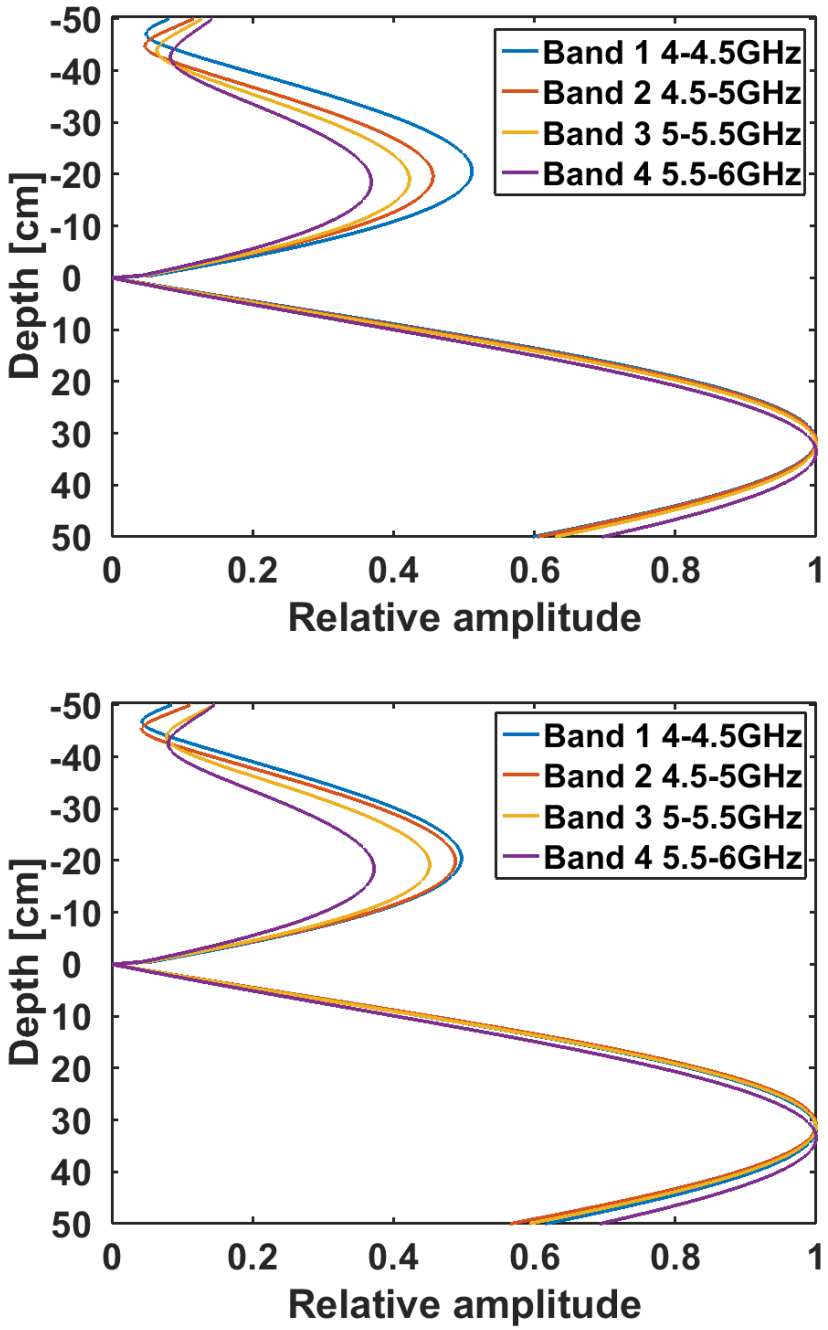

Figure 5.34: VB-SAR depth profiles produced using the phase history of the buried trihedral across the four 500MHz wide bands in VV (top) and HH (bottom). TP reconstruction used 10° incidence angle.

10° and 20° in order to demonstrate the utility of the multispectral technique across two polarisations and two incidence angles. 10° and 20° incidence angles have previously been shown to give good responses from the buried target which gives the best opportunity for examining frequency dependencies, without undue concern about other effects.

The results of this processing are shown in Figure 5.35. In these figures each band has been normalised relative to itself to highlight where the peak response is in each band. As can be seen, the depth of the peak response is generally consistent across bands and reasonably close to the actual depth of the buried target. There does appear to be a systematic error that is making the peak consistently appear slightly below its actual depth. This could be due to sand moisture estimation errors caused by the drying between scans in the period during which the water was being added to the sand or inaccuracies in the Hallikainen soil model used to convert the sand moisture estimates into refractive indices. Such inaccuracy may arise because the Hallikainen model is a general model, rather than one specifically tuned for the sand in use in the GB-SAR laboratory.

5.5 Conclusion

This chapter has presented the experimental work conducted as part of this study.

The basic operation and validity of the VB-SAR scheme has been demonstrated; the scheme both resolves a buried target at the correct depth and enhances the subsurface resolution. The demonstration then moved on to encompass other polarisations and incidence angles, which shows that the usage of the VB-SAR scheme with sidelooking SAR systems is feasible.

Following this, the VB-SAR scheme was applied across a wide range of real bandwidths and centre frequencies. This showed that the VB-SAR scheme would be applicable to bands other than C-band which was used during this study.

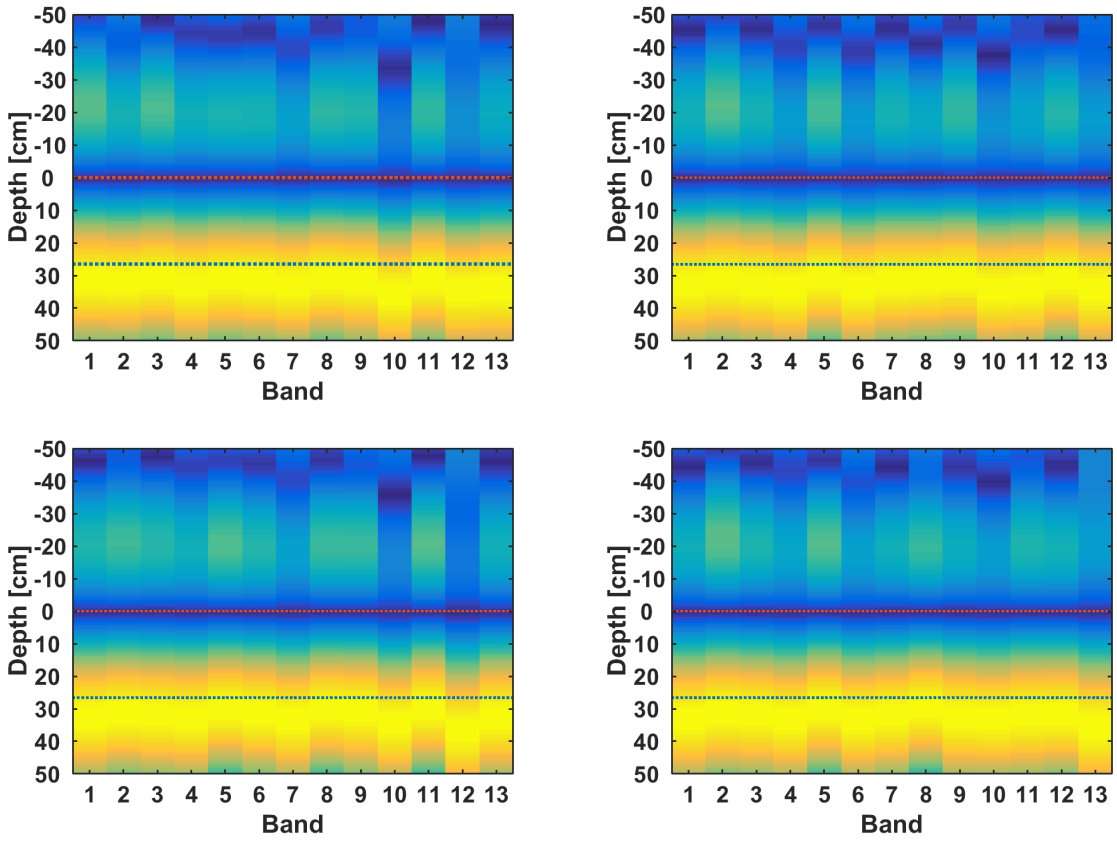

Figure 5.35: Left: Multispectral VB-SAR results obtained using the latter part of the drying period's complex history in VV (top) and HH (bottom) at 10° TP incidence angle. Dashed red line indicates position of ground surface (surpressed using DC subtraction) and dashed blue line indicates 26.5cm
Right: Multispectral VB-SAR results obtained using the latter part of the drying period's complex history in VV (top) and HH (bottom) at 20° TP incidence angle. Dashed red line indicates position of ground surface (surpressed using DC subtraction) and dashed blue line indicates 26.5cm

However, some further work is necessary to rigorously demonstrate the wider applicability of the VB-SAR scheme. The following suggestions are made for future work:

1. Buried targets that respond strongly to cross polarisations should be studied. The work presented here used a buried trihedral which did not present a strong response in cross polarisations and therefore the cross polarisation work was severely limited.

2. Buried targets that present a more consistent return across incidence angles should be considered. An unexpectedly significant incidence angle dependency was observed, both in terms of the extracted phase history of the buried target and the results of the VB-SAR process. Whilst they were not overly significant, it is important to gain a thorough understanding of them and whether they are artefacts of using a buried trihedral or limitations of the VB-SAR scheme.

3. More generally, this work has only used a single buried target and 100% sand soil. An obvious avenue for future work would be to use buried targets buried at differing depths and explore the use of VB-SAR with other soil textures.

Chapter 6

Realworld Considerations

6.1 Introduction

This Chapter considers and explores certain situations which may be encountered during a real-world implementation of VB-SAR.

Firstly, the possibility of operating VB-SAR when absolute SMC information is not available is evaluated. Simulations are presented which explore the feasibility of operating VB-SAR in "detection mode", where the presence of buried targets is indicated, but accurate depth information is not retrieved.

Secondly, the effect of soil texture is explored via simulation. A comparison of VB-SAR simulated with 100% sand and sandy loam is presented, in order to demonstrate the ability of the VB-SAR scheme to work equally well in two different soils.

After this, side-looking VB-SAR is simulated. Whereas the laboratory experiment and simulations previously presented used the TP imaging scheme, any real-world use involving airborne or spaceborne SAR systems would involve side-looking imaging. For this reason, a side-looking situtation is simulated and the results presented. Full 3-D VB-SAR images are presented, along with ground plane images which demonstrate the correct

location of buried targets. The side-looking simulation also includes simulations which use Sentinel-1's imaging parameters, in order to explore whether the VB-SAR process operates correctly given the limitations imposed by a realistic spaceborne radar system.

Next, a brief discussion of the best ground conditions for a realworld VB-SAR deployment is presented.

Finally, the ability of spaceborne systems to detect buried targets is considered and compared, both to other spaceborne systems and a typical airborne SAR systems.

6.2 Detection Mode VB-SAR

As previously discussed, the ideal situation for VB-SAR operation is to have a reliable source of SMC information for each DInSAR image used. In this case, the VB-SAR processor can use the SMC data to reorder the image stack to a consistent SMC increase or decrease (if necessary) and then perform an interpolation step to linearise the SMC trend.

However, it is possible that a reliable source of SMC information will not be available. In this case, it may be possible to operate VB-SAR in a "detection" mode, where reordering and interpolation of the image stack is skipped and the images are fed to the VB-SAR processor in temporal order. Keeping in mind that only subsurface targets are expected to respond to SMC this should still enable separation of surface targets from subsurface targets. However, because the virtual frequency chirp will not be linear it is expected that the response of any buried target will be distorted and the application of a depth scale will not be possible. Nonetheless, such a scheme would still provide at least an indication of the presence or absence of a buried target.

In order to test this, the VB-SAR simulator was setup to simulate a target buried at 26.5cm under a 100% sand soil, with a series of targets placed at 0cm depth to represent

the soil surface. The SMC was varied linearly between 3.5% and 9.5% with 100 equally spaced scans simulated, using 2GHz of bandwidth from 4 to 6GHz. The TP processor was then used to process the first 150MHz of bandwidth at a 10° incidence angle to produce images in which the surface and buried target responses had merged together.

To simulate the situation of unknown and inconsistent SMC over the image stack the images were randomly sorted using MATLAB's randperm() function. This randomised order was then passed through the VB-SAR processor and compared to the non-randomised image stack which contained a consistent shift in SMC. In all cases, the VB-SAR processor was set to assume a linear SMC decrease over the image stack, which meant that no interpolation was performed. The depth scales shown in the results are calculated using this assumed SMC decrease, which does allow accurate placement of the surface.

The results of doing this are shown in Figures 6.1 and 6.2, which show the situation when there is a buried target present and the situation when there is no buried target, respectively. As expected, randomising the image order defocuses the buried target, preventing any estimation of depth or resolution of multiple subsurface targets. What is significant is that the surface is accurately placed and the amplitude away from the surface in the randomised order derived depth profiles is substantially greater relative to the surface amplitude when a buried target is present as compared to when a buried target is not present. This demonstrates that "detection mode" VB-SAR is indeed feasible.

In order to check that these results are not due to simple chance, the VB-SAR processing was repeated with 20 different random image orderings, giving the results shown in Figures 6.3 and 6.4. As can be seen, the absence of a subsurface target results in a very clean depth profile in all cases, whereas the presence of a subsurface target results in a much more cluttered depth profile.

To show the effect of detection mode SAR across an entire VB-SAR image, the four images shown in Figure 6.5 were produced. The upper pair of images, show the results

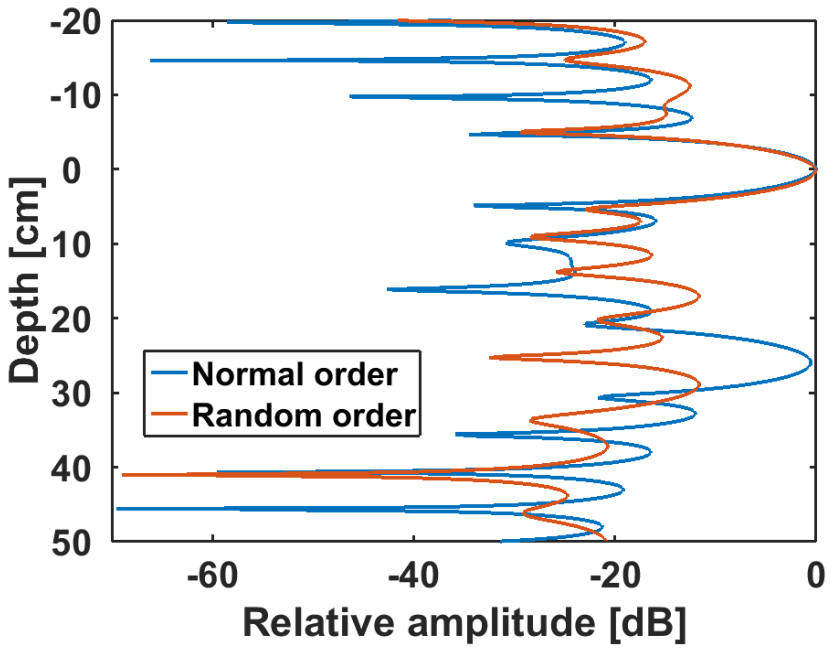

Figure 6.1: Comparison of VB-SAR depth profiles of a region containing a buried and a surface target produced with and without accurate SMC knowledge. Normal order shows the result of accurate SMC information, random order represents unknown and inconsistent SMC trend by randomising the scan order prior to VB-SAR processing.

of known SMC and unknown SMC VB-SAR processing with no DC subtraction. As expected, the known SMC processing gives a very well formed subsurface image, whereas the unknown SMC processing results in a smeared subsurface image that appears rather dim compared to the surface responses. By applying DC subtraction to remove the ground returns the lower pair of images were formed. The subsurface image in the known SMC case has not been substantially improved, but in the unknown SMC case it is now immediately obvious in which columns the buried target appears.

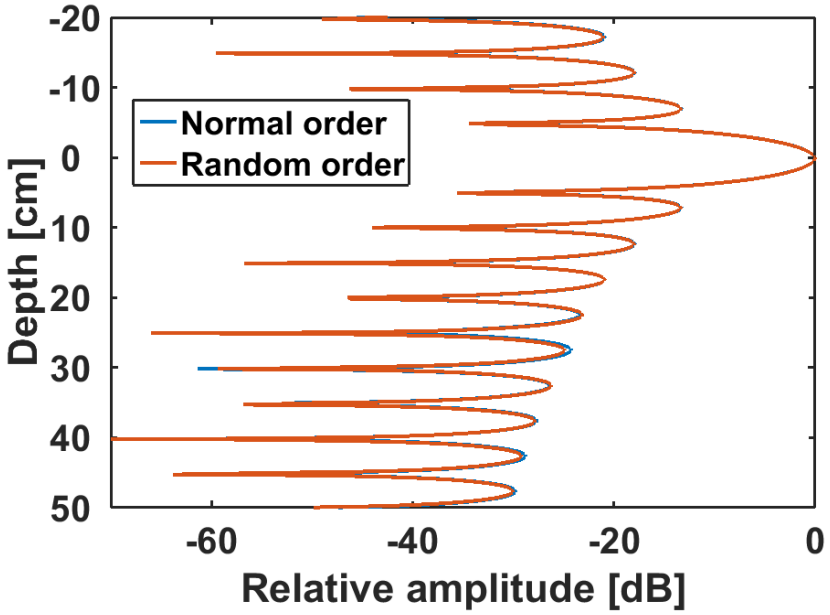

Figure 6.2: Comparison of the depth profiles of a region containing only a surface target produced with and without accurate SMC knowledge. Normal order shows the result of accurate SMC information, random order represents unknown and inconsistent SMC trend by randomising the scan order prior to VB-SAR processing.

6.3 Soil Texture Effects

All the simulated scenes presented so far in this chapter have used soil consisting of 100% sand. Obviously in the real world many other soils would be encountered and hence it is vital that the VB-SAR process can handle different soils successfully. As a test, an example soil from [17] ("Field 1", described as "Sandy Loam" consisting of 51.51% sand and 13.43% clay) was used with the simulator and the same targets as used to produce Figure 4.18, which when processed with the TP imager using a real bandwidth of 150MHz and the resulting complex histories fed to the VB-SAR processor gave the results shown in the upper part of Figure 6.6. Comparing the two plots shows that the buried targets and the surface have been resolved at the correct depth in both plots. However, the target responses show increased levels of distortion in the Sandy Loam soil. This is due to

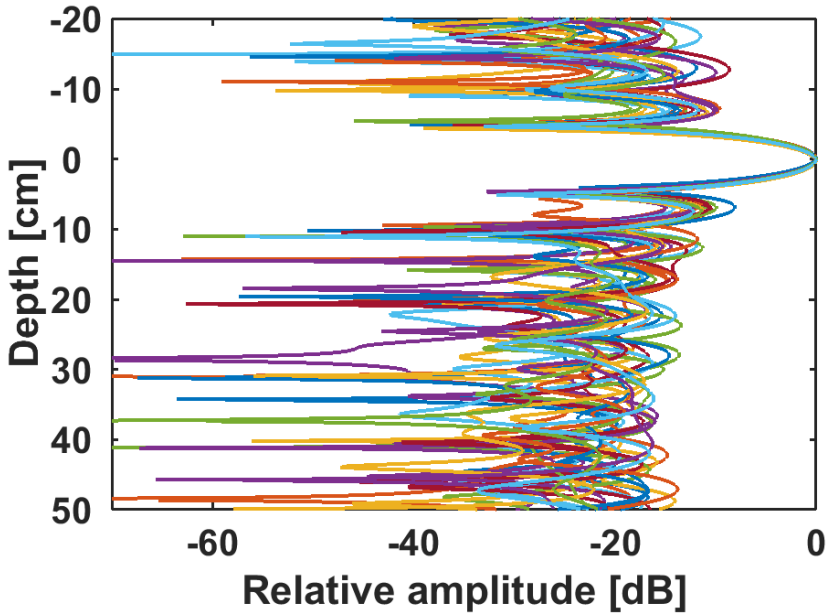

Figure 6.3: Depth profiles of a region containing a buried and a surface target produced from 20 unique reorderings of the image stack prior to VB-SAR processing.

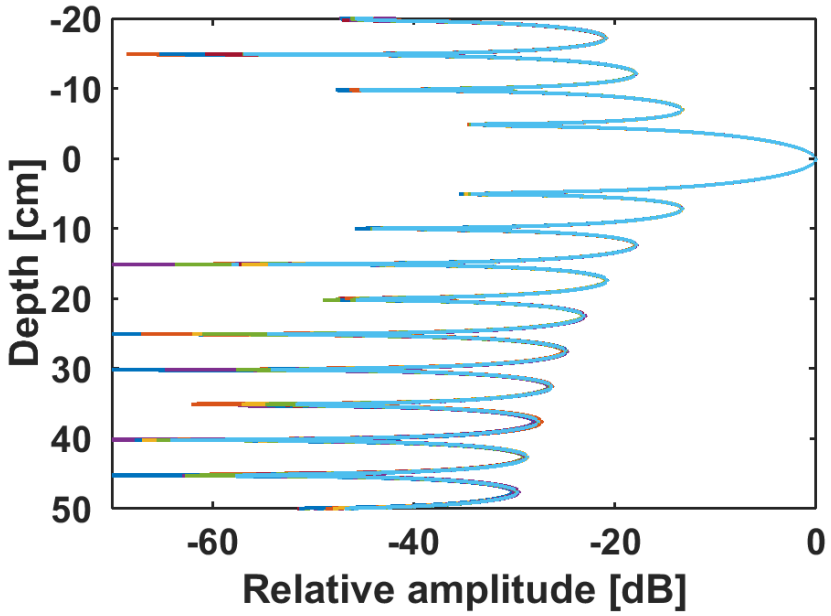

Figure 6.4: Depth profiles of a region containing only a surface target produced from 20 unique reorderings of the image stack prior to VB-SAR processing.

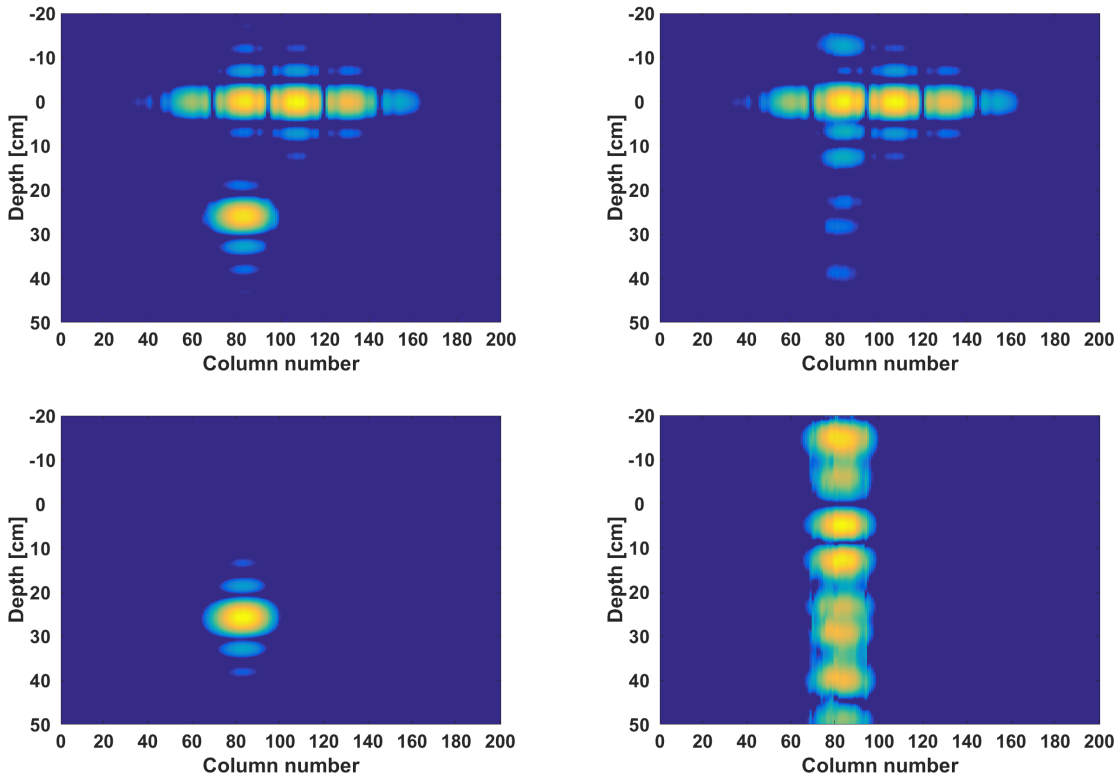

Figure 6.5: Demonstration of detection mode VB-SAR
Upper left: VB-SAR image produced with known, linear SMC trend
Lower left: VB-SAR image produced with known, linear SMC trend with DC subtraction enabled to remove the surface response
Upper right: VB-SAR image produced with randomised image stack
Lower right: VB-SAR image produced with randomised image stack with DC subtraction enabled to remove the surface response

this soil's refractive index being less sensitive to SMC changes than the 100% sand soil, leading to a decreased virtual bandwidth for a given SMC change.

The decrease in refractive index shift can be confirmed by reproducing Figure 4.14 using the Sandy Loam. This reproduction is shown in Figure 6.7 and as can be seen the phase shifts across time have decreased in all bands compared to those seen in the 100% sand soil. This confirms the decrease in refractive index change and hence the decrease in VB-SAR resolution.

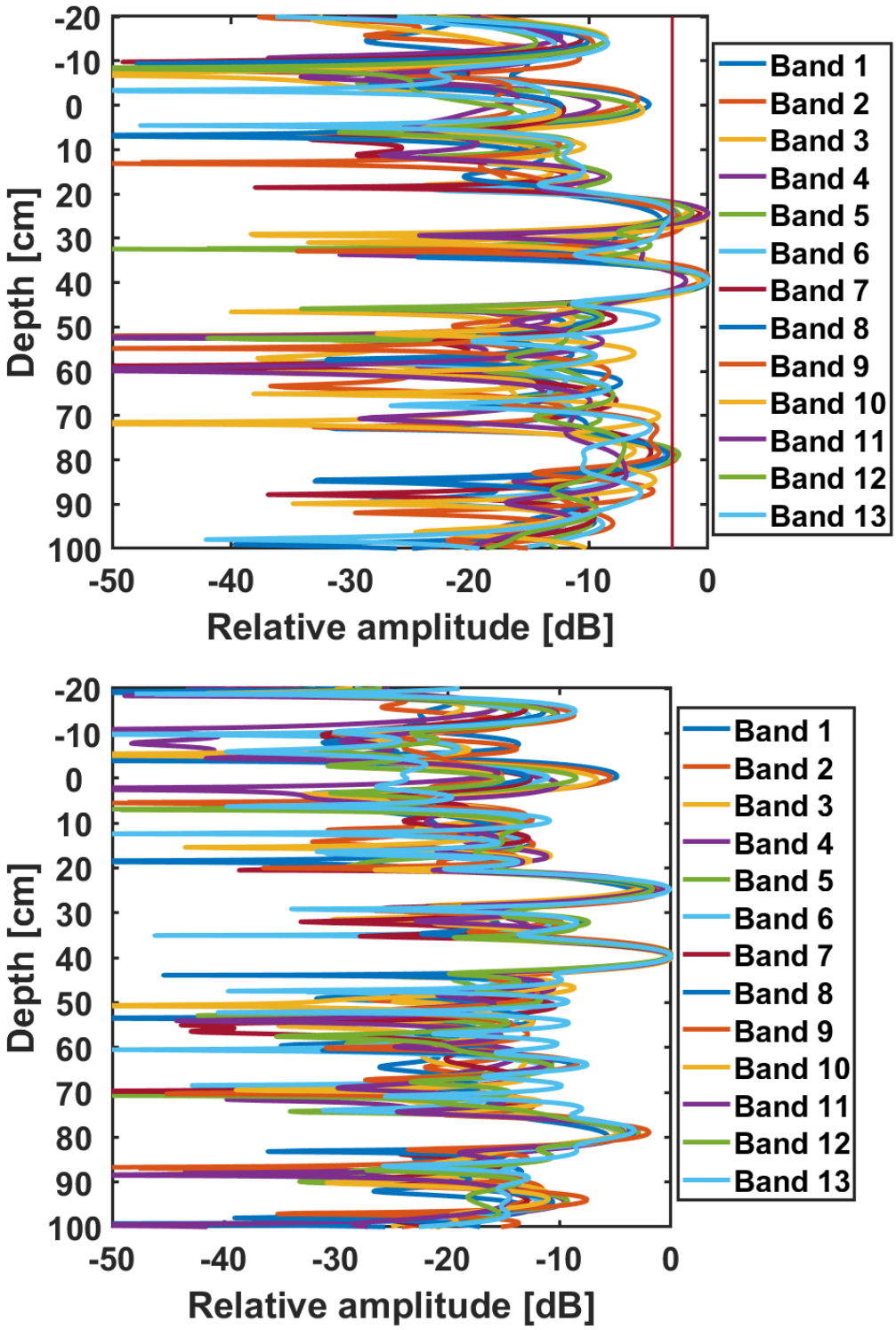

Figure 6.6: Results of the VB-SAR processor using the phase histories extracted from a scene with a vertical stack of three buried targets processed at low TP resolution.
Top: Buried targets placed at 25, 40 and 80cm below the soil surface, soil consists of 51.51% sand and 13.43% clay.
Bottom: Buried targets placed at 25, 40 and 80cm below the soil surface, soil consists of 100% sand. (Rescaled reproduction of Figure 4.18, presented for convenience of reader)

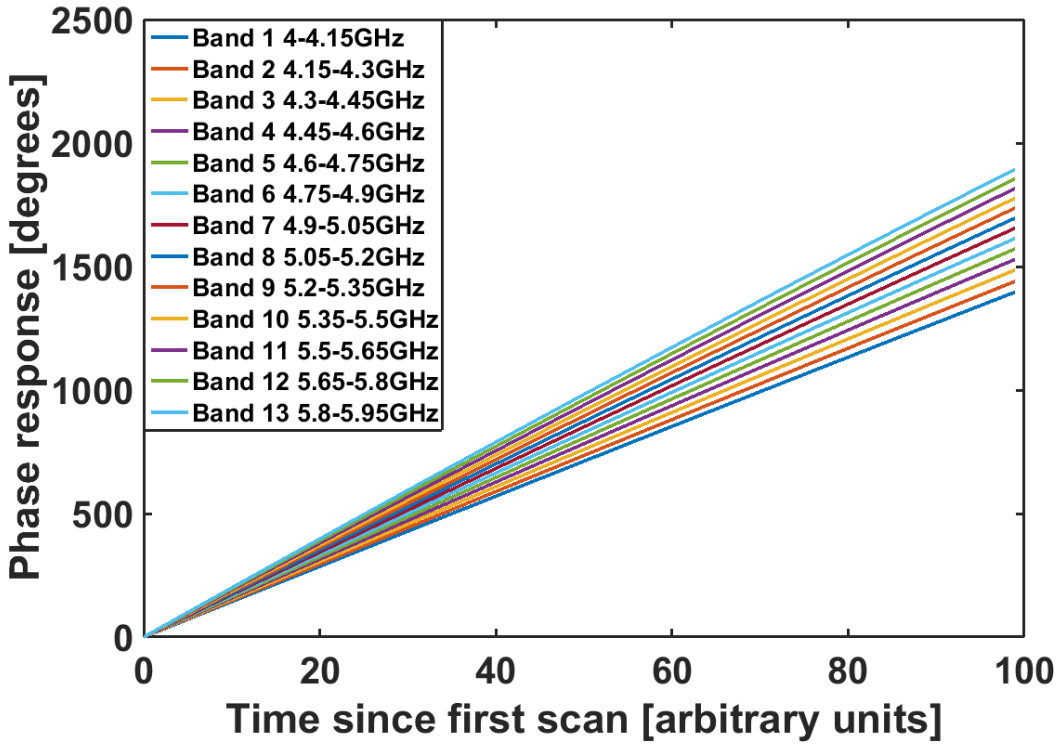

Figure 6.7: Phase histories extracted from 150MHz TP images from the VB-SAR simulator, containing a single target buried under 26.5cm of soil consisting of 51.51% sand and 13.43% clay.

6.4 Side-looking VB-SAR Simulation

The simulation and experimental results shown so far have all been based around the trough scanner geometry, namely a geometry whereby the antenna's real beam points towards the ground under the direction of motion. In contrast to this, real world airborne and spaceborne systems are configured so that their antenna's real beam points towards the ground in the direction perpendicular to the direction of flight. In this situation, the beam is side-looking which presents a 3-D problem. To this end, the SAR simulator and backprojection processor were reconfigured to operate in side-looking mode in order to investigate the effects of a side-looking radar on the VB-SAR process.

As detailed in Chapter 4, the SAR simulator is capable of modelling the side-looking

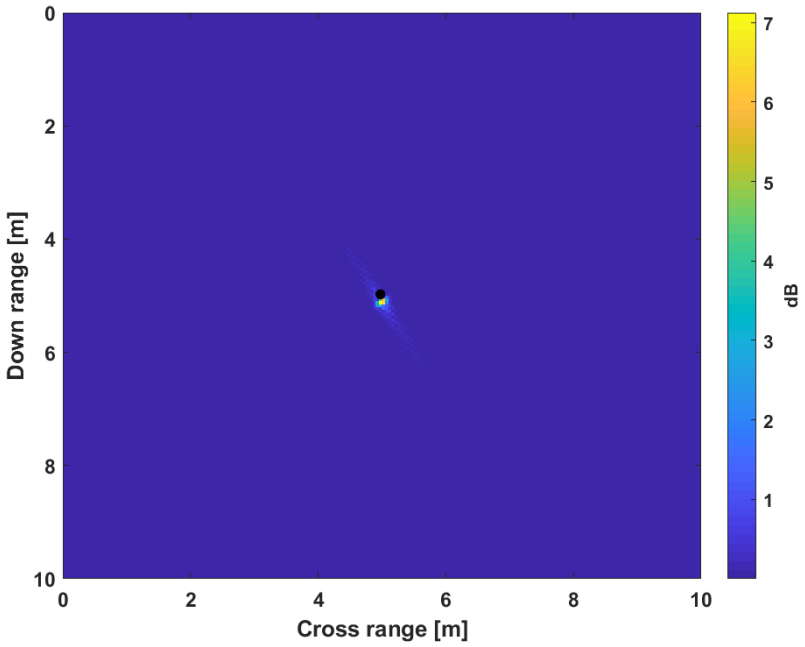

Figure 6.8: Example output from SAR simulator operating in side-looking mode with a full 2GHz bandwidth (4 to 6GHz). Target positioned at (2, 2, -0.265). Black dot placed at (2, 2, 0); note subsurface target displays down range migration.

case by using the 3-D Snell's law solver presented by [100]. Coupled with the backprojection processor which handles side-looking SAR image processing full side-looking SAR simulation is possible. An example image produced by the simulator, showing four surface targets and a single buried target is shown in Figure 6.8. As can be seen, the buried target has migrated down-range. This is due to the extra phase added by the subsurface path being interpreted by the backprojection processor as being due to a surface target further away from the radar platform.

From this scene the phase response of the buried target was extracted and compared to that extracted from a target buried at the same depth under the same soil in the trough scanner geometry. This comparison is shown in Figure 6.9. As can be seen, the side-looking SAR case shows a slightly increased phase shift over the trough scanner geometry, this is due to the ray's path through the soil being longer due to it being angled relative to

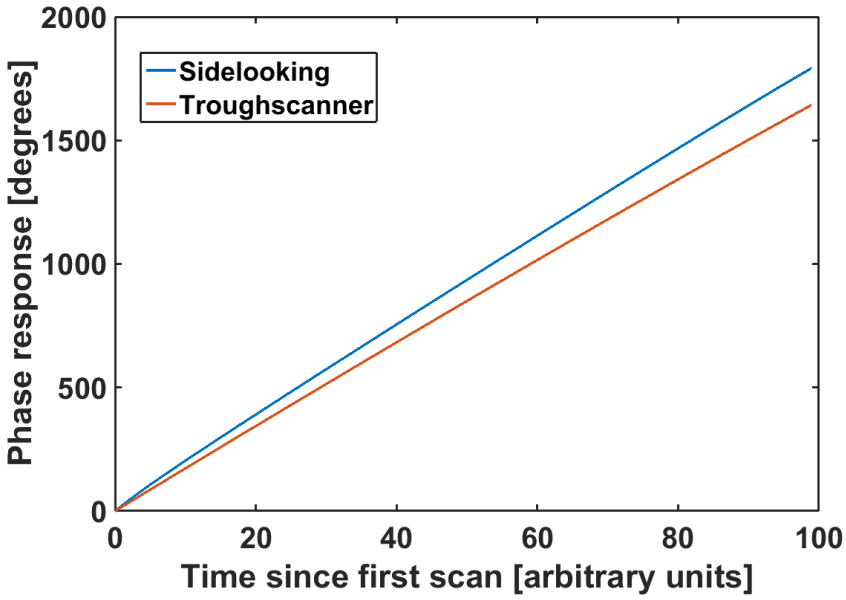

Figure 6.9: Comparison between the phase history of a target buried under 26.5cm of Field 1 soil when imaged using the trough scanner geometry and side-looking SAR geometry.

the normal in two dimensions, rather than just one dimension as per the trough scanner. This will have the effect of making the buried target appear slightly deeper in the VB-SAR depth profile than it actually is.

To illustrate this, a comparison of the VB-SAR depth profile produced from the trough scanner geometry and side-looking SAR geometry is shown in Figure 6.10. As can be seen, as expected the side-looking geometry produces a slighter deeper response for the buried target due to the increased path length through the soil.

At this point, the full 2GHz real bandwidth of the simulator can be divided into the same 150MHz sub-bands previously used in order to demonstrate the range resolution improvement of the VB-SAR process. An example side-looking SAR image formed with this restricted real bandwidth is shown in Figure 6.11. Compared to the image formed with the full 2GHz bandwidth (Figure 6.8), it is clear that this image displays substantially lowered range resolution.

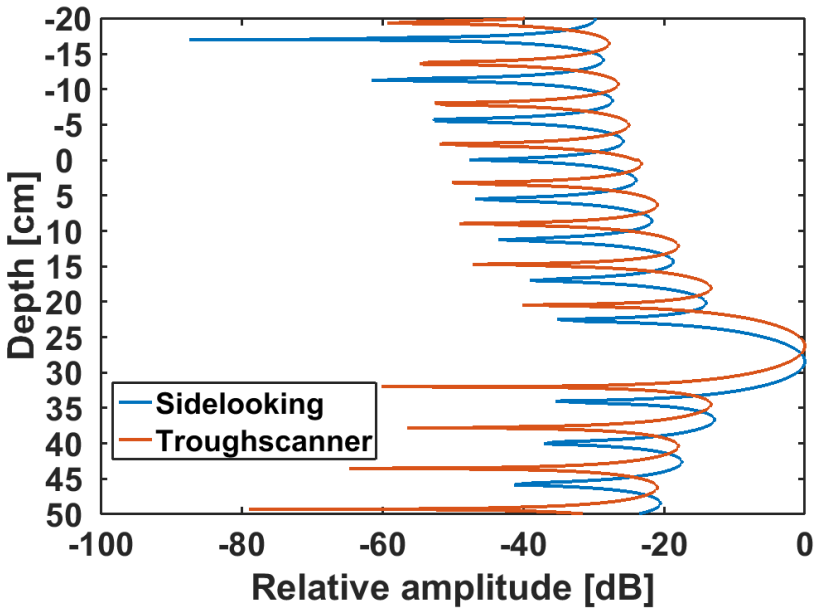

Figure 6.10: Comparison between the VB-SAR depth profiles of a target buried under 26.5cm of Field 1 soil produced using trough scanner geometry and side-looking SAR geometry.

By performing VB-SAR on each pixel within the SAR image sets it is possible to build up a 3-D subsurface image, in a similar fashion to the production of the 2-D VB-SAR images previously shown. For this work, 4 additional targets were placed on the surface of the soil to ensure that targets at zero depth are resolved correctly. Taking the SAR images formed with the full 2GHz resolution first, the results of this process are shown in Figure 6.12. As with the single SAR image shown in Figure 6.8, the buried target's response has moved down range of the actual position of the target. It may be possible to correct for this by applying a shearing operation to the 3-D image, the necessary shear calculated using the imaging geometry and the average refractive index of the soil over the image stack. As can be seen, the VB-SAR process has successfully resolved the buried target's depth and placed the surface targets at the correct positions.

The next step taken was to use the 150MHz bandwidth SAR images and apply the

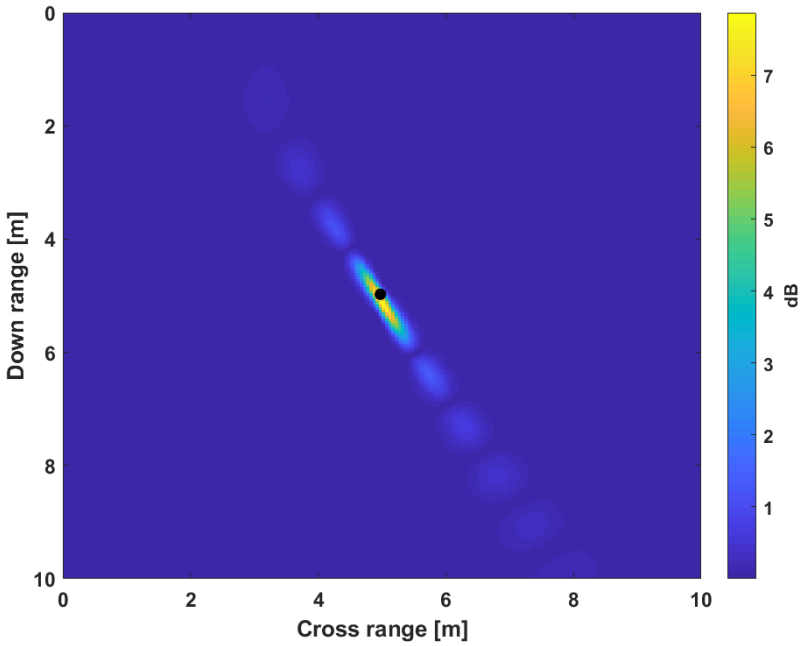

Figure 6.11: Example output from SAR simulator operating in side-looking mode with a restricted 150MHz bandwidth (4 to 4.15GHz). Target positioned at (5, 5, -0.265). Black dot placed at (5, 5, 0); note subsurface target displays slight down range migration.

VB-SAR process to them. For brevity, only three sub bands are presented here. The resulting VB-SAR images are shown in Figure 6.13. It is immediately noticeable that the reduced bandwidth has caused the surface targets to elongate as expected due to the reduced resolution. As per the 2GHz bandwidth case previously shown, the buried target has been resolved at the correct depth and its response has moved slightly down range of the target's actual position. Compared to the surface target responses, the buried target displays an improvement in both depth and down range resolutions. This comes about because the VB-SAR process gives an improvement to the slant range resolution which in this case is not vertical.

In order to test the theory that the down range migration of the buried target was caused by refraction at the air-soil interface a second 3-D VB-SAR simulation was run, with three buried targets. These were placed at 25, 40 and 80cm below the surface. The expected

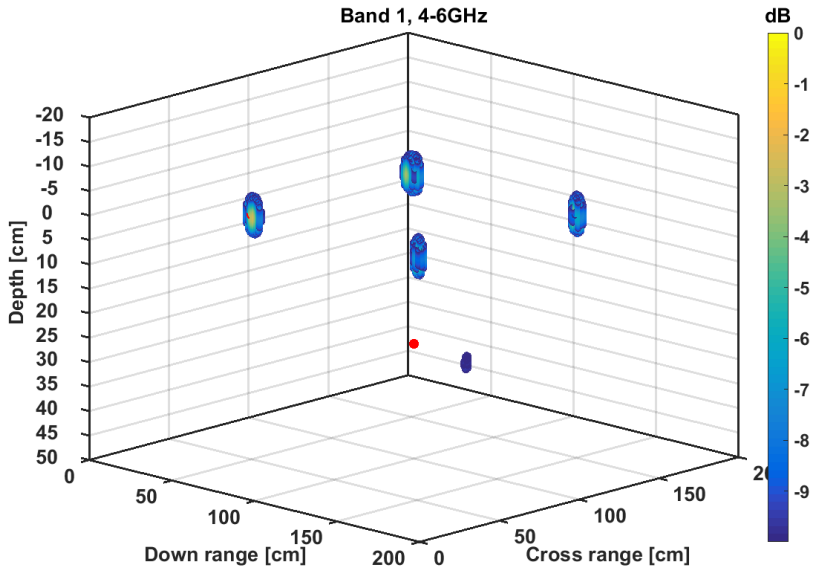

Figure 6.12: 3-D VB-SAR image formed using the SAR images formed with the full 2GHz bandwidth. Buried target positioned at (2, 2, -0.265). Red dots placed at the actual target positions; note subsurface target displays down range migration.

symptom of the migration being caused by refraction is that all buried target responses will be shifted down range by a distance proportional to depth, i.e. the responses will lie along a straight line. This would enable correction via an image shear.

The result of 3-D VB-SAR processing using SAR images produced using the full 2GHz bandwidth is shown in Figure 6.14. This image strongly supports the theory that the down range migration of buried targets is caused by refraction at the soil surface as all three buried targets lie in a straight line at an angle to the surface. In addition, all targets are resolved at the correct depth.

Again, the 150MHz sub bands were also explored and the results from three bands (1, 7 and 13) from across the total spectrum are shown in Figure 6.15. These bands perform as expected, though it is more difficult to see the straight line through all buried targets as the lowered real bandwidth has caused the targets to spread in the down range distance.

This refraction influence is similar to the situation seem during TP imaging when an

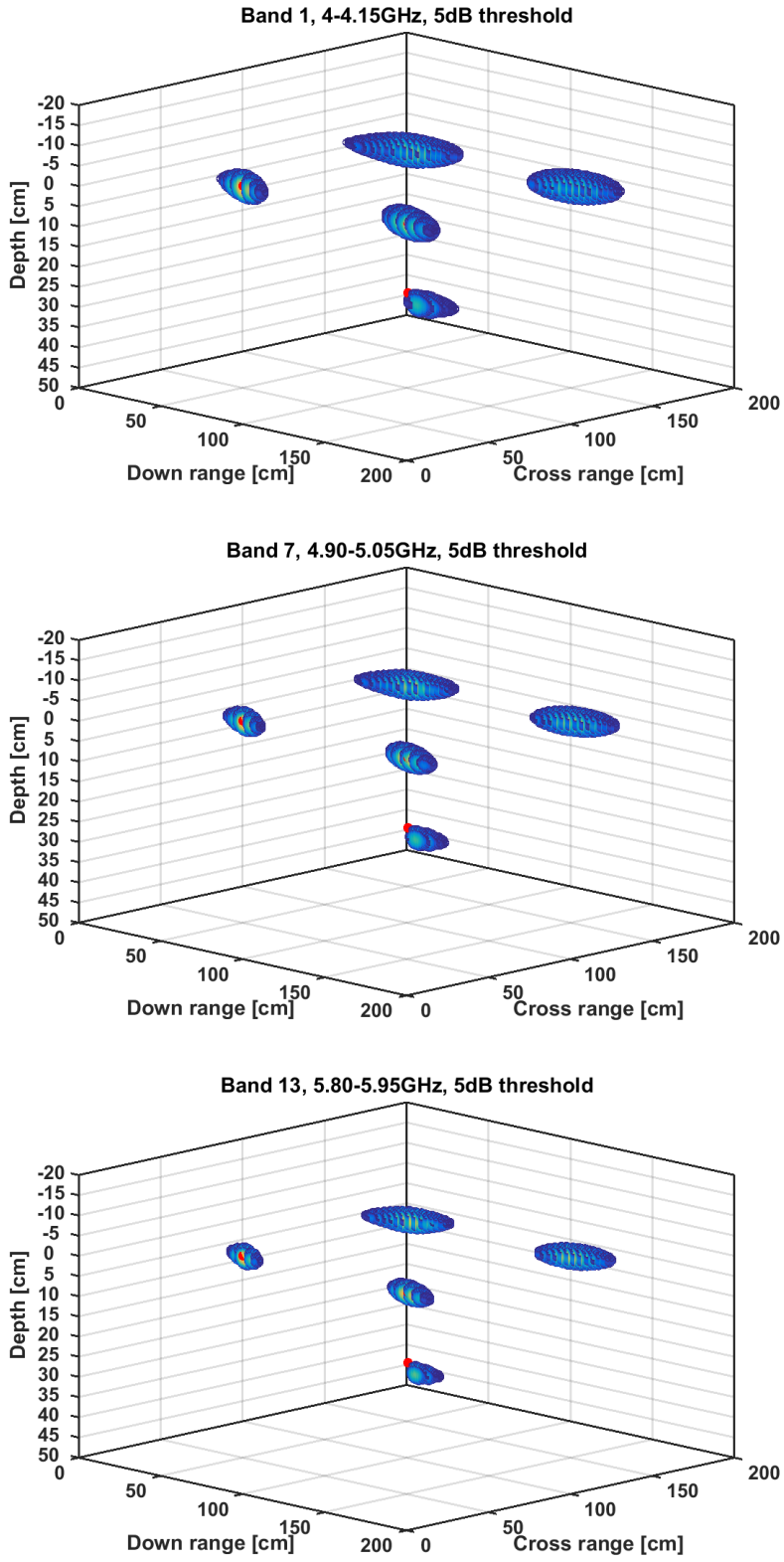

Figure 6.13: 3-D VB-SAR image formed using the SAR images formed with the first 150MHz wide band (4-4.15GHz) (top), seventh 150MHz wide band (4.90 - 5.05GHz) (middle), thirteenth 150MHz wide band (5.80 - 5.95GHz) (bottom). Buried target positioned at (2, 2, -0.265). Red dots placed at the actual target positions.

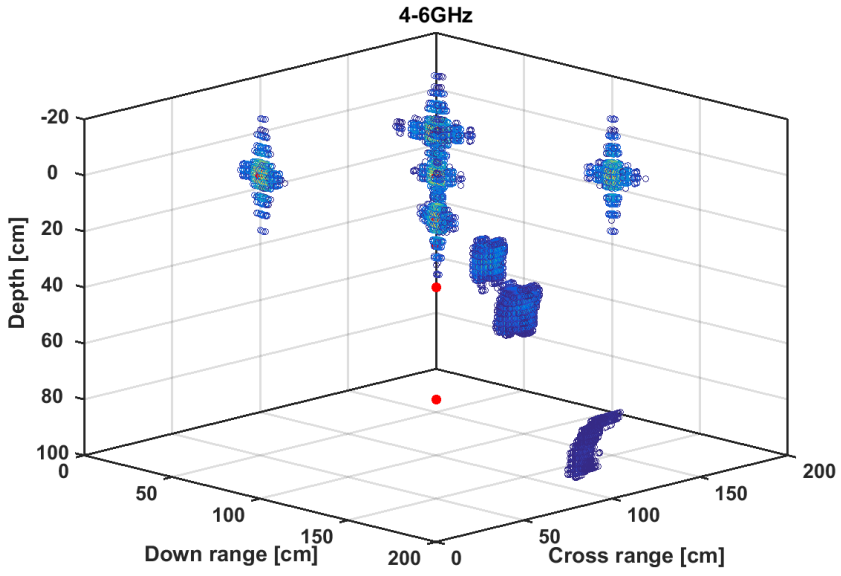

Figure 6.14: 3-D VB-SAR image formed using the SAR images formed with the full 2GHz bandwidth. Buried targets positioned at (2, 2, -0.25), (2,2,-0.40) and (2,2,-0.80)m. Red dots placed at the actual target positions; note subsurface targets display down range migration.

image is skewed due to the imaging algorithm assuming a vertical beam when an angled beam is in use. It should be similarly possible to correct for this by applying a shear to the subsurface volume in the down range direction. The shear needed would be calculated using the average refractive index of the soil over the series of images and the incidence angle, which is calculated using the true ground position of the buried targets and the imaging geometry, to calculate the angle of transmission.

6.5 Satellite Simulation

As shown in the previous section, a buried target imaged by a side-looking SAR shows a slight increase in phase shift over a given change in SMC when compared to the trough scanner geometry used to demonstrate VB-SAR in the laboratory. This effect presents a

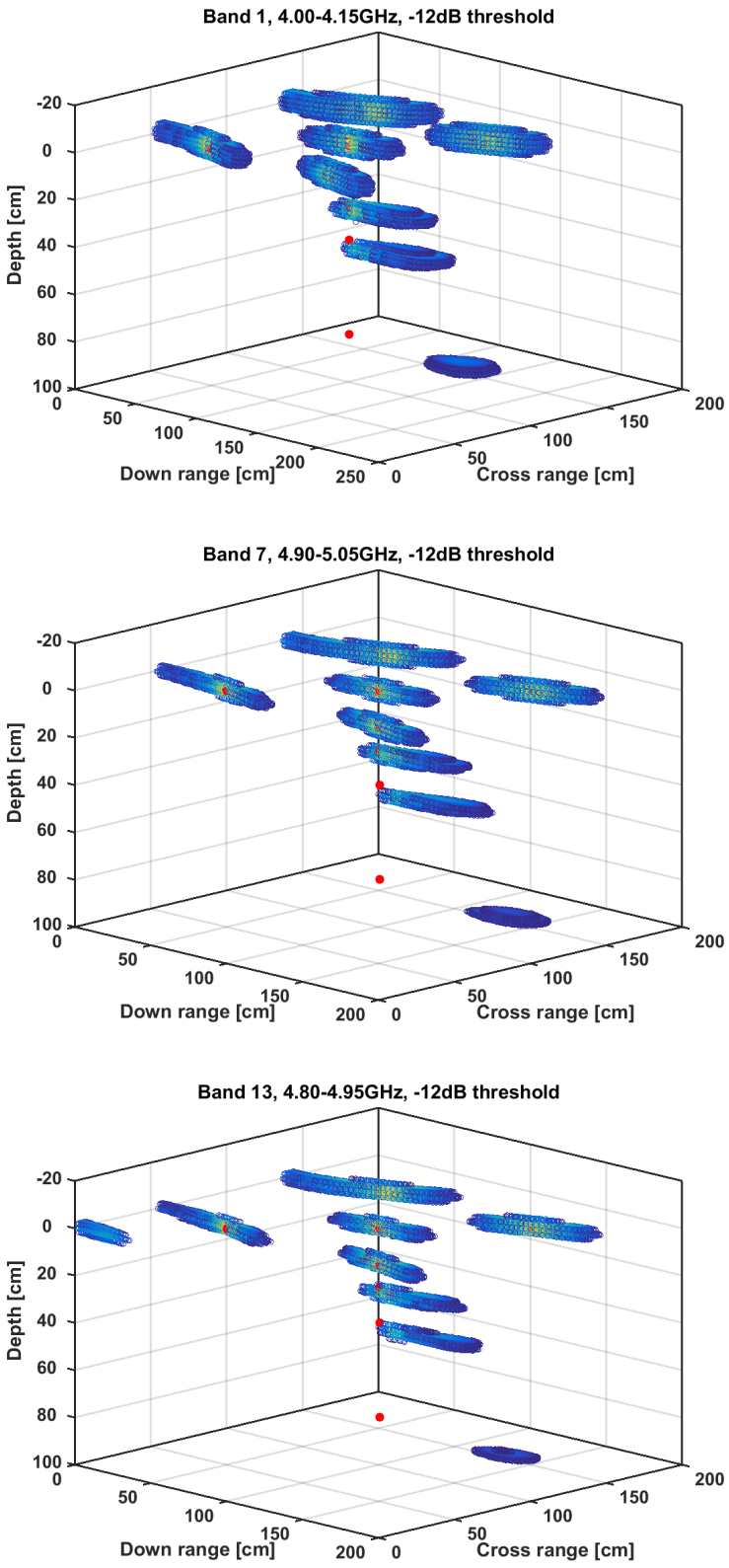

Figure 6.15: 3-D VB-SAR images formed using the SAR images formed with the first 150MHz wide band (4-4.15GHz) (top), seventh 150MHz wide band (4.90 - 5.05GHz) (middle), thirteenth 150MHz wide band (5.80 - 5.95GHz) (bottom). Buried targets positioned at (2, 2, -0.25), (2,2,-0.40) and (2,2,-0.80)m. Red dots placed at the actual target positions; note subsurface targets display down range migration.

Platform height	693km
Ground range	385.7km
Incidence angle	29.1 °
Centre frequency	5.405GHz
Chirp Bandwidth (derived from range resolution equation)	7.5MHz
Resolution	20x22m
Pixel Spacing	10x10m
PRF	3000Hz
Platform speed (derived from orbital mechanics)	7.51km/s
Pulse spacing (derived from PRF and platform speed)	2.50m
Number of pulses (derived from cross range resolution equation)	401

Table 6.1: Simulation parameters used for the Sentinel-1 simulation

concerning problem; potentially it could lead to inaccurate location of subsurface objects. In order to investigate this issue, the simulator was reconfigured away from a "laboratory" situation (radar close to target scene, target scene on the order of a few square meters and high bandwidth in use) to a typical Sentinel-1 High resolution L1 GRD IWS configuration, detailed in Table 6.1.

This new imaging geometry required some modifications to the SAR simulator. As detailed in Section 4.5.1, the SAR simulator solves for the point of refraction at the ground surface by constructing a vector containing all possible solution points between the platform and buried target. The spacing of the solution points is specified by the user and this spacing should be much smaller than the pixel spacing in use (a factor of 10 being a good rule of thumb). In this case, the spacing should be 1m, which leads to a huge number of points in the vector, leading to very slow simulations. By realising that the point of refraction should always be closer to a shallow buried target than the ground position of the remote radar platform it is possible to put a restriction on the region to search; a restriction of within 200m from the buried target's ground location is more than adequate to account for all possible situations and enables rapid simulation.

The other modification is to have the SAR simulator and backprojection processor

make use of differential ranges relative to the range to the centre of the imaging scene. This has the effect of shifting the imaging scene back to the antennas, so that a very large unambiguous range (and hence a very large number of frequency points which is computationally intensive) is not necessary.

The soil and moisture parameters used were the same (51.51% sand, 13.43% clay and a moisture range of between 9.6 and 3.55%) as for the previous simulations. For the first test, a single target was buried in the centre of the scene at a depth of 25cm and four targets were placed on the soil surface. The VB-SAR process applied was the same as previously used, each pixel's phase and amplitude history was used to generate a vertical depth profile for that pixel. The VB-SAR processor used each pixel in turn to produce a complete 3-D subsurface image. Amplitude thresholding and MATLAB's scatter3() function were then used to produce a point cloud type image. The results of this first simulation are shown in Figure 6.16. As can be seen, the surface and subsurface targets still line up well with their actual positions despite the vastly increased ground range to the scene and radar platform height over previous simulations.

Sentinel-1's IWS mode produces 250km-wide (in the down range direction) swaths. In order to check that the VB-SAR process produces valid results at the extremes of these swaths a repeat of the first Sentinel-1 simulation was performed with an additional 247km of ground range distance added to the edge of the imaging scene. The results of the near and far-swath edge simulations are shown in Figure 6.17. As can be seen, the two images are almost identical, demonstrating the consistent behaviour of the VB-SAR scheme over the entire swath width.

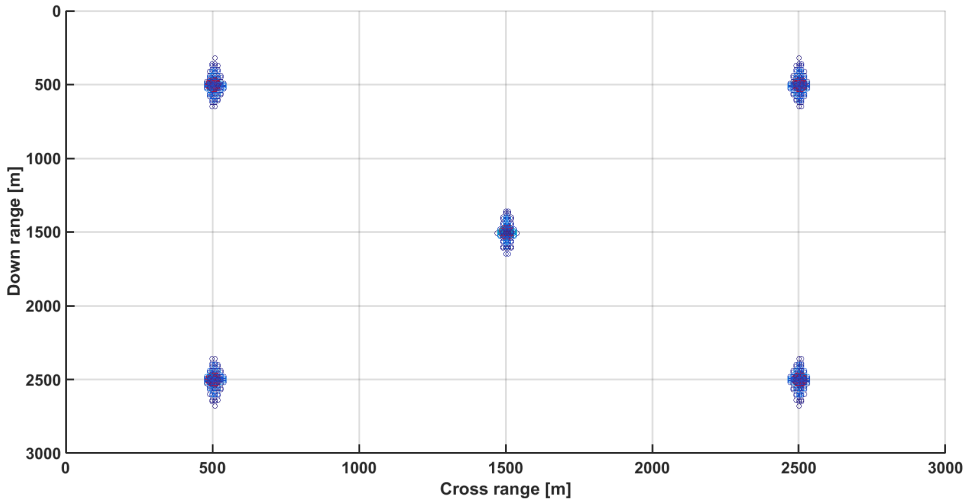

Figure 6.16: Groundplane VB-SAR image formed using the SAR images formed with the Sentinel-1 simulation parameters. Buried target positioned at 25cm below the soil surface. Actual positions of targets denoted by solid red markers.

6.6 Climatic Considerations

As previously detailed, the VB-SAR process requires a change in SMC in order to produce subsurface radar images. Whereas in the laboratory and small scale experimentation changes in SMC can be easily created and controlled, any large scale real-world VB-SAR deployment would need to use naturally occurring SMC variations.

Certain areas of the Earth's surface are better suited to VB-SAR than others. Very dry areas such as desert present very poor conditions for VB-SAR, as the SMC is consistently very low. This means that the virtual bandwidth would be very small and therefore subsurface resolution would be poor. Similarly, areas where SMC is expected to be high (for instance, tropical areas) would provide poor data for VB-SAR as the soil attenuation would likely be very high, hindering the ability of the radar system to detect buried targets.

Areas with large amounts of vegetation cover also present challenges for accurate

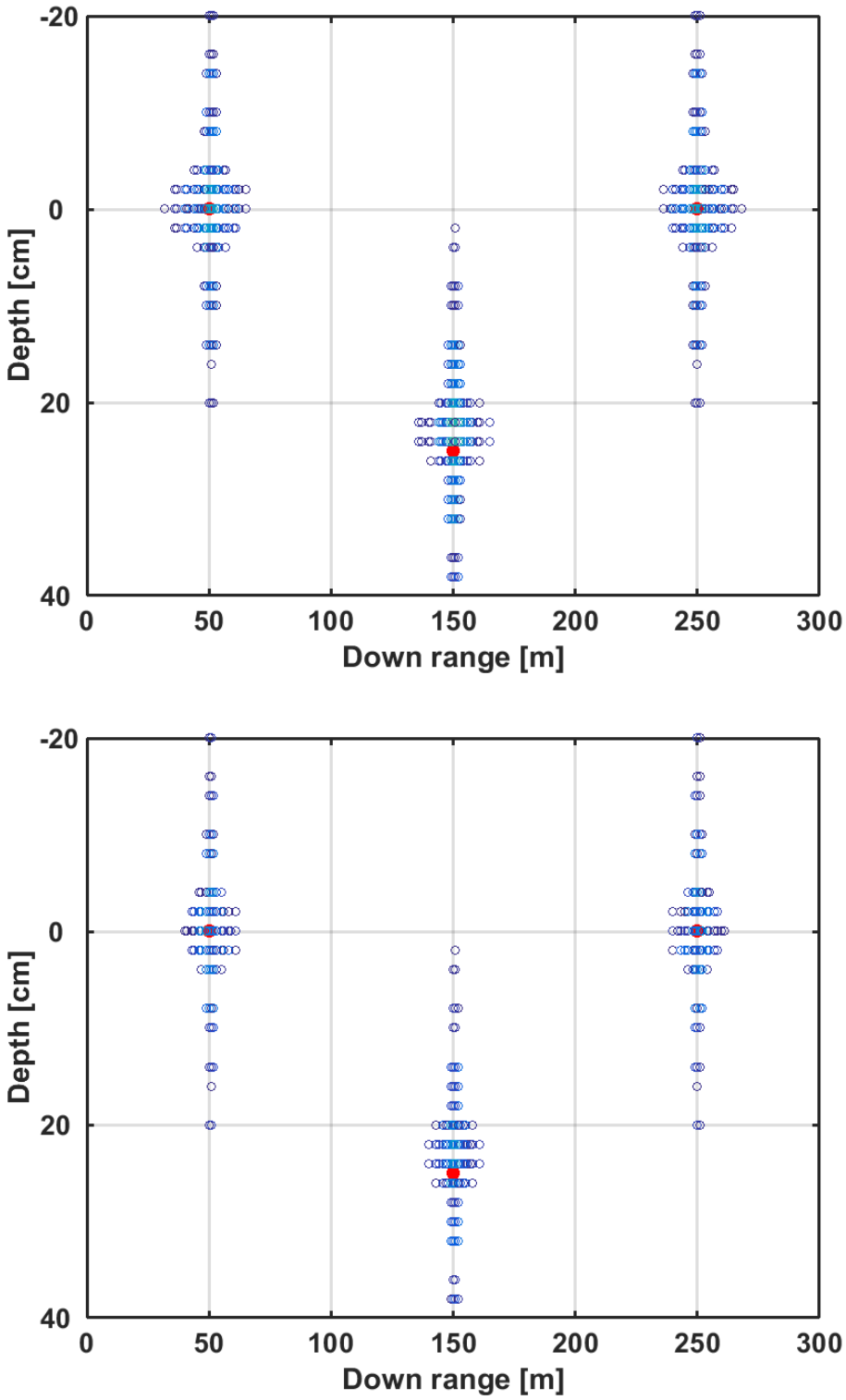

Figure 6.17: 2-D VB-SAR image formed using the SAR images formed with the Sentinel-1 simulation parameters at the near (top) and far (bottom) edges of the IWS mode imaging scene. Buried target positioned at 25cm below the soil surface. Actual positions of targets denoted by solid red markers.

VB-SAR imaging. The amount of vegetation in a given scene is likely to vary over the course of a year. This would present an additional moisture change over the SMC change. As VB-SAR assumes that the soil surface experiences zero moisture change, vegetation moisture variations would cause the surface return to appear below the surface level in the VB-SAR depth profile. Similarly, it would also cause the returns of subsurface targets to appear deeper than the targets actually are.

Another issue with a realworld VB-SAR deployment is the need to have a source of accurate SMC measurements available (unless VB-SAR operation is limited to "detection mode" as detailed in Section 6.2). As discussed in Section 2.4.3, for VB-SAR the optimum source of wide area SMC measurements is likely to be active sensing.

[26] details one method of active SMC sensing, and states that at significant vegetation levels ($NDVI > 0.4$) the algorithm tends to underestimate SMC. To give these values some significance, Figure 6.18 shows average NDVI values for the UK during June and October 2003. As can be seen, little of the UK has a suitably low NDVI during June but the situtation is much better during October. It is speculated that the difference is primarily due to the harvesting of crops between the two dates. It is clear that this method is of limited utility for VB-SAR imaging of a typical temperate climate area during the summer months, but usable during the winter months when vegetation levels are lower.

In summary, the optimal area for VB-SAR is one where the SMC is low (to minimise soil attenuation) and variable (to ensure good VB-SAR subsurface resolution) with light vegetation cover (to minimise the effects of vegetation moisture on the produced VB-SAR depth profiles). Such an area could be found in a temperate country during the winter months.

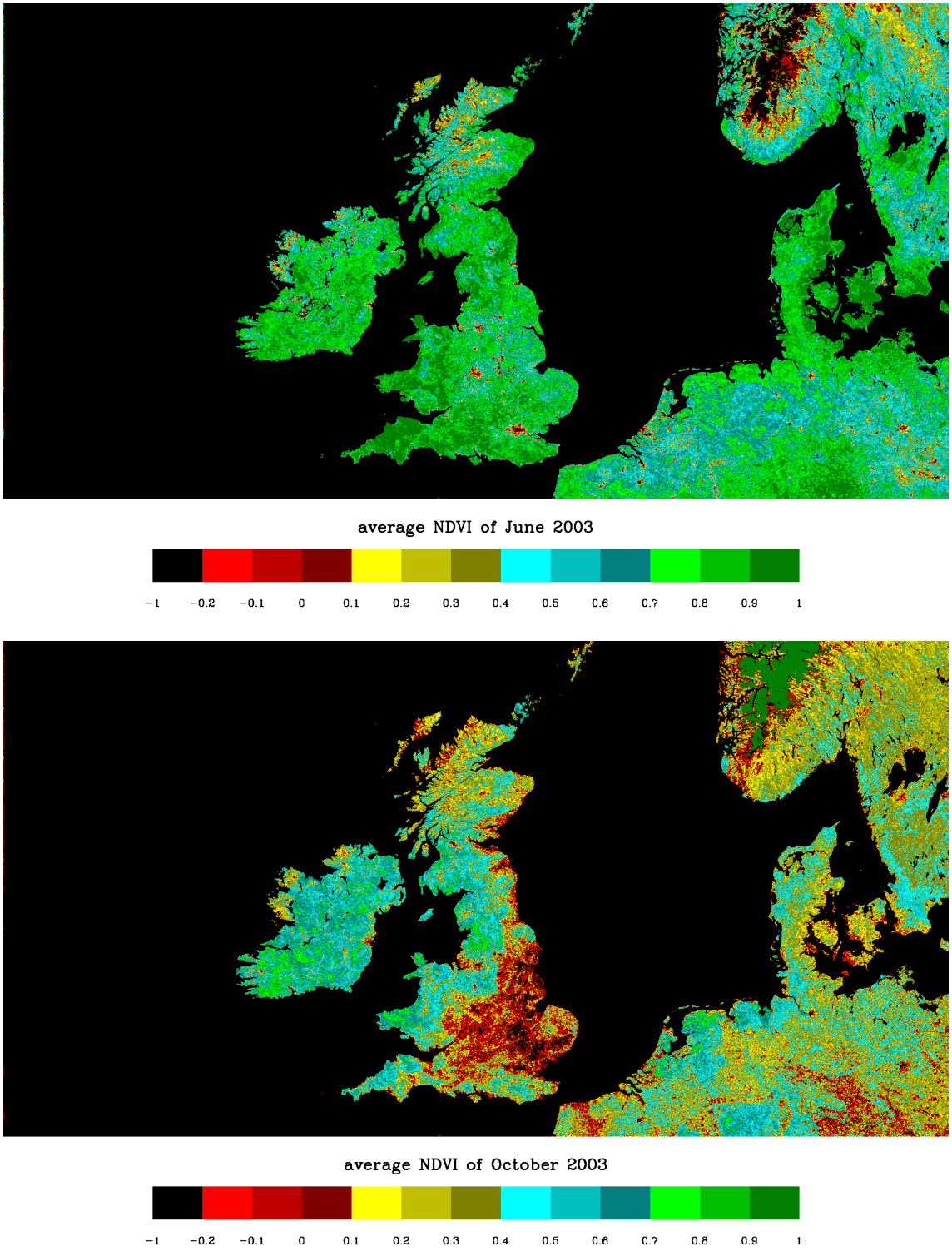

Figure 6.18: NDVI maps of the UK during June 2003 (top) and October 2003 (bottom). Images from [104].

6.7 Detection of Buried Targets by Spaceborne Radars

As discussed in Section 3.2.5 there are many spaceborne radar systems in orbit, producing DInSAR images that could potentially be used for VB-SAR. This section considers each system in turn and examines its potential utility as a data source for VB-SAR.

In order to address the question of whether a given system could be expected to detect a buried target a very simple method has been chosen. Firstly, the NESZ of each system has been identified from published literature. This has been converted into a noise equivalent RCS by multiplying the NESZ value by the resolution cell area of the radar system in question. Next, the theoretical RCS of a 1m square sided trihedral (a target that would be reasonable to construct and emplace during an initial trial) has been calculated. The difference between the noise equivalent RCS and the trihedral is calculated in order to give the maximum soil attenuation that can be tolerated whilst still allowing the target to be theoretically detectable. The depth of soil which would present that amount of attenuation was calculated in the following manner. Firstly, calculate the attenuation in Nepers/m [1]

$$\alpha = k\sqrt{\varepsilon_r}[(1+\tan^2\delta)]^{\frac{1}{4}}\sin(\frac{\delta}{2}) \tag{6.1}$$

Then, calculate the depth of a target that gives the allowable amount of attenuation in the following manner:

$$depth = \frac{atten}{\alpha * 8.68 * 2} \tag{6.2}$$

Where $atten$ is the allowable attenuation, 8.68 is a conversion factor between Nepers and dB and the factor of 2 accounts for the two way trip of the radar wave through the soil.

Whilst this is a gross simplification of the actual imaging scenario (ignoring such things as surface reflection, vegetation, target misalignments etc.) it does serve as a rela-

tive comparison between different spaceborne systems and airborne systems.

6.7.1 TerraSAR-X/TanDEM-X

TanDEM-X is a spaceborne radar interferometer consisting of two TerraSAR-X radar satellites orbiting in an accurately controlled, close formation . This arrangement allows for single pass interferometry, primarily intended to generate DEM products at a higher spatial resolution, accuracy and global coverage level than that produced by the SRTM. The system is fully polarimetric and operates in X-band[105]. The system occupies an orbit with a repeat period of 11 days

From a VB-SAR perspective, TanDEM-X has a significant attraction in that it provides single pass interferometry. This means that the interferograms it produces are free from temporal decorrelation and the influence of atmospheric disturbances that are inherent to multiple pass interferometry. In addition, using single pass interferometry means that the elapsed time between interferograms in the DInSAR stack is just the revisit time, rather than double the revisit time as with other systems.

Data availability appears to be good, with InSAR images available as a standard product at a reasonable price [106], [107].

Counting against TanDEM-X is the fact that it operates at X-band, which severely limits the penetration depth through all types of soil. In addition, a typical NESZ of the system is given by [11] to be no better than -23dB.

Considering TanDEM-X's centre frequency of 9.65GHz, and using the square sided trihedral RCS calculation for a 1m edge length of;

$$\sigma[dBsm] = 10log10(\frac{12 * \pi * a^4 * f}{c}) \tag{6.3}$$

we get a target RCS of 30.8dBsm.

The resolution of TanDEM-X is 3m x 3m whilst operating in stripmap mode [108], converting the NESZ from dB/m^2 to dBsm using this resolution gives a NESZ of -13.4dBsm. This gives an allowable soil attenuation figure of 44dB before our 1m trihedral becomes invisible.

For a soil consisting of 100% sand and having an SMC of 5% this gives a maximum detection depth of 10.5cm. In reality, any realistic buried target is likely to have a much lower RCS than the large trihedral under consideration meaning that such a target would have to be much closer to the soil than this trihedral. It is obvious from this that TanDEM-X is not well suited to detecting buried targets.

6.7.2 Radarsat2

Radarsat-2 is a Canadian SAR satellite that operates at C-band. The design of the satellite is similar to that of Cosmo-Skymed. The onboard radar is capable of polarimetric observations by transmitting alternating H and V polarised pulses and receiving both polarisations simultaneously. The repeat period of the orbit is listed as 25 days, but the spacecraft supports both left- and right-looking radar imaging meaning that the revisit time for a particular patch of ground is likely to be less.

The satellite and data ordering system both support interferometric imaging, although unlike TanDEM-X only multiple pass interferometry is supported with all the issues that brings in terms of decorrelation and slower DInSAR stack update rate. Examination of archived data is also possible [57].

For VB-SAR Radarsat-2 is not an especially attractive radar platform. The repeat period is long and operating at C-band, whilst preferable to X-band, does not provide substantial ground penetration. However, in ultra-fine mode the estimated minimum NESZ is approximately -31dB/m^2 which is very good for a spaceborne radar [56]. Ultra-fine mode

gives a resolution of 3mx3m, therefore the minimum NESZ is -21.5dBsm.

As was done for TanDEM-X previously, a 1m square sided trihedral is used as an example target. Repeating the RCS calculation at Radarsat-2's centre frequency of 5.405GHz gives an RCS value of 28.3dBsm. This gives a soil attenuation allowance of 49.8dB.

Using the same soil parameters as for the TanDEM-X calculation (100% sand, 5% SMC), the maximum detectable burial depth for the trihedral is 35cm. This is an improvement over TanDEM-X, but as noted previously the repeat period is long which limits the utility of Radarsat-2 for VB-SAR.

6.7.3 PALSAR-2 (ALOS-2)

PALSAR-2 is an L-band SAR carried as the sole payload of the ALOS-2 satellite. This system is operated by JAXA and is a follow on mission to the PALSAR payload on ALOS. However, PALSAR was not the sole instrument on ALOS leading to limitations on the amount of SAR observing possible, due to daytime observations being prioritised for optical imaging.

ALOS-2 is in a sun-synchronous noon orbit (i.e. crosses the equator at noon local time), whereas other SAR missions are often in dawn/dusk orbits (crossing the equator early in the morning or late in the evening). The revisit period is specified as 14 days. As is typical for modern SAR systems, multiple observation modes are offered including spotlight, stripmap and scanSAR. NESZ figures for PALSAR-2 range from -23dB in scanSAR mode to -28dB in high-sensitivity stripmap mode [12].

PALSAR-2 represents an interesting satellite for VB-SAR. The use of L-band as opposed to X or C band allows greater penetration through the earth to buried targets due to reduced attenuation.

The centre frequency PALSAR-2 uses is 1270MHz. The soil model presented by [17]

only runs down to 1.4GHz, so for this approximate calculation a frequency of 1.4GHz has been passed to the soil model.

The 1m square sided trihedral displays an RCS of 22.0dBsm at 1270MHz. In high-sensitivity stripmap mode ALOS-2 offers 6m x 6m resolution, which gives a NESZ of -12.43dBsm. Thus, the maximum soil attenuation that can be allowed is -32.43dB.

Using a frequency of 1.4GHz to work within the limitations of the Hallikainen soil model gives a maximum detectable depth of 51cm; over 5 times that of the X-band TerraSAR-X despite a slightly worse NESZ which demonstrates the significance of radar frequency.

6.7.4 RISAT-1

RISAT-1 (Radar Imaging Satellite 1) carries a C-band radar as its sole payload. The satellite is intended to provide scientific data and data products are available online. True quad polarisation operation is only available in one mode (a moderate resolution stripmap mode operating at 9m x 4m resolution). Other modes support resolutions up to 1m x 0.67m whilst operating in hybrid polarisation mode, transmitting in circular polarisation and receiving in both horizontal and vertical polarisations.

The radar does not support left and right side imaging and the satellite sits in a dawn/dusk orbit with a revisit period of 25 days [65]. NESZ varies from -16dB to -20dB.

RISAT-1 does not appear to present a particularly promising option for VB-SAR usage. The combination of operating at C-band, relatively poor NESZ values and a long revisit period make this system less attractive than the other space-based possibilities.

6.8 Detection of Buried Targets by Airborne Radars

Whilst spaceborne systems offer worldwide coverage, airborne SAR systems offer advantages for VB-SAR usage over them. For instance, whilst spaceborne systems are essentially confined to fixed orbits with set revisit times for a given area an airborne system can offer varied revisit times over a given area. In this way, the system can respond to variations in soil moisture in order to optimise the DInSAR stack for VB-SAR exploitation. For instance, following a heavy rainfall event the airborne radar could be tasked to repeatedly overfly an area of interest as the soil moisture decreases.

In addition, whereas spaceborne systems are typically limited to one frequency airborne systems often offer the ability to acquire multiple bands simultaneously [109]. This would be tremendously helpful during the initial deployments of VB-SAR as it would allow the effects of real frequency to be characterised.

6.8.1 DLR F-SAR

DLR operate F-SAR, an airborne SAR system mounted on a DO228 aircraft. It operates over X, C, S, L and P (UHF) bands, offering single pass polarimetric interferometry in X and S band. Repeat pass polarimetric interferometry is available in all bands. Azimuth resolution ranges from 0.2m in X band to 1.5m in UHF; range resolution ranges from 0.3m in X band to 2.25m in UHF. NESZ figures vary from -46dB to -27dB. [109].

F-SAR presents a very attractive platform to use for evaluating VB-SAR. It offers very high resolutions compared to satellite systems, which should offer improved signal to clutter ratios for physically small buried targets.

Using a 1m square sided trihedral buried in 100% sand containing 5% SMC as before and considering each band in turn, the following figures for maximum detection depth of a target are found:

In X band, the quoted NESZ is -34dB at 45°, and the resolution is 0.3x0.2m. This translates to a NESZ in dBsm of -46.2dBsm. Using F-SAR's X-band frequency of 9.60GHz the 1m square sided trihedral has an RCS of 30.8dBsm; allowing for an attenuation of 77dB. In the 100% sand soil at 5% SMC this gives a maximum detection depth of 19.7cm.

In C band, the quoted NESZ is -40dB at 45°, and the resolution is 0.6x0.3m. This gives a NESZ of -47.4dBsm. Using F-SAR's C-band frequency of 5.30GHz the 1m square sided trihedral has an RCS of 28.2dBsm. In this band the maximum soil attenuation possible is 75.6dB. At C band in this soil the maximum detection depth is 54.7cm.

In S band, the quoted NESZ is -34dB at 45°, and the resolution is 0.75x0.35m, which gives a NESZ of -39.8dBsm. Using F-SAR's S-band frequency of 3.25GHz the 1m square sided trihedral has an RCS of 26.1dBsm, so the maximum tolerable soil attenuation is 65.9dB. This leads to a maximum detection depth of 66.9cm in a 100% sandy soil containing 5% SMC.

In L band, the quoted NESZ is -46dB at 45°, and the resolution is 1.5x0.4m, leading to a NESZ of -48.2dBsm. Using F-SAR's L-band frequency of 1.325GHz the 1m square sided trihedral has an RCS of 22.2dBsm, therefore the soil can exhibit an attenuation of 70.4dB before the target becomes undetectable. As this is outside the range of the Hallikainen soil model, the soil model presented by [20] was used, giving a maximum detection depth of 2.11m.

Finally, in P band, the quoted NESZ is -46dB at 45°, and the resolution is 2.25x1.5m, which gives a NESZ of -40.7dBsm. Using F-SAR's P-band frequency of 435MHz the 1m square sided trihedral has an RCS of 17.4dBsm. This allows a maximum soil attenuation of 58.1dB. At this low frequency, the soil model presented by [20] has to be used. giving a maximum detection depth of 4.49m.

6.9 Spaceborne versus Airborne Systems for VB-SAR

From the previous discussions and calculations it is clear that, for initial development work at least, an airborne system such as F-SAR has numerous advantages over current spaceborne systems.

Most significantly, an airborne system benefits from higher ground resolutions and lower NESZ figures than a spaceborne system. As demonstrated in the previous calculations, this means that a given target can be detected at a much deeper depth by an airborne system than a spaceborne system. Conversely, a smaller target than the 1m trihedral used for the calculations could be buried at a shallower depth, reducing the amount of effort needed to setup a test area.

The ability of F-SAR to operate in multiple frequency bands simultaneously allows the effects of frequency to be rigorously examined using data collected under identical conditions, rather than having to compare data collected at different times by different systems which could lead to ambiguities.

An airborne system also benefits from an essentially arbitrary revisit period. This means that an initial demonstration using controlled wetting of the soil above the buried target could be conducted in a much shorter time, with much more control of the soil moisture, than a similar experiment using a spaceborne system. In addition, the flexibility of the revisit time could allow natural variations in soil moisture to be exploited to derive VB-SAR images.

Finally, whereas any investigation using spaceborne data would likely involve ”piggy backing” onto other data collections and using fixed imaging parameters, an investigation that uses airborne radar could set (within the limitations of the system) the imaging parameters. This would offer further opportunities to explore the effects of parameters such as look angle, target range and polarisation etc.

6.10 Conclusions

This chapter has explored several issues which will be encountered during real-world implementation of the VB-SAR scheme.

The ability of VB-SAR to operate without absolute SMC information was demonstrated. In this situation, VB-SAR operates in ”detection mode”, indicating the presence of buried targets without giving accurate depth indications.

The insensitivity of VB-SAR to soil texture was shown, by comparing depth profiles obtained from 100% sand and sandy loam soils.

The most significant result was the simulation of VB-SAR using a side-looking imaging geometry. 3-D simulations were carried out using the SAR simulator and the backprojection imager was used to produce side-looking SAR images. The VB-SAR algorithm successfully produced depth profiles which placed the buried target at the correct depth, although the buried targets migrated down range by an amount proportional to their depth. It is thought that this could be corrected for by applying a shear operation in order to correct for the effects of refraction at the soil surface, however further work would be needed to confirm that this is the cause and solution.

The best climatic conditions for a VB-SAR deployment were discussed, leading to a recommendation that the optimum conditions are likely to be found within a temperate climate, in an area with light vegetation coverage.

Finally, the feasibility of operating VB-SAR using radar data obtained from several spaceborne and an airborne SAR system was explored.

Chapter 7

Conclusions

7.1 Introduction

This thesis has presented work which investigated the VB-SAR technique, demonstrating that it is a feasible technique for subsurface imaging in the real world. This chapter concludes this thesis by presenting a brief summary of the research performed during this project. Included within this chapter is a brief summary of the results obtained, answers to the initial research questions and a selection of suggestions for future research.

7.2 Summary of Results

The key result of this work is the world's first experimental demonstration of the VB-SAR technique in a laboratory environment. The laboratory work validated the VB-SAR technique and demonstrated the ability of the technique to produce subsurface images at higher resolutions than that offered by the raw radar data. In addition to this, the frequency independence of the VB-SAR scheme was also proven. Both of these results are significant as real-world side-looking SAR systems operate at relatively low bandwidths

and across a range of centre frequencies.

Furthermore, it was experimentally shown that the VB-SAR process is applicable across a range of incidence angles. This was verified by using the TP imaging technique which allowed a single radar dataset to be used to generate radar images with differing incidence angles, avoiding any variance due to collecting multiple datasets. This is a key result as it implies that a side-looking SAR based VB-SAR processor does not necessarily need to take the varying incidence angle across an imaging scene into account when constructing subsurface images.

Within the laboratory environment only a single soil texture, namely 100% sand, was used. Obviously in the real world a wide range of soil textures could be encountered by the VB-SAR process. Simulation using a standard soil model [17] demonstrated that the VB-SAR process would work over a range of soil textures.

Whilst the TP process is a convenient imaging algorithm for laboratory use (due to the previously mentioned ability to create radar images formed at different incidence angles from a single radar dataset) it is not a practical imaging solution for large-area data collection, due to the cross-range resolution being given solely by the antenna's real beamwidth. It is certain that any large-area implementation of the VB-SAR scheme would involve side-looking SAR, as this is the imaging technique used by almost all airborne and spaceborne imaging radars. To this end, simulation has demonstrated that the VB-SAR process is compatible with the side-looking SAR imaging process at both the laboratory scale and the spaceborne radar scale.

7.3 Answers to Research Questions

The following research questions were posed in Chapter 1, and this work has provided the following answers.

Q1: Is the VB-SAR imaging scheme feasible in a laboratory environment?

A1: Yes, the VB-SAR imaging scheme has been proven to be feasible in the laboratory environment. VB-SAR subsurface imaging has been successfully conducted, during which several key predictions of the VB-SAR theory have proved to be correct.

Q2: Are there likely issues with operating a VB-SAR scheme in a non-laboratory environment?

A2: The largest issue with operating VB-SAR in the real world (ignoring system limitations discussed in A4 below) is the accurate determination of SMC over a large area, accurate SMC information being required in order to apply the correct depth scale to subsurface images (although it has been shown that the VB-SAR scheme can successfully operate in "detection mode" when no accurate SMC information is available, indicating the presence or absence of buried targets). Further possible limitations, explored by simulations performed during this work but requiring experimental verification, include the effects of different soil textures, the effect of incidence angle changes and the responses of different buried targets.

Q3: What limitations does the VB-SAR scheme suffer from?

A3: The largest limitation to the VB-SAR scheme is the high attenuation presented by moist soils which severely limits the depth at which buried targets are detectable by spaceborne SAR systems. Other limitations are as discussed in A2 above.

Q4: Given the current state of spaceborne SAR systems, is it possible to demonstrate the VB-SAR scheme with them?

A4: It is likely not feasible to demonstrate the VB-SAR scheme with existing spaceborne SAR systems. Analysis presented in Chapter 6 has shown that the combina-

tion of relatively poor NESZ figures, high frequencies and long revisit times make the current spaceborne SAR systems poor candidates for VB-SAR demonstration. However, it was also shown that airborne systems such as F-SAR are likely to be well suited for VB-SAR demonstrations, given their substantially improved NESZ, wider choice of frequency bands and the ability to choose imaging times (rather than being in a fixed orbit).

7.4 Suggestions for Future Research

This work has made several significant novel contributions and proved the fundamental feasibility of the VB-SAR process. However, there are still several questions that need to be answered before large scale exploitation of this technique is feasible.

The most pressing issue, given the previously identified issues with operating this technique from airborne and spaceborne platforms at C-band is the applicability of the VB-SAR process to other frequency bands, most significantly lower frequencies such as L-band. At these lower frequencies the attenuation of vegetation and the soil above a target should be substantially reduced, enabling successful detection of deeper buried targets at higher soil moisture contents. Experimentation with multispectral VB-SAR across the C-band dataset collected as part of this work and simulation within C-band strongly suggests that the VB-SAR process is applicable across a range of frequencies with no frequency dependence. In order to validate the process at these lower frequencies a similar combined experimentation and simulation approach as used within this thesis is suggested.

The experimental and simulation work presented here has only considered point and trihedral targets. In a real-world usage, buried targets are likely to present responses that vary considerably over the range of incidence angles that a side-looking SAR would ob-

serve them over. It is suggested that during any subsequent laboratory work a range of buried targets are used. Coupled to this is the necessity to use targets suitable for both copolarisation and crosspolarisation observations. The crosspolarisation case is particularly important as the work presented here did not use any crosspolarisation-friendly buried targets.

A key area that must be explored is the effects of different soil textures on the fundamental principles of the VB-SAR technique. Whilst simulation using published soil models has shown that there should be no reason (other than the need to consider increased soil attenuation) that the VB-SAR technique would not be equally applicable to a range of soils, provided that a SMC metric exists, this is an obvious avenue for exploration. It is suggested that an experimental scene that contains volumes of both sand (as used during this work) and a different soil containing the same buried targets is used, so that the effects of soil texture can be directly compared.

Any practical implementation of the VB-SAR scheme will use data obtained from side-looking SAR images. For this initial demonstration the TP imaging algorithm offered the advantage of being able to study the responses of buried targets over a range of incidence angles, and simulation has shown that there is not a fundamental limitation of the VB-SAR scheme which would prevent the usage of side-looking SAR imagery as a datasource. Despite this, a laboratory evaluation of the VB-SAR scheme using a small side-looking SAR system (as described by [110]) is prudent before any large-scale experimentation is attempted.

Additional exploration of the effects of surface vegetation should be considered. Vegetation can contain significant amounts of moisture which can both attenuate the radar signal and, given seasonal variations, present an additional source of buried target phase variation above that caused by changes in SMC. Such attenuation and variation is likely to be insignificant over light vegetation cover such as grassland, but assessment is needed

to get an appreciation for the situation in areas of heavier vegetation.

All of the future work suggested so far could be carried out in the laboratory, where the experimental environment is tightly controlled. Any practical deployment of the VB-SAR process will, of course, be outside this well controlled situation. As a stepping stone to a large scale investigation using very expensive resources such as an airborne SAR system, it is suggested that a GB-SAR system (such as that described by [110]) is used to demonstrate VB-SAR outside. It is suggested that the radar scene for such a trial should contain surface reference targets and artificially placed buried targets in addition to any buried objects that are already present in the scene. The SMC would need to be independently measured over the course of the experiment as, unlike in the experiment presented in this thesis, the starting SMC of the soil volume would not be accurately known and so it would not be possible to derive the SMC as the experiment progressed. It is suggested that controlled wetting of the soil volume is used, so that the experiment can be conducted relatively rapidly, avoiding the need to deploy and stow the GB-SAR many times.

The ultimate verification and validation of the VB-SAR imaging scheme would be to use radar data from an airborne or spaceborne SAR system to form VB-SAR images. A key attraction of the VB-SAR process is that it can use standard DInSAR datasets. This means that, provided suitable buried targets are provided or identified, experimentation with VB-SAR can be piggybacked onto other experimental campaigns. However, there are several key questions that should be answered before attempting a large area demonstration, as listed above. Due to this, the use of such a system in a VB-SAR experiment is currently considered to be overambitious.

References

[1] K. Morrison and J. Bennett, "Virtual-bandwidth SAR (VB-SAR) for sub-surface imaging," 2014, pp. 1139–1142.

[2] T. K. Sarkar, M. S. Palma, and E. L. Mokole, "Echoing Across the Years: A History of Early Radar Evolution," *IEEE Microwave Magazine*, vol. 17, no. 10, pp. 46–60, Oct 2016.

[3] R. Torres, P. Snoeij, D. Geudtner, D. Bibby, M. Davidson, E. Attema, P. Potin, B. Rommen, N. Floury, M. Brown, I. Traver, P. Deghaye, B. Duesmann, B. Rosich, N. Miranda, C. Bruno, M. L'Abbate, R. Croci, A. Pietropaolo, M. Huchler, and F. Rostan, "GMES Sentinel-1 mission," *Remote Sensing of Environment*, vol. 120, pp. 9–24, 2012.

[4] K. Morrison and J. Bennett, "SubSAR - Distinguishing between surface and sub-surface features in SAR imagery," 2012, Unpublished Report.

[5] A. Edwards-Smith and K. Morrison, "VB-SAR For Remote Stand-off Subsurface Imaging: First Demonstration," in *Proceedings of EUSAR 2016: 11th European Conference on Synthetic Aperture Radar*, June 2016, pp. 1–4.

[6] A. Edwards-Smith, K. Morrison, S. Zwieback, and I. Hajnsek, "Verification of the Virtual Bandwidth SAR Scheme for Centimetric Resolution Subsurface Imag-

ing From Space," *IEEE Transactions on Geoscience and Remote Sensing*, vol. 56, no. 1, pp. 25–34, Jan 2018.

[7] P. Lacomme, J.-P. Hardange, J.-C. Marchais, and E. Normant, *Air and Spaceborne Radar Systems*. William Andrew Publishing, 2001, ISBN:9781891121135.

[8] A. Jain and I. Patel, "Dynamic imaging and RCS measurements of aircraft," *IEEE Transactions on Aerospace and Electronic Systems*, vol. 31, no. 1, pp. 211–226, Jan 1995.

[9] S. K. Wong, E. Riseborough, G. Duff, and K. K. Chan, "Radar cross-section measurements of a full-scale aircraft duct/engine structure," *IEEE Transactions on Antennas and Propagation*, vol. 54, no. 8, pp. 2436–2441, Aug 2006.

[10] Y. Oh, K. Sarabandi, and F. T. Ulaby, "An empirical model and an inversion technique for radar scattering from bare soil surfaces," *IEEE Transactions on Geoscience and Remote Sensing*, vol. 30, no. 2, pp. 370–381, 1992.

[11] M. Martone, B. Brutigam, P. Rizzoli, and G. Krieger, "Impact of SAR data quantization on TanDEM-X performance," in *2013 IEEE International Geoscience and Remote Sensing Symposium - IGARSS*, July 2013, pp. 4487–4490.

[12] Y. Kankaku, S. Suzuki, and Y. Osawa, "ALOS-2 mission and development status," in *2013 IEEE International Geoscience and Remote Sensing Symposium - IGARSS*, July 2013, pp. 2396–2399.

[13] A. G. Fore, B. D. Chapman, B. P. Hawkins, S. Hensley, C. E. Jones, T. R. Michel, and R. J. Muellerschoen, "UAVSAR Polarimetric Calibration," *IEEE Transactions on Geoscience and Remote Sensing*, vol. 53, no. 6, pp. 3481–3491, June 2015.

[14] M. Shimada, N. Kawano, M. Watanabe, T. Motooka, and M. Ohki, "Calibration and validation of the Pi-SAR-L2," in *Conference Proceedings of 2013 Asia-Pacific Conference on Synthetic Aperture Radar (APSAR)*, Sept 2013, pp. 194–197.

[15] K. Morrison and J. Bennett, "Virtual bandwidth SAR (VB-SAR) for centimetric-scale sub-surface imaging from space," *International Journal of Remote Sensing*, vol. 36, no. 7, pp. 1789–1808, 2015.

[16] J. Moeys, "The soil texture wizard: R functions for plotting, classifying, transforming and exploring soil texture data," 2018.

[17] M. Hallikainen, F. Ulabz, M. Dobson, M. El-Rayes, and L.-K. Wu, "Microwave Dielectric Behavior of Wet Soil-Part I: Empirical Models and Experimental Observations," *IEEE Transactions on Geoscience and Remote Sensing*, vol. GE-23, no. 1, pp. 25–34, 1985.

[18] N. Peplinski, F. Ulaby, and M. Dobson, "Dielectric Properties of Soils in the 0.3 [to] 1.3GHz Range," *IEEE Transactions on Geoscience and Remote Sensing*, vol. 33, no. 3, pp. 803–807, 1995.

[19] V. Mironov, M. Dobson, V. Kaupp, S. Komarov, and V. Kleshchenko, "Generalized refractive mixing dielectric model for moist soils," *IEEE Transactions on Geoscience and Remote Sensing*, vol. 42, no. 4, pp. 773–785, 2004.

[20] V. Mironov, L. Kosolapova, and S. Fomin, "Physically and mineralogically based spectroscopic dielectric model for moist soils," *IEEE Transactions on Geoscience and Remote Sensing*, vol. 47, no. 7, pp. 2059–2070, 2009.

[21] D. Entekhabi, E. Njoku, P. O'Neill, K. Kellogg, W. Crow, W. Edelstein, J. Entin, S. Goodman, T. Jackson, J. Johnson, J. Kimball, J. Piepmeier, R. Koster, N. Martin,

K. McDonald, M. Moghaddam, S. Moran, R. Reichle, J. Shi, M. Spencer, S. Thurman, L. Tsang, and J. Van Zyl, "The soil moisture active passive (SMAP) mission," *Proceedings of the IEEE*, vol. 98, no. 5, pp. 704–716, 2010.

[22] Y. Kerr, P. Waldteufel, J.-P. Wigneron, J.-M. Martinuzzi, J. Font, and M. Berger, "Soil moisture retrieval from space: The Soil Moisture and Ocean Salinity (SMOS) mission," *IEEE Transactions on Geoscience and Remote Sensing*, vol. 39, no. 8, pp. 1729–1735, 2001.

[23] V. Mulder, S. de Bruin, M. Schaepman, and T. Mayr, "The use of remote sensing in soil and terrain mapping - a review," *Geoderma*, vol. 162, no. 1-2, pp. 1–19, 2011.

[24] D. Singh and A. Kathpalia, "An efficient modeling with ga approach to retrieve soil texture, moisture and roughness from ers-2 sar data," *Progress In Electromagnetics Research*, vol. 77, pp. 121–136, 2007.

[25] B. Rawlins, R. Webster, A. Tye, R. Lawley, and S. O'Hara, "Estimating particlesize fractions of soil dominated by silicate minerals from geochemistry," vol. 60, pp. 116–126, 01 2009.

[26] P. Dubois, J. Van Zyl, and T. Engman, "Measuring soil moisture with imaging radars," *Geoscience and Remote Sensing, IEEE Transactions on*, vol. 33, no. 4, pp. 915–926, Jul 1995.

[27] A. W. Western, R. B. Grayson, and G. Blöschl, "Scaling of Soil Moisture: A Hydrologic Perspective," *Annual Review of Earth and Planetary Sciences*, vol. 30, pp. 149–180, 2002.

[28] S. Kim, J. van Zyl, S. Dunbar, E. Njoku, J. Johnson, M. Moghaddam, J. Shi, and L. Tsang, *Soil Moisture Active Passive (SMAP) Algorithm Theoretical Basis Doc-*

ument Level 2 and 3 Soil Moisture (Active) Data Products, JPL, December 2014, Revision A.

[29] E. Njoku and D. Entekhabi, "Passive microwave remote sensing of soil moisture," *Journal of Hydrology*, vol. 184, no. 1-2, pp. 101–129, 1996.

[30] Y. Kerr, P. Waldteufel, J.-P. Wigneron, S. Delwart, F. Cabot, J. Boutin, M.-J. Escorihuela, J. Font, N. Reul, C. Gruhier, S. Juglea, M. Drinkwater, A. Hahne, M. Martin-Neira, and S. Mecklenburg, "The SMOS Mission: New tool for monitoring key elements of the global water cycle," *Proceedings of the IEEE*, vol. 98, no. 5, pp. 666–687, 2010.

[31] "Recommendation ITU-R RA.314-10; Preferred frequency bands for radio astronomical measurements," ITU, 2003.

[32] R. Oliva, E. Daganzo-Eusebio, Y. Kerr, S. Mecklenburg, S. Nieto, P. Richaume, and C. Gruhier, "SMOS radio frequency interference scenario: Status and actions taken to improve the RFI environment in the 1400-1427MHz passive band," *IEEE Transactions on Geoscience and Remote Sensing*, vol. 50, no. 5 PART 1, pp. 1427–1439, 2012.

[33] K. D. McMullan, M. A. Brown, M. Martin-Neira, W. Rits, S. Ekholm, J. Marti, and J. Lemanczyk, "SMOS: The Payload," *IEEE Transactions on Geoscience and Remote Sensing*, vol. 46, no. 3, pp. 594–605, March 2008.

[34] Y. Kerr, P. Waldteufel, P. Richaume, P. Ferrazzoli, and J. Wigneron, "Algorithm Theoretical Basis Document (ATBD) for the SMOS level 2 soil moisture processor development continuation project," *SMOS Level 2 Processor for Soil Mois.*, no. 3-6, 2011.

[35] Y. H. Kerr, P. Waldteufel, P. Richaume, J. P. Wigneron, P. Ferrazzoli, A. Mahmoodi, A. A. Bitar, F. Cabot, C. Gruhier, S. E. Juglea, D. Leroux, A. Mialon, and S. Delwart, "The SMOS Soil Moisture Retrieval Algorithm," *IEEE Transactions on Geoscience and Remote Sensing*, vol. 50, no. 5, pp. 1384–1403, May 2012.

[36] P.O'Neill, S. Chan, E. Njoku, T. Jackson, and R. Bindlish, *Soil Moisture Active Passive (SMAP) Algorithm Theoretical Basis Document Level 2 and 3 Soil Moisture (Passive) Data Products*, JPL, September 2015.

[37] T. Jackson and T. Schmugge, "Vegetation effects on the microwave emission of soils," *Remote Sensing of Environment*, vol. 36, no. 3, pp. 203 – 212, 1991. [Online]. Available: http://www.sciencedirect.com/science/article/pii/003442579190057D

[38] B. Choudhury, T. J. Schmugge, A. Chang, and R. Newton, "Effect of surface roughness on the microwave emission from soils," *Journal of Geophysical Research: Oceans*, vol. 84, no. C9, pp. 5699–5706, 1979.

[39] K. Morrison and J. Bennett, "Tomographic profiling - A technique for multi-incidence-angle retrieval of the vertical sar backscattering profiles of biogeophysical targets," *IEEE Transactions on Geoscience and Remote Sensing*, vol. 52, no. 2, pp. 1250–1255, 2014.

[40] A. Moreira, P. Prats-Iraola, M. Younis, G. Krieger, I. Hajnsek, and K. Papathanassiou, "A tutorial on synthetic aperture radar," *Geoscience and Remote Sensing Magazine, IEEE*, vol. 1, no. 1, pp. 6–43, March 2013.

[41] C. Sherwin, J. Ruina, and R. Rawcliffe, "Some Early Developments in Synthetic Aperture Radar Systems," *IRE Transactions on Military Electronics*, vol. MIL-6, no. 2, pp. 111–115, 1962.

[42] *Technical Background and Analysis Methods for SAR*, Centre for Space Research, University of Texas, http://www.csr.utexas.edu/projects/rs/whatissar/sar.html.

[43] M. I. Skolnik, "Radar handbook," 1970.

[44] G. Stimson, *Introduction to Airborne Radar*, 2nd ed., , Ed. Mendham: SciTech Publishing, 1998.

[45] M. Eineder, T. Fritz, J. Mittermayer, A. Roth, E. Börner, and T. Breit, *TerraSAR-X Ground Segment Basic Product Specification Document*, DLR, 2008.

[46] D. Geudtner, R. Torres, P. Snoeij, M. Davidson, and B. Rommen, "Sentinel-1 System capabilities and applications," in *2014 IEEE Geoscience and Remote Sensing Symposium*, July 2014, pp. 1457–1460.

[47] *ASAR Product Handbook*, ESA, 2007, available at https://earth.esa.int/handbooks/asar/.

[48] J. P. Ford, "Resolution versus speckle relative to geologic interpretability of spaceborne radar images: A survey of user preference," *IEEE Transactions on Geoscience and Remote Sensing*, vol. GE-20, no. 4, pp. 434–444, Oct 1982.

[49] V. S. Frost, J. A. Stiles, K. S. Shanmugan, and J. C. Holtzman, "A model for radar images and its application to adaptive digital filtering of multiplicative noise," *IEEE Transactions on Pattern Analysis and Machine Intelligence*, vol. PAMI-4, no. 2, pp. 157–166, March 1982.

[50] I. Elizavetin, "Radiometric artifacts on SAR images," 2010.

[51] M. D. Desai and W. K. Jenkins, "Convolution backprojection image reconstruction for spotlight mode synthetic aperture radar," *IEEE Transactions on Image Processing*, vol. 1, no. 4, pp. 505–517, Oct 1992.

[52] L. Gorham and L. Moore, "SAR image formation toolbox for MATLAB," vol. 7699, 2010.

[53] D. B. Tridon, M. Bachmann, D. Schulze, C. Ortega-Míguez, M. D. Polimeni, M. Martone, J. Böer, and M. Zink, "TanDEM-X: DEM acquisition in the third year era," *International Journal of Space Science and Engineering 5*, vol. 1, no. 4, pp. 367–381, 2013.

[54] S. Lehner, J. Horstmann, and J. Schulz-Stellenfleth, "TerraSAR-X for oceanography mission overview," in *IGARSS 2004. 2004 IEEE International Geoscience and Remote Sensing Symposium*, vol. 5, Sept 2004, pp. 3303–3306 vol.5.

[55] *TerraSAR-X: predicted performance*, vol. 4881, 2003. [Online]. Available: https://doi.org/10.1117/12.463009

[56] M. Ltd., "RADARSAT-2 PRODUCT DESCRIPTION," MDA Ltd., Tech. Rep., 2015.

[57] C. E. Livingstone, I. Sikaneta, C. Gierull, S. Chiu, and P. Beaulne, "RADARSAT-2 System and Mode Description," in *Proc. NATO CTI Symp*.

[58] F.Covello, F. Battazza, A. Coletta, E. Lopinto, C. Fiorentino, L. Pietranera, G. Valentini, and S. Zoffoli, "COSMO-SkyMed an existing opportunity for observing the Earth," *Journal of Geodynamics*, vol. 49, no. 3, pp. 171 – 180, 2010, wEGENER 2008 - Proceedings of the 14th General Assembly of Wegener.

[59] *COSMO-SkyMed System Description and User Guide*, Italian Space Agency.

[60] Italian Space Agency, *COSMO-SkyMed Mission and Products Description*.

[61] P. Snoeij, E. Attema, B. Duesmann, M. Davidson, N. Floury, B. Rosich, B. Rommen, and G. Levrini, "GMES Sentinel-1 Mission, System and Products," in *Proceedings of the 4th International POLinSAR 2009 Workshop*, 2009.

[62] P. Snoeij, E. Attema, M. Davidson, B. Duesmann, N. Floury, G. Levrini, B. Rommen, and B. Rosich, "Sentinel-1 radar mission: Status and performance," *IEEE Aerospace and Electronic Systems Magazine*, vol. 25, no. 8, pp. 32–39, Aug 2010.

[63] E. Attema, M. Davidson, P. Snoeij, B. Rommen, and N. Floury, "Sentinel-1 mission overview," in *2009 IEEE International Geoscience and Remote Sensing Symposium*, vol. 1, July 2009, pp. 36–39.

[64] J. S. Palma, A. S. Gonzalez, I. M. Hervas, F. M. Sanz, M. Labriola, J. M. Cengotitabengoa, F. M. G. Molleda, S. M. Aguado, P. S. Perez, J. C. Soteras, and V. B. Juzgado, "SAR Panel Design and Performance for the PAZ Mission," in *8th European Conference on Synthetic Aperture Radar*, June 2010, pp. 1–4.

[65] T. Misra and A. S. Kirankumar, "RISAT-1: Configuration and performance evaluation," in *2014 XXXIth URSI General Assembly and Scientific Symposium (URSI GASS)*, Aug 2014, pp. 1–4.

[66] Y. Desnos, C. Buck, J. Guijarro, J. Suchail, R. Torres, and E. Attema, "ASAR-Envisat's advanced synthetic aperture radar."

[67] E. P. Attema, "The active microwave instrument on-board the ERS-1 satellite," *Proceedings of the IEEE*, vol. 79, no. 6, pp. 791–799, 1991.

[68] A. Rosenqvist, M. Shimada, and M. Watanabe, "ALOS PALSAR: Technical outline and mission concepts," in *4th International Symposium on Retrieval of Bio-and*

Geophysical Parameters from SAR Data for Land Applications. Innsbruck, Austria, 2004, pp. 1–7.

[69] K. Rokosh, "RADARSAT," Canadian Space Agency, Tech. Rep.

[70] T. Shimada, H. Kawamura, M. Shimada, I. Watabe, and S. I. Iwasaki, "Evaluation of JERS-1 SAR images from a coastal wind retrieval point of view," *IEEE Transactions on Geoscience and Remote Sensing*, vol. 42, no. 3, pp. 491–500, March 2004.

[71] R. L. Jordan, "The Seasat-A synthetic aperture radar system," *IEEE Journal of Oceanic Engineering*, vol. 5, no. 2, pp. 154–164, April 1980.

[72] J. Cimino and C. Elachi, "Shuttle Imaging Radar-A (SIR-A) Experiment," NASA/JPL, Tech. Rep., December 1982.

[73] J. Cimino, C. Elachi, and M. Settle, "SIR-B-The Second Shuttle Imaging Radar Experiment," *IEEE Transactions on Geoscience and Remote Sensing*, vol. GE-24, no. 4, pp. 445–452, July 1986.

[74] R. Jordan, B. Huneycutt, and M. Werner, "The SIR-C/X-SAR Synthetic Aperture Radar system," *Geoscience and Remote Sensing, IEEE Transactions on*, vol. 33, no. 4, pp. 829–839, Jul 1995.

[75] R. Bamler, "The SRTM mission: A world-wide 30 m resolution DEM from SAR interferometry in 11 days," Tech. Rep., 01 1999.

[76] H. Zebker, P. Rosen, R. Goldstein, A. Gabriel, and C. Werner, "On the derivation of coseismic displacement fields using differential radar interferometry: the Landers earthquake," *Journal of Geophysical Research*, vol. 99, no. B10, pp. 19,617–19,634, 1994.

[77] A. Ferretti, A. Monti-Guarnieri, C. Prati, F. Rocca, D. Massonnet, and J. Lichtenegger, *Guidelines for SAR Interferometry Processing and Interpretation (ESA TM-19)*, ESA Publications, 2007.

[78] A. Sowter, "Differential InSAR," Unpublished Lecture.

[79] I. Cumming and W. Xu, "Comparison of phase unwrapping performance using a noisy interferogram (ESA SP414 Part 3) ," 1997, pp. 1697–1700.

[80] F. T. G., R. P. A., C. Edward, C. Robert, D. Riley, H. Scott, K. Michael, P. Mimi, R. Ernesto, R. Ladislav, S. David, S. Scott, S. Joanne, U. Jeffrey, W. Marian, O. Michael, B. Douglas, and A. Douglas, "The shuttle radar topography mission," *Reviews of Geophysics*, vol. 45, no. 2.

[81] B. Rabus, M. Eineder, A. Roth, and R. Bamler, "The shuttle radar topography mission - A new class of digital elevation models acquired by spaceborne radar," *ISPRS Journal of Photogrammetry and Remote Sensing*, vol. 57, no. 4, pp. 241–262, 2003.

[82] G. Krieger, M. Zink, M. Bachmann, B. Brutigam, D. Schulze, M. Martone, P. Rizzoli, U. Steinbrecher, J. Walter Antony, F. De Zan, I. Hajnsek, K. Papathanassiou, F. Kugler, M. Rodriguez Cassola, M. Younis, S. Baumgartner, P. Lpez-Dekker, P. Prats, and A. Moreira, "TanDEM-X: A radar interferometer with two formation-flying satellites," *Acta Astronautica*, vol. 89, pp. 83–98, 2013.

[83] A. Debaisieux, J. P. Aubry, E. Gerard, and M. Brunet, "A Satellite Oscillator for Very Precise Orbitography : the DORIS Program," in *39th Annual Symposium on Frequency Control*, May 1985, pp. 202–211.

[84] R. Bamler and P. Hartl, "Synthetic aperture radar interferometry," *Inverse Problems*, vol. 14, no. 4, pp. r1–r54, 1998.

[85] E. Sansosti, P. Berardino, M. Manunta, F. Serafino, and G. Fornaro, "Geometrical sar image registration," *IEEE Transactions on Geoscience and Remote Sensing*, vol. 44, no. 10, pp. 2861–2870, Oct 2006.

[86] J. van Zyl, "Interferometric synthetic aperture radar," lecture Notes.

[87] D. Just, N. Adam, M. Schwabisch, and R. Bamler, "Comparison of phase unwrapping algorithms for sar interferograms," in *Geoscience and Remote Sensing Symposium, 1995. IGARSS '95. 'Quantitative Remote Sensing for Science and Applications', International*, vol. 1, Jul 1995, pp. 767–769 vol.1.

[88] Y. Sheng, Y. Wang, C. Linlin Ge, and C. Rizos, "Differential radar interferometry and its application in monitoring underground coal mining-induced subsidence," in *International Conference on Geo-spatial Solutions for Emergency Management and the 50th Anniversary of the Chinese Academy of Surveying and Mapping*. ISPRS, 2009.

[89] R. Bamler, "Radar interferometry for surface deformation assessment," Presentation, 2006.

[90] A. Ferretti, C. Prati, and F. Rocca, "Permanent scatterers in SAR interferometry," in *Geoscience and Remote Sensing Symposium, 1999. IGARSS '99 Proceedings. IEEE 1999 International*, vol. 3, 1999, pp. 1528–1530 vol.3.

[91] F. Rocca, "The Permanent Scatterers Technique," 2007, lecture.

[92] D. J. Daniels, Ed., *Ground Penetrating Radar*, 2nd ed. Institution of Engineering and Technology, 2004.

[93] K. Morrison, J. C. Bennett, and M. Nolan, "Using DInSAR to Separate Surface and Subsurface Features," *IEEE Transactions on Geoscience and Remote Sensing*, vol. 51, no. 6, pp. 3424–3430, June 2013.

[94] F. Ulaby, P. Dubois, and J. Van Zyl, "Radar mapping of surface soil moisture," *Journal of Hydrology*, vol. 184, no. 1-2, pp. 57–84, 1996.

[95] A. I. Lvovsky, *Encyclopedia of Optical Engineering*, ch. Fresnel Equations, pp. 1–6.

[96] *Sentinel-1 SAR User Guide*, ESA, 2016.

[97] S. H. Yueh, S. V. Nghiem, and R. Kwok, "Symmetrization of cross-polarized responses in polarimetric radar images using reciprocity," *IEEE Transactions on Geoscience and Remote Sensing*, vol. 31, no. 6, pp. 1180–1185, Nov 1993.

[98] J.-J. Greffet and M. Nieto-Vesperinas, "Field theory for generalized bidirectional reflectivity: derivation of helmholtzs reciprocity principle and kirchhoffs law," *JOSA A*, vol. 15, no. 10, pp. 2735–2744, 1998.

[99] M. Weston, P. Mudge, C. Davis, and A. Peyton, "Time efficient auto-focussing algorithms for ultrasonic inspection of dual-layered media using Full Matrix Capture," *NDT and E International*, vol. 47, pp. 43–50, 2012.

[100] J. Dziewierz and A. Gachagan, "Correspondence: Computationally efficient solution of snell's law of refraction," *IEEE Transactions on Ultrasonics, Ferroelectrics, and Frequency Control*, vol. 60, no. 6, pp. 1256–1259, 2013.

[101] K. Morrison, G. Cookmartin, J. Bennett, S. Quegan, and A. Race, "Polarimetric calibration strategy for long-duration imaging with a ground-based SAR," *Canadian Journal of Remote Sensing*, vol. 31, no. 1, pp. 1–6, 2005.

[102] *Agilent Laser and Optics Users Manual, Volume I.*

[103] K. Morrison, J. Bennett, M. Nolan, and R. Menon, "Laboratory Measurement of the DInSAR Response to Spatiotemporal Variations in Soil Moisture," *Geoscience and Remote Sensing, IEEE Transactions on*, vol. 49, no. 10, pp. 3815–3823, Oct 2011.

[104] G. Cappelluti, "UK NDVI Maps," Online, retrieved from http://www.crazyverse.com/cappelluti/docs/anims/leicester/.

[105] G. Krieger, A. Moreira, H. Fiedler, I. Hajnsek, M. Werner, M. Younis, and M. Zink, "TanDEM-X: A Satellite Formation for High-Resolution SAR Interferometry," *IEEE Transactions on Geoscience and Remote Sensing*, vol. 45, no. 11, pp. 3317–3341, Nov 2007.

[106] T. Fritz, S. Duque, B. Brutigam, and J. L. Bueso Bello, *TanDEM-X Experimental Product Description*, 1st ed., DLR, 2012.

[107] "COFUR Prices for scientific TanDEM-X products," Online.

[108] R. Werninghaus and S. Buckreuss, "The TerraSAR-X Mission and System Design," *Geoscience and Remote Sensing, IEEE Transactions on*, vol. 48, no. 2, pp. 606–614, Feb 2010.

[109] R. Horn, M. Jaeger, M. Keller, M. Limbach, A. Nottensteiner, M. Pardini, A. Reigber, and R. Scheiber, "F-SAR - recent upgrades and campaign activities," in *2017 18th International Radar Symposium (IRS)*, June 2017, pp. 1–10.

[110] K. Morrison and M. L. Williams, "High resolution PolInSAR with the ground-based SAR (GB-SAR) system: measurement and modelling," in *Proceedings. 2005*

IEEE International Geoscience and Remote Sensing Symposium, 2005. IGARSS '05., vol. 2, July 2005, pp. 1105–1108.

Appendix A

Published Work

A.1 IEEE TGRS Paper

IEEE TRANSACTIONS ON GEOSCIENCE AND REMOTE SENSING, VOL. 56, NO. 1, JANUARY 2018 25

Verification of the Virtual Bandwidth SAR Scheme for Centimetric Resolution Subsurface Imaging From Space

Alexander Edwards-Smith, Keith Morrison, Simon Zwieback, and Irena Hajnsek, *Fellow, IEEE*

***Abstract*— This paper presents the first experimental demonstration of the virtual bandwidth synthetic aperture radar (VB-SAR) imaging scheme. VB-SAR is a newly developed subsurface imaging technique which, in stark contrast to traditional close proximity ground penetrating radar schemes, promises imaging from remote standoff platforms such as aircraft and satellites. It specifically exploits the differential interferometric SAR (DInSAR) phase history of a radar wave within a drying soil volume to generate high-resolution vertical maps of the scattering through the soil volume. For this study, a stack of C-band vertically polarized DInSAR images of a sandy soil containing a buried target was collected in the laboratory while the soil moisture was varied—first during controlled water addition, and then during subsequent drying. The wetting image set established the moisture-phase relationship for the soil, which was then applied to the drying DInSAR image set using the VB-SAR scheme. This allowed retrieval of high-resolution VB-SAR imagery with a vertical discrimination of 0.04 m from a stack of 1-m vertical resolution DInSAR images. This paper unequivocally shows that the basic principles of the VB-SAR technique are valid and opens the door to further investigation of this promising technique.**

***Index Terms*— Ground penetrating radar (GPR), radar, radar imaging, spaceborne radar, synthetic aperture radar (SAR).**

I. Introduction

SUBSURFACE radar imaging is traditionally performed by nadir viewing, ground penetrating radar (GPR) systems that rely on close contact with the ground surface [1]. This limits the areas that can be safely surveyed to areas that are nonhazardous and easily accessible. Even for sites that are easily accessible the relatively slow process of GPR means that surveying large areas is slow, and hence expensive, not to mention difficult [2]. Relatively benign terrain undulations can introduce an additional level of complication to the surveying process, requiring extremely precise measurement of the antenna position during the surveying process [3]. Conversely, radar imaging from standoff distances, such as that performed by airborne or spaceborne systems overcomes site access issues and speed of acquisition. However, standoff systems have major drawbacks when compared to traditional GPR systems. They typically operate over narrow bandwidths (due to regulatory and technical limitations), leading to significantly decreased slant range resolution.

Whereas GPR systems produce depth profiles which provide the ability to unambiguously discriminate between the depths of different returns, synthetic aperture radar (SAR) systems cannot easily discern between surface and subsurface returns. Although subsurface features have previously been reported in SAR imagery [4]–[7], in these papers there is no presentation of a depth profile; rather identification of subsurface geological-scale features relied upon intelligent supposition, contextual information, and cross-referencing against optical imagery. Arid desert conditions allowed for significant penetration of the radar signal to tens of meters. However, in more temperate climes with more moisture present in the soil, penetration depths (where the signal has fallen to 1/e of its strength at the soil surface) will be drastically lower and on the order of a wavelength [8]. Surveying the current crop of existing (L-, C-, and X-band) and near-future satellites (adding P-band), quickly indicates that their slant range resolutions are significantly poorer than a wavelength. Thus, all returns will anyway appear unresolved within the viewing depth of the radar, such that meaningful subsurface imaging is not possible. It is in the context of these demanding challenges that the virtual bandwidth SAR (VB-SAR) scheme was proposed [9]. It offers the possibility of addressing these problems by offering a radical new scheme which delivers a depth resolution capability independent of a radar's bandwidth. Based on a soil radar model, VB-SAR exploits the differing temporal phase behaviors of soil features at different depths associated with changes in soil moisture content (SMC). Using a differential interferometric SAR (DInSAR) image stack, the scheme can isolate returns with a depth resolution which may be far superior to the formal range resolution of the radar. Thus, objects (including both distinct features such as landmines or archaeological remains and geological features such as bedrock) within the penetration depth of the radar system may now be resolved. Although data will very likely not be collected in equal increments of moisture change, for the imagery to be correctly scaled in depth first requires linearization of the

Manuscript received June 15, 2016; revised September 12, 2016 and January 23, 2017; accepted March 12, 2017. Date of publication October 17, 2017; date of current version December 27, 2017. The work of A. Edwards-Smith was supported by Cranfield University through an internal Ph.D. bursary award. *(Corresponding author: Keith Morrison.)*

A. Edwards-Smith was with the Centre for Electronic Warfare, Cranfield University, Swindon SN6 8LA, U.K. He is now with Martin-Baker, Oxfordshire OX44 7RJ, U.K.

K. Morrison is with the Department of Meteorology, University of Reading, Reading RG6 6BB, U.K. (e-mail: k.morrison@reading.ac.uk).

S. Zwieback was with the Institute of Environmental Engineering, ETH Zurich, CH-8093 Zurich, Switzerland. He is now with Guelph University, Guelph, ON N1G 2W1, Canada (e-mail: zwieback@uoguelph.ca).

I. Hajnsek is with the Institute of Environmental Engineering, ETH Zurich, CH-8093 Zurich, Switzerland, and also with the German Aerospace Center, Radar Concepts Department, Microwaves and Radar Institute, D-82234 Wessling, Germany (e-mail: hajnsek@ifu.baug.ethz.ch; irena.hajnsek@dlr.de).

Digital Object Identifier 10.1109/TGRS.2017.2717340

Fig. 1. View of the soil trough and linear scanner with the C-band antennas attached. Note that this photograph was taken while a different experiment was being performed, and hence the wetted area and reference trihedral deployment are different to the situation in this study. Dashed square on trough surface shows area actually wetted during this study. Solid white lines represent the real antenna beam pattern and resolution cell, and dotted-dashed black lines indicate the beam pattern and resolution cell obtained using TP. Coordinate notation as used in text.

moisture changes before application of the VB-SAR scheme. In this paper, we present experimental results utilizing a buried trihedral to validate the basic principles of the VB-SAR scheme. We derive imagery with depth resolutions far superior to that across the input DInSAR stack. We also discuss its real-world application and consider possible limitations of the scheme.

II. Measurements

A. Laboratory Details

The experimental data for this paper were collected using an indoor microwave measurement facility. A view of the facility is shown in Fig. 1. A linear scanner is centrally located down the length of a 4 m (l)$\times$ 1 m (w)$\times$ 0.9 m (h) soil trough. The trough is constructed from plywood with no metal fasteners in order to avoid unwanted radar returns. The radio frequency (RF) subsystem consists of an HP 8719ES vector network analyser, which acts as both the RF source and RF receiver for the system, connected to the antennas by means of flexible coaxial cable runs. Movement is by a computer controlled servomotor which allows accurate mechanical positioning of the antennas along the scanner in order to allow synthetic aperture techniques to be used. The antennas are momentarily static while each RF measurement is made. The system can be automatically set to acquire image sequences at precisely timed intervals. This enables unsupervised regular sampling over long periods of time to study the slowly evolving scattering behavior of a scene.

B. Soil Study

The schematic of the target scene used in this experiment is shown in Fig. 2. The trough volume was filled with fine kiln-dried building sand to act as the soil, except for the central 1 m $\times$ 1 m region. This region contained a

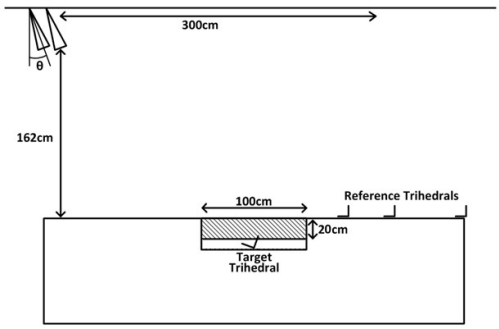

Fig. 2. Schematic of the experimental setup. The hatched area shows the position of the gravel-soil mixture. The blank area below the hatched area indicates the assumed furthest extent of the added moisture. The apex of the target trihedral is 26.5 cm below the trough surface.

Fig. 3. (Top) Preparation of the soil target. (Bottom right) Wetted 1 m $\times$ 1 m area at the location of the gravel-soil mixture. (Bottom left) Positioning of the reference trihedrals. Darkening of soil surface in vicinity of surface reference trihedrals is caused by shadow.

10%-gravel:90%-soil mixture by volume, which extended down to a depth of 20 cm. The gravel was randomly shaped and around 1 cm in diameter. The surface of the sand was smoothed off, level with the trough edges. The gravel-soil mixture sat directly above a square 12-cm trihedral with a theoretical radar cross section (RCS) of 2.2 m^2 at 5 GHz. It was tilted backwards to present a maximum RCS at a free space incidence angle of 20°. The apex of the trihedral was placed at a depth of 26.5 cm. Several surface-mounted reference trihedrals were placed at various positions on the soil and trough. Fig. 3 illustrates the preparation of the soil sample, showing the gravel-soil mixture placed over the buried trihedral, the wetting of the mixture and the positioning of the surface reference targets.

The first stage of the experiment involved adding carefully controlled amounts of water to the dry soil and gravel volume above the buried trihedral. This allowed the phase response of the trihedral to changes in SMC to be characterized. The total amount of water added was 26 L; initially in steps of 200 mL up to 2 L and then in steps of 2 L up to 26 L, added in total. Moisture additions were equally spaced at half-hour intervals. The water was added by using a trigger sprayer for the 200 mL additions, and then a watering can with a rose sprinkler was used for the 2 L additions. A volume of 26 L was chosen as previous experience indicated this amount of water would

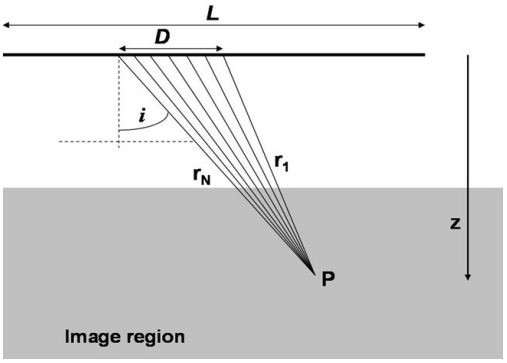

Fig. 4. Schematic of the principle of the TP imaging technique. A scan is made up of a sequence of elemental measurements across the synthetic aperture L. A subaperture D provides a single profile through the image volume at a series of equally spaced points along the slant-range direction. By sliding the subaperture along the full aperture, a continuous series of profiles build up the TP image. Importantly, each image point is reconstructed at the same incidence angle i as used for the point P at depth z.

cause moisture to travel down to a depth of 26.5 cm, which informed on the depth placement of the trihedral. Additionally, 26 L was estimated to represent the point at which attenuation would cause the trihedral to just be lost in the radar imagery, thus providing a maximum variation in signal as the trihedral feature reappeared during the drying phase. Assuming all the water stayed within an 1 m × 1 m × 0.265 m active wet region bounded by the soil surface and the trihedral apex, leads to a final maximum volumetric SMC of 9.8%. While the wetting study was done over one day, the drying study commenced after the final water addition and extended over a much longer 35-day interval. During this time, the scene was reimaged at approximately 80-min intervals. In order to promote evaporation, two portable fans were used to blow air over the surface of the soil during most daytime intervals, positioned so that they were well outside the antenna beam patterns and the airflow did not disturb the surface.

C. Radar Imaging

Radar imagery in this paper was generated using the tomographic profiling (TP) process [10]. TP does not provide a tomographic scene reconstruction per se, however, the presented result has similarity to the final image product from tomographic schemes, namely, a 2-D vertical backscattering profile through a volume.

The TP process requires data collected in a similar fashion to conventional SAR imaging across a synthetic aperture; the difference is that for TP the antennas are rotated 90° so they look along the direction of platform travel and so only image a transect directly below the scanner, rather than out to the side. As such, with TP we sacrifice information in the across-track direction, to importantly gain information in the vertical direction. This is important, and it allows us to spatially isolate surface and subsurface features, and visualize spatially the dynamic processes that occur within a soil that are normally hidden from us in SAR imagery. Fig. 4 shows a schematic of the TP process.

For this paper, a cluster of C-band antennas was mounted on the scanner, pointing forward at 20° from nadir. The antennas had 30° and 50° 3-dB real beamwidths in the along- and across-track directions, respectively, such that surface and volume returns would suffer significant range layover and offer no vertical discrimination through the soil. To overcome this, in the TP scheme, the beam is sharpened across a subaperture of the collected synthetic aperture. It is steered to the desired look angle by applying a suitable phase ramp across the subaperture elements. In the slant range direction, resolution is provided by the frequency bandwidth. In the across-track direction (across the width of the trough), however, the synthetic aperture processing does not sharpen the antenna beam; rather, this is given by the width of the real beam. Each subaperture provides an independent narrow-slice look through the soil at the chosen angle, and their successive along-track offsets builds up an image of the scene below the scanner transect. An important property of TP imagery is that the incidence angle is the same at any pixel throughout the image, here chosen to be 10°. The achieved vertical and horizontal resolutions in a TP image are a combination of contributions from the sharpened beam, bandwidth, and real across-track beam [10]. The look angle was chosen as a compromise between high resolutions obtained with a steep angle and representative SAR imaging geometry.

All scans were collected over a 3-m aperture using 151 aperture points and a sampling interval of 2 cm. At each sample position, 1601 frequency points were collected over a 2-GHz bandwidth across a frequency range of 4–6 GHz. Each scan took just over 6 min to collect. In order to remove positioning drift, the system was set to "home" against an end stop microswitch after each scan. Analysis indicates that the residual positioning error is controlled to a fraction of a millimeter, insignificant compared to the wavelength in use and the large phase shifts observed from the buried target.

Two sets of imagery were produced from the data collection. A high-resolution image set was produced utilizing the full bandwidth available. Slant range, cross-slant range, and across-track resolutions were estimated to be 7.5 cm, 35 cm, and 1.3 m, respectively, at the soil surface. This leads to vertical and horizontal resolutions of 14 and 36 cm, respectively, at the soil surface. A second low-resolution image set was produced using the same parameters as the high-resolution reconstructions, but with a reduced bandwidth of 150 MHz across the frequency range of 4–4.15 GHz. This gave a slant range estimate of 1 m, leading to a free-space vertical resolution of 105 cm, and a horizontal resolution of 52 cm at the soil surface. Fig. 5 shows an example of a high-resolution TP image (produced from the last scan from the drying period). The buried trihedral is clearly visible in the image. The returns on the right side of the image are two surface reference trihedrals, as well as a group of subsurface features not associated with this study.

III. Data Analysis

The analysis strategy is to first use the high-resolution imagery to investigate the "best-performance" result for VB-SAR. The resolution allows us to separate the returns from

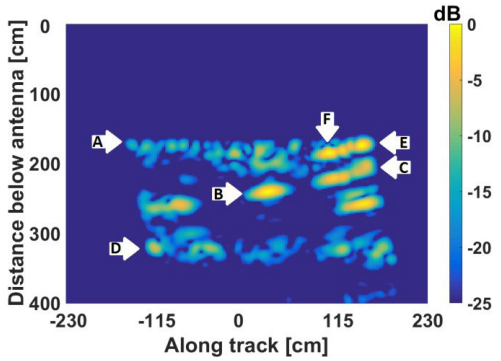

Fig. 5. Example of high–range-resolution TP image prepared using entire real bandwidth. Arrow A indicates the soil surface, with the strong returns at right being generated by some of the surface reference trihedrals, B shows the buried trihedral of interest to this study, C shows the returns caused by soil moisture probes present in the sand trough, D shows the returns from the floor of the trough (note attenuated returns in middle of floor, caused by the wetted soil in the region above the trihedral), E shows the return from the single surface reference trihedral in the middle of the trough, and F shows the combined return from the reference trihedrals placed at the edge of the trough. (These appear below the surface as they were placed on the edges of the trough and the TP process provides no resolution in the cross track direction and so places them onto the central plane of the image.)

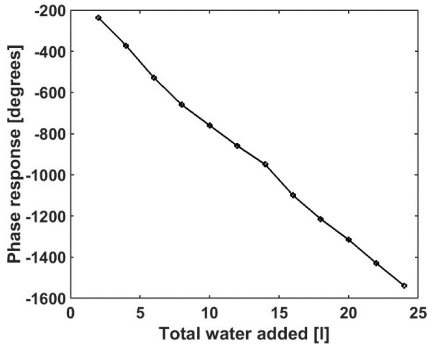

Fig. 6. Corrected phase history of buried trihedral during 2 L water additions. Trend not plotted after 24 L added due to soil attenuation obscuring the trihedral.

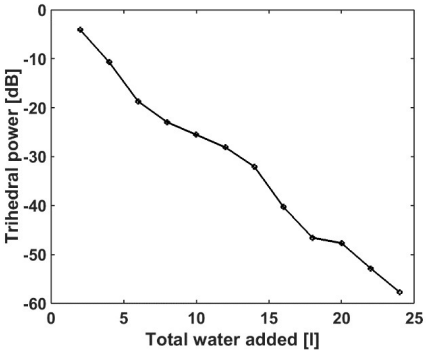

Fig. 7. Backscatter history of buried trihedral during 2 L water additions. Trend not plotted after 24 L added due to soil attenuation obscuring the trihedral.

the surface, soil volume, and buried feature. This scheme is then applied to the low-resolution imagery in which the returns are no longer separable by depth, and which better represents a real-world SAR application.

The temporal amplitude-phase behavior of the buried trihedral is extracted, first in the wetting period to establish a moisture-phase relationship, and second in the drying period for exploitation in a demonstration of the VB-SAR scheme. Behavior is compared with the returns from the surface in the wetted area and from a subsurface feature within a dry region.

A. Moisture-Phase Relation

The phase history during the wetting period is of key interest to establish the moisture-phase relationship for the soil, to be utilized in the analysis of the drying period data. A key assumption of VB-SAR is that the variation in phase of a buried target is linear with SMC change [11]. Fig. 6 plots the phase response of the buried trihedral to the 2 L additions of water. As can be seen, the phase decreases linearly with SMC. The phase value extracted from the 26 L scan is not shown as the buried trihedral was no longer visible due to strong soil attenuation. From Fig. 6, we derive a moisture-phase relationship γ of 0.057°/mL.

For comparison, the backscatter history of the buried trihedral is shown in Fig. 7. This can be expected to be linear in decibel [11]. While this is mostly the case, there are significantly more fluctuations away from linear than for the phase curve. This supports the idea that the phase is the more robust parameter in the measurement of SMC, a result found in [11].

B. Drying Period

Fig. 8 shows a sequence of three TP images over the drying period, from the wettest to driest soil. The buried trihedral was seen to recover in brightness through the interval. Figs. 9 and 10 show the phase and backscatter histories, respectively, over the entire drying interval extracted from the pixel corresponding to the buried trihedral from the high-resolution TP data set.

The curves have been corrected for any unwanted artifacts of the measurement system by referencing them against the primary reference trihedral on the soil surface. This corrected for system drift which is principally due to diurnal temperature fluctuations in the laboratory.

With the value of γ derived above from the wetting period, it was possible to quantitatively interpret the observed phase curve in Fig. 9 in terms of SMC. As phase change should be linear with SMC change [9], [11], Fig. 9 shows that the change in SMC was very nonlinear over the drying period. It is interesting to note that visually two different drying processes appear to be present; a rapid one dominant until the differential phase had returned to $-600°$ after around 150 h of drying, which then rapidly settled into a much slower drying process until the end of the experiment. We might conjecture that this can be explained by the initial drying process being dominated by the evaporation of moisture from the upper portion of the

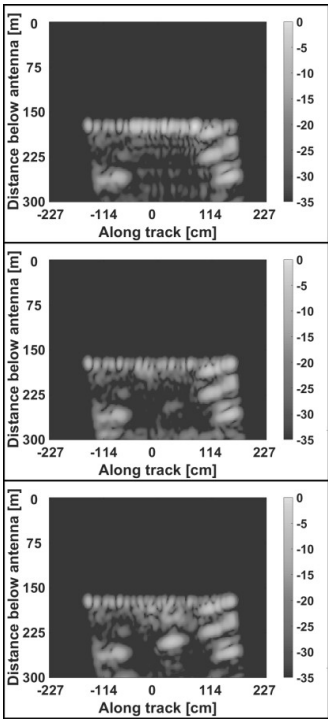

Fig. 8. Selection of TP images from the drying period, with an SMC change of 3.5% between each image showing the re-emergence of the buried trihedral and the decrease in the surface backscatter as the soil dries. (Top) First scan of the drying period (with an SMC of 9.8%), (Middle) From the middle of the drying period (6.3% SMC). (Bottom) Last scan collected as part of this study (2.7% SMC). Presented over a 35-dB dynamic range, images normalized relative to each other.

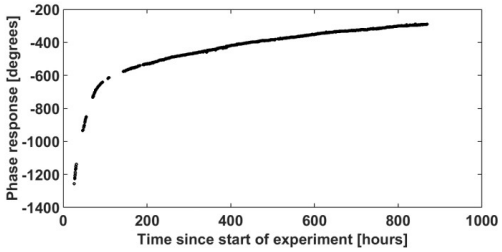

Fig. 9. Phase history for the buried trihedral during drying period after corrections applied.

soil volume, then once the upper portion was dry the loss of moisture was from the lower portions which could reasonably be expected to be a slower process.

With a starting SMC of 9.8%, the total phase change in Fig. 9 indicates a drying to 2.7%. These SMC estimates assume that the added water spread homogeneously within the active gravel-sand region and did not move outside this region. Previous work [11] informed on the choice of total water added, which was expected to travel down to just the depth of the trihedral. Previous work has also shown the phase result is little affected by the distribution of SMC above a buried target, only by the total water column above a target [9].

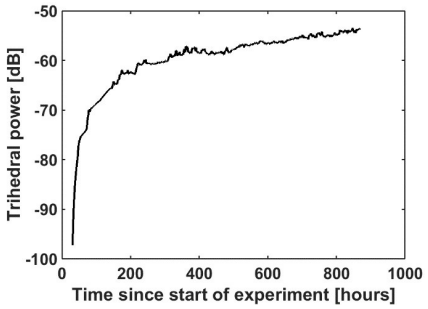

Fig. 10. Backscatter history for the buried trihedral during drying period after corrections applied.

There are small gaps in the measurements in Fig. 9, primarily near the start of the data. Because the phase variation is smooth it was meaningful to interpolate across these regions to recover missing data. It was decided to resample the whole data set to 1-h intervals, slightly higher than the nominal sampling rate of 80 min, to ease data manipulation and visualization.

IV. VB-SAR

A. VB-SAR Theory

The dielectric properties of a soil perceived by a radar wave are set by its chemical makeup and water content. Over the timescales of interest for remote sensing, only the moisture can be expected to change so the variations in dielectric properties can be assumed to be solely dependent upon SMC variations [8], [12]. The VB-SAR imaging scheme proposed by [9] leverages upon the fact that the soil dielectric properties over a series of DInSAR acquisitions will vary in a predictable manner quantifiable according to the SMC variations.

The details of the VB-SAR model and technique have previously been described in [9], but are briefly reviewed here. As the refractive index of a soil is higher than the refractive index of air, a radar wave is compressed within the soil. Thus, a given real frequency in air f_R will behave with respect to phase as a wave of a higher virtual frequency f_V within the soil according to

$$f_V = f_R \sqrt{\epsilon}_r \tag{1}$$

where $\sqrt{\epsilon}_r$ is the refractive index. This is a central principle of the VB-SAR process. Consider a temporal sequence of DInSAR acquisitions over a drying soil; the changing refractive index of the soil will lead to the fixed real frequency being transported across a range of virtual frequencies. This synthesises a virtual bandwidth (VB) B_V over the series of images set by the total change in the refractive index

$$B_V = f_R \Delta \sqrt{\epsilon}_r. \tag{2}$$

These virtual frequencies can be treated just as for a real bandwidth.

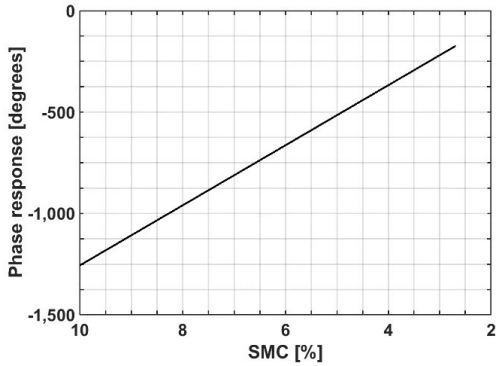

Fig. 11. Phase history of buried trihedral interpolated to linear steps in SMC.

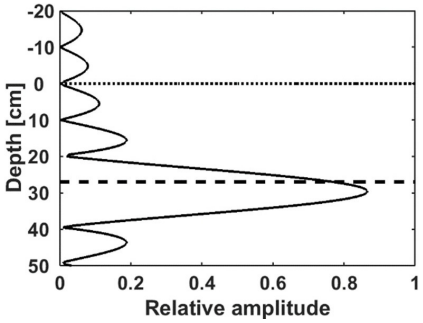

Fig. 12. VB-SAR depth profile formed using only phase history extracted from high-resolution TP images. Dotted line indicates the position of soil surface, and dashed line indicates the position of the buried trihedral.

B. Data Preparation

Fig. 9 indicates that the SMC change was not linear over the image stack during this study. The VB-SAR scheme expects the provision of an interferometric time series at equal intervals of soil moisture change. Thus, in order to prepare the data for use with VB-SAR, the data shown Figs. 9 and 10 were resampled to be linear in SMC. Knowing the starting SMC was 9.8%, and using the γ term with Fig. 9 phase changes, it was possible to calculate the absolute SMC for each measurement. This was then resampled to provide a linear change in SMC as shown in Fig. 11.

C. VB-SAR Processing

The resampled and windowed amplitude and phase histories are then passed through a complex fast Fourier transform (FFT) to translate the data from the frequency domain to the time (equivalently, range) domain. A Kaiser window with β set to 0.2 was found to give acceptable sidelobe reductions, and allowed sidelobes to be almost eliminated from the final displayed VB-SAR image while keeping spreading in the depth dimension to an acceptable level.

The VB-SAR process detailed so far would provide a subsurface depth profile, albeit one without any sense of scale in the depth direction. In order to apply a scale to the depth profile, the unambiguous range in the image R_{unabg} must be calculated. This is calculated in the usual fashion but using the virtual frequency step size (f_{vstep}) and scaling by the average refractive index of the soil across the DInSAR stack n_{av} that is

$$R_{\text{unabg}} = \frac{cn_{\text{av}}}{2f_{\text{vstep}}} \tag{3}$$

where c is the speed of light in free space. Note that in order to calculate f_{vstep} and n_{av} accurately, the absolute SMC in each scan must be known. With a known SMC in each scan and a known soil texture, the refractive index of the moist soil can be calculated using published soil models [8], [12], from which (2) can be used to calculate f_{vstep}

$$f_{\text{vstep}} = \frac{B_V}{n_{\text{scans}}} \tag{4}$$

where n_{scans} is the number of scans across which the VB was generated. If calibrated SMC information is not available, the VB-SAR process can still be performed but it will not be possible to apply a depth scale to the profiles produced.

The above process provides a single depth profile from a single pixel in the input images. To obtain a VB-SAR image, this process is repeated pixel-by-pixel across the input image stack. Stacking the resulting color-coded range profiles next to each other, forms a complete 2-D VB-SAR image across the TP transect. In the case of side-looking SAR, the use of each ground pixel across the 2-D scene would provide a full 3-D VB-SAR image.

D. VB-SAR From High-Resolution TP

The initial test of VB-SAR was performed using the complex history of the buried trihedral extracted from the high-resolution TP data. After resampling to a linear SMC trend, the phase history fed to the VB-SAR processor will be a straight line. An FFT of a linear phase history will produce a single peak, at an offset from zero range defined by the gradient. For the buried trihedral, the appearance of this peak at the correct depth in the FFT output with a depth scale applied would demonstrate successful VB-SAR processing.

The result of performing VB-SAR on the phase history of the buried trihedral extracted from the high-resolution TP is shown in Fig. 12. For this process, the amplitude history was artificially set to be constant at 1 to minimize any unwanted effects that might otherwise arise from the asymmetric weighting of the phase history by the brightening of the trihedral over the study period.

In order to apply an accurate depth scale, the model presented in [8] and the SMC estimates previously produced were used to calculate the refractive index of the soil in each scan. By using the average refractive index of the soil over the series of scans it was possible to calculate the B_V. This gave the unambiguous range, and hence the depth for each output bin from the VB-SAR FFT. This calculation resulted in estimates of 2.21 for the average refractive index of the soil, and from (1) and (2), 3.38 GHz for the B_V, providing a range

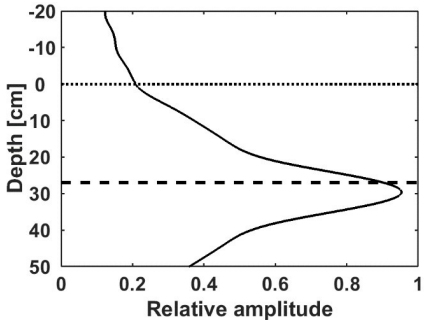

Fig. 13. VB-SAR depth profile formed using complex history extracted from high-resolution TP images. Dotted line indicates the position of soil surface, and dashed line indicates the position of buried trihedral.

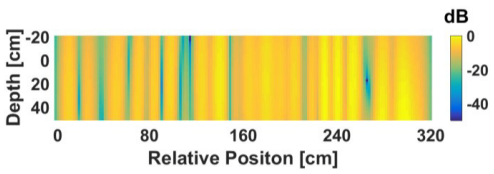

Fig. 14. Example of one of the low-resolution TP images used in the VB-SAR DInSAR stack, showing that surface and subsurfaces returns are no longer separable.

resolution of 0.04 m and an unambiguous range of 46 m. The retrieved depth for the buried trihedral is almost 30 cm—close to the actual depth of 26.5 cm—demonstrating that the VB-SAR process is effective.

The process was repeated, but this time including the asymmetric amplitude weighting shown in Fig. 10. As shown in Fig. 13, its inclusion causes the impulse response to widen and distort, although the depth of the peak is unchanged.

E. VB-SAR From Low-Resolution TP

The extraction of the buried feature's complex history is an unrealistic data set with regard to side-looking SAR imagery gathered by satellites and aircraft. In such imagery, it would not have been possible to separate the buried trihedral returns from the overlain combination of all returns within the ground pixel. In order to emulate the data that is obtained from spaceborne side-looking SAR systems with one single complex ground pixel per soil column, it is necessary to use the low-resolution TP data. The lowered range resolution of 1 m means that a single pixel contains contributions from the soil surface, soil volume, and the buried trihedral. Application of the VB-SAR process should still lead to a high-resolution image product in which the buried trihedral and surface appear as separated features. Fig. 14 shows an example of a low-resolution TP image. The surface and subsurface features can no longer be resolved, in particular, the surface and subsurface returns are no longer separable.

The VB-SAR process still requires provision of a time series in which the soil moisture changes are linear (or equivalently, the linear phase change). As such, the SMC estimates extracted from the high-resolution TP data were used, which meant that the parameters calculated using the SMC estimates (average refractive index of the soil, VB, range resolution, and unambiguous range) were identical.

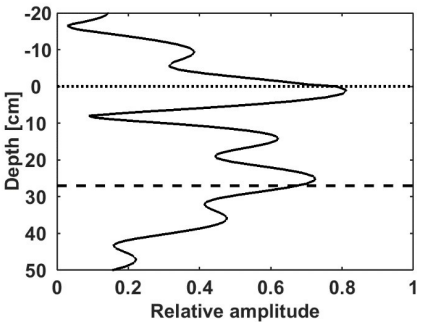

Fig. 15. VB-SAR depth profile produced from low-range-resolution TP data. Dotted line indicates the position of soil surface, and dashed line indicates the position of buried trihedral.

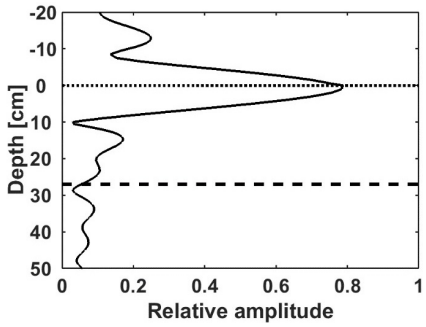

Fig. 16. VB-SAR depth profile obtained using surface pixel from dry soil area of low-range-resolution TP data, showing surface and all other returns correctly resolved to 0 depth. Dotted line indicates the position of soil surface, and dashed line indicates the position of buried trihedral.

Fig. 15 shows the result of applying VB-SAR to a single pixel extracted at the position of the buried trihedral across the low-resolution DInSAR stack. Significantly, the surface return and the buried trihedral returns have been separated, clearly demonstrating the improvement in range resolution generated by VB-SAR processing. The buried trihedral appears at a slightly shallower depth compared to the high-resolution retrievals in Figs. 12 and 13, likely due to blending with the sidelobes of the surface return. This conclusion is further supported by noting that the surface return has moved fractionally deeper than 0 cm. For Fig. 16, the VB-SAR technique was applied to a region of sand that was left dry and undisturbed over the DInSAR stack. All returns, irrespective of their depth, appear at 0m, as the zero change in phase will be interpreted by the VB-SAR scheme as a surface target with no volume contribution. The depth scale for this depth profile was generated using the SMC history extracted from the wetted area.

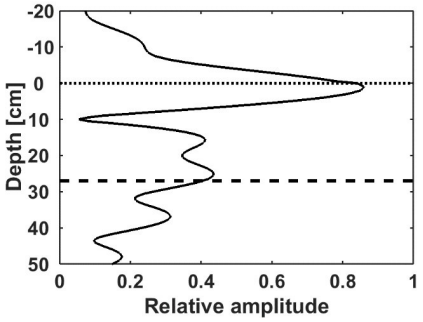

Fig. 17. VB-SAR depth profile produced from low-range-resolution and low cross-slant range resolution TP data. Dotted line indicates the position of soil surface, and dashed line indicates the position of buried trihedral.

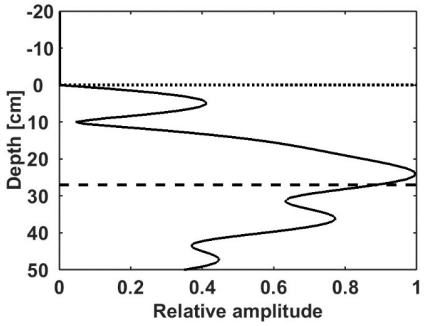

Fig. 18. VB-SAR depth profile produced from low-range-resolution and low cross-slant range resolution TP data with dc component of complex history removed. Dotted line indicates the position of soil surface, and dashed line indicates the position of buried trihedral.

By shortening the subaperture used during TP processing, it was possible to degrade the along-track resolution to 1 m, which will have increased the clutter return (clutter being the surface and soil volume). As could be reasonably expected, the VB-SAR result in Fig. 17 shows that the surface return and its associated sidelobes have increased relative to the buried target's return, due to the lowered resolution primarily capturing more surface return. However, the depth of the trihedral has again been correctly recovered.

As the surface should have a negligible phase change over the change in SMC [11], a direct current (dc) removal scheme should reduce the near unchanging surface response from the depth profile. The result is shown in Fig. 18, which shows that the dc removal has worked well in suppressing the surface return to improve the view of the buried feature.

F. Full VB-SAR Imagery

As a final demonstration of the VB-SAR scheme, a full image formed by repeating the VB-SAR process at each pixel along the trough is shown in Fig. 19; a 10° horizontal shear operation has been applied to the entire image in order to obtain the correct geometry. Note that the artifacts at

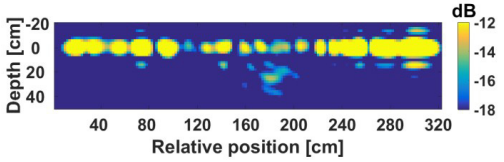

Fig. 19. Full VB-SAR image retrieved from the high-resolution imagery.

approximately ±15 cm depth are residual sidelobes of the strong soil surface returns that remain after the application of the Kaiser window. A heavier windowing function could further reduce these at the expense of widening the surface and buried target peaks. The remarkable improvement the VB-SAR scheme has provided in the vertical resolution of the scene can be appreciated by comparison with Fig. 14.

In the dry areas of the scene (in this image approximately 0−110 and 220–320 cm horizontal position) all targets, including those buried (as indicated by arrow "C" in Fig. 5), appear at zero depth. This is further evidence that the VB-SAR process is working as the VB-SAR theory predicts these dry areas experienced no SMC change during the experiment so no B_V was synthesised. Presentation of a flat phase history to the FFT results in a peak at zero depth. In these areas, all returns from all depths over the series of radar images are effectively summed and placed at zero depth which explains the very strong surface return seen in these dry areas in Fig. 19.

G. Real-World Considerations

The application of the VB-SAR process is via interferometric processing, and production of an interferometric set would use standard DInSAR processing techniques to deal with unwanted above-ground phase terms associated with baseline separation, platform positional errors, and atmospheric moisture. The need for the maintenance of coherence between interferometric pairs means the angular separation between baselines is always small such that the fractional change in the subsurface path (and hence phase) associated with angular differences between interferometric collections will be correspondingly small and of secondary consideration.

This study operated in a laboratory environment which allowed some simplifications and removal of likely real-world impediments. In side-looking SAR data, the phase history of any buried targets will not be isolatable from other contributions, and so the method of extracting SMC used here will not be feasible except for a dominant subsurface feature. The effect of increasing surface roughness will be to increase the surface return relative to the subsurface return [25], likely compromising detection of the subsurface signal.

VB-SAR separates features by virtue of differing linear phase histories, which ideally requires presentation of the phase history to the processor in equal steps of soil moisture change. While *in situ* measurement (either manually or with fixed automated stations) of SMC would be acceptable over small study regions, a global implementation of the scheme will require estimation of needed parameters from the SAR

imagery itself. Current implementations of SMC retrieval are based on relationships between moisture and backscatter brightness, and these could be utilized for the estimation of moisture parameters for use by the VB scheme [13]–[16]. If SMC information is not available, it is possible to operate the VB-SAR scheme in a "detection mode." This would omit the SMC linearization step and pass the phase history directly to the FFT. For moderate phase nonlinearity subsurface objects would still show a phase shift and so appear separated and below the surface, although the depth scale would be inaccurate [9]. In a case of extreme divergence from linearity, the phase disturbance evident at a pixel would indicate the presence of a buried feature but without being able to produce a properly focused image or correct depth scale. For a sloping or uneven surface, a subsurface feature will appear at a representative "effective depth" just as is the case for an interferometric height retrieval across an undulating forest canopy. The VB-SAR scheme only improves the below ground slant range resolution; cross-slant range resolution is unimproved so objects at the same depth in a ground pixel will appear as one combined return in the VB-SAR depth pixel.

There is a question of whether subsurface objects would be detectable using existing radar platforms. Current spaceborne SAR systems have Noise Equivalent Sigma Zero (NESZ) figures on the order of -20 dB [17]–[19], such that even modest attenuations associated with low SMC will rapidly compromise measurement of subsurface features. In comparison, airborne systems typically have an extra 30 dB of sensitivity and so are currently more suited to VB-SAR [20]–[22]. Geologic and climatic considerations produce preferred regions for VB-SAR; a soil should be as dry as possible to minimize attenuation while still providing a large enough change in SMC to generate sufficient VBs. This tradeoff will vary for different targets and different radar systems but it can be modeled using the soil model found in [8].

V. Conclusion

This study has demonstrated VB-SAR imaging within the laboratory environment. A scene consisting of a buried trihedral under a sand and gravel mixture was set up and the scene repeatedly imaged. Controlled amounts of water were then added to the surface of the sand and gravel mixture, and the scene was allowed to dry naturally which produced a radar data set covering both wetting and drying periods. The imagery was fed to the VB-SAR processor which successfully produced high-resolution subsurface imagery for two different cases; first using the complex history of a buried trihedral only, and second using the combined complex histories that contained contributions from the surface, soil volume, and a buried trihedral. The latter case better emulated the situation with data from a real-world, side-looking SAR system.

The study has validated the basic concept of VB-SAR; it has successfully demonstrated standoff subsurface imaging with a vastly increased range resolution over that given by the real bandwidth of the radar system, and provided direct and unambiguous discrimination of surface and subsurface objects. Techniques for mitigating complications that a real-world VB-SAR scheme may have to contend with were also discussed. Future experimental work will include polarimetric dependencies of VB-SAR.

Acknowledgment

The authors would like to thank Dr. M. Finnis for extensive assistance with the GB-SAR system and Dr. D. Andre for useful technical discussions.

References

[1] D. J. Daniels, *Ground Penetrating Radar, Encyclopaedia of RF and Microwave Engineering*. Hoboken, NJ, USA: Wiley, 2005.
[2] A. G. Yarovoy, T. G. Savelyev, P. J. Aubry, and L. P. Ligthart, "Array-based GPR for shallow subsurface imaging," in *Proc. 4th Int. Workshop Adv. Ground Penetrating Radar*, Jun. 2007, pp. 12–15.
[3] M. Sato, K. Doi, and K. Takahashi, "Advanced GPR for archaeological survey," in *Proc. IEEE Int. Geosci. Remote Sens. Symp. (IGARSS)*, Jul. 2013, pp. 1395–1398.
[4] T. G. Farr and P. Paillou, "Radar remote sensing of the Sahara landscape," in *Proc. 9th Eur. Conf. Synth. Aperture Radar (EUSAR)*, Apr. 2012, pp. 717–718.
[5] P. Paillou and A. Rosenqvist, "A JERS-1 radar mosaic for subsurface geology mapping in East Sahara," in *Proc. IEEE Int. Geosci. Remote Sens. Symp. (IGARSS)*, vol. 3. Jul. 2003, pp. 1870–1872.
[6] P. Paillou, S. López, T. Farr, and A. Rosenqvist, "Mapping subsurface geology in Sahara using L-band SAR: First results from the ALOS/PALSAR imaging radar," *IEEE J. Sel. Topics Appl. Earth Observ. Remote Sens.*, vol. 3, no. 4, pp. 632–636, Dec. 2010.
[7] J. Mccauley *et al.*, "Subsurface valleys and geoarcheology of the eastern Sahara revealed by shuttle radar," *Science*, vol. 218, no. 4576, pp. 1004–1020, 1982.
[8] M. T. Hallikainen, F. T. Ulaby, M. C. Dobson, M. A. El-Rayes, and L.-K. Wu, "Microwave dielectric behavior of wet soil-part 1: Empirical models and experimental observations," *IEEE Trans. Geosci. Remote Sens.*, vol. GE-23, no. 1, pp. 25–34, Jan. 1985.
[9] K. Morrison and J. C. Bennett, "Virtual bandwidth SAR (VB-SAR) for centimetric-scale sub-surface imaging from space," *Int. J. Remote Sens.*, vol. 36, no. 7, pp. 1789–1808, 2015.
[10] K. Morrison and J. C. Bennett, "Tomographic profiling—A technique for multi-incidence-angle retrieval of the vertical SAR backscattering profiles of biogeophysical targets," *IEEE Trans. Geosci. Remote Sens.*, vol. 52, no. 2, pp. 1250–1255, Feb. 2014.
[11] K. Morrison, J. C. Bennett, and M. Nolan, "Using DInSAR to separate surface and subsurface features," *IEEE Trans. Geosci. Remote Sens.*, vol. 51, no. 6, pp. 3424–3430, Jun. 2013.
[12] V. L. Mironov, M. C. Dobson, V. H. Kaupp, S. A. Komarov, and V. N. Kleshchenko, "Generalized refractive mixing dielectric model for moist soils," *IEEE Trans. Geosci. Remote Sens.*, vol. 42, no. 4, pp. 773–785, Apr. 2004.
[13] P. C. Dubois, J. V. Zyl, and T. Engman, "Measuring soil moisture with imaging radars," *IEEE Trans. Geosci. Remote Sens.*, vol. 33, no. 4, pp. 915–926, Jul. 1995.
[14] P. J. van Oevelen and D. H. Hoekman, "Radar backscatter inversion techniques for estimation of surface soil moisture: EFEDA-Spain and HAPEX-Sahel case studies," *IEEE Trans. Geosci. Remote Sens.*, vol. 37, no. 1, pp. 113–123, Jan. 1999.
[15] M. Zribi, N. Baghdadi, N. Holah, and O. Fafin, "New methodology for soil surface moisture estimation and its application to ENVISAT-ASAR multi-incidence data inversion," *Remote Sens. Environ.*, vol. 96, nos. 3-4, pp. 485–496, 2005.
[16] N. G. Meade, L. D. Hinzman, and D. L. Kane, "Spatial estimation of soil moisture using synthetic aperture radar in Alaska," *Adv. Space Res.*, vol. 24, no. 7, pp. 935–940, 1999.
[17] G. Krieger *et al.*, "TanDEM-X: A satellite formation for high-resolution SAR interferometry," *IEEE Trans. Geosci. Remote Sens.*, vol. 45, no. 11, pp. 3317–3341, Nov. 2007.
[18] *Sentinel-1: ESA's Radar Observatory Mission for GMES Operational Services*, document ESA SP 1322/1, Mar. 2012.
[19] Y. Kankaku, M. Sagisaka, and S. Suzuki, "PALSAR-2 launch and early orbit status," in *Proc. IEEE Int. Geosci. Remote Sens. Symp. (IGARSS)*, Jul. 2014, pp. 3410–3412.
[20] A. G. Fore *et al.*, "UAVSAR polarimetric calibration," *IEEE Trans. Geosci. Remote Sens.*, vol. 53, no. 6, pp. 3481–3491, Jun. 2015.
[21] A. Reigber *et al.*, "System status and calibration of the F-SAR airborne SAR instrument," in *Proc. IEEE Int. Geosci. Remote Sens. Symp. (IGARSS)*, Vancouver, BC, Canada, Jul. 2011, pp. 1520–1523.

[22] R. Baque, R. Baqué, and P. Dreuillet, "The airborne SAR-system: RAMSES NG airborne microwave remote sensing imaging system," in *Proc. IET Int. Conf. Radar Syst. (Radar)*, Glasgow, U.K., Oct. 2012, pp. 1–4.
[23] S. Zwieback, S. Hensley, and I. Hajnsek, " Polarimetric first-order model of soil moisture effects on the DInSAR coherence," *Remote Sens.*, vol. 7, no. 6, pp. 7571–7596, 2015.
[24] A. Moreira, P. Prats-Iraola, M. Younis, G. Krieger, I. Hajnsek, and K. P. Papathanassiou, "A tutorial on synthetic aperture radar," *IEEE Geosci. Remote Sens. Mag.*, vol. 1, no. 1, pp. 6–43, Mar. 2013.
[25] J. Shi, J. Wang, A. Y. Hsu, P. E. O'Neill, and E. T. Engman, "Estimation of bare surface soil moisture and surface roughness parameter using L-band SAR image data," *IEEE Trans. Geosci. Remote Sens.*, vol. 35, no. 5, pp. 1254–1266, May 1997.

Alexander Edwards-Smith received the M.Eng. degree in electronic and electrical engineering from the University of Bath, Bath, U.K., in 2012.

He was a Research Student with Cranfield University, Shrivenham, U.K., from 2014 to 2017. He is currently with Martin-Baker, Oxfordshire, U.K.

Keith Morrison received the B.Sc. degree in physics with astrophysics from the University of Leicester, Leicester, U.K., in 1983, and the Ph.D. degree in astronomy and astrophysics from the University of St. Andrews, St. Andrews, U.K., in 1987.

He has been involved in SAR research for over two decades. His first job was with the British Antarctic Survey, Cambridge, U.K. This was followed by a research post at the University of Sheffield, Sheffield, U.K., from 1994 to 2000, based within the Sheffield Centre for Earth Observation Science. From 2000 to 2002, he was with DERA/QinetiQ, Malvern, U.K. From 2002 to 2016, he was with Cranfield University, Shrivenham, U.K. Over this interval, he also undertook a sabbatical at the University of Adelaide, Adelaide, SA, Australia, in 2005, and then at the Microwaves Institute of the German Aerospace Centre, Wessling, Germany, in 2007. Since 2016, he has been a Professor in earth observation with satellite radars with the University of Reading, Reading, U.K. His primary interest has been the design and construction of world-leading indoor laboratory and outdoor field-based systems for the measurement of biogeophysical parameters with SAR.

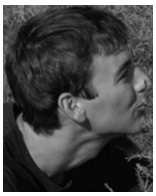

Simon Zwieback received the M.Sc. degree in geodesy and geophysics from the Vienna University of Technology, Vienna, Austria, in 2011, and the Ph.D. degree in environmental engineering from the Swiss Federal Institute of Technology, ETH Zurich, Zürich, Switzerland, in 2016.

He is currently a Swiss National Science Foundation Post-Doctoral Fellow with the University of Guelph, Guelph, ON, Canada. His main research interests include the hydrology and geomorphology of periglacial environments, and the development of forward and inverse models in microwave remote sensing (especially radar interferometry). He is also interested in the uncertainty characterization of remote sensing products.

Irena Hajnsek (AM'01–M'06–SM'09–F'14) received the Diploma degree (Hons.) from the Free University of Berlin, Berlin, Germany, in 1996, and the Ph.D. degree (Hons.) from the Friedrich Schiller University of Jena, Jena, Germany, in 2001.

She has been a Professor of earth observation with the Institute of Environmental Engineering, ETH Zurich, Zürich, Switzerland, since 2009, and also the Head of the Polarimetric SAR Interferometry Research Group, German Aerospace Center, Microwaves and Radar Institute, Wessling, Germany. Her main research interests include electromagnetic propagation and scattering theory, radar polarimetry, SAR and interferometric SAR data processing techniques, and environmental parameter modeling and estimation. Since 2010, she has been a Science Coordinator of the German satellite mission TanDEM-X.

Dr. Hajnsek was the Technical Program Co-Chair of the IEEE IGARSS 2012 Symposium, Munich, Germany. Since 2013, she has been a member of the IEEE Geoscience and Remote Sensing Society (GRSS) Administrative Committee. Since 2016, she has been the Vice President of the IEEE GRSS Technical Committees.

A.2 EUSAR-2016 Paper

11th European Conference on Synthetic Aperture Radar
EUSAR 2016

VB-SAR For Remote Stand-off Subsurface Imaging: First Demonstration

Alexander Edwards-Smith, Centre for Electronic Warfare, Cranfield University, Defence Academy of the United Kingdom, Shrivenham, Swindon, SN6 8LA, +44 (0)1793 785605, a.edwardssmith@cranfield.ac.uk, UK
Keith Morrison, Centre for Electronic Warfare, Cranfield University, k.morrison@cranfield.ac.uk, UK

Abstract

The first experimental demonstration of the Virtual Bandwidth SAR (VB-SAR) scheme is provided. VB-SAR promises high-resolution imaging of subsurface features at large stand-off distances. This study collected a stack of C-band tomographic profiles of the backscattering through a soil as it dried. With 1m vertical resolution, a buried trihedral at a depth of 0.26m was inseparable from the soil returns, namely the surface return. Using the differing phase behaviours from the scene during drying, it was possible to separate soil and trihedral returns, and the 10cm resolution is much improved on the formal resolution offered by the real bandwidth.

1 Introduction

Virtual Bandwidth SAR (VB-SAR) is a novel technique that promises to open up a new remote sensing capability in subsurface imaging at large stand-off distances applicable to aircraft and spacecraft [1]. Ground-based and near-ground systems currently provide the only practical method for high-resolution, subsurface ground imaging. These systems rely on close-proximity measurement in order to spatially isolate vertically the surface and subsurface backscatter returns [2].

The VB-SAR scheme exploits the change in soil dielectric properties which occur when a soil's moisture changes. A real radar wave entering a soil is compressed and behaves like a wave at a higher frequency. As it dries, the real radar frequency is sequentially transported across a virtual bandwidth of frequencies. Even moderate changes in moisture can produce large virtual bandwidths; an SMC change of 10% can provide 3cm vertical resolution at C-band, and double that at X-band. In addition, the VB-SAR scheme provides an unambiguous discrimination between surface and subsurface returns. Only objects within the soil will respond in sympathy to the changes in SMC. Above ground will not experience a virtual bandwidth and so will appear at zero depth in a reconstruction. Implemented from an aircraft or spacecraft platform, it would require collection of a stack of conventional DInSAR images over an SMC change. The differential phase history at each image pixel would be processed to produce a VB-SAR depth profile at that pixel. Repeating this across the image would provide a 3D map of the soil backscatter.

This paper presents the results of a laboratory experiment which provides the first experimental demonstration of VB-SAR capability, and validation of the scheme.

2 Measurements

The measurements were carried out at Cranfield University's Ground-Based SAR (GB-SAR) Microwave Measurement Facility. In this system a 4m linear scanner sits centrally along the length of a 4m x 1m x 0.9m soil trough. Imagery is obtained by driving the antenna cluster under computer control along the length of the scanner.

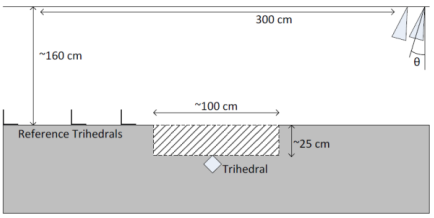

Figure 1: Overview sketch of the imaging scene. Hatched volume was filled with 90/10% sand/gravel mixture and wetted with known amounts of water.

Figure 1 shows a schematic of the soil trough during this study. The trough was filled with fine kiln-dried sand, aside from in the hatched volume. This consisted of a mixture of 10% gravel and 90% sand by volume. The randomly-shaped gravel pieces were nominally around 1cm in size. At a depth of 26cm, directly below the gravel-sand mixture, a trihedral was placed and angled to give a maximum return for the imaging geometry. The surface of the sand was level and smooth.

ISBN 978-3-8007-4228-8 / ISSN 2197-4403

11th European Conference on Synthetic Aperture Radar
EUSAR 2016

Several reference trihedrals were placed on the surface of the sand in order to allow monitoring and correction of any unwanted system-related phase and amplitude variations.

The antenna platform of the trough scanner was positioned to give an incidence angle of 20º. For each scan the platform moved along a 300cm long aperture, taking a sample every 2cm (for a total of 151 samples per scan). VV C-band measurements were made using a bandwidth of 2GHz over the interval 4-6GHz.

Subsequently, water was added to the surface of the sand/gravel mixture in precisely controlled amounts. After each addition the scene was reimaged. These wetting scans were only used to characterise the phase response of the buried trihedral to a change in SMC. In total, 28000ml of water was added. Assuming a homogeneous distribution of moisture in the wetted volume, and neglecting exfiltration of water away from this volume, this corresponds to a maximum SMC within the wetted volume of 10.6%. Subsequently, the SMC at the end of the drying period was calculated to be 4.3%. After the water addition was complete, the entire scene was allowed to dry whilst being reimaged every 30 minutes. These scans formed the basis of the dataset used for VB-SAR processing.

For the trough scanner's imaging geometry Tomographic Profiling (TP), described by [3] provides a suitable imaging algorithm. This process produces focused complex radar images by a means of synthetic beam forming across a synthetic sub aperture which is used to create an image of the scene along a transect directly below the scanner. The key attraction of TP processing for this work is that it provides vertical looks through a target volume, in this case, the sand trough. Vertical backscattering profiles of the internal volume are produced, which enables the complex development of the soil and its internal features to be studied and extracted over the TP image set.

The data was processed at two range resolutions; the maximum of 7.5cm allowed by the 2GHz bandwidth collected and an artificially lowered range resolution of 1m by only using the first 150MHz of the bandwidth. In both cases the cross-range (x-axis) resolution was the same. A sample high resolution image is shown in **Figure 2** and the same image processed at low range resolution is shown in **Figure 3**.

In Figure 2, the soil surface appears at 165cm below the antennas, and the buried trihedral is the strong isolated below-ground response close to 0m cross-range. The two returns at the top right of the soil volume are two of the surface reference trihedrals, the responses below them are the returns from a set of soil moisture probes present in the trough.

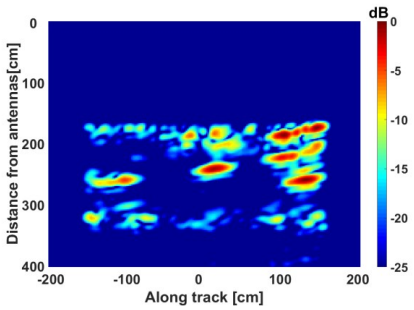

Figure 2: Example high range resolution TP image prepared using entire real bandwidth.

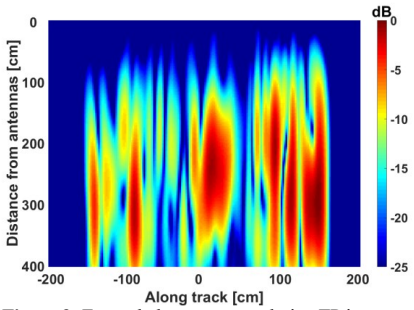

Figure 3: Example low range resolution TP image prepared using subset of real bandwidth.

The high range resolution TP images were used to generate estimates for SMC in each scan and validate a key assumption for VB-SAR, namely that the phase history of a buried target is linear with SMC change. With TP imaging we have the luxury of being able to monitor the phase response of the pixel containing the peak response of the buried trihedral. By monitoring this phase change during the wetting process (during which the SMC was known) a phase/SMC relationship (º/%) was derived. Changes in phase measured at the trihedral then informed on changes in SMC during the drying scans.

Conversely, the low range resolution images were solely used as a data source for the VB-SAR processor. By producing TP images with dramatically reduced range resolution it was possible to emulate side looking SAR data as might be acquired from an air or spaceborne SAR system where one pixel represents the entire surface and sub surface column collapsed into a ground pixel.

ISBN 978-3-8007-4228-8 / ISSN 2197-4403

11th European Conference on Synthetic Aperture Radar
EUSAR 2016

3 VB-SAR Processing

VB-SAR, as proposed by [1], promises to allow subsurface imaging at enhanced range resolutions by exploiting the variability of the dielectric properties of a soil with SMC (as described by [4]).

The core principle behind VB-SAR is that a radar wave of a given real frequency, f_r, entering a soil volume behaves as if it were a wave of a higher "virtual" frequency, f_v, due to the soil's refractive index being higher than 1. Over a series of radar images the refractive index of the soil will change due to SMC variation. This implies that over the series of images the virtual frequency also varies which leads to a virtual bandwidth, B_v, being synthesised. The virtual bandwidth generated can be calculated by

$$B_v = f_R \Delta\sqrt{\varepsilon_r} \qquad (1)$$

Where $\Delta\sqrt{\varepsilon_r}$ is the change in the refractive index of the soil over the series of radar images.

The process performed by the VB-SAR processor in this scenario is to resample the complex input data to a linear SMC change and then pass the resampled data through an FFT to produce a single depth profile of the subsurface environment. By repeating this process across the TP image a complete VB-SAR image can be produced.

The initial VB-SAR processing for this study consisted of passing the complex history of the buried trihedral extracted from the high resolution TP images through the VB-SAR processor. VB-SAR theory indicates that the phase change of a buried target is linear with changes in SMC. This assumption can be validated by passing a complex history of a buried target through a complex FFT- if the assumption is correct then a peak will appear in the output of the FFT at the correct depth. The phase history extracted from the buried trihedral during the drying period is shown in **Figure 4**.

It is clear that the phase history is non-linear over time. This is presumed to be due to uneven drying rates; in the early drying period it is reasonable to assume that the rate of SMC decrease was higher due to higher evaporation.

However, it is possible to resample this history to a linear SMC change by converting the phase value to an SMC value for each sample. This will then result in a linear phase history being fed to the FFT.

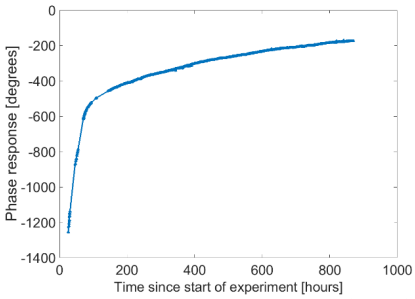

Figure 4: Phase history of buried trihedral during drying phase.

The depth scale applied to a VB-SAR output must be altered to take into account the refractive index of the soil. Firstly, using the estimated SMC history it is possible to calculate the virtual bandwidth generated by using the method presented in [4] to calculate the refractive index of the soil at each data point. From this (and knowledge of the number of samples) it was possible to calculate the range resolution and unambiguous range in free space. These values could then be corrected for the soil by using the average soil refractive index over the series of scans. The result of this process is shown in Figure 5, as can be seen the peak is very close to the correct depth which validates the assumption.

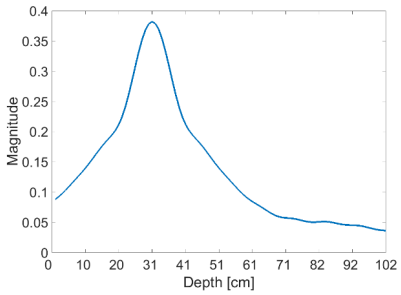

Figure 5: Output of VB-SAR FFT when complex history of buried trihedral processed.

In the low resolution TP data each subsurface column can be represented by a single pixel as there is degeneracy between pixels. Thus, the phase and amplitude history for each column was extracted by a single pixel from the centre of the pixel across the TP image set. By applying the VB-SAR processor to each column's complex history in turn a complete VB-SAR image can be formed. The result of this process is shown in **Figure 6**. Comparing this image to the TP images used as the data source (an example of which is shown in Figure

11th European Conference on Synthetic Aperture Radar
EUSAR 2016

3), notice how not only has the buried trihedral been resolved at 28cm below the surface but the surface trihedrals have appeared at the surface of the VB-SAR image. This demonstrates the secondary appeal of VB-SAR; the direct discrimination of surface and subsurface targets, as opposed to the need to use additional information sources to make this distinction in the "direct" subsurface imaging presented to date [5].

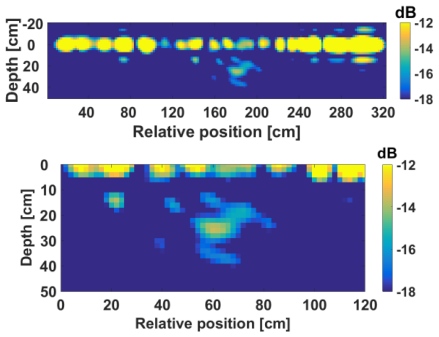

Figure 6: Complete VB-SAR image (top) and zoomed view highlighting buried target (bottom).

Note that in the dry areas at the sides of the image scene all targets including those buried within the soil appear at zero depth. This is evidence that the VB-SAR process is working as expected as the theory states that in areas that experience no SMC variation no virtual bandwidth is synthesised and so a completely flat phase history is presented to the VB-SAR processor which gives a peak at zero depth. All returns from all depths in the dry areas are effectively summed together and placed at zero depth, hence the strong surface return seen in Figure 6.

4 Summary

This study has explored the practical implementation of VB-SAR imaging. An image dataset which captured a controlled increase and then decrease in SMC was collected in the laboratory under carefully controlled conditions. By applying the TP process to the dataset a series of complex tomographic radar images was generated. The TP images were then fed into the VB-SAR processor.

From this, the basic principles of VB-SAR processing have been validated. Namely, a virtual bandwidth can be created and used to significantly enhance the subsurface range resolution compared to that produced using the formal range resolution generated by the radar's "real" bandwidth. In addition, the direct and unambiguous separation of surface and subsurface objects was demonstrated.

There are undoubtedly additional considerations and complications to the real-world application of the VB-SAR scheme. An absence of SMC measurements can be anticipated for wide-area imaging collected from air or spaceborne platforms. Non-linear sampling will compromise the performance of the scheme, and a knowledge of absolute SMC is necessary to provide an accurate depth scale (which depends on accurately assessing the virtual frequency step between samples). However, many conventional amplitude-based SMC retrieval schemes have been proposed [6].

Acknowledgements

This work was funded by Cranfield University.

References

[1] Morrison, K. and Bennett, J.: Virtual bandwidth SAR (VB-SAR) for centimetric-scale sub-surface imaging from space, International Journal of Remote Sensing, Taylor & Francis, 2015.

[2] D.J. Daniels, Ground Penetrating Radar, Encyclopedia of RF and Microwave Engineering, John Wiley & Sons, 2005

[3] Morrison, K. and Bennett, J.: Tomographic profiling - A technique for multi-incidence-angle retrieval of the vertical SAR backscattering profiles of biogeophysical targets, IEEE Transactions on Geoscience and Remote Sensing, IEEE., 2014.

[4] Hallikainen, M.T. and Ulabz, F.T. and Dobson, M.C. and El-Rayes, M.A. and Wu, L.-K.: Microwave Dielectric Behavior of Wet Soil-Part I: Empirical Models and Experimental Observations IEEE Transactions on Geoscience and Remote Sensing, IEEE., 1985.

[5] Mccauley, J.F. and Schaber, G.G. and Breed, C.S. and Grolier, M.J. and Haynes, C.V. and Issawi, B. and Elachi, C. and Blom, R.: Subsurface valleys and geoarcheology of the Eastern Sahara revealed by shuttle radar, Science, AAAS, 1982.

[6] Dubois, P.C., van Zyl, J., Engman, T.: Measuring soil moisture with imaging radars, IEEE Trans. Geosci. Remote Sens., IEEE, 1995.

A.3 CDSDS 2015 Poster

VB-SAR: Subsurface Radar Imaging From Space

Mr Alex Edwards-Smith
Supervisors: Dr Keith Morrison, Dr Daniel Andre

Cranfield UNIVERSITY

Motivation:

Virtual-Bandwidth Synthetic Aperture Radar (VB-SAR) is a new technique that enables sub-surface imaging from stand off distances, in contrast to current systems that require the sensing platform to be in immediate proximity to the soil surface.

The ability to acquire subsurface images from long distances is of great interest to many users; the remote nature of the sensing allows very large and difficult to access areas to be rapidly mapped.

Historically sub surface imaging from satellites has been limited to very dry areas illuminated with relatively low frequencies to minimise interaction with the soil

VB-SAR uses variations in soil moisture over a series of DInSAR images to synthesise a virtual bandwidth to produce a dramatic increase in range resolution.

VB-SAR Theory:

In a traditional (real bandwidth) SAR image the range resolution is directly related to the bandwidth of the transmitted radar signal; the higher the bandwidth, the better the resolution.

However, transmitting very high real bandwidths is difficult in practice, for both technological (there are issues with designing transmit and receive circuits that operate over very wide bandwidths) and regulatory (spectrum licensing) reasons.

VB-SAR eschews these problems by exploiting the dependence between soil moisture and the electrical properties of said soil to generate very large bandwidths

Formally, the virtual bandwidth generated is given by

$$B_v = f_R \Delta n$$

Where B_v is the Virtual Bandwidth generated, f_R is the real frequency in use and Δn is the change in refractive index of the soil over the series of radar images.

A key VB-SAR concept is that relatively small changes in soil moisture can produce very large bandwidths; for example, a moisture change of 15% will generate a virtual frequency of 6.4GHz when using a real frequency of 4GHz. This is because the refractive index of a soil varies rapidly with changes in soil moisture content, as shown below.

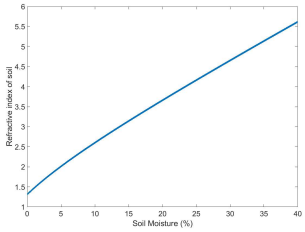

Method:

Within the laboratory a buried target was imaged with the radar system (pictured right) at regular intervals as water was added and the soil was then allowed to dry naturally

Knowledge of the amount of water added and the phase change exhibited by the target in each image allowed the moisture content in each image to be calculated

By using a model of the soil electrical properties the virtual frequency in each image was calculated, allowing an accurate depth scale to be applied to the VB-SAR depth plot

Results:

The radar images obtained in the laboratory were processed to give a very low range resolution. A single depth profile which intersects the buried trihedral from such an image is shown below.

As can be seen, the soil surface and buried target returns have combined to form a single poorly defined peak. The small peak around 40cm is due to antenna cross talk; the soil surface is approximately 180cm from the antennas

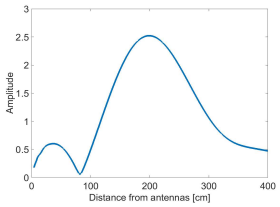

By applying the VB-SAR technique to the series of 1m range resolution images the depth profile below was obtained.

In this profile, the separate soil surface and buried target returns have been clearly resolved, showing the large increase in range resolution VB-SAR theory predicts.

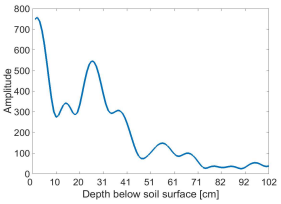

By stacking these depth profiles across the entire radar scene it is possible to build a complete VB-SAR image, an example of which is shown below. It is hoped that further processing will refine this image and remove the vertical banding present in dry areas.

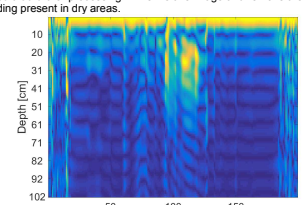

Future Work:

The proposed future work for this project includes investigating polarimetric VB-SAR and exploring the possibility of performing VB-SAR testing with data from spaceborne SAR systems.

PhD funded by Cranfield University

www.cranfield.ac.uk
Centre for Electronic Warfare, Cranfield University, Shrivenham, Swindon, SN6 8LA
a.edwardssmith@cranfield.ac.uk

A.4 Wavelength 2016 Poster

VB-SAR: Subsurface Radar Imaging From Space

Mr Alex Edwards-Smith
Supervisors: Dr Keith Morrison, Dr Daniel Andre

Cranfield UNIVERSITY

Motivation:

Virtual-Bandwidth Synthetic Aperture Radar (VB-SAR) is a new technique that enables high resolution subsurface imaging from stand off distances.

The ability to acquire subsurface images from large distances is of great interest to many users; the remote nature of the sensing allows very large and difficult to access areas to be rapidly mapped.

Historically subsurface imaging from satellites has been limited to very dry areas illuminated with relatively low frequencies to minimise interaction with the soil. It is not possible to separate returns from above and below ground objects in this situation so cross checking with visual images or other sources of information is necessary.

VB-SAR uses variations in soil moisture over a series of DInSAR images to synthesise a virtual bandwidth to produce a dramatic increase in depth resolution and directly image subsurface objects.

VB-SAR Theory:

In a traditional (real bandwidth) SAR image the range resolution is directly related to the bandwidth of the transmitted radar signal: the higher the bandwidth, the better the resolution.

However, transmitting very high real bandwidths is difficult in practice, for both technological and regulatory reasons: there are issues with designing transmit and receive circuits that operate over very wide bandwidths and spectrum licensing constraints preclude the use of certain frequencies.

VB-SAR avoids these problems by exploiting the dependence between soil moisture and the dielectric properties of a soil to generate very large bandwidths. When a wave of a given real frequency in air enters the soil volume the wave behaves as a wave of a higher, "virtual", frequency. If the soil moisture varies over a period of time this virtual frequency will also vary, creating a virtual bandwidth which can be exploited.

Formally, the virtual bandwidth generated is given by

$$B_v = f_R \Delta n$$

Where B_v is the Virtual Bandwidth generated, f_R is the real frequency in use and Δn is the change in relative refractive index of the soil over the series of radar images.

A key VB-SAR concept is that relatively small changes in soil moisture can produce very large bandwidths; for example, a moisture change of 15% will generate a virtual bandwidth of 6.4GHz when using a real frequency of 4GHz. This is because the relative refractive index of a soil varies rapidly with changes in soil moisture content.

Method:

Within the laboratory a buried target (26cm below the soil surface) was imaged with the radar system (pictured below) at regular intervals as water was added. The soil was then allowed to dry naturally. Knowledge of the amount of water added and the phase change exhibited by the target in each image allowed the soil moisture content in each image to be calculated. This knowledge of soil moisture allowed an accurate depth scale to be applied to the produced depth profiles.

Results:

By applying the VB-SAR technique to the set of 1m range resolution images the depth profile below (in black) was obtained. For comparison the depth profile produced by the 1m range resolution is shown in purple.

In this VB-SAR profile, the separate soil surface and buried target returns have been clearly resolved, showing the large increase in range resolution VB-SAR theory predicts.

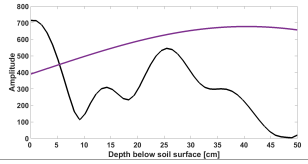

Further processing allows us to scale the returns of the surface and trihedral relative to one another. This is necessary for complete imaging of a subsurface scene. However, in this case it has left the relatively weak trihedral return swamped by the sidelobes of the strong surface return.

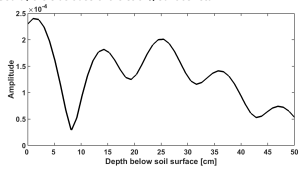

As the response of the surface of the soil does not significantly change over the change in soil moisture it is easy to remove it from the VB-SAR data. This also removes the sidelobes that were obscuring the trihedral, as shown below.

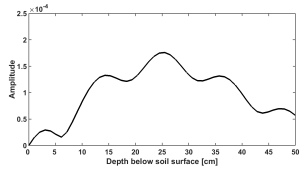

By stacking these depth profiles across the entire radar scene it is possible to build a complete VB-SAR image, an example of which is shown below. The buried target is now clearly visible at a depth of 26cm.

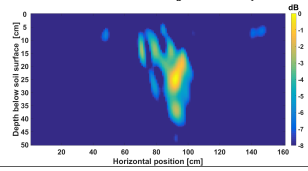

Future Work:
The proposed future work for this project includes investigating polarimetric VB-SAR and exploring the possibility of testing VB-SAR with data from spaceborne SAR systems.

PhD funded by Cranfield University

www.cranfield.ac.uk

Centre for Electronic Warfare, Cranfield University, Shrivenham, Swindon, SN6 8LA
a.edwardssmith@cranfield.ac.uk